RAY-OPTICS ANALYSIS OF INHOMOGENEOUS OPTICALLY ANISOTROPIC MEDIA

Proefschrift

ter verkrijging van de graad van doctor
aan de Technische Universiteit Delft,
op gezag van de Rector Magnificus prof.ir. K.C.A.M. Luyben,
voorzitter van het College voor Promoties,
in het openbaar te verdedigen op

maandag 25 januari 2010 om 12:30 uur

door

Maarten SLUIJTER

natuurkundig ingenieur
geboren te Weert.

Dit proefschrift is goedgekeurd door de promotor:
Prof.dr. H.P. Urbach

Samenstelling promotiecommissie:

Rector Magnificus,	voorzitter
Prof.dr. H.P. Urbach,	Technische Universiteit Delft, promotor
Prof.dr. P. Török,	Imperial College London
Prof.dr.ir. A. Gisolf,	Technische Universiteit Delft
Prof.dr.ir. G.M.W. Kroesen,	Technische Universiteit Eindhoven
Prof.dr.ir. J.J.M. Braat,	Technische Universiteit Delft
Dr. B.J. Hoenders,	Rijksuniversiteit Groningen
Dr. D.K.G. de Boer,	Philips Research Eindhoven

Dick K.G. de Boer heeft als begeleider in belangrijke mate aan de totstandkoming van het proefschrift bijgedragen.

The work described in this thesis has been carried out at Philips Research Eindhoven, the Netherlands, in the framework of the Philips Research Van der Pol programme.

Cover: the picture shows an optically birefringent calcite crystal. Photo: M. Sluijter

ISBN 978-90-74445-90-0

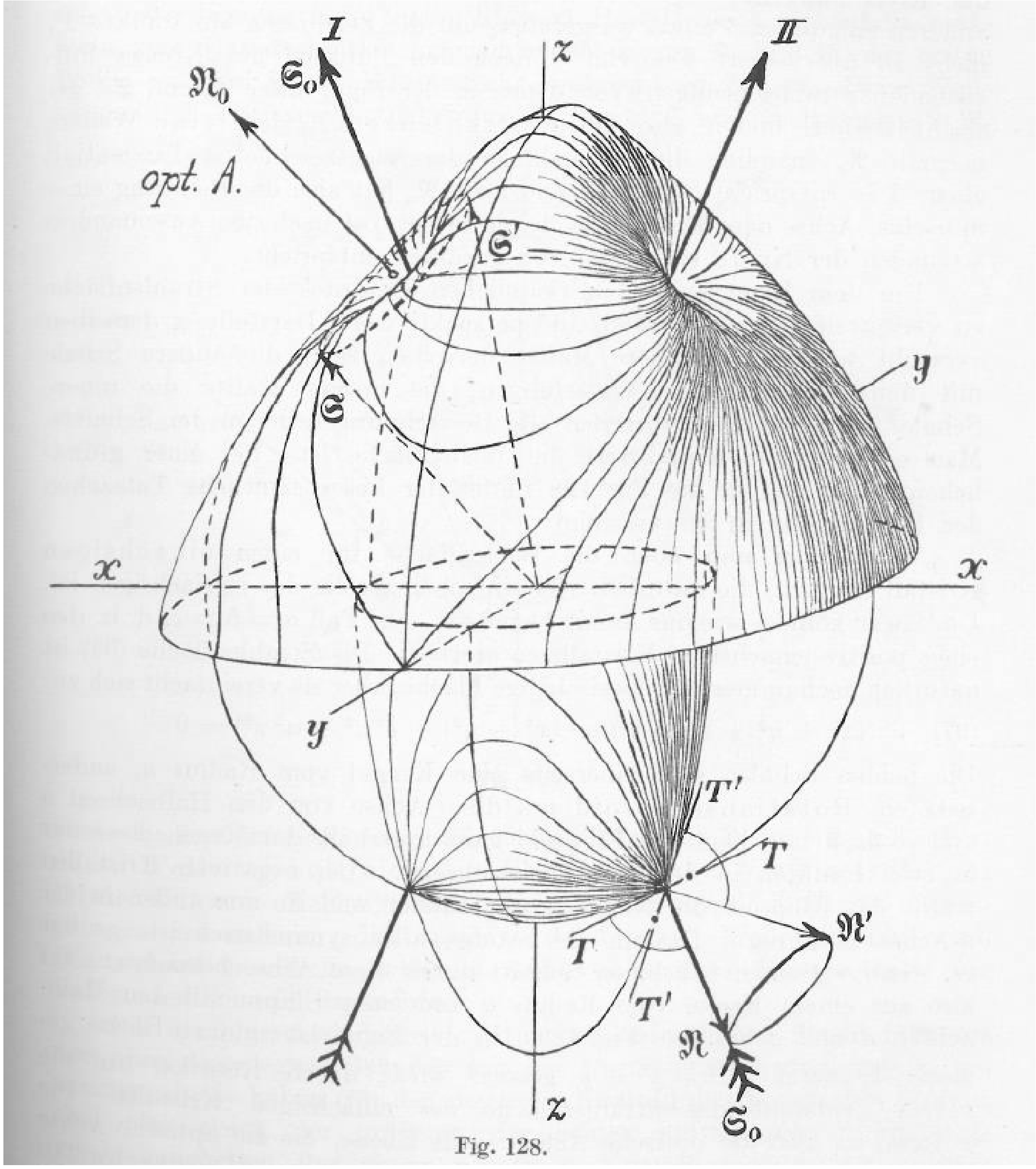

Fig. 128.

Schaefer's visualization of the biaxial optical indicatrix.
Clemens Schaefer, *Einführung in die Theoretische Physik*
(Walter de Gruyter & Co, Berlin, 1932).

Summary

Ray-optics analysis of inhomogeneous optically anisotropic media

When the optical behavior of light in a medium depends on the direction in which light is traveling, the medium is called optically anisotropic. Light is an electromagnetic wave and in this thesis, we discuss the electromagnetic theory on optical anisotropy. We do this with the assumption that the wavelength of light approaches zero. The field in optics in which this approach is applied is called geometrical optics. Then the wave character of light is not taken into account. In addition, we define a light wave as a set of rays, each with a certain direction and polarization state. The polarization state of a light ray defines the direction and the phase of the oscillating electric field of the light. In general, the light path of a light ray in an anisotropic medium depends on both the direction and the polarization state. The study of optical systems by means of calculating ray paths of polarized light rays is called polarized ray tracing.

Optical anisotropy in the geometrical-optics approach is a classical problem, and most of the theory has been known for more than a century. Since the 1970s optical anisotropy is frequently discussed in the literature due to the rapid advances in liquid-crystal applications, such as the Liquid-Crystal Display (LCD). Liquid crystal is attractive for high-tech applications since it has the material properties of a fluid and the optical properties of an anisotropic crystal. Moreover, the optical properties of liquid crystal can be controlled with electric or magnetic fields.

In the past few years Philips Research has had several activities in the field of liquid crystal. Novel liquid-crystal devices and applications have been investigated and developed into proof-of-principle demonstration models. In 2004 Philips Research introduced an auto-stereoscopic display technique based on liquid-crystal technology. Other examples are liquid-crystal-based backlight architectures for LCDs, liquid-crystal lenses and beam steering devices. Most of these liquid-crystal technologies are characterized by inhomogeneous material properties. This means that the optical properties depend on the position inside the liquid crystal. In view of the development of these technologies it is desired to understand and predict the propagation of light in inhomogeneous optically anisotropic media. This is the main goal of this thesis.

Optical anisotropy exists in two forms, namely uniaxial and biaxial anisotropy. Uniaxially anisotropic media are characterized by one optical axis and biaxially anisotropic media by two optical axes. The optical axis is a local direction of symmetry in the optical properties. The literature frequently discusses uniaxial anisotropy in the geometrical-optics approach at the boundary between two different media. However, the literature

does not provide a straightforward procedure to calculate ray paths of light rays in the bulk of inhomogeneous uniaxially anisotropic media. Moreover, the literature is nearly silent about the propagation of light rays in inhomogeneous biaxially anisotropic media. In this thesis we provide a general and rigorous overview of the classical theory on the propagation of light through inhomogeneous anisotropic media, either uniaxial or biaxial.

The literature provides the fundamental principle for the ray-tracing process in inhomogeneous media in geometrical optics, called the Hamiltonian principle. Building further on the Hamiltonian principle, we introduce general ray-tracing equations for inhomogeneous anisotropic media. These equations are new and define the state-of-the-art in the field of polarized ray tracing.

We apply our ray-tracing equations to study the optical properties of a number of liquid-crystal applications. For example, we study the residual lens action of a switchable lens structure for application in auto-stereoscopic three-dimensional (3D) displays. Auto-stereoscopic 3D displays enable a viewer to perceive depth in an image without any additional appliances, such as 3D glasses. With the help of a liquid-crystal lens structure, images can be switched between a normal (2D) mode and a 3D mode. With the help of our ray-tracing procedure, we propose an improved anisotropic lens design to minimize residual lens actions in the 2D mode, without compromising the performance of the 3D mode.

The desired lens effect in 3D displays can also be achieved with so-called liquid-crystal gradient-index (GRIN) lenses. The lens effect in these type of lenses is due to gradients in the material properties rather than a physically curved lens surface. For the first time in the literature, we simulate the angular-dependent optical properties of an advanced GRIN lens structure for application in auto-stereoscopic 3D displays.

With our advanced ray-tracing method, we have also studied the optical properties of liquid-crystal micro structures for application in for example side-lit LCD backlights. With this exercise, we have shown that our ray-tracing method can be applied to assess complex anisotropic optical configurations. Finally, we formulate a criterion for the applicability of geometrical optics to typical in-plane liquid-crystal configurations in terms of the inhomogeneous material properties.

In general, we can conclude that we have worked out the electromagnetic theory of inhomogeneous anisotropic media in the geometrical-optics approach. This has resulted in an advanced ray-optics analysis procedure. This procedure has been applied to study the optical properties of novel liquid-crystal applications. In contrast with other methods addressing optical anisotropy, the advanced ray-tracing procedure provides solid physical insight into the subject, is able to handle large computational domains and can be applied relatively easy to assess complex anisotropic electro-optical devices.

M. Sluijter Philips Research Eindhoven

Samenvatting

Stralen-optica analyse van inhomogeen optisch anisotrope materialen

Een medium waarvan het optische gedrag afhangt van de richting waarlangs licht zich voortplant wordt optisch anisotroop genoemd. Licht is een elektromagnetische golf en in dit proefschrift wordt de elektromagnetische theorie over optisch anisotrope media bestudeerd. Hierbij nemen we aan dat de golflengte van het licht verwaarloosbaar klein is. Het vakgebied waarin deze benadering wordt toegepast wordt geometrische optica genoemd. Hierbij wordt het golfkarakter van licht niet in rekening gebracht. Bovendien beschouwen we een golf als een verzameling lichtstralen, elk met een individuele richting en polarisatietoestand. De polarisatietoestand van licht definiëert de richting en de fase van het trillende elektrische veld van het licht. In het algemeen hangt het lichtpad van een lichtstraal in een anisotroop medium af van zowel de richting als de polarisatietoestand. Het bestuderen van optische systemen door het berekenen van het pad van gepolariseerde lichtstralen wordt 'polarized ray tracing' genoemd.

Optische anisotropie in de benadering van de geometrische optica is een klassiek onderwerp en vindt zijn oorsprong meer dan honderd jaar geleden. Sinds de jaren zeventig van de twintigste eeuw heeft het onderwerp aanzienlijk meer aandacht gekregen door de snelle ontwikkelingen in toepassingen van vloeibaar kristal, zoals de Liquid-Crystal Display (LCD). Vloeibaar kristal is met name geschikt voor toepassing in de high-tech industrie, omdat het zowel de eigenschappen heeft van een vloeistof als van een optisch anisotroop kristal. Bovendien kunnen de optische eigenschappen van vloeibaar kristal worden gecontroleerd met behulp van elektrische en magnetische velden.

In de afgelopen jaren zijn er door Philips Research nieuwe toepassingen van vloeibaar kristal geïntroduceerd. Zo heeft Philips Research in 2004 een techniek geïntroduceerd voor toepassing in autostereoscopische beeldschermen die gebaseerd is op de speciale eigenschappen van vloeibaar kristal. Andere voorbeelden zijn de toepassing van vloeibaar kristal in backlights voor LCD's, lenzen en 'beam-steering' toepassingen. In veel van deze technologiën zijn de materiaaleigenschappen inhomogeen. Dat wil zeggen dat de optische eigenschappen afhangen van de positie binnenin een materiaal. Daarom is het noodzakelijk om de voortplanting van licht in inhomogeen optisch anisotrope media te begrijpen en te voorspellen. Dit is het belangrijkste doel van het werk dat is beschreven in dit proefschrift.

Optische anisotropie komt voor in twee vormen, namelijk uniaxiale en biaxiale anisotropie. Uniaxiaal anisotrope materialen worden gekenmerkt door een enkele optische as en biaxiaal anisotrope materialen door twee optische assen. De optische as is een lokale richting die een symmetrie in de optische eigenschappen aanduidt. Uniaxiale anisotropie aan een grensvlak tussen twee verschillende media wordt in de literatuur uitvoerig behandeld binnen de benadering van de geometrische optica. De literatuur voorziet echter niet in een procedure om het pad van lichtstralen uit te rekenen in inhomogeen uniaxiaal anisotrope media. Bovendien worden biaxiaal inhomogeen anisotrope media nauwelijks behandeld. In dit proefschrift geven we een algemeen overzicht van de klassieke theorie over inhomogeen optisch anisotrope media, voor zowel uniaxiale als biaxiale media.

De literatuur behandeld het fundamentele principe om het pad van lichtstralen in de geometrische optica uit te rekenen in inhomogeen anisotrope media. Dit principe noemen we het Hamiltoniaanse principe. Met het Hamiltoniaanse principe als fundamentele basis introduceren we algemene vergelijkingen voor het berekenen van lichtpaden van lichtstralen in inhomogeen anisotrope media. Deze vergelijkingen zijn nieuw en definiëren de state-of-the-art in polarized ray tracing.

Met de nieuwe vergelijkingen bestuderen we een aantal toepassingen met vloeibaar kristal. In een voorbeeld simuleren we ongewenste lenseffecten in een schakelbare lensstructuur met vloeibaar kristal voor toepassing in autostereoscopische driedimensionale (3D) displays. Deze 3D displays creëren diepte in een beeld zonder dat de kijker gebruik hoeft te maken van extra hulpmiddelen, zoals een 3D bril. Door middel van een lensstructuur met vloeibaar kristal kunnen beelden worden geschakeld tussen een normale (2D) mode en een 3D mode. Met behulp van onze methode, presenteren we een verbeterd ontwerp voor de anisotrope lensstructuur waardoor ongewenste lenseffecten worden geminimaliseerd in de 2D mode zonder de 3D mode negatief te beïnvloeden.

Het gewenste lens effect in 3D displays kan ook worden bewerkstelligd met vloeibaar kristal in gradient-index (GRIN) lenzen. De lenswerking in dit type lenzen is gebaseerd op de afhankelijkheid van positie in de materiaaleigenschappen van het vloeibare kristal in plaats van de geometrische kromming van het oppervlak van een lens. Voor het eerst in de literatuur simuleren we de hoekafhankelijke optische eigenschappen van een geavanceerde GRIN lensstructuur voor toepassing in autostereoscopische 3D displays.

Met behulp van onze geavanceerde methode om lichtpaden van lichtstralen uit te rekenen bestuderen we ook de optische eigenschappen van microstructuren met vloeibaar kristal voor toepassing in bijvoorbeeld backlights voor LCD's. Hiermee laten we zien dat onze methode kan worden gebruikt om ingewikkelde optische structuren door te rekenen en te analyseren. Tenslotte formuleren we een criterium voor de toepasbaarheid van geometrische optica op typische tweedimensionale configuraties van vloeibaar kristal in termen van de inhomogene materiaaleigenschappen.

In het algemeen kunnen we concluderen dat we de elektromagnetische theorie van inhomogeen anisotrope media hebben uitgewerkt in de geometrische optica. Dit heeft geresulteerd in een geavanceerde procedure om lichtpaden van lichtstralen uit te rekenen. Deze procedure is toegepast om de optische eigenschappen van nieuwe toepassingen met vloeibaar kristal te onderzoeken. In tegenstelling tot andere methoden die optische anisotropie behandelen geeft onze procedure grondig fundamenteel inzicht in het onderwerp en kan het worden toegepast op rekendomeinen met grote afmetingen. Bovendien kan de procedure relatief makkelijk worden toegepast om complexe anisotrope optische configuraties door te rekenen en te analyseren.

M. Sluijter Philips Research Eindhoven

Contents

Chapter 1

Introduction

1.1 Optical anisotropy

Anisotropy is defined as the property of being directionally dependent. Anisotropy is the opposite of isotropy, which means invariance of direction. In physics, anisotropy can be found in many fields of interest. The most common example of anisotropic materials are crystals of solid elements or compounds in which atoms, ions or molecules are arranged in regular lattices. The anisotropy of a crystal manifests itself in the elastic, electric, magnetic and optical properties: measurements of an elastic modulus, dielectric constant, magnetic susceptibility or index of refraction give different results depending on the direction along which is measured. In this thesis, we confine our attention to optical anisotropy.

1.1.1 Solid crystals

A well-known example of an optically anisotropic crystal is calcite. The basic molecular unit of calcite is $CaCO_3$ (calcium carbonate) which is arranged in a pyramidal structure as is depicted in Fig. 1.1. The carbon and oxygen atoms form the base of the pyramid, with carbon lying in the center of the triangle of oxygen atoms. The calcium atom is positioned above the carbon atom, at the top of the pyramid. The direction of the line that goes through the carbon and calcium atoms defines the axis of symmetry of the molecule, and thus also the crystal. In a calcite crystal, this direction of symmetry is called the optical axis (cf. [1], p. 307).

Let us consider a plane electromagnetic light wave entering the crystal from below. The oscillating electric field of the incident plane wave is perpendicular to the optical axis (see Fig. 1.1) and interacts with the electrons in the crystal. The interactions with the electrons influence the speed of the propagating electromagnetic wave. However, the change in speed when entering the crystal is independent of the direction in which the electric field oscillates. Now let us consider an electromagnetic plane wave propagating perpendicular to the optical axis (see Fig. 1.1). Then the interaction of the electrons with the oscillating electric field component parallel to the optical axis ($E_{||}$) is different from the interaction with the electric field component perpendicular to the optical axis ($E_\perp$). In calcite, the speed of the electric field component $E_\perp$ is reduced more than the

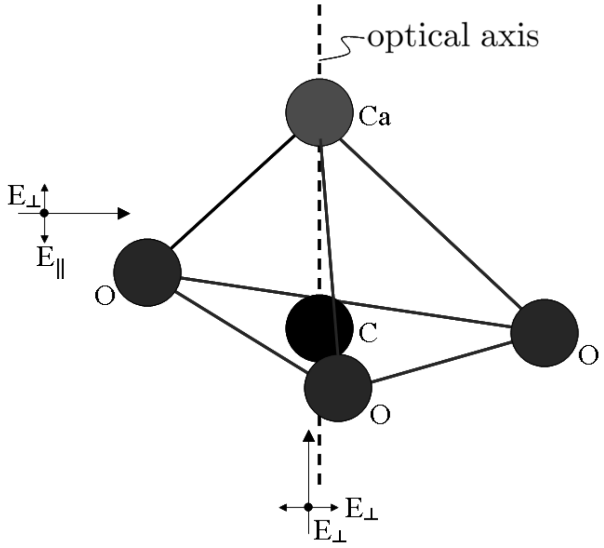

Figure 1.1: *Molecular unit of calcite ($CaCO_3$). The atoms are arranged in a pyramidal structure. The direction of symmetry is indicated by the dashed line and is called the optical axis.*

speed of the component $E_{||}$. The ratio between the speed of light in vacuum c and the speed of light in a medium v is defined the index of refraction n: $n = \frac{c}{v}$. For calcite, we then find two indices of refraction: $n_\perp = 1.658$ and $n_{||} = 1.486$ (cf. [2], p. **4**-141). These values apply for light with a wavelength of 589.3 nm. The index $n_\perp$ is called the ordinary index of refraction and $n_{||}$ is called the extraordinary index of refraction. The ordinary and extraordinary index of refraction of an anisotropic medium are usually indicated by n_o and n_e, respectively.

Apparently, in a general crystal, the index of refraction depends on the direction of propagation and the vibration direction of the electric field. The direction of vibration of the total electric field can be described as the sum of two independent directions of vibration. If the electric field components along these independent directions are uncorrelated, light is said to be unpolarized. If the electric field is vibrating along one particular direction, the light is linearly polarized. This means that the independently vibrating electric field components are exactly in phase. On the other hand, if the electric field components are not in phase, we say that the light is elliptically polarized.

The anisotropy of a crystal manifests itself in the property that an incident unpolarized light beam is split into two light beams when refracted at the surface of a crystal. Then the two refracted light beams inside the crystal have different directions of propagation. In addition, these two light beams are linearly polarized. For special optically anisotropic materials, the light beams are in general elliptically polarized. This special topic receives more attention later in this chapter. The bifurcation of a light beam by an anisotropic crystal is called double refraction (cf. [3], p. 340). Fig. 1.2 shows the principle of double refraction and the effect observed from a calcite sample.

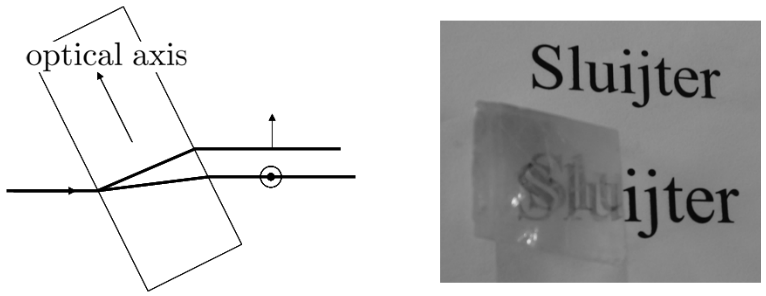

(a) (b)

Figure 1.2: *Principle of double refraction is depicted in (a). An unpolarized beam of light enters a crystal with the optical axis in the plane of the drawing. The beam is refracted by the crystal and splits into two linearly polarized light beams. The two refracted light beams that emerge from the crystal are parallel. In (b), the effect of double refraction by a calcite crystal is shown [4]. Clearly, the letters 'Slu' are imaged twice by the crystal.*

In general, the optical properties of a crystal are determined by three independent principal indices of refraction (cf. [5], p. 48 and 87). If all the principal indices are different, there are two optical axes and then we speak of biaxial optical anisotropy. When two of the principal indices are identical, there are two independent indices (ordinary and extraordinary) and one optical axis. When this is the case, we speak of uniaxial optical anisotropy. When all principal indices are identical, we speak of optical isotropy and then there is no optical axis.

Cubic crystals such as diamond (C) or salt (NaCl) are optically isotropic. Crystals with a tetragonal, rhombohedral or hexagonal lattice system are uniaxially anisotropic. Examples of uniaxial crystals are calcite, sapphire (Al_2O_3) or ice. Crystals with a triclinic, monoclinic or orthorhombic lattice system are biaxially anisotropic, such as mica (cf. [6], p. 679).

1.1.2 Liquid crystals

Besides solid crystals, other materials like plastics and polymers can also be optically anisotropic. Moreover, some anisotropic materials occur in the liquid phase. An anisotropic material of which the properties are associated with both solids and liquids is liquid crystal. The molecules of a liquid crystal behave like the molecules of a liquid, but at the same time they maintain some degree of orientational and positional order, like in a solid crystal. In other words, liquid crystal is a state of matter that is intermediate between the crystalline solid and the amorphous liquid.

The most common type of molecule that forms liquid crystal is a rod-shaped molecule. An example is the 5CB (4-n-pentyl-4'-cianobiphenyl) liquid crystal (cf. [5], p. 6). The different phases of the 5CB liquid crystal are depicted in Fig. 1.3. Below 24.0°C the phase of 5CB is the crystalline solid. Then the crystal has both positional and orientational order. Between 24.0°C and 35.3°C the sequence of phase changes on rising temperature

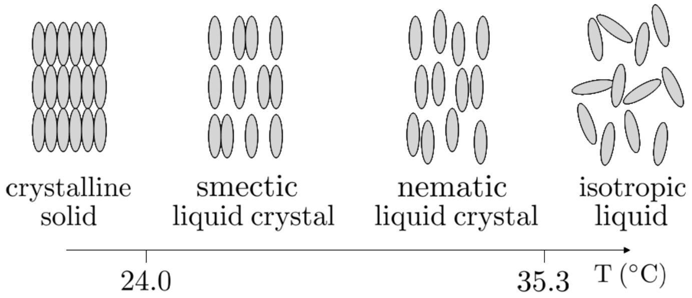

Figure 1.3: *The sequence of phase changes of 5CB on rising temperature. The melting point is* 24.0° *C and the clearing point is* 35.3° *C.*

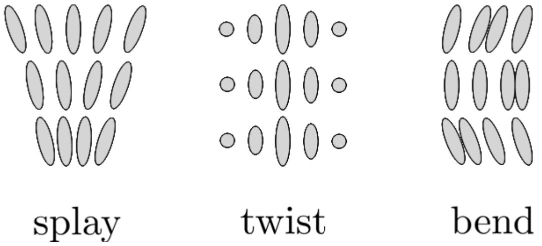

Figure 1.4: *Splay, twist and bend deformations of liquid crystal.*

is from the smectic to the nematic phase. In the smectic phase, the liquid crystal has a lower degree of positional order than in the crystalline solid. The nematic phase has a long range orientational order, but no positional order. Then the nematic liquid crystal may appear milky if the orientational order exists in many different domains. The nematic liquid crystal is clear only when a long range order exists in the whole medium. At 35.3°C, the liquid crystal neither has positional nor orientational order and becomes isotropic. This temperature is known as the clearing point. Next to rod-shaped molecules there also exist for example disk-shaped molecules. These type of molecules are in general uniaxially anisotropic. Liquid crystals can also be biaxially anisotropic, for example boomerang-shaped molecules. Next to the smectic and nematic phases, liquid crystals can also have chiral (also known as cholesteric) phases [7]. Chiral molecules lack inversion symmetry and are optically active. However, chiral liquid crystals will not be considered in this thesis.

The unit vector that points along the rod-shaped molecule axis (i.e. the optical axis) is called the director. In a nematic liquid crystal the director varies with position and we can distinguish between three types of deformation, namely splay, twist and bend deformations. Fig. 1.4 shows the different types of deformations schematically. These deformations can be induced by external factors, such as electric or magnetic fields [8] and mechanical distortions. The free elastic energy density of a deformed nematic liquid crystal in terms of the director $\hat{\mathbf{d}}$ is given by (cf. [9], p. 32)

$$U = \frac{1}{2}K_{11}(\nabla \cdot \hat{\mathbf{d}})^2 + \frac{1}{2}K_{22}(\hat{\mathbf{d}} \cdot \nabla \times \hat{\mathbf{d}})^2 + \frac{1}{2}K_{33}(\hat{\mathbf{d}} \times \nabla \times \hat{\mathbf{d}})^2, \tag{1.1}$$

where K_{11}, K_{22} and K_{33} are elastic constants with which the associated splay, twist and bend deformation energies scale. These constants describe how stiff the liquid crystal is to deformations of the director. The unit of these constants is Newton and typical values are about 10^{-11} Newton.

1.1.3 Liquid-crystal mixtures

A single liquid-crystal compound cannot fulfill all the specifications for applications. The small temperature window for the nematic phase of for example 5CB (24.0°C$-$35.3°C) is not adequate for most industrial applications operating between -20°C and 80°C. This problem can be overcome by using mixtures of liquid-crystal compounds. The melting point of a binary mixture of compounds is smaller than either of its constituent compounds. The clearing point is usually the linear average of the composition. Both the melting point and the clearing point of a mixture depend on the mixture ratio. In conclusion, a mixture of two or more liquid-crystal compounds can offer a much larger temperature range that exhibits the nematic phase.

In this thesis, we discuss applications of two industrial liquid-crystal mixtures, namely the TL213 and BL009 mixture. In Table 1.1 the material properties of these mixtures are listed. Next to the parameters discussed above, the static dielectric permittivity $\triangle\varepsilon = \varepsilon_{||} - \varepsilon_{\perp}$ and the viscosity γ of the liquid-crystal mixtures are also indicated. Finally, Table 1.1 gives the wavelength dependency of the indices n_o and n_e for the TL213 mixture. The human eye is most sensitive for wavelengths near 555 nm under daylight circumstances. For reasons of simplicity, we will assume the values of the indices for liquid crystal TL213 at 589.3 nm (yellow) for the remainder of this thesis.

Table 1.1: *Liquid-crystal properties of BL009 and TL213 mixtures [10].*

parameter	BL009	TL213	TL213		
melting point (°C)	< -20	< -20	wavelength (nm)	n_o	n_e
clearing point (°C)	108	87	508.5	1.5354	1.7906
n_o (589 nm)	1.5266	1.5271	546.1	1.5310	1.7772
n_e (589 nm)	1.8181	1.7658	589.3	1.5271	1.7658
K_{11} (pN)	17.9	16.8	632.8	1.5233	1.7560
K_{22} (pN)	7.0	6.5			
K_{33} (pN)	33.5	22.0			
$\Delta\varepsilon$	15.5	5.7			
γ (cSt)	83	49			

Nematic liquid crystals have the material properties of a fluid and when properly aligned it has the optical properties of an anisotropic crystal. In addition, the director can be controlled by external electric or magnetic fields. Moreover, liquid-crystal mixtures enables the control of the temperature range that exhibits the nematic phase. As a result, nematic liquid crystal is a highly appropriate material for industrial electro-optical applications.

1.2 Nematic liquid-crystal applications

The discovery of liquid crystals is usually attributed to an Austrian botanist Friedrich Reinitzer [11]. In 1888, he experimented with a substance and noted that it had two melting points. At 145.5°C it melted from a solid to a cloudy liquid and at 178.5°C it turned into a clear liquid. Reinitzer sent samples of this substance to Otto Lehman, a professor of natural philosophy (physics) in Germany. Lehman studied Reinitzer's substance and noted its similarity with some of his own samples. As he became more convinced that the opaque phase was a uniform phase of matter sharing properties of both liquids and solid crystals, he began to call them liquid crystals.

Nowadays, liquid crystals are an important phase of matter both scientifically and technologically. This situation is quite a recent development. Before 1960, work on liquid crystals did not receive much attention, probably due to the fact that no one saw an application for them. In the period 1945-1958 it was all quiet on the liquid crystal front and the subject did not even appear in textbooks. However, in the 60s the interest in liquid crystals awakened in the United States, Great Britain and the Soviet Union and in the early 70s, the introduction of the liquid-crystal display (LCD) became a fact. Nowadays, nematic liquid crystal is used in virtually all commercially available displays. But displays are not the only application to nematic liquid crystals. Fig. 1.5 shows the result of a literature search [12]: the number of scientific publications related to nematic liquid-crystal applications, except LCDs, is depicted as a function of time in the period 1932-2009. Clearly, the interest in liquid crystals exploded during the 70s and 80s (stimulated by the arrival of the LCD) and the activity in this field is still growing. Examples of liquid-crystal applications (other than display-related applications) are thermometers, optical switches and waveguides [13]-[16], optical fiber couplers [17], switchable lenses [18], spatial light modulators for beam steering [19] or tunable color laser arrays [20]. More exotic applications of liquid crystals can be found in for example

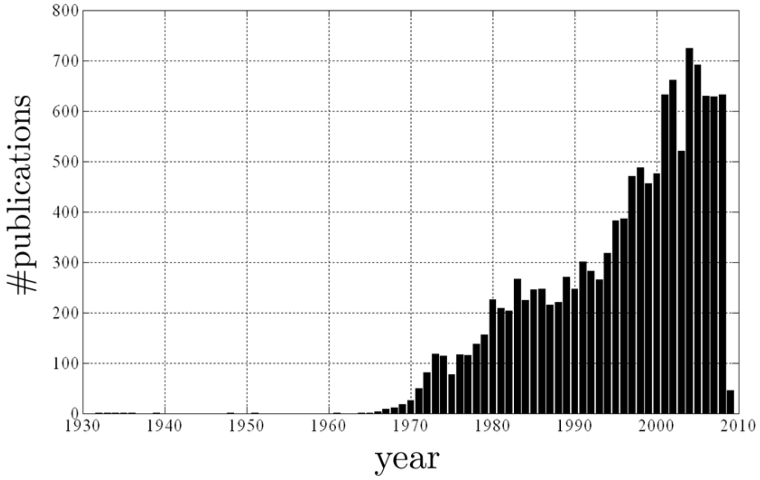

Figure 1.5: *Number of scientific publications related to nematic liquid-crystal applications (except liquid-crystal displays) in the period 1932-2009 [12]. The search was performed in February 2009.*

eye-wear devices [21][22] or even cosmetics [23].

1.2.1 Liquid-crystal-based lenses for 3D displays

In what follows, we will explain why nematic liquid crystal is an important component in the technology of switchable 2D/3D displays. The reason for this is that a significant part of the scientific work described in this thesis is based on the application of liquid crystal in 3D displays (Chapters 6 and 7).

With stereoscopic imaging techniques it is possible to provide distinct images to each eye of a viewer, creating the binocular disparity depth cue. Binocular disparity is the difference in images projected to the left and right eye of a viewer. In addition to other depth cues (cf. [24], p. 2), binocular disparity enables us to perceive depth. One pair of distinct images is called a stereo pair. One of many options to create stereo pairs is the projection of multiple images towards multiple viewing angles, see Fig. 1.6-(a). This concept is called auto-stereoscopic imaging for which no additional appliances are necessary, such as polarized glasses (cf. [24], p. 108). Then each individual image corresponds to a different viewpoint of for example an object or scene and is called a view. Next to the binocular disparity depth cue, the application of multiple views also induces the motion parallax depth cue. Motion parallax means that objects close to a viewer appear to move more than objects further away. Views can be generated by for example a three-dimensional imaging display.

There are two important methods for auto-stereoscopic imaging, which differ in the way the views are separated for presentation to each eye. These are lenticular sheet and barrier strip techniques, using refraction and occlusion, respectively (cf. [24], p. 30).

A parallax barrier consists of an array of vertical slits in an otherwise opaque barrier. Such a barrier can be placed a slight distance in front of for example a display. Then the barrier ensures that the image intended for the left eye of a viewer is blocked for the right eye and vice versa. The main disadvantage of the parallax barrier technique is that the auto-stereoscopic image is often dim since so much light is blocked by the barrier.

A lenticular sheet consists of an array of cylindrical lenses. This lenticular sheet is placed in front of, for example, a display as is shown in Fig. 1.6-(b). The light from the (sub-)pixels of the display is then collimated by the lenticular and directed towards different viewing angles. The contribution of all pixels of a display produce the individual views. Lenticular-based three-dimensional imaging techniques have one significant advantage over barrier methods: image brightness is superior since the lenticular sheet is based on refraction rather than occlusion.

In general, a multi-view 3D display suffers from a resolution loss, since the pixels of a display are used to generate multiple images. The resolution loss of each view in a multi-view 3D display is equal to a factor that is the total number of views. In 2004, Philips Research has developed an innovative technique of creating auto-stereoscopic three-dimensional (3D) images by combining a multi-view lenticular-based 3D display technology with advanced computer graphics and image analysis techniques [25]. The display technology involved makes use of a lenticular sheet that is able to switch between a conventional 2D mode and an auto-stereoscopic 3D mode with the help of nematic

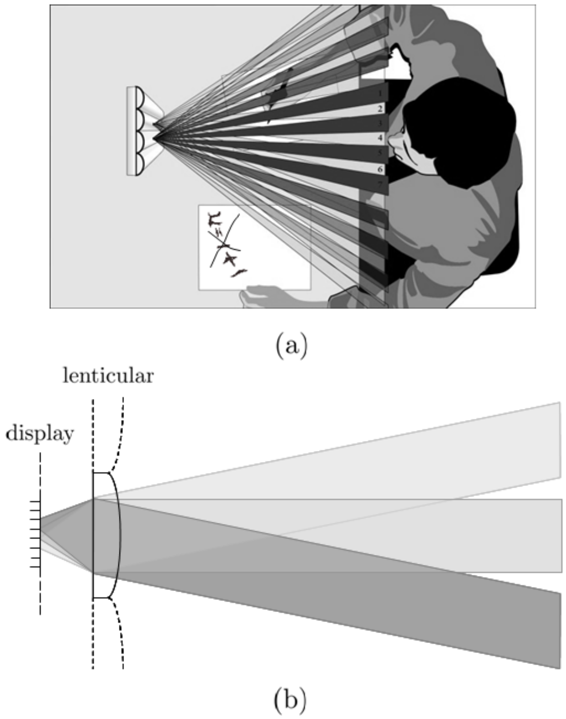

Figure 1.6: *Schematic principle of an auto-stereoscopic lenticular-based three-dimensional imaging display. In (a), multiple images are projected to multiple viewing directions. The neighboring images form stereo pairs, thus enabling the binocular disparity and motion parallax depth cues. The lenticular is placed in front of a display, as depicted in (b). The light from sub-pixels of the display is collimated by the lenticular and directed towards different viewing directions. The contribution of all pixels of a display produce the individual views.*

liquid-crystal material. In this way it is possible to have a high-brightness 3D display capable to regain the full native 2D resolution of the underlying display [26][27].

The lenticular sheet is an array of negative lenses filled with liquid crystal. The liquid crystal can be switched between two optical states with the help of an electric field. As a result, the lens effect of the lenticular can be switched on and off. Another option to enable the switchable lens effect is the use of a liquid-crystal gradient-index lens structure. This technology does not require a lenticular sheet since the lens effect is generated by the opposed gradients in the nematic liquid crystal itself. In this treatise, we will investigate the issues involved for both the lenticular and the gradient-index solutions in 3D displays.

1.2.2 Liquid-crystal-based light guide structure

Besides the application of nematic liquid crystal in 3D displays, other liquid-crystal devices will be investigated as well (Chapter 8). One important example is a liquid-crystal-based optical element that can actively control guiding and local extraction of polarized light. A promising application of such a device can be found in for example beam control devices for lighting applications or applications requiring local dimming and highlighting [28]. Light that is extracted from the optical element is linearly polarized, a feature that is desired for applications such as backlight architectures for liquid-crystal displays. In contrast with direct-lit geometries, the optical element is suitable for side-lit configurations. The principle of side-lit geometries is explained in Fig. 1.7. The advantage of this technology is that it offers a reduction in power consumption, since it is capable of local dimming and highlighting with a low number of light sources. Different types of side-lit configurations that produce light with a specific polarization have been investigated in the past. One approach consists of a system using birefringent material applied on a micro-structured light guide [29]. However, the optical element discussed here forms a basis for a novel approach to enable a side-lit geometry. This approach does not require the manufacturing of microstructures. It enables a controlled guiding and extraction of polarized light and a high resolution that is independent of the number of light sources.

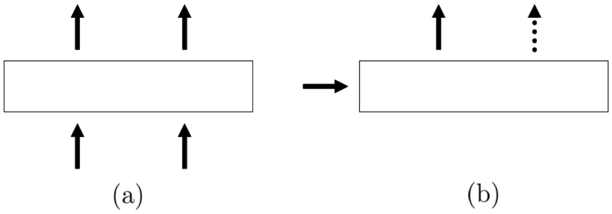

Figure 1.7: *Principle of direct-lit and side-lit geometries. In (a) unpolarized light enters the system at the bottom and polarized light comes out from the top side. In (b) unpolarized light enters the system at the side and polarized light emerges from the top side. The liquid-crystal-based side-lit configuration we discuss enables a controlled local extraction of polarized light and a high resolution that is independent of the number of light sources.*

1.2.3 Recent discovery biaxial nematic phase

The liquid-crystal applications discussed involve uniaxially anisotropic nematic liquid crystals. Firm evidence of the biaxial nematic phase in liquid crystals has only been established recently in 2004 [30]-[32]. The discovery of this new type of nematic liquid crystals has created considerable excitement, for it has opened up new areas of both fundamental and applied research, see for example [33]. It is predicted that the application of biaxial nematic liquid crystal in, for example, displays could result in decreased response times to electric fields and improved performance and efficiency. The electromagnetic theory for inhomogeneous media discussed in this thesis includes both uniaxial and biaxial anisotropy and can therefore be considered as a valuable supplement to these recent developments in the field of nematic liquid crystals.

1.3 Modeling optical anisotropy

Due to the rapid advances in liquid-crystal applications it is desired to understand and model the propagation of light waves through anisotropic media. In the type of applications mentioned in the previous section, the material properties depend on the position inside the medium. Then the material properties of a medium are said to be inhomogeneous. There are many methods available to model the optical properties of inhomogeneous optically anisotropic media. These methods provide the necessary assistance in the design and characterization of liquid-crystal devices. In this section, we briefly discuss various approaches to model the optics of optically anisotropic media. Moreover, we explain which approach is most appropriate for our objective: to understand and simulate the optical properties of inhomogeneous optically anisotropic media in applications mentioned in Subsections 1.2.1 and 1.2.2.

1.3.1 Overview of methods

The (extended) Jones and Berreman matrix-type methods are techniques used for predicting the transmission and reflection properties of liquid-crystal optics for displays (cf. [5], p. 306). These methods are based on a stratified medium approximation, assuming a one-dimensional variation of the liquid-crystal orientation [34]-[36]. However, the matrix-type methods are not appropriate for applications with inhomogeneous material properties in two or three dimensions and diffraction effects are not taken into account.

The Finite Difference Time Domain (FDTD) method is a numerical method providing a solution to Maxwell equations considering both the spatial and temporal variations of the electromagnetic field. The FDTD method was first introduced for isotropic media by Yee [37]. Extensions of the method to anisotropic media have been developed later in the 90s [38][39]. The FDTD method is based on a discretization of Maxwell's equations in space and time by using central-difference expressions for the space and time derivatives. The FDTD method correctly accounts for all types of reflections, diffraction and scattering effects introduced by the media involved. Although the FDTD method is rigorous and accurate, its application to large dimensions is limited by memory requirements.

When an electromagnetic wave propagates along a waveguide for a large distance, rigorous numerical simulation is difficult. A well established numerical technique in the area of integrated optics is the Beam Propagation Method (BPM). This method is applicable to a very broad range of optical wave propagation problems in wave guide optics, such as optical fibers or switches, and a wide variety of algorithms has been developed in the past decades. Similar to the FDTD method, the BPM allows variations of the material properties on a scale similar to the wavelength of light. However, the BPM does not include time and is in general formulated in the paraxial approach. In the past decade the BPM has also been extended with algorithms for the analysis of anisotropic media, see for example [40] and [41]. In the range of its applicability the BPM can be used advantageously instead of the FDTD method, providing a definite enhancement over any matrix-type method, without the computational drawbacks associated with the FDTD method. However, the BPM ignores reflections and the most useful wide-angle

BPM (beyond the paraxial approach) is restricted to propagation angles of few tens of degrees.

The scattering of a plane wave by anisotropic periodic gratings can be studied with for example the Fourier Modal Method (FMM). In the FMM the material structure and the electromagnetic fields are expanded in terms of Fourier series. The extension of the FMM to anisotropic media is a non-trivial matter [42][43]. Another method for solving electromagnetic scattering problems is the Finite Element Method (FEM). The FEM is a general numerical method for solving boundary value problems in mathematical physics. In [44] the FEM is applied to anisotropic gratings and there it is concluded that the method is highly appropriate for anisotropic and inhomogeneous media. However, the computational domain is restricted to approximately 50 × 50 wavelengths because of memory constraints.

In general the methods discussed above involve solving a large coupled system of linear equations and require numerical computation techniques. These methods are able to handle complex anisotropic configurations, but provide little physical insight into the electromagnetic properties of light waves propagating in anisotropic media. At the same time, we would like to understand the relation between the anisotropic material properties, the direction of propagation and the electromagnetic field of a light wave. There is one appropriate discipline which can provide us with answers to these type of questions: geometrical optics.

1.3.2 Geometrical optics

In geometrical optics optical laws are obtained in the limit where the wavelength of the light vanishes. In practice this means that the characteristic dimensions of an optical system are assumed much larger than the wavelength. Geometrical optics is highly appropriate for didactic purposes and provides us with a good 'language' to study the optical properties of anisotropic media. Moreover, geometrical optics enables the modeling of inhomogeneous anisotropic media in three dimensions assuming that the material properties change slowly over the distance over one wavelength. If the material properties change rapidly within the distance of one wavelength, the wave character of light can no longer be ignored. Optical phenomena for which the wave character of light is important, such as the diffraction of light by a grating, is beyond the scope of geometrical optics. This restriction is not necessarily a problem for the type of applications that we are interested in in this thesis. This we can explain as follows.

Consider an inhomogeneous anisotropic medium in which the director is rotated by an angle of 90° over a distance L_d, see Fig. 1.8. Then the change in optical properties over the distance L_d is maximum (for constant principal indices of refraction). As a rule of thumb the distance L_d should be in the order of 20 wavelengths or higher to allow geometrical optics. This statement is further discussed in Chapter 5 of this thesis. With a wavelength of approximately 500 nm, the distance L_d should then be in the order of 10 μm. The typical dimensions of for example a liquid-crystal gradient-index lens are 10×150 μm or higher with modest director variations. The dimensions of a liquid-crystal element in the light guide structure are typically 6×12 μm. As a consequence, the application of geometrical optics to the latter application is a subject of debate. However, in Chapter 5 we will see that the application of geometrical optics to dimensions smaller than 20 wavelengths can still be acceptable to form an idea of the main qualitative char-

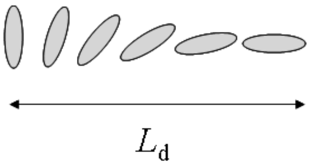

Figure 1.8: *Rotation of the director by an angle of* 90° *over a distance* L_d*. Then* L_d *is the distance over which a maximum change in optical properties occurs (for constant principal indices of refraction). Geometrical optics can be applied if the change in optical properties over the distance of a wavelength* λ *is small:* $\frac{\lambda}{L_d} \ll 1$*.*

acteristics of an optical system. In Chapter 8 we will see that the simulated qualitative characteristics of the light guide structure match experimental results. In general we conclude that for the liquid-crystal applications discussed in this thesis, we can apply geometrical optics provided that we know the validity conditions to ensure a proper interpretation of the results.

Optical anisotropy in the geometrical-optics approach is a classical problem, and most of the theory has been known for more than a century. In particular, uniaxial anisotropy is frequently discussed in the literature [45]-[74]. The basic equations for ray paths of light rays in inhomogeneous media are discussed by Kline and Kay [75]. However, the literature does not provide a straightforward procedure to calculate ray paths of light rays in inhomogeneous uniaxially anisotropic media from which it is clear how the anisotropic material properties can influence the propagation of light. Moreover, the literature discusses geometrical optics at interfaces between biaxially anisotropic media [76]-[82], but is silent about the propagation of light rays in inhomogeneous biaxially anisotropic media. Clearly, the modeling of the optical properties of anisotropic media in the geometrical-optics approach is not a trivial matter. In this thesis we provide a general and rigorous overview of the classical theory on the propagation of light through inhomogeneous anisotropic media.

1.3.3 Hermitian dielectric permittivity tensor

The general character of the theory presented in this thesis manifests itself by the definition of a complex Hermitian dielectric permittivity tensor. The dielectric permittivity tensor $\underline{\underline{\varepsilon}}$ defines the mathematical relation between the electric flux density vector $\mathbf{D}$ and the electric field $\mathbf{E}$ by

$$\mathbf{D} = \varepsilon_0 \underline{\underline{\varepsilon}} \mathbf{E}, \tag{1.2}$$

where ε_0 is the dielectric permittivity constant in vacuum. The (complex) elements of the tensor $\underline{\underline{\varepsilon}}$ define the optical properties of a medium and on the Cartesian basis $\{\hat{\mathbf{x}}, \hat{\mathbf{y}}, \hat{\mathbf{z}}\}$ the permittivity tensor is represented by a 3x3 matrix

$$\underline{\underline{\varepsilon}} = \begin{pmatrix} \varepsilon_{xx} & \varepsilon_{xy} & \varepsilon_{xz} \\ \varepsilon_{yx} & \varepsilon_{yy} & \varepsilon_{yz} \\ \varepsilon_{zx} & \varepsilon_{zy} & \varepsilon_{zz} \end{pmatrix}. \tag{1.3}$$

Because the dielectric permittivity tensor is assumed Hermitian, the elements on the diagonal are real by definition. This means that a complex Hermitian tensor only includes media without absorption. A discussion on optically anisotropic media with absorption goes beyond the scope of this thesis.

In general, there exists a complex orthonormal basis $\{\hat{\mathbf{u}}, \hat{\mathbf{v}}, \hat{\mathbf{w}}\}$ on which the Hermitian tensor is diagonal:

$$\underline{\underline{\varepsilon}} = \begin{pmatrix} \varepsilon_u & 0 & 0 \\ 0 & \varepsilon_v & 0 \\ 0 & 0 & \varepsilon_w \end{pmatrix}. \tag{1.4}$$

The complex orthonormal basis $\{\hat{\mathbf{u}}, \hat{\mathbf{v}}, \hat{\mathbf{w}}\}$ is called the principal basis. When the elements on the diagonal of the tensor in Eq. 1.4 have different values, a medium is said to be optically anisotropic. When two of the diagonal elements are equal, the medium is uniaxially anisotropic and when all elements differ in value, the medium is biaxially anisotropic. Here it is assumed that anisotropic media have optical axes, but there are cases in which a complex Hermitian dielectric permittivity tensor does not give rise to an optical axis. This will become more clear in Chapters 2-4.

Standard textbooks discussing optical anisotropy are usually restricted to a real symmetric dielectric permittivity tensor. Then there are always optical axes and light in anisotropic media is always linearly polarized. However, a real symmetric permittivity tensor is a special case of a complex Hermitian permittivity tensor. Hence a complex Hermitian dielectric permittivity tensor represents a more general class of optically anisotropic media. Moreover, we will see that light in these type of media is in general elliptically polarized. Hermitian permittivity tensors occur in for example optically active media. These are media which actively rotate the plane of polarization of a beam of light, such as quartz or chiral liquid crystals. Yeh et al. describe an anisotropic complex Hermitian permittivity tensor with optical activity for which there is no optical axis (cf. [5], p. 80). Optical activity also occurs in magneto-optical effects, such as media in the presence of a static magnetic field. This type of optical activity is called Faraday rotation ([5], p. 85). Landau et al. also describe optical activity in anisotropic media and mention the absence of an optical axis (cf. [83], footnote on p. 350). Another example in which Hermitian permittivity tensors occur are photoanisotropic media (cf. [44], p. 55). Photoanisotropic media are sensitive to both intensity and polarization of light. In general, we remark that in case of a complex Hermitian permittivity tensor, the literature broadly discusses (anisotropic) media with optical activity, but is silent about the classical electromagnetic theory of optically anisotropic media.

In this thesis, the classical theory on the propagation of light through inhomogeneous anisotropic media with a complex Hermitian dielectric permittivity tensor will be thoroughly discussed in Chapters 2, 3 and 4. Here we assume that the macroscopic (non-dispersive) constitutive relations in anisotropic materials are of the form given by Eq. 1.2 and

$$\mathbf{B} = \mu_0 \underline{\underline{\mu}} \mathbf{H}, \tag{1.5}$$

where $\mathbf{B}$ and $\mathbf{H}$ are the magnetic flux density vector and the magnetic field, respectively, and μ_0 is the magnetic permeability constant in vacuum. We remark that in this thesis we only consider nonmagnetic media. This means that the permeability tensor $\underline{\underline{\mu}}$ is assumed the unit tensor:

$$\underline{\underline{\mu}} = \mathbf{1}. \tag{1.6}$$

In contrast with Eqs. 1.2 and 1.5, the constitutive relations for optically active media are of the form (cf. [57], p. 2385)

$$\mathbf{D} = \varepsilon_0 \underline{\underline{\varepsilon}} \mathbf{E} + i \underline{\underline{G}} \mathbf{H}, \tag{1.7}$$

$$\mathbf{B} = \mu_0 \underline{\underline{\mu}} \mathbf{H} - i \underline{\underline{G}} \mathbf{E}, \tag{1.8}$$

where $\underline{\underline{G}}$ is called the gyrotropic tensor or the optical activity tensor. Crystals with optical activity are also called circularly birefringent (cf. [84], p. 432). For a general discussion on the constitutive relations, we refer to [85], where various types of birefringence of nonmagnetic crystals are classified in terms of their multipole origins. In this thesis, we consider media for which the gyrotropic tensor is zero and the constitutive relations are given by Eqs. 1.2 and 1.5: we consider nonmagnetic, linearly birefringent media with Hermitian permittivity tensors (no absorption).

1.4 Thesis outline

The propagation of light waves in optically anisotropic media is described by the Maxwell equations. From the Maxwell equations we can learn what optical anisotropy is and understand the electromagnetic properties of light waves in anisotropic media. The electromagnetic theory on optical anisotropy is classical and is known for more than a century. In Chapter 2, however, we discuss the classical electromagnetic theory assuming a position-dependent complex Hermitian dielectric permittivity tensor. In that sense, the classical theory is formulated in a unique way. We discuss both uniaxial and biaxial anisotropy, assuming anisotropic media for which there always exist optical axes.

In general we can define two main regions of interest in an anisotropic medium: 1) the interface region between two anisotropic media and 2) the anisotropic bulk region. At the interface between two different media, the optical wave field is determined by boundary conditions. From the boundary conditions, we derive the optical properties of both uniaxial and biaxial interfaces and discuss a general ray-tracing procedure for anisotropic interfaces in Chapter 3. The theory discussed in Chapter 3 is equivalent to what can be found in the literature, but has been formulated in such a way that it applies to complex Hermitian permittivity tensors as well. In a number of didactic examples we apply the theory to uniaxial and biaxial interfaces, assuming a real symmetric permittivity tensor. In addition, we briefly discuss the role of optical anisotropy in photolithographic systems. In general we can say that the content of Chapter 3 provides a good overview of the classical electromagnetic theory for anisotropic interfaces assuming a complex Hermitian permittivity tensor.

In Chapter 4, we introduce a general ray-tracing procedure for the bulk region of inhomogeneous anisotropic media with a complex Hermitian permittivity tensor. These equations are presented in complex notation and comprise the position-dependent material properties explicitly. These material properties are the position-dependent director and the position-dependent principal indices of refraction. The special cases of biaxial anisotropy, uniaxial anisotropy and isotropy are also addressed. The ray-tracing equations discussed define the state-of-the-art in the field of polarized ray tracing of (nonabsorbing, optically inactive) inhomogeneous anisotropic media within the framework of geometrical optics. The theory is applied to a number of intriguing examples in which we consider the inhomogeneous director profile of a liquid crystal induced by the electric field of one or more electric point charges. In this particular case, the permittivity tensor is real symmetric.

An unanswered question in geometrical optics is how much change in optical properties per unit wavelength is allowed in inhomogeneous anisotropic media. In Chapter 5, we present the results of an exercise in which we compare ray- and wave-optics simulations of a periodic inhomogeneous two-dimensional director profile. Based on these results, we propose a criterion for the applicability of geometrical optics to typical in-plane liquid-crystal configurations. This criterion is a first approximation to the maximum change in material properties per unit wavelength that is allowed in geometrical optics. To the best of our knowledge, such an exercise has never been published before. In addition, we discuss the implications of geometrical optics to the propagation of light rays and briefly discuss the full Maxwell equations beyond the geometrical-optics approach.

In Chapters 6, 7 and 8 we apply the electromagnetic theory described above to simulate the optical properties of liquid-crystal devices. We remark that for the liquid-crystal material used in these devices the permittivity tensor is real symmetric.

First we study residual lens effects of a liquid-crystal-based switchable lenticular for application in auto-stereoscopic 3D displays in Chapter 6. There we propose an improved lens design of which the working principle is supported by the results of our ray-tracing simulations. This improved lens design is filed in a patent application of which the author is co-inventor. This technology is mainly involved with homogeneous anisotropic material properties.

The functionality of a switchable lenticular can also be achieved with inhomogeneous anisotropic liquid-crystal gradient-index (GRIN) lenses. Although the optical properties of GRIN-type lenses have been investigated before, a discussion on the angular-dependent lens action of a GRIN lens for application in auto-stereoscopic 3D displays has not received much attention until now. In Chapter 7, we investigate the angular-dependent optical properties of an advanced GRIN lens structure. To this end, we will use two methods: 1) our ray-tracing procedure and 2) a simple but effective method based on the Huygens principle with a one-dimensional approach.

Finally, we investigate the applicability of our ray-tracing procedure to technically complex liquid-crystal devices in Chapter 8. To this end, we consider two inhomogeneous liquid-crystal-based optical micro structures. First we introduce simulations of a novel electro-optical device having a liquid-crystal layer with an inhomogeneous director profile called the Freédericksz alignment. When applied between two capacitive parallel mirrors, our simulations show that this director profile enables a back reflection phenomenon. Then the propagation direction of light can be controlled electronically and the device behaves like an electro-optical switch. In a second example, we consider the liquid-crystal-based light guide structure recently developed by Philips Research. We simulate the optical properties and compare the results with experimental results. With these two exercises, our aim is to show that our ray-tracing procedure implemented in a simulation program enables us to assess the optical properties of complex inhomogeneous anisotropic optical systems.

Chapter 2

Geometrical optics of anisotropic media

In this chapter, we work out the classical electromagnetic theory for media with optical anisotropy in general. The classical theory discussed applies to non-magnetic, optically inactive media with a complex Hermitian dielectric permittivity tensor. In addition, we make one important assumption in this treatise: we apply geometrical optics, the lowest-order approximation of the optical wave field. In geometrical optics, it is assumed that $\lambda_0 \rightarrow 0$ with λ_0 the wavelength of light in vacuum. This assumption implies that optical laws may be obtained by a complete neglect of the finiteness of the wavelength of light (cf. [6], p. 109). This definition of geometrical optics is widely accepted, but can be formulated in another way. A similar definition of geometrical optics is the assumption that the characteristic dimensions of an optical system are much larger than the wavelength of light. In general, all definitions of geometrical optics have one thing in common: the wave character of light is not taken into account.

2.1 Maxwell equations

The electromagnetic field associated with the propagation of light is described by the Maxwell equations. These equations are the most fundamental equations in electrodynamics. The macroscopic Maxwell equations (in SI units) read

$$\begin{aligned}
\nabla \times \mathbf{H} - \frac{\partial \mathbf{D}}{\partial t} &= \mathbf{J}, && (2.1)\\
\nabla \times \mathbf{E} + \frac{\partial \mathbf{B}}{\partial t} &= 0, && (2.2)\\
\nabla \cdot \mathbf{D} &= \rho, && (2.3)\\
\nabla \cdot \mathbf{B} &= 0, && (2.4)
\end{aligned}$$

where t represents time and all quantities depend on position $\mathbf{r}$. The vectors $\mathbf{E}$ and $\mathbf{H}$ are the electric field vector and the magnetic field vector, respectively. The vectors $\mathbf{D}$ and $\mathbf{B}$ are the electric flux density vector and the magnetic induction vector, respectively. The quantities ρ and $\mathbf{J}$ are the electric charge density and the current density, respectively, and may be considered as the sources of the fields $\mathbf{E}$ and $\mathbf{H}$.

The vectors representing the electromagnetic field defined by Eqs. 2.1-2.4 are complex vectors. This means that they have a direction, a magnitude and a phase. For the real physical electromagnetic field, we need to take the real part of these complex vectors. However, for the remainder of this thesis, we will work with complex electromagnetic field vectors. The definition of the complex field vectors will receive more attention in the next section.

The macroscopic Maxwell equations are completed with the non-dispersive macroscopic material equations (for media without optical activity)

$$\mathbf{D} = \varepsilon_0 \underline{\underline{\varepsilon}} \mathbf{E}, \tag{2.5}$$

$$\mathbf{B} = \mu_0 \underline{\underline{\mu}} \mathbf{H}. \tag{2.6}$$

As mentioned in the introduction, $\underline{\underline{\varepsilon}}(\mathbf{r})$ and $\underline{\underline{\mu}}(\mathbf{r})$ represent the dielectric tensor and the permeability tensor, respectively.

In this treatise, we make a number of assumptions. First, we do not take into account magnetic media, that is to say $\underline{\underline{\mu}} = \mathbf{1}$, where $\mathbf{1}$ is the unit tensor. This means that we only allow electrical anisotropy. In addition, we only investigate non-conducting media ($\mathbf{J} = 0$) and media free of charge ($\rho = 0$). Then the macroscopic Maxwell equations can be reduced to

$$\nabla \times \mathbf{H} - \varepsilon_0 \underline{\underline{\varepsilon}} \frac{\partial \mathbf{E}}{\partial t} = 0, \tag{2.7}$$

$$\nabla \times \mathbf{E} + \mu_0 \frac{\partial \mathbf{H}}{\partial t} = 0, \tag{2.8}$$

$$\nabla \cdot \underline{\underline{\varepsilon}} \mathbf{E} = 0, \tag{2.9}$$

$$\nabla \cdot \mathbf{H} = 0. \tag{2.10}$$

In this thesis, we consider these fundamental equations to be the basis for the classical electromagnetic theory of light in media with optical anisotropy. In the next section, we discuss a general solution for the (complex) electric and magnetic field vectors $\mathbf{E}$ and $\mathbf{H}$ that satisfies the Maxwell equations 2.7-2.10.

2.2 Quasi-plane waves

Without loss of generality, we are looking for solutions of the electromagnetic wave field of the form given by

$$\mathbf{E}(\mathbf{r}, t) = \tilde{\mathbf{E}}(\mathbf{r}) e^{i(k_0 \psi(\mathbf{r}) - \omega t)}, \tag{2.11}$$

$$\mathbf{H}(\mathbf{r}, t) = \tilde{\mathbf{H}}(\mathbf{r}) e^{i(k_0 \psi(\mathbf{r}) - \omega t)}, \tag{2.12}$$

with $\tilde{\mathbf{E}}(\mathbf{r})$ and $\tilde{\mathbf{H}}(\mathbf{r})$ the complex amplitude vectors for the electric and magnetic fields and $\psi(\mathbf{r})$ the optical path length function, which is also called the eikonal function. In addition, k_0 is the wave number in vacuum and ω is the radial frequency. This type of wave field is a time-harmonic quasi-plane wave (cf. [6], p. 111) and applies in particular to regions far away from light sources. The quasi-plane wave was suggested by Sommerfeld and Runge (cf. [86], p. 291) and is also referred to as the Sommerfeld-Runge Ansatz.

The complex amplitude vector can be written as

$$\tilde{\mathbf{E}}(\mathbf{r}) = A(\mathbf{r}) e^{i\delta(\mathbf{r})} \hat{\mathbf{E}}(\mathbf{r}), \tag{2.13}$$

where $\hat{\mathbf{E}}(\mathbf{r})$ is a complex unit vector, i.e. $|\hat{E}_x(\mathbf{r})|^2 + |\hat{E}_y(\mathbf{r})|^2 + |\hat{E}_z(\mathbf{r})|^2 = 1$, the amplitude $A(\mathbf{r})$ is real and positive and the phase term $\delta(\mathbf{r})$ is real. In general, the complex amplitude vector can change with position due to changes in the material properties of a medium.

When we substitute the quasi-plane wave of Eqs. 2.11 and 2.12 into the macroscopic Maxwell equations, we obtain (cf. [6], p. 111)

$$\begin{aligned}
\nabla\psi \times \tilde{\mathbf{H}} + c\varepsilon_0 \underline{\underline{\varepsilon}} \tilde{\mathbf{E}} &= -\frac{1}{ik_0} \nabla \times \tilde{\mathbf{H}}, && (2.14)\\
\nabla\psi \times \tilde{\mathbf{E}} - c\mu_0 \tilde{\mathbf{H}} &= -\frac{1}{ik_0} \nabla \times \tilde{\mathbf{E}}, && (2.15)\\
\nabla\psi \cdot \underline{\underline{\varepsilon}} \tilde{\mathbf{E}} &= -\frac{1}{ik_0} \nabla \cdot \underline{\underline{\varepsilon}} \tilde{\mathbf{E}}, && (2.16)\\
\nabla\psi \cdot \tilde{\mathbf{H}} &= -\frac{1}{ik_0} \nabla \cdot \tilde{\mathbf{H}}, && (2.17)
\end{aligned}$$

where c is the speed of light in vacuum. In the next section, we discuss the Maxwell equations as presented in Eqs. 2.14-2.17 when we apply geometrical optics.

2.3 Geometrical optics

In the geometrical-optics approach, we are interested in solutions of the wave field for large values of $k_0 = \frac{2\pi}{\lambda_0}$. As long as the right-hand side terms in Eqs. 2.14-2.17 are small with respect to one, they may be neglected. However, rapid changes in the optical properties of the medium could lead to large values of the divergence of $\underline{\underline{\varepsilon}}\tilde{\mathbf{E}}$. Hence, we demand that

$$\frac{|\nabla \cdot \underline{\underline{\varepsilon}} \tilde{\mathbf{E}}|}{k_0} \ll 1. \tag{2.18}$$

This condition implies that the elements of the dielectric tensor (i.e. the material properties) and the wave amplitude should change very slowly over the distance of a wavelength.

Because the right-hand side terms in Eqs. 2.14-2.17 vanish, we can express the magnetic amplitude vector $\tilde{\mathbf{H}}$ in terms of the electric amplitude vector $\tilde{\mathbf{E}}$:

$$\tilde{\mathbf{H}} = \frac{1}{c\mu_0} \nabla\psi \times \tilde{\mathbf{E}}. \tag{2.19}$$

Therefore, when we know the electric amplitude vector $\tilde{\mathbf{E}}$, we also know the magnetic amplitude vector $\tilde{\mathbf{H}}$. Hence, for the remainder of this thesis, it is sufficient to discuss the electric amplitude vector $\tilde{\mathbf{E}}$.

In this thesis we consider only non-absorbing media. The implications of this assumption are further discussed in the next section. In addition to this, we assume that the wave field can not be scattered by, for example, impurities in the material properties or boundary surfaces. Together with condition 2.18, these conditions have important consequences for the amplitude A and phase δ of the optical wave field: they are constant and independent of position throughout the medium. These statements receive further attention in Chapter 5.

Within the framework of geometrical optics, the amplitude and phase terms can change at a surface of discontinuity in material properties, despite the fact that in that case condition 2.18 is not valid. This can be the case at, for example, an interface between two different media. To avoid the effect of scattering, a surface of discontinuity should be described by a smooth surface.

In the remainder of this thesis we assume that a medium can be described by two main regions of interest: the interface region and the bulk region. The interface region is defined by the boundary surface between two different media represented by a surface of discontinuity in the material properties. The bulk region is defined by the medium itself with the boundary surface excluded. We assume that in the bulk region condition 2.18 is satisfied and that there are no discontinuities of any kind, except when mentioned otherwise. According to the considerations discussed, the amplitude A and phase term δ can change in the interface region but are constant and independent of position in the bulk region. For this reason, it is only necessary to calculate the entire wave field in the interface region. In the bulk region of an (an)isotropic medium, it is sufficient to calculate the light path of a propagating quasi-plane wave.

In this chapter, we discuss the fundamental electromagnetic theory for optically anisotropic media in the geometrical-optics approach. For this discussion it is not yet necessary to make a distinction between the interface region and the bulk region. The optical properties of anisotropic media in these specific regions will receive more attention in Chapters 3 and 4.

2.4 The Hermitian dielectric permittivity tensor

The elements of the dielectric permittivity tensor represent the material properties of a medium and depend on the position. In general, the position-dependent material properties are defined on a fixed orthonormal basis $\{\hat{\mathbf{x}}, \hat{\mathbf{y}}, \hat{\mathbf{z}}\}$ which represents our laboratory system. In addition to this, we introduce a position-dependent orthonormal basis $\{\hat{\mathbf{u}}(\mathbf{r}), \hat{\mathbf{v}}(\mathbf{r}), \hat{\mathbf{w}}(\mathbf{r})\}$. This local orthonormal basis is defined in such a way that on this basis the local dielectric tensor $\underline{\underline{\varepsilon}}(\mathbf{r})$ is diagonal. When the dielectric tensor is diagonal, the presentation of the physical laws of optical anisotropy are significantly simplified, which will become clear in the sections that follow. In fact, in this treatise we demand that the dielectric tensor can be diagonalized and has an orthonormal basis of eigenvectors. In what follows, we will explain these conditions in more detail.

In the most general case, the elements of the dielectric tensor are all complex. Then locally, $\underline{\underline{\varepsilon}}$ is not necessarily diagonalizable. On the other hand, if $\underline{\underline{\varepsilon}}$ is diagonalizable, in general there exists a biorthonormal basis of complex eigenvectors. Only when $\underline{\underline{\varepsilon}}$ is represented by a normal matrix, it can be diagonalized and also has an orthonormal basis of (three) complex eigenvectors. A square matrix $\mathcal{M}$ is called normal if it commutes with its conjugate transpose $\mathcal{M}^\dagger$:

$$[\mathcal{M}, \mathcal{M}^\dagger] = \mathcal{M}\mathcal{M}^\dagger - \mathcal{M}^\dagger\mathcal{M} = 0. \tag{2.20}$$

The conjugate transpose of a matrix $\mathcal{M}$ is called the Hermitian matrix of $\mathcal{M}$.

Based on the definitions discussed, we can conclude that if the dielectric tensor is represented by a normal matrix, it can be diagonalized on the local complex orthonormal basis $\{\hat{\mathbf{u}}(\mathbf{r}), \hat{\mathbf{v}}(\mathbf{r}), \hat{\mathbf{w}}(\mathbf{r})\}$. In this thesis, this orthonormal basis is also called the principal coordinate system. In the principal coordinate system, the dielectric tensor is given by

$$\underline{\underline{\varepsilon}}(\mathbf{r}) = \begin{pmatrix} \varepsilon_u(\mathbf{r}) & 0 & 0 \\ 0 & \varepsilon_v(\mathbf{r}) & 0 \\ 0 & 0 & \varepsilon_w(\mathbf{r}) \end{pmatrix}, \tag{2.21}$$

where the eigenvalues $\varepsilon_u(\mathbf{r})$, $\varepsilon_v(\mathbf{r})$, and $\varepsilon_w(\mathbf{r})$ are defined the relative principal dielectric values. In general, these eigenvalues are complex. This means that the dielectric tensor includes media with absorption. However, as mentioned in the previous section, we will only consider non-absorbing media. Therefore we need to make sure that the principal dielectric values are real. This can only be the case if $\underline{\underline{\varepsilon}}$ is represented by a Hermitian matrix. By definition, a matrix $\mathcal{M}$ is Hermitian if it equals its conjugate transpose:

$$\mathcal{M} = \mathcal{M}^\dagger. \tag{2.22}$$

In conclusion we can say that if the dielectric tensor is represented by a Hermitian matrix, it can be diagonalized on the local complex orthonormal basis $\{\hat{\mathbf{u}}(\mathbf{r}), \hat{\mathbf{v}}(\mathbf{r}), \hat{\mathbf{w}}(\mathbf{r})\}$ and the principal dielectric values are real.

On the complex orthonormal basis $\{\hat{\mathbf{u}}(\mathbf{r}), \hat{\mathbf{v}}(\mathbf{r}), \hat{\mathbf{w}}(\mathbf{r})\}$ complex vector calculus applies and this is different from the vector calculus on a real basis. Since we will apply complex vector calculus, we need to discuss the definition of the complex vector inner product.

On a real Cartesian basis $\{\hat{\mathbf{x}}, \hat{\mathbf{y}}, \hat{\mathbf{z}}\}$, a vector $\mathbf{a}$ in $\mathbb{R}^3$ is defined

$$\mathbf{a} = a_x\hat{\mathbf{x}} + a_y\hat{\mathbf{y}} + a_z\hat{\mathbf{z}}, \tag{2.23}$$

with a_x, a_y and a_z real. The dot product between two real vectors $\mathbf{a}$ and $\mathbf{b}$ is then given by

$$\mathbf{a} \cdot \mathbf{b} = a_x b_x + a_y b_y + a_z b_z. \tag{2.24}$$

On the other hand, a vector $\mathbf{a}$ in $\mathbb{C}^3$ is defined

$$\mathbf{a} = a_x\hat{\mathbf{x}} + a_y\hat{\mathbf{y}} + a_z\hat{\mathbf{z}}, \tag{2.25}$$

with a_x, a_y and a_z complex. In this case, the complex inner product between two complex vectors $\mathbf{a}$ and $\mathbf{b}$ is defined

$$\langle \mathbf{a}, \mathbf{b} \rangle = a_x b_x^* + a_y b_y^* + a_z b_z^*, \tag{2.26}$$

where '*' denotes complex conjugation.

The Hermitian dielectric tensor represents a more general class of optical properties than a symmetric dielectric tensor of which the elements are real. In general, the theory of electromagnetic waves in anisotropic media is discussed by the literature assuming a real symmetric tensor. In that sense, the theory that will follow in the next sections goes beyond the scope of the literature. In what follows, we will work our way towards a generic formulation of the theory on optically anisotropic non-absorbing (optically inactive) media.

2.5 The optical indicatrix

From the Maxwell equations in the geometrical-optics approach, we will derive what forms a basis for a solid understanding of optical anisotropy. In the following analysis we allow the material properties of a medium to change with position, that is as long as condition 2.18 is satisfied with the exception of a surface of discontinuity. Moreover, we assume a complex Hermitian permittivity tensor for which there exist optical axes.

2.5.1 The biaxial optical indicatrix

In the geometrical-optics approach, the right-hand side terms of Eqs. 2.14-2.17 vanish. As a result, we can confine attention to Eqs. 2.14 and 2.15, since the last two follow from them on scalar multiplication with $\nabla\psi$. By introducing the vector $\mathbf{p} = \nabla\psi$ (wave normal) and eliminating $\tilde{\mathbf{H}}$ we obtain the 'eikonal equation' for media with electrical anisotropy

$$\mathbf{p} \times (\mathbf{p} \times \tilde{\mathbf{E}}) + \underline{\underline{\varepsilon}}\tilde{\mathbf{E}} = 0. \tag{2.27}$$

By definition, the wave normal $\mathbf{p}$ is equivalent to the wave vector $\mathbf{k}$ scaled by the wave number in vacuum k_0. Hence, $|\mathbf{p}| = n$ with n the index of refraction. The elements of the dielectric tensor are determined by the material properties and the definition of our coordinate system. In the previous section, we have assumed that $\underline{\underline{\varepsilon}}(\mathbf{r})$ is represented by a Hermitian matrix. Then on the local complex orthonormal basis $\{\hat{\mathbf{u}}(\mathbf{r}), \hat{\mathbf{v}}(\mathbf{r}), \hat{\mathbf{w}}(\mathbf{r})\}$ the dielectric tensor is given by Eq. 2.21. The u-, v- and w-axes are the local principal axes of the medium and define the principal coordinate system. From now on, for convenience, we will assume that the principal dielectric values satisfy

$$\varepsilon_u < \varepsilon_v < \varepsilon_w. \tag{2.28}$$

The principal indices of refraction n_u, n_v and n_w are defined by

$$n_i = \sqrt{\varepsilon_i}, \quad i = u, v, w. \tag{2.29}$$

A medium is called biaxially anisotropic when the principal indices of refraction are all different.

We can write Eq. 2.27 as a matrix equation,

$$\mathcal{M}(\mathbf{p})\tilde{\mathbf{E}} = 0, \tag{2.30}$$

with $\mathcal{M}$ the corresponding 3×3 matrix. The solutions $\tilde{\mathbf{E}}$ define the null space of the matrix $\mathcal{M}$ according to

$$\mathrm{Null}(\mathcal{M}) = \Big\{ \tilde{\mathbf{E}} \in \mathbb{C}^3 | \mathcal{M}\tilde{\mathbf{E}} = 0 \Big\}. \tag{2.31}$$

Eq. 2.30 has only non-trivial solutions for the eigenmodes $\tilde{\mathbf{E}}$ if the determinant of the matrix $\mathcal{M}$ vanishes. This demand leads to a quadratic equation $\mathcal{H}(|p_u|^2, |p_v|^2, |p_w|^2) = 0$ and its solutions are represented by two three-dimensional surfaces in **p**-space. This surface is called the biaxial optical indicatrix (cf. [87], p. 20) and, in the principal coordinate system, is given by (see also [88], p. 383)

$$\begin{aligned} \mathcal{H} \;=\; & \Big(\varepsilon_u|p_u|^2 + \varepsilon_v|p_v|^2 + \varepsilon_w|p_w|^2\Big)\Big(|p_u|^2 + |p_v|^2 + |p_w|^2\Big) \\ & -\varepsilon_u|p_u|^2(\varepsilon_v + \varepsilon_w) - \varepsilon_v|p_v|^2(\varepsilon_u + \varepsilon_w) - \varepsilon_w|p_w|^2(\varepsilon_u + \varepsilon_v) \\ & +\varepsilon_u\varepsilon_v\varepsilon_w = 0. \end{aligned} \tag{2.32}$$

Given Eq. 2.32, it is convenient to write the wave normal **p** in terms of its magnitude and direction:

$$\mathbf{p} = |\mathbf{p}|\hat{\mathbf{p}}, \tag{2.33}$$

where $\hat{\mathbf{p}}$ is a unit vector and $|\mathbf{p}| = n$. When we substitute Eq. 2.33 into Eq. 2.32, we obtain

$$\begin{aligned} \mathcal{H} \;=\; & \Big(\varepsilon_u|\hat{p}_u|^2 + \varepsilon_v|\hat{p}_v|^2 + \varepsilon_w|\hat{p}_w|^2\Big)|\mathbf{p}|^4 \\ & -\Big[\varepsilon_u|\hat{p}_u|^2(\varepsilon_v + \varepsilon_w) + \varepsilon_v|\hat{p}_v|^2(\varepsilon_u + \varepsilon_w) + \varepsilon_w|\hat{p}_w|^2(\varepsilon_u + \varepsilon_v)\Big]|\mathbf{p}|^2 \\ & +\varepsilon_u\varepsilon_v\varepsilon_w = 0. \end{aligned} \tag{2.34}$$

Eq. 2.34 implies that, for any arbitrary direction of propagation $\hat{\mathbf{p}}$, there are two solutions for $|\mathbf{p}|^2$. If we solve Eq. 2.34 for $|\mathbf{p}|^2 = n^2$, we obtain

$$n^2(\hat{\mathbf{p}}) = \frac{-b_n \pm \sqrt{b_n^2 - 4a_nc_n}}{2a_n}, \tag{2.35}$$

where

$$a_n = \varepsilon_u|\hat{p}_u|^2 + \varepsilon_v|\hat{p}_v|^2 + \varepsilon_w|\hat{p}_w|^2, \tag{2.36}$$

$$b_n = \varepsilon_u|\hat{p}_u|^2(\varepsilon_v + \varepsilon_w) + \varepsilon_v|\hat{p}_v|^2(\varepsilon_u + \varepsilon_w) + \varepsilon_w|\hat{p}_w|^2(\varepsilon_u + \varepsilon_v), \tag{2.37}$$

$$c_n = \varepsilon_u\varepsilon_v\varepsilon_w. \tag{2.38}$$

Hence, the index of refraction is a function of the direction of propagation. In conclusion we can say that the optical indicatrix, given by Eq. 2.32, determines the anisotropy of the wave normal **p**.

The three-dimensional surface represented by Eq. 2.32 consists of two concentric shells: an inner and an outer shell. These two shells have four points in common of which two are the opposite of the other two (cf. [75], p. 93). The two lines that go through these points and the origin are called the optical axes. Note that these optical axes can vary with position since the principal coordinate system depends on position. In case $\hat{\mathbf{p}}$ is parallel to one of the optical axes, the two solutions for the refractive index $|\mathbf{p}|$ are identical. Fig. 2.1 shows one octant of the optical indicatrix in the principal coordinate system and the intersections of the optical indicatrix with the principal uv-, uw- and vw-planes.

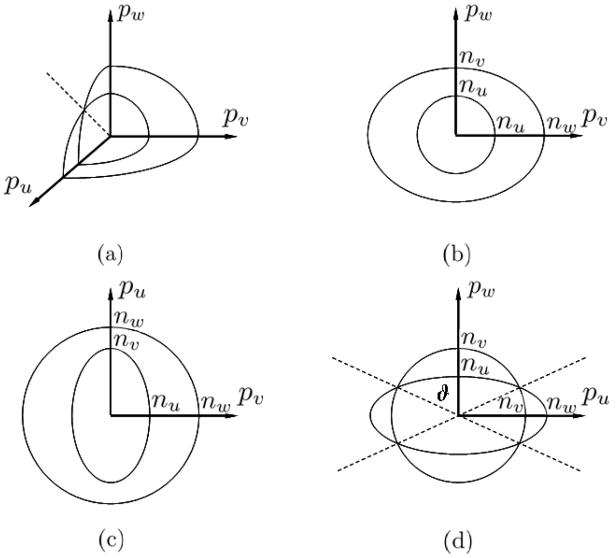

Figure 2.1: *Schematic presentation of the biaxial optical indicatrix. Fig. (a) shows one octant of the biaxial optical indicatrix in the principal coordinate system. Fig. (b), (c) and (d) show the intersections of the optical indicatrix with the principal planes (vw-, uv- and uw-plane, respectively). The two concentric shells touch each other in their common points of intersection in the uw-plane. The lines that go through these points and the origin are called the optical axes. The optical axes are indicated by the dashed lines. The angle between the optical axes and the w-axis is indicated by the angle* ϑ*. In this case, we assumed* $n_w > n_v > n_u$.

At this point, we need to explain the way in which the optical indicatrix is presented in Fig. 2.1. In principle, Eq. 2.32 is real and represents a three-dimensional surface on the real orthonormal basis $\{\hat{\mathbf{u}}(\mathbf{r}), \hat{\mathbf{v}}(\mathbf{r}), \hat{\mathbf{w}}(\mathbf{r})\}$. But we have assumed a Hermitian dielectric tensor. Hence the basis $\{\hat{\mathbf{u}}(\mathbf{r}), \hat{\mathbf{v}}(\mathbf{r}), \hat{\mathbf{w}}(\mathbf{r})\}$ is complex and on this basis the optical indicatrix might look very different from the indicatrix depicted in Fig. 2.1. However, for the sake of clarity, we will present the optical indicatrix in its real form despite the fact that we work on the complex basis $\{\hat{\mathbf{u}}(\mathbf{r}), \hat{\mathbf{v}}(\mathbf{r}), \hat{\mathbf{w}}(\mathbf{r})\}$.

Recall that we have assumed that $\varepsilon_w > \varepsilon_v > \varepsilon_u$. Then the optical axes lie in the uw-plane. The angle ϑ between the w-axis and the optical axis is the same for both optical axes (see Fig. 2.1-(d)). This angle is determined by the material properties and satisfies (cf. [89], p. 3127, Eq. 115)

$$\tan(\vartheta) = \sqrt{\frac{\varepsilon_w(\varepsilon_v - \varepsilon_u)}{\varepsilon_u(\varepsilon_w - \varepsilon_v)}}. \tag{2.39}$$

For propagation along an optical axis, we have $|\mathbf{p}| = \sqrt{\varepsilon_v}$ and the four corresponding directions of propagation are given by

$$\hat{\mathbf{p}} = \pm\sqrt{\frac{\varepsilon_w(\varepsilon_v - \varepsilon_u)}{\varepsilon_v(\varepsilon_w - \varepsilon_u)}}\hat{\mathbf{u}} + 0\hat{\mathbf{v}} \pm \sqrt{\frac{\varepsilon_u(\varepsilon_w - \varepsilon_v)}{\varepsilon_v(\varepsilon_w - \varepsilon_u)}}\hat{\mathbf{w}}, \tag{2.40}$$

with all quantities depending on position $\mathbf{r}$ and assuming that $\{\hat{\mathbf{u}}(\mathbf{r}), \hat{\mathbf{v}}(\mathbf{r}), \hat{\mathbf{w}}(\mathbf{r})\}$ is real. For this particular direction of propagation, the surfaces of the biaxial optical indicatrix have a singularity. This singularity is associated with unusual optical behavior, often referred to as conical refraction. This special topic is further discussed in Chapter 3.

Up to this point, we have assumed that there exists a real vector $\mathbf{p}^{oa}$ on the fixed real Cartesian basis $\{\hat{\mathbf{x}}, \hat{\mathbf{y}}, \hat{\mathbf{z}}\}$ (our laboratory system) along which the two solutions for $|\mathbf{p}^{oa}| = \sqrt{\varepsilon_v}$ are identical. Then, by definition, there is an optical axis in the direction of $\mathbf{p}^{oa}$. However, if this vector $\mathbf{p}^{oa}$ with $|\mathbf{p}^{oa}| = \sqrt{\varepsilon_v}$ is complex on $\{\hat{\mathbf{x}}, \hat{\mathbf{y}}, \hat{\mathbf{z}}\}$, there is no optical axis. An example of such a case is discussed in Appendix A. For the remainder of this thesis, we assume that there always exist optical axes in anisotropic media.

2.5.2 The uniaxial optical indicatrix

In general it is possible that two of the relative principal dielectric values are equal. In this thesis, we will consider the case when $\varepsilon_u = \varepsilon_v = \varepsilon_1$ and $\varepsilon_w = \varepsilon_2$. Then Eq. 2.32 reduces to

$$\mathcal{H} = \left[\Big(|p_u|^2 + |p_v|^2\Big)\varepsilon_1 + |p_w|^2\varepsilon_2 - \varepsilon_1\varepsilon_2\right]\Big(|\mathbf{p}|^2 - \varepsilon_1\Big) = 0. \tag{2.41}$$

Apparently, the optical indicatrix consists of a sphere with radius $\sqrt{\varepsilon_1}$ and an ellipsoid with semi-axes $\sqrt{\varepsilon_1}$ and $\sqrt{\varepsilon_2}$. The corresponding principal indices of refraction are defined the ordinary index of refraction $n_o = \sqrt{\varepsilon_1}$ and extraordinary index of refraction $n_e = \sqrt{\varepsilon_2}$.

The optical indicatrix gives rise to two types of light waves: the ordinary and the extraordinary wave. When the wave normal $\mathbf{p}$ satisfies

$$\mathcal{H}_o = |\mathbf{p}|^2 - n_o^2 = 0, \tag{2.42}$$

the wave normal corresponds to an ordinary wave. On the other hand, when the wave normal satisfies

$$\mathcal{H}_e = (|p_u|^2 + |p_v|^2)n_o^2 + |p_w|^2 n_e^2 - n_o^2 n_e^2 = 0, \tag{2.43}$$

the wave normal corresponds to an extraordinary wave.

In contrast with the biaxial optical indicatrix the sphere and ellipsoid surfaces only have two points in common, namely for $\mathbf{p} = \pm n_o\hat{\mathbf{w}}$. Hence, there is only one optical axis: the $\hat{\mathbf{w}}$-axis. This type of anisotropy is therefore called uniaxial anisotropy and Eq. 2.41 represents the uniaxial optical indicatrix. Fig. 2.2 shows one octant of the optical indicatrix. Note that in the principal coordinate system, the optical axis is always in the w-direction, since we assumed that $n_u = n_v = n_o$ and $n_w = n_e$. In the definition that we apply, $n_e > n_o$ and in general this is called positive birefringence. In the case of positive birefringence, the ellipsoid surface is oblate. Negative birefringence, i.e. $n_o > n_e$, corresponds to a prolate ellipsoid. In contrast with the biaxial optical indicatrix, the uniaxial optical indicatrix has no singularities.

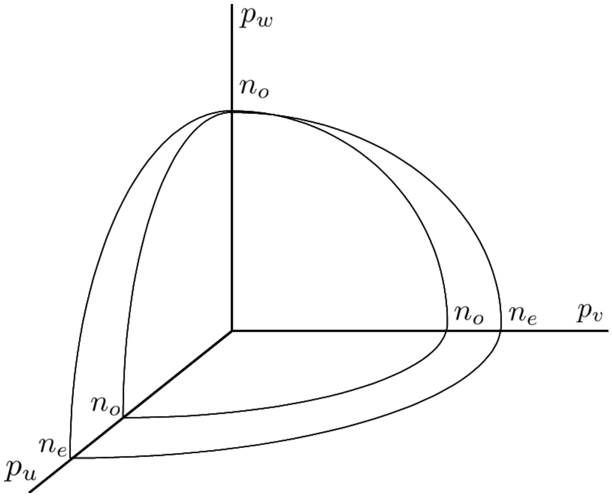

Figure 2.2: *Schematic presentation of the uniaxial optical indicatrix. The figure shows one octant of the optical indicatrix in the principal coordinate system. The two surfaces, sphere and ellipsoid, touch each other in their common points of intersection with the w-axis. Here, we assumed positive birefringence, i.e.* $n_e > n_o$.

In case the relative principal dielectric values are all equal, Eq. 2.32 can be reduced to

$$\mathcal{H} = |\mathbf{p}|^2 - n^2 = 0, \tag{2.44}$$

with n the index of refraction of the medium. Eq. 2.44 represents the optical indicatrix for isotropic media. In contrast with anisotropic media, the optical properties of isotropic media are not directionally dependent. This is because a sphere as the one represented by Eq. 2.44 is fully rotationally symmetric. The same type of rules apply to ordinary light waves in uniaxially anisotropic media, see Eq. 2.42. Although propagating in an anisotropic medium, ordinary light waves have a phase velocity that is independent from the direction of propagation.

2.6 Analysis of the polarization vectors

According to the theory presented in the previous section, the anisotropy of the wave normal $\mathbf{p}$ in an anisotropic medium is determined by the optical indicatrix or, in other words, by the optical axes and the indices of refraction of the medium. Both biaxially and uniaxially anisotropic media can produce two different light waves for one direction of propagation only. However, it is possible that only one of these two modes is present. This is due to the fact that light is a transverse electromagnetic wave and has a polarization state. In this section, we derive how the polarization state of light is related to the anisotropy of the wave normal.

2.6.1 Biaxial anisotropy

As discussed in Section 2.2, the complex amplitude vector can be written as $\tilde{\mathbf{E}} = A(\mathbf{r})e^{i\delta(\mathbf{r})}\hat{\mathbf{E}}(\mathbf{r})$ with $\hat{\mathbf{E}}(\mathbf{r})$ a complex unit vector. The unit vector $\hat{\mathbf{E}}(\mathbf{r})$ is called the electric polarization vector. In anisotropic media, the electric (and magnetic) polarization vectors depend on the direction of propagation and the orientation of the optical indicatrix with respect to a reference coordinate system. In this section, we derive concise expressions for the electric and magnetic polarization vectors.

On the local principal basis $\{\hat{\mathbf{u}}(\mathbf{r}), \hat{\mathbf{v}}(\mathbf{r}), \hat{\mathbf{w}}(\mathbf{r})\}$, $\underline{\underline{\varepsilon}}(\mathbf{r})$ is diagonal. Then, using the vector identity $\mathbf{A} \times (\mathbf{B} \times \mathbf{C}) = \mathbf{B}(\mathbf{C} \cdot \mathbf{A}) - \mathbf{C}(\mathbf{A} \cdot \mathbf{B})$, Eq. 2.27 can be written

$$\begin{aligned}
|\mathbf{p}|^2 \tilde{E}_u - \varepsilon_u \tilde{E}_u &= \langle \tilde{\mathbf{E}}, \mathbf{p} \rangle p_u, & (2.45)\\
|\mathbf{p}|^2 \tilde{E}_v - \varepsilon_v \tilde{E}_v &= \langle \tilde{\mathbf{E}}, \mathbf{p} \rangle p_v, & (2.46)\\
|\mathbf{p}|^2 \tilde{E}_w - \varepsilon_w \tilde{E}_w &= \langle \tilde{\mathbf{E}}, \mathbf{p} \rangle p_w. & (2.47)
\end{aligned}$$

Hence, in the principal coordinate system, the vector components of $\hat{\mathbf{E}}$ can be written as

$$\hat{E}_i = C \frac{\langle \tilde{\mathbf{E}} \cdot \mathbf{p} \rangle p_i}{|\mathbf{p}|^2 - \varepsilon_i}, \quad i = u, v, w, \tag{2.48}$$

where C is a complex normalization constant and $|\mathbf{p}|^2 \neq \varepsilon_i$. Eq. 2.48 is proportional to a complex vector. Therefore, in general, Eq. 2.48 corresponds to an elliptic polarization state. If the dielectric tensor is a real symmetric tensor, the orthonormal basis $\{\hat{\mathbf{u}}(\mathbf{r}), \hat{\mathbf{v}}(\mathbf{r}), \hat{\mathbf{w}}(\mathbf{r})\}$ is real. Then Eq. 2.48 represents a vector that is proportional to a real vector and corresponds to a linear polarization state.

In conclusion we can say that light waves inside anisotropic media are elliptically polarized, provided that the dielectric tensor is represented by a complex Hermitian matrix. In the special case the dielectric tensor is real and symmetric, light waves in anisotropic media are linearly polarized.

Now consider the case for which $|\mathbf{p}|^2 = \varepsilon_u$, $|\mathbf{p}|^2 \neq \varepsilon_v$ and $|\mathbf{p}|^2 \neq \varepsilon_w$. Then, from Eq. 2.45, we deduce that either $\langle \tilde{\mathbf{E}}, \mathbf{p} \rangle = 0$ or $p_u = 0$. In case $\langle \tilde{\mathbf{E}} \cdot \mathbf{p} \rangle = 0$, Eqs. 2.46 and 2.47 tell us that $\tilde{E}_v = 0$, $\tilde{E}_w = 0$ and the value of $\tilde{E}_u$ is arbitrary. Hence we conclude that $\hat{\mathbf{E}} = \pm e^{i\phi}\hat{\mathbf{u}}$, with ϕ an arbitrary phase term. In case $p_u = 0$, the wave normal $\mathbf{p}$ lies in the vw-plane (see also Fig. 2.1-(b)). Eqs. 2.46 and 2.47 do not depend on $\tilde{E}_u$ and are a homogeneous system for $\tilde{E}_v$ and $\tilde{E}_w$. The determinant of this homogeneous system can be shown to be nonzero, hence $\tilde{E}_v = \tilde{E}_w = 0$ and the value for $\tilde{E}_u$ is arbitrary. We can conclude that, if $|\mathbf{p}|^2 = \varepsilon_u$, $|\mathbf{p}|^2 \neq \varepsilon_v$ and $|\mathbf{p}|^2 \neq \varepsilon_w$ then the polarization vector is given by:

$$\hat{\mathbf{E}} = \pm e^{i\phi}\hat{\mathbf{u}}. \tag{2.49}$$

Similarly, if $|\mathbf{p}|^2 = \varepsilon_v$, $|\mathbf{p}|^2 \neq \varepsilon_u$ and $|\mathbf{p}|^2 \neq \varepsilon_w$ we obtain $\hat{\mathbf{E}} = \pm e^{i\phi}\hat{\mathbf{v}}$ and if $|\mathbf{p}|^2 = \varepsilon_w$, $|\mathbf{p}|^2 \neq \varepsilon_u$ and $|\mathbf{p}|^2 \neq \varepsilon_v$ we have $\hat{\mathbf{E}} = \pm e^{i\phi}\hat{\mathbf{w}}$. For convenience, the phase term ϕ can be set to zero.

The magnetic polarization vector is defined (see also Eq. 2.19)

$$\mathbf{H} = \pm \frac{1}{c\mu_0} \mathbf{p} \times \hat{\mathbf{E}}. \tag{2.50}$$

Hence, the magnetic polarization vectors defined in this way are by definition not unit vectors. Note that the equations for the polarization vectors only apply in the principal coordinate system.

At this point, we have derived concise expressions for the electric and magnetic polarization vectors. In what follows, we will investigate the orientation of the polarization vectors with respect to the position-dependent optical indicatrix.

Let us consider the optical indicatrix $\mathcal{H}(\mathbf{r},\mathbf{p})$ in a fixed point $\mathbf{r}$ of space. Let the basis $\{\hat{\mathbf{u}}(\mathbf{r}),\hat{\mathbf{v}}(\mathbf{r}),\hat{\mathbf{w}}(\mathbf{r})\}$ be the orthonormal principal basis on which $\underline{\underline{\varepsilon}}(\mathbf{r})$ is diagonal at the given point $\mathbf{r}$. Since this basis is orthonormal, the gradient of $\mathbf{p}\mapsto\mathcal{H}(\mathbf{r},\mathbf{p})$ is given by

$$\begin{aligned}\nabla_p\mathcal{H}(\mathbf{r},\mathbf{p}) \quad &= \quad \frac{\partial\mathcal{H}(\mathbf{r},\mathbf{p})}{\partial p_u}\hat{\mathbf{u}}(\mathbf{r})+\frac{\partial\mathcal{H}(\mathbf{r},\mathbf{p})}{\partial p_v}\hat{\mathbf{v}}(\mathbf{r})\\ &\quad +\frac{\partial\mathcal{H}(\mathbf{r},\mathbf{p})}{\partial p_w}\hat{\mathbf{w}}(\mathbf{r}).\end{aligned}\tag{2.51}$$

We shall now show that the vector $\nabla_p\mathcal{H}(\mathbf{r},\mathbf{p})$ is perpendicular to both $\hat{\mathbf{E}}(\mathbf{r})$ and $\mathbf{H}(\mathbf{r})$ (at the same point $\mathbf{r}$).

First, we will investigate the complex inner product $\langle\hat{\mathbf{E}},\nabla_p\mathcal{H}\rangle$. When we expand this inner product with the help of Eqs. 2.32 and 2.48, we obtain

$$\langle\hat{\mathbf{E}},\nabla_p\mathcal{H}\rangle=\frac{C\langle\tilde{\mathbf{E}},\mathbf{p}\rangle f(p_u,p_v,p_w)}{(|\mathbf{p}|^2-\varepsilon_u)(|\mathbf{p}|^2-\varepsilon_v)(|\mathbf{p}|^2-\varepsilon_w)}\mathcal{H},\tag{2.52}$$

with $f(p_u,p_v,p_w)$ a polynomial of degree four, given by

$$\begin{aligned}f(p_u,p_v,p_w) \quad &= \quad 2|\mathbf{p}|^4-p_u^2(\varepsilon_v+\varepsilon_w)\\ &\quad -p_v^2(\varepsilon_u+\varepsilon_w)-p_w^2(\varepsilon_u+\varepsilon_v).\end{aligned}\tag{2.53}$$

By definition, $\mathcal{H}=0$ and as a result, the complex inner product of Eq. 2.52 vanishes, provided that $|\mathbf{p}|^2\neq\varepsilon_i$. It can be shown that in case $|\mathbf{p}|^2=\varepsilon_i$, the complex inner product between $\nabla_p\mathcal{H}$ and $\hat{\mathbf{E}}$ also vanishes.

Next, we will show that $\langle\mathbf{H},\nabla_p\mathcal{H}\rangle=0$. Given Eq. 2.19, the complex inner product between $\mathbf{H}$ and $\nabla_p\mathcal{H}$ satisfies

$$\langle\mathbf{H},\nabla_p\mathcal{H}\rangle\propto\langle(\mathbf{p}\times\hat{\mathbf{E}}),\nabla_p\mathcal{H}\rangle.\tag{2.54}$$

Then, with the help of Eqs. 2.32 and 2.48, we obtain

$$\begin{aligned}\langle(\mathbf{p}\times\hat{\mathbf{E}}),\nabla_p\mathcal{H}\rangle \quad &\propto \quad 2p_up_vp_w(\varepsilon_w-\varepsilon_v)+2p_vp_wp_u(\varepsilon_u-\varepsilon_w)\\ &\quad +2p_wp_up_v(\varepsilon_v-\varepsilon_u)=0.\end{aligned}\tag{2.55}$$

In addition, since $\mathcal{H}$ is real, we have

$$\begin{aligned}\langle\mathbf{H},\nabla_p\mathcal{H}\rangle \quad &= \quad H_u\left(\frac{\partial\mathcal{H}}{\partial p_u}\right)^*+H_v\left(\frac{\partial\mathcal{H}}{\partial p_v}\right)^*+H_w\left(\frac{\partial\mathcal{H}}{\partial p_w}\right)^*\\ &= \quad H_u\frac{\partial\mathcal{H}}{\partial p_u}+H_v\frac{\partial\mathcal{H}}{\partial p_v}+H_w\frac{\partial\mathcal{H}}{\partial p_w}\\ &= \quad \frac{\partial\mathcal{H}}{\partial p_u}(H_u^*)^*+\frac{\partial\mathcal{H}}{\partial p_v}(H_v^*)^*+\frac{\partial\mathcal{H}}{\partial p_w}(H_w^*)^*\\ &= \quad \langle\nabla_p\mathcal{H},\mathbf{H}^*\rangle.\end{aligned}\tag{2.56}$$

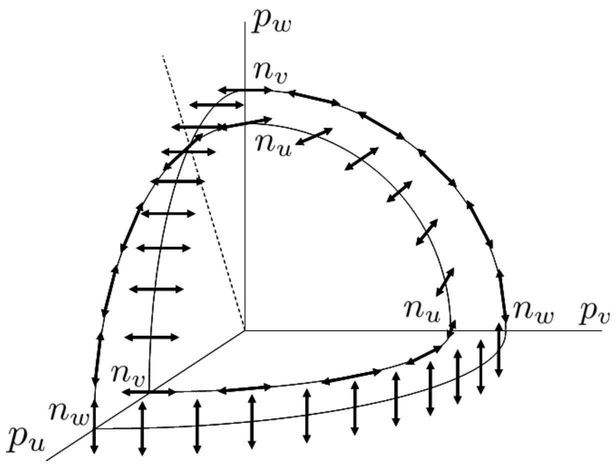

Figure 2.3: *Octant of the biaxial optical indicatrix as in Fig. 2.1-(a), but now with the electric polarization vectors indicated in the principal uv-, uw- and vw-planes by the arrows. In general, the polarization state is elliptical. Both the electric and magnetic polarization vectors are tangent with respect to the biaxial optical indicatrix. As a consequence, for each arbitrary direction of propagation* $\mathbf{p}$*, the Poynting vector is in the direction of* $\nabla_p H$*, perpendicular to the optical indicatrix.*

Hence, we can conclude that $\langle \mathbf{H}, \nabla_p \mathcal{H} \rangle = \langle \nabla_p \mathcal{H}, \mathbf{H}^* \rangle = 0$.

Fig. 2.3 shows the biaxial optical indicatrix again (in its real form), but now with the electric polarization vectors indicated in the principal uv-, uw- and vw-planes (see also [5], p. 91). In general, the polarization vectors are elliptically polarized. In addition, we conclude that both the electric and magnetic polarization vectors are tangent to the biaxial optical indicatrix. The properties of the polarization vectors are general, since they are independent of the choice of the coordinate system. As a consequence, the time-averaged Poynting vector, given by

$$\langle \mathbf{S} \rangle = \frac{1}{2} \mathrm{Re}(\mathbf{E} \times \mathbf{H}^\star), \tag{2.57}$$

is perpendicular to the optical indicatrix. Then, the vector $\langle \mathbf{S} \rangle$ is proportional to the vector $\nabla_p \mathcal{H}$:

$$\langle \mathbf{S} \rangle \propto \nabla_p \mathcal{H}. \tag{2.58}$$

Moreover, it can be shown that

$$\langle \mathbf{p}, \langle \mathbf{S} \rangle \rangle = C_s \Bigg[|\mathbf{p}|^2 |\mathbf{E}|^2 - |\langle \mathbf{p}, \mathbf{E} \rangle|^2 \Bigg] \geq 0, \tag{2.59}$$

with C_s a positive constant, and

$$\langle \mathbf{p}, \nabla_p \mathcal{H} \rangle \geq 0. \tag{2.60}$$

Therefore, $\langle \mathbf{S} \rangle$ and $\nabla_p \mathcal{H}$ are always parallel and never anti-parallel.

We can conclude that the electric and magnetic polarization vectors for biaxial anisotropy are always tangent to the optical indicatrix. Moreover, the time-averaged Poynting vector is always perpendicular with respect to the optical indicatrix and is proportional to the vector $\nabla_p \mathcal{H}$. In the next subsection, we discuss the polarization vectors for uniaxial anisotropy.

2.6.2 Uniaxial anisotropy

In case a medium is uniaxially anisotropic, we can derive the polarization vectors for ordinary waves and extraordinary waves. The polarization vector for biaxially anisotropic media is given by Eq. 2.48. However, this equation only applies on the local basis $\{\hat{\mathbf{u}}(\mathbf{r}), \hat{\mathbf{v}}(\mathbf{r}), \hat{\mathbf{w}}(\mathbf{r})\}$ where $\underline{\underline{\varepsilon}}(\mathbf{r})$ is diagonal. In what follows, we derive expressions for the ordinary and extraordinary polarization vectors that apply in any arbitrary coordinate system.

We consider Eqs. 2.45-2.47. For ordinary waves $|\mathbf{p}_o|^2 = n_o^2$, see Eq. 2.42, where $\mathbf{p}_o$ represents the ordinary wave normal. Then, $\langle \tilde{\mathbf{E}}, \mathbf{p}_o \rangle = 0$ or $p_u = p_v = 0$. In case $\langle \tilde{\mathbf{E}}, \mathbf{p}_o \rangle = 0$, we conclude that the values for $\tilde{E}_u$ and $\tilde{E}_v$ satisfy $\langle \tilde{\mathbf{E}}, \mathbf{p}_o \rangle = 0$ while $\tilde{E}_w = 0$. Hence, $\tilde{\mathbf{E}} \propto p_{ov}^* \hat{\mathbf{u}} - p_{ou}^* \hat{\mathbf{v}}$. If $\langle \tilde{\mathbf{E}}, \mathbf{p}_o \rangle \neq 0$ and $p_{ou} = p_{ov} = 0$, $\tilde{E}_u$ and $\tilde{E}_v$ are arbitrary. As a consequence, $\mathbf{p}_o = \pm n_o \hat{\mathbf{w}}$ and Eq. 2.47 reduces to

$$(|\mathbf{p}_o|^2 - n_e^2)\tilde{E}_w = n_o^2 \tilde{E}_w. \tag{2.61}$$

Eq. 2.61 only holds if $\tilde{E}_w = 0$. Hence the inner product $\langle \tilde{\mathbf{E}}, \mathbf{p}_o \rangle$ vanishes. Altogether, we conclude that $\langle \tilde{\mathbf{E}}_o, \mathbf{p}_o \rangle = 0$ and $\langle \tilde{\mathbf{E}}_o, \hat{\mathbf{w}} \rangle = 0$. As a result, the ordinary polarization vector can be written as a vector cross product:

$$\hat{\mathbf{E}}_o = \pm \frac{\mathbf{p}_o \times \hat{\mathbf{w}}}{|\mathbf{p}_o \times \hat{\mathbf{w}}|}. \tag{2.62}$$

In case $\mathbf{p}_o = \pm n_o \hat{\mathbf{w}}$, Eq. 2.62 does not apply. Then, $\hat{\mathbf{E}}_o$ can be chosen arbitrarily perpendicular to $\mathbf{p}_o$. The magnetic polarization vector for ordinary waves is given by

$$\mathbf{H}_o = \pm \frac{1}{c\mu_0} \mathbf{p}_o \times \hat{\mathbf{E}}_o. \tag{2.63}$$

The applicability of Eqs. 2.62 and 2.63 is not restricted to the principal coordinate system and applies in any arbitrary coordinate system.

The electric polarization vector for extraordinary waves is given by Eq. 2.48 provided that $n_o < |\mathbf{p}_e| < n_e$, with $\mathbf{p}_e$ the extraordinary wave normal. If $|\mathbf{p}_e| = n_o$, then $\tilde{E}_{ew} = 0$ and $\tilde{E}_{eu}$ and $\tilde{E}_{ev}$ are arbitrary. If $|\mathbf{p}_e| = n_e$, we have $p_{ew} = 0$ and $\tilde{E}_{ew}$ is arbitrary. Then Eqs. 2.45 and 2.46 do not depend on $\tilde{E}_{ew}$ and are a homogeneous system for $\tilde{E}_{eu}$ and $\tilde{E}_{ev}$. The determinant of this homogeneous system can be shown to be nonzero, hence $\tilde{E}_{eu} = \tilde{E}_{ev} = 0$. Therefore, we conclude that $\hat{\mathbf{E}}_e = \pm e^{i\phi} \hat{\mathbf{w}}$ if $|\mathbf{p}_e| = n_e$.

In case the dielectric tensor is a real symmetric tensor, we can derive a more elegant expression for the extraordinary polarization vector. This expression is given by

$$\hat{\mathbf{E}}_e = \pm \frac{(\mathbf{p}_e \times \hat{\mathbf{w}}) \times \nabla_p \mathcal{H}_e}{|(\mathbf{p}_e \times \hat{\mathbf{w}}) \times \nabla_p \mathcal{H}_e|}, \tag{2.64}$$

where $\hat{\mathbf{w}}$ represents the optical axis. Eq. 2.64 applies in any arbitrary coordinate system. The corresponding magnetic polarization vector is of course given by

$$\mathbf{H}_e = \pm\frac{1}{c\mu_0}\mathbf{p}_e \times \hat{\mathbf{E}}_e. \tag{2.65}$$

Apparently, the electric polarization vector $\hat{\mathbf{E}}_e$ is perpendicular to both $\mathbf{p}_e \times \hat{\mathbf{w}}$ and $\nabla_p \mathcal{H}_e$, provided that the dielectric tensor is real and symmetric. In what follows, we will prove this.

For extraordinary waves, the inner product $\langle \hat{\mathbf{E}}_e, \mathbf{p}_e \rangle$ does not necessarily vanish. In this case, we can derive from Eq. 2.48 that the complex inner product between the vectors $\mathbf{p}_e \times \hat{\mathbf{w}}$ and $\hat{\mathbf{E}}_e$ satisfies

$$\langle (\mathbf{p}_e \times \hat{\mathbf{w}}), \hat{\mathbf{E}}_e \rangle \propto \frac{\mathrm{Im}(p_{eu}^* p_{ev})}{|\mathbf{p}_e|^2 - n_o^2}, \tag{2.66}$$

with $|\mathbf{p}_e|^2 - n_o^2 \neq 0$. Hence, if $p_{eu} = 0$, $p_{ev} = 0$ or $p_{eu} = p_{ev}$, the inner product $\langle (\mathbf{p}_e \times \hat{\mathbf{w}}), \hat{\mathbf{E}}_e \rangle$ vanishes. If the dielectric tensor is real and symmetric and therefore $\mathbf{p}_e$ is real, the inner product vanishes by definition.

Next, we show that $\langle \hat{\mathbf{E}}_e, \nabla_p \mathcal{H}_e \rangle = 0$. When we expand the inner product with the help of Eqs. 2.43 and 2.48, we obtain

$$\langle \hat{\mathbf{E}}_e, \nabla_p \mathcal{H}_e \rangle = \frac{C \langle \tilde{\mathbf{E}}_e, \mathbf{p}_e \rangle |\mathbf{p}_e|^2}{(|\mathbf{p}_e|^2 - n_o^2)(|\mathbf{p}_e|^2 - n_e^2)} \mathcal{H}_e, \tag{2.67}$$

with $\mathcal{H}_e$ defined on the local principal basis $\{\hat{\mathbf{u}}(\mathbf{r}), \hat{\mathbf{v}}(\mathbf{r}), \hat{\mathbf{w}}(\mathbf{r})\}$. For extraordinary waves, $\mathcal{H}_e = 0$. As a result, the complex inner product of Eq. 2.67 vanishes. If $|\mathbf{p}_e| = n_o$ or $|\mathbf{p}_e| = n_e$, we apply l'Hôpital's rule to Eq. 2.67 and still find that $\langle \hat{\mathbf{E}}_e, \nabla_p \mathcal{H}_e \rangle$ vanishes. Note that this result applies for a Hermitian dielectric tensor.

In the special case that the dielectric tensor is real and symmetric, we conclude that $\hat{\mathbf{E}}_e$ is perpendicular to both $\mathbf{p}_e \times \hat{\mathbf{w}}$ and $\nabla_p \mathcal{H}_e$ and therefore Eq. 2.64 is proved. In addition, we conclude that the orthogonality of the vectors $\nabla_p \mathcal{H}_e$ and $\hat{\mathbf{E}}_e$ always applies for a Hermitian dielectric tensor.

The uniaxial optical indicatrix is depicted again in Fig. 2.4, but now with the electric polarization vectors of the ordinary and the extraordinary modes indicated. Since $\nabla_p \mathcal{H}_o \propto \mathbf{p}_o$, we have $\langle \hat{\mathbf{E}}_o, \nabla_p \mathcal{H}_o \rangle = 0$ and $\langle \mathbf{H}_o, \nabla_p \mathcal{H}_o \rangle = \langle \nabla_p \mathcal{H}_o, \mathbf{H}_o^* \rangle = 0$ (see Eqs. 2.55 and 2.56). In addition, $\langle \hat{\mathbf{E}}_e, \nabla_p \mathcal{H}_e \rangle = 0$ (see Eq. 2.67) and $\langle \mathbf{H}_e, \nabla_p \mathcal{H}_e \rangle = \langle \nabla_p \mathcal{H}_e, \mathbf{H}_e^* \rangle = 0$. These properties lead to the same conclusions as mentioned for biaxial anisotropy: the time-averaged Poynting vector is perpendicular to the uniaxial optical indicatrix and proportional to the vector $\nabla_p \mathcal{H}$ (see Eq. 2.58).

We conclude that, similar to the case of biaxial anisotropy, the electric and magnetic polarization vectors are tangent with respect to the optical indicatrix and the Poynting vector is proportional to the vector $\nabla_p \mathcal{H}$. In addition, the ordinary and extraordinary polarization vectors can be calculated with the concise vector equations given by Eqs. 2.62-2.65. Here it should be noted that Eq. 2.64 only applies in the special case that the dielectric tensor is real and symmetric. If the dielectric tensor is Hermitian, Eq. 2.48 applies. In contrast with the vector equations for the biaxial polarization vectors, these vector equations are not restricted to the principal coordinate system.

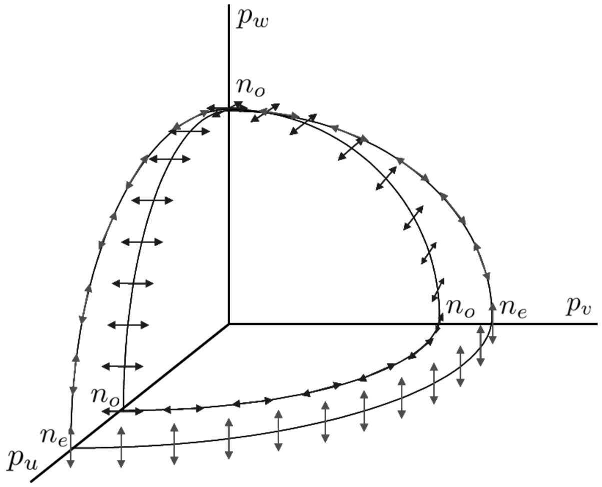

Figure 2.4: *Octant of the optical indicatrix in the principal coordinate system, but now with the polarization vectors indicated. The electric polarization vectors of the ordinary waves are indicated by the arrows on the sphere surface. The electric polarization vectors of the extraordinary waves are indicated by the arrows on the ellipsoid surface. The polarization vectors of both the ordinary and extraordinary waves are tangent to the optical indicatrix.*

2.7 Conclusions

In this chapter, we have derived the electromagnetic theory for inhomogeneous media with optical anisotropy in the (classical) geometrical-optics approach. One of the consequences of geometrical optics is that the material properties of media are only allowed to change slowly with respect to the wavelength of light. If the material properties would change rapidly with respect to the wavelength, the wave character of light cannot be neglected. In that case, we leave the domain of validity of geometrical optics, which is beyond the scope of this thesis.

Within the framework of geometrical optics, we assume that the optical properties of (an)isotropic media can be described by two main regions of interest: the interface region and the bulk region. In the bulk region we assume that condition 2.18 is satisfied. However, at an interface between two different media the material properties are discontinuous and then condition 2.18 is not satisfied. This special case will be addressed in the next chapter.

We have considered inhomogeneous anisotropic media which are defined by a complex Hermitian dielectric permittivity tensor. This Hermitian permittivity tensor represents a more general class of anisotropic media than a real symmetric permittivity tensor does. In that sense, the theory presented so far exceeds the scope of the literature on optical anisotropy. Anisotropic media with complex Hermitian permittivity tensors do not necessarily have optical axes. The mathematical equations presented in this chapter apply to anisotropic media in general, and thus also to anisotropic media without optical axes. However, we have explained the theory in the context of anisotropic media with optical axes, since this form of anisotropy is most relevant for the work presented in this thesis.

In general, we can make a distinction between two types of optical anisotropy: biaxial and uniaxial anisotropy. Biaxial anisotropy is a general form of anisotropy and in the limit where two of the three eigenvalues of the dielectric tensor coincide we have uniaxial anisotropy. Further simplification of the material properties leads to optical isotropy. For both forms of anisotropy, we have derived the optical indicatrix, a twofold surface that determines the anisotropy of the wave normal. In addition, we have investigated the correspondence between the polarization state and the anisotropy of the wave normal. One important conclusion is that light waves inside anisotropic media are in general elliptically polarized, provided that the dielectric tensor is complex Hermitian. In the special case the dielectric tensor is real and symmetric, light waves are always linearly polarized. Furthermore, we have derived general and concise vector equations for the polarization vectors in terms of the material properties and the wave normal for both biaxial and uniaxial anisotropy. These vector equations are essential for the calculation of the optical wave field in anisotropic media, in particular in the interface region.

Chapter 3

Ray-optics analysis of homogeneous anisotropic media

In the geometrical-optics approach, the material properties of media are allowed to change slowly over the distance of one wavelength. However, in this chapter, we assume that the material properties of a medium are independent of position. This type of medium is called a homogeneous medium. In the bulk region of a homogeneous medium, light waves propagate along straight lines. Moreover, in the approximations that we use, the wave amplitude and phase are constant. Only at an interface between two different media, the amplitude, phase and direction of propagation of a light wave can change. Because of this, the optical properties of homogeneous media are mainly determined by the interface region. Although condition 2.18 is not satisfied at a surface of discontinuity, we will derive the classical theory of light waves at interfaces between different anisotropic media within the framework of geometrical optics. We will assume a complex Hermitian permittivity tensor for which there exist optical axes. In a number of didactic examples, we apply this theory to isotropic, uniaxial and biaxial interfaces. In a final example, we investigate the effect of optical anisotropy in photolithographic systems.

3.1 Definition of a light ray

The light paths of light waves in isotropic media are defined by the integral curve of the wave normal $\mathbf{p}$:

$$\frac{d\mathbf{r}}{d\tau} = \mathbf{p}(\mathbf{r}(\tau)), \tag{3.1}$$

where τ is a parameter that can be considered as time. In other words, the light path of a light wave can be considered as the trajectory of a vector that is orthogonal to the wave front $\psi =$ constant (cf. [6], p. 114). The light path defined by Eq. 3.1 is called a light ray. In the same way, we can define a ray as the integral curve of the time-averaged Poynting vector $\langle\mathbf{S}\rangle$, since $\mathbf{p}$ and $\langle\mathbf{S}\rangle$ have the same direction in isotropic media. However, in anisotropic media, $\mathbf{p}$ and $\langle\mathbf{S}\rangle$ do not have the same direction since the electric field vector **E** and the electric flux density vector **D** are not parallel. Then a light ray can be defined as the integral curve of either the wave normal or the time-averaged Poynting vector. For the type of applications we are interested in, we are mainly concerned with the energy flux, represented by the Poynting vector. Therefore, for the remainder of this thesis, we define a light ray as the integral curve of the time-averaged Poynting vector:

$$\frac{d\mathbf{r}}{d\tau} = \langle \mathbf{S}(\mathbf{r}(\tau)) \rangle. \tag{3.2}$$

Moreover, in anisotropic media, a light ray has a polarization state that satisfies the equations presented in Chapter 2.

The study of optical systems by means of calculating ray paths of polarized light rays is called polarized ray tracing. In homogeneous media, ray paths of light rays are straight lines. However, the direction of propagation of a light ray can change at a surface of discontinuity. With the help of the theory discussed in Chapter 2, we will derive the optical wave field in the interface region of anisotropic media in the next section.

3.2 Optical wave field at anisotropic interfaces

Consider a boundary that forms the interface between two different transparent anisotropic media. In general, a boundary can be curved but locally, a boundary can be considered plane. In Fig. 3.1 we consider a light ray incident to a plane boundary. The local normal vector to the boundary is defined by the unit vector $\hat{\mathbf{n}}$. The incident light ray is partially reflected and partially transmitted by the anisotropic interface. Both the reflected and transmitted rays are twofold, since the optical indicatrix for anisotropic media gives rise to two independent solutions. In what follows, we will derive the wave normals that correspond to the reflected and transmitted rays for biaxial anisotropy and uniaxial anisotropy. In addition, we derive equations for the corresponding amplitude A and phase δ (see Eq. 2.13) of the reflected and transmitted rays.

3.2.1 Wave normals at anisotropic interfaces

In practice, one usually begins the process of ray tracing in an isotropic medium. Let us consider a normalized incident Poynting vector $\langle \hat{\mathbf{S}}_{inc} \rangle$ of a ray incident to a boundary that forms the interface between an isotropic medium and an anisotropic medium. In the isotropic medium, the incident wave normal is given by

$$\mathbf{p}_{inc} = n \langle \hat{\mathbf{S}}_{inc} \rangle, \tag{3.3}$$

where n is the index of refraction of the isotropic medium. In anisotropic media, the incident wave normal at an interface is determined by the ray-tracing process in the bulk region. Hence, it is always possible to define an incident wave normal $\mathbf{p}_{inc}$ which satisfies $\mathcal{H}(\mathbf{r}, \mathbf{p}) = 0$.

For a proper determination of the reflected and refracted wave normals at an interface we apply boundary conditions. The boundary conditions for the optical wave field at an interface demand that the spatial (and time) variation of the incident, reflected and refracted wave field is the same at a surface of discontinuity in the material properties (cf. [6], p. 36). From these boundary conditions, we obtain the law of refraction and

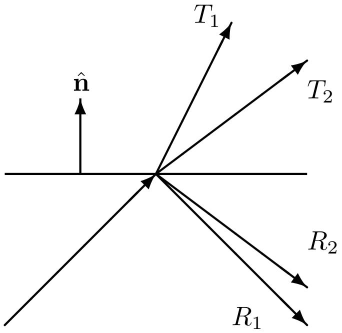

Figure 3.1: *Transmission and reflection at an interface between two anisotropic media. The local normal vector to the boundary is defined by the unit vector* $\hat{\mathbf{n}}$. *The transmitted rays are indicated by* T_1 *and* T_2 *and the reflected rays are indicated by* R_1 *and* R_2.

reflection: Snell's law. An alternative way to derive Snell's law is discussed in Born & Wolf (cf. [6], p. 124). In vector notation, Snell's law reads

$$\mathbf{p}_{inc} \times \hat{\mathbf{n}} = \mathbf{p} \times \hat{\mathbf{n}}, \tag{3.4}$$

where $\mathbf{p}$ is the corresponding refracted or reflected wave normal. Snell's law demands that the tangential components of the wave normal ($\mathbf{p}_{tn}$) are continuous across the interface. The component in the direction of $\hat{\mathbf{n}}$ is in general discontinuous. With a definition of the incident wave normal $\mathbf{p}_{inc}$, the tangential wave normal $\mathbf{p}_{tn}$ can be calculated by subtracting the normal component from the incident wave normal:

$$\mathbf{p}_{tn} = \mathbf{p}_{inc} - (\mathbf{p}_{inc} \cdot \hat{\mathbf{n}})\hat{\mathbf{n}}. \tag{3.5}$$

In what follows, we will derive a general procedure for the calculation of the reflected and refracted wave normals in anisotropic media.

The refracted wave normals are determined by substitution of the vector

$$\mathbf{p} = \mathbf{p}_{tn} + \xi\hat{\mathbf{n}}, \quad \xi \geq 0, \tag{3.6}$$

in the equation $\mathcal{H}(\mathbf{r}, \mathbf{p}) = 0$ and solve for ξ. Since the optical indicatrix consists of two shells, there are two solutions for ξ and therefore two solutions for $\mathbf{p}$. In the special case that ξ is complex, the light is totally reflected. This special case will be addressed later in this chapter. For the moment, we will assume ξ to be real. In Eqs. 2.32 and 2.41 the optical indicatrix is defined in the principal coordinate system $\{\hat{\mathbf{u}}, \hat{\mathbf{v}}, \hat{\mathbf{w}}\}$. However, in general, the principal coordinate system does not necessarily coincide with the coordinate system on which the local normal vector $\hat{\mathbf{n}}$ and the tangential wave normal $\mathbf{p}_{tn}$ are defined. Therefore, these vectors should be transformed to a coordinate system in which Eqs. 2.32 and 2.41 do apply. Consider a matrix $\mathcal{T}$ which represents a linear orthogonal transformation that transforms a vector on the orthonormal basis $\{\hat{\mathbf{x}}, \hat{\mathbf{y}}, \hat{\mathbf{z}}\}$ to the orthonormal basis $\{\hat{\mathbf{u}}, \hat{\mathbf{v}}, \hat{\mathbf{w}}\}$, the principal coordinate system. Then, the 'new' vectors are given by $\hat{\mathbf{n}}^p = \mathcal{T}\hat{\mathbf{n}}$ and $\mathbf{p}_{tn}^p = \mathcal{T}\mathbf{p}_{tn}$, where the index p denotes the principal coordinate system. Hence, on the basis $\{\hat{\mathbf{u}}, \hat{\mathbf{v}}, \hat{\mathbf{w}}\}$, Eq. 3.6 can be written

$$\mathbf{p}^p = \mathcal{T}\mathbf{p} = \mathcal{T}(\mathbf{p}_{tn} + \xi\hat{\mathbf{n}}) = \mathcal{T}\mathbf{p}_{tn} + \mathcal{T}\xi\hat{\mathbf{n}} = \mathbf{p}_{tn}^p + \xi\hat{\mathbf{n}}^p. \tag{3.7}$$

With the vectors in the principal coordinate system, we can determine the refracted wave normals if we substitute the wave normal defined by Eq. 3.7 into $\mathcal{H}(\mathbf{r},\mathbf{p}) = 0$. Then we obtain a polynomial of ξ of degree four and we can find numerical solutions by any of the standard methods described in Numerical Recipes (cf. [90], Chapter 9, p. 355). Alternatively, an analytical procedure for solving a polynomial of fourth degree is described in Griffiths (cf. [91], p. 32). When the solutions for ξ are obtained, the vectors $\hat{\mathbf{n}}^p$, $\mathbf{p}^p_{tn}$ and $\mathbf{p}^p$ can be transformed back to the coordinate system $\{\hat{\mathbf{x}},\hat{\mathbf{y}},\hat{\mathbf{z}}\}$. To this end, we apply the inverse of the matrix $\mathcal{T}$, denoted by $\mathcal{T}^{-1}$.

For reflected rays at an anisotropic interface, Eq. 3.6 changes into $\mathbf{p} = \mathbf{p}_{tn} - \xi\hat{\mathbf{n}}$, with $\xi \geq 0$. Of course now the indicatrix in the incident medium should be used. We conclude that for any arbitrary type of medium (isotropic, uniaxial or biaxial), the reflected and refracted wave normals can be calculated according to the procedure discussed in this subsection.

3.2.2 Wave normals at uniaxial interfaces

Uniaxially anisotropic interfaces involve equations that are polynomials of degree two (see Eqs. 2.42 and 2.43). As a consequence, for uniaxial interfaces, we can solve the reflected and refracted wave normals in a simple analytical way. In this subsection, we will do this for both ordinary and extraordinary wave normals.

We consider a normalized incident Poynting vector $\langle\hat{\mathbf{S}}_{inc}\rangle$ of an extraordinary ray incident to an interface between two uniaxially anisotropic media. This unit vector defines the direction of the energy transfer of the incident ray. The corresponding incident wave normal $\mathbf{p}_{inc}$ can be obtained from the ray-tracing process in the bulk region, which will be discussed in the next chapter. On the other hand, once $\langle\hat{\mathbf{S}}_{inc}\rangle$ is defined, we can also derive an analytical expression for $\mathbf{p}_{inc}$ in terms of the vector components of $\langle\hat{\mathbf{S}}_{inc}\rangle$. According to Eq. 2.58, $\langle\hat{\mathbf{S}}_{inc}\rangle$ is proportional to $\nabla_p\mathcal{H}$. Then for an extraordinary ray, the normalized incident Poynting vector can be written as

$$\langle\hat{\mathbf{S}}_{inc}\rangle = \frac{\nabla_p\mathcal{H}_e}{|\nabla_p\mathcal{H}_e|}. \tag{3.8}$$

On the basis $\{\hat{\mathbf{u}},\hat{\mathbf{v}},\hat{\mathbf{w}}\}$, $\mathcal{H}_e$ satisfies Eq. 2.43. With Eq. 2.43 and Eq. 3.8 we have four equations with three unknowns, namely $|p_{inc,u}|$, $|p_{inc,v}|$ and $|p_{inc,w}|$. This set of equations can be solved analytically. As a result, we know $|\mathbf{p}_{inc}|$. If the basis $\{\hat{\mathbf{u}},\hat{\mathbf{v}},\hat{\mathbf{w}}\}$ is complex, we have $\mathbf{p}_{inc} = |\mathbf{p}_{inc}|\hat{\mathbf{p}}_{inc}$, but $\hat{\mathbf{p}}_{inc}$ is still unknown. If the basis $\{\hat{\mathbf{u}},\hat{\mathbf{v}},\hat{\mathbf{w}}\}$ is real, we have

$$\mathbf{p}_{inc} = |p_{inc,u}|\hat{\mathbf{u}} + |p_{inc,v}|\hat{\mathbf{v}} + |p_{inc,w}|\hat{\mathbf{w}}. \tag{3.9}$$

In conclusion, we can derive an expression for $\mathbf{p}_{inc}$ in terms of the vector components of $\langle\hat{\mathbf{S}}^p_{inc}\rangle$ provided that the basis $\{\hat{\mathbf{u}},\hat{\mathbf{v}},\hat{\mathbf{w}}\}$ is real, and therefore the dielectric tensor is real and symmetric. Then, in the principle coordinate system, the incident extraordinary wave normal satisfies

$$\mathbf{p}_{inc} = \frac{n_e^2\langle\hat{S}_{inc,u}\rangle\hat{\mathbf{u}} + n_e^2\langle\hat{S}_{inc,v}\rangle\hat{\mathbf{v}} + n_o^2\langle\hat{S}_{inc,w}\rangle\hat{\mathbf{w}}}{\sqrt{n_e^2 + (n_o^2 - n_e^2)\langle\hat{S}_{inc,w}\rangle^2}}. \tag{3.10}$$

For ordinary rays in uniaxially anisotropic media, $n_e = n_o$ and then Eq. 3.10 reduces to $\mathbf{p}_{inc} = n_o\langle\hat{\mathbf{S}}_{inc}\rangle$. In isotropic media, $n_e = n_o = n$ and Eq. 3.10 reduces to Eq. 3.3. Hence, for arbitrary values of n_o and n_e, we can apply Eq. 3.10 to both isotropic and uniaxially anisotropic media in the real principal coordinate system.

Subsequently, we can apply Snell's law and calculate the tangential wave normal $\mathbf{p}_{tn}$ with Eq. 3.5.

For ordinary rays, the wave normal is determined by the intersection of the vector $\mathbf{p}_o = \mathbf{p}_{tn} + \xi\hat{\mathbf{n}}$ with the surface $\mathcal{H}_o = 0$. Since $\mathcal{H}_o = 0$ represents a sphere with radius n_o, ξ must satisfy the condition $|\mathbf{p}_{tn}|^2 + \xi^2 = n_o^2$. Therefore, we conclude that the refracted or reflected ordinary wave normal reads

$$\mathbf{p}_o = \mathbf{p}_{tn} \pm \sqrt{n_o^2 - |\mathbf{p}_{tn}|^2}\hat{\mathbf{n}}. \tag{3.11}$$

In the definition that we use, the plus sign applies to transmitted rays and the minus sign applies to reflected rays. In isotropic media, we can apply Eq. 3.11 if the index o is removed.

Similarly, the extraordinary wave normal is given by

$$\mathbf{p}_e = \mathbf{p}_{tn} + \xi\hat{\mathbf{n}}. \tag{3.12}$$

The constant ξ is determined by the condition that the endpoint of the wave normal $\mathbf{p}_e$ lies on the ellipsoid surface $\mathcal{H}_e = 0$. Therefore, on the complex basis $\{\hat{\mathbf{u}}, \hat{\mathbf{v}}, \hat{\mathbf{w}}\}$, ξ is now given by

$$\begin{aligned}
\xi &= \frac{-B_\xi \pm \sqrt{B_\xi^2 - 4A_\xi C_\xi}}{2A_\xi}, && (3.13)\\
A_\xi &= \frac{|\hat{n}_w|^2}{n_o^2} + \frac{|\hat{n}_u|^2 + |\hat{n}_v|^2}{n_e^2}, && (3.14)\\
B_\xi &= \frac{2\mathrm{Re}(p_{tn,w}\hat{n}_w)}{n_o^2} + \frac{2\mathrm{Re}(p_{tn,u}\hat{n}_u) + 2\mathrm{Re}(p_{tn,v}\hat{n}_v)}{n_e^2}, && (3.15)\\
C_\xi &= \frac{|p_{tn,w}|^2}{n_o^2} + \frac{|p_{tn,u}|^2 + |p_{tn,v}|^2}{n_e^2} - 1. && (3.16)
\end{aligned}$$

The plus sign in Eq. 3.13 applies to refracted rays and the minus sign applies to reflected rays. If $n_e = n_o = n$, $A_\xi = \frac{1}{n^2}$, $B_\xi = \frac{2}{n^2}(\langle\mathbf{p}_{tn}, \hat{\mathbf{n}}\rangle + \langle\hat{\mathbf{n}}, \mathbf{p}_{tn}\rangle) = 0$ and $C_\xi = \frac{|\mathbf{p}_{tn}|^2}{n^2} - 1$. Then, $\xi = \pm\sqrt{n^2 - |\mathbf{p}_{tn}|^2}$ which applies to rays in isotropic media.

Fig. 3.2 shows a schematic procedure of the process discussed. In this particular example, the incident medium is isotropic and the second medium is uniaxially anisotropic with a tilted optical axis. The figure shows the intersections of the optical indicatrix of both media with the plane of incidence. For the isotropic medium, the intersection of the optical indicatrix is a circle with radius n. For the anisotropic medium, the intersection consists of a circle with radius n_o and a tilted ellipse with semi-axes n_o and n_e. The optical axis is denoted by the unit vector $\hat{\mathbf{w}}$ and lies in the plane of incidence. The incident medium shows the incident wave normal $\mathbf{p}_{inc}$ and the corresponding tangential wave normal $\mathbf{p}_{tn}$. In the incident medium, there is one reflected wave normal denoted by

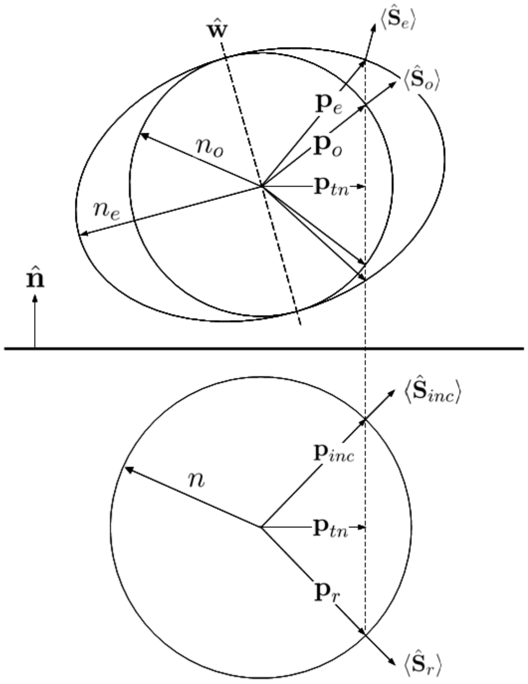

Figure 3.2: *Refraction and reflection at an isotropic-anisotropic interface with local normal vector* $\hat{\boldsymbol{n}}$. *The anisotropic medium has a tilted optical axis, denoted by* $\hat{\boldsymbol{w}}$. *The figure shows the intersections of the optical indicatrix of both media with the plane of incidence. For an incident normalized Poynting vector* $\langle\hat{\boldsymbol{S}}_{inc}\rangle$, *the corresponding incident wave normal* $\boldsymbol{p}_{inc}$ *and tangential wave normal* $\boldsymbol{p}_{tn}$ *are depicted. The reflected and refracted wave normals that match the vector* $\boldsymbol{p}_{tn}$ *are indicated by* $\boldsymbol{p}_r$, $\boldsymbol{p}_o$ *and* $\boldsymbol{p}_e$. *In addition, the corresponding reflected and refracted normalized Poynting vectors are denoted by* $\langle\hat{\boldsymbol{S}}_r\rangle$, $\langle\hat{\boldsymbol{S}}_o\rangle$ *and* $\langle\hat{\boldsymbol{S}}_e\rangle$.

$\mathbf{p}_r$. In the anisotropic medium, we can find four wave normals that match the vector $\mathbf{p}_{tn}$. Only two of them represent the refracted wave normals. In order to make sure we find the right wave normals, we must apply the plus sign in Eqs. 3.11 and 3.13. The ordinary and extraordinary refracted wave normals are denoted by $\mathbf{p}_o$ and $\mathbf{p}_e$, respectively. The corresponding reflected and refracted normalized Poynting vectors are defined by Eq. 3.8. These unit vectors are perpendicular with respect to the circle and ellipse intersections. In Fig. 3.2, the normalized Poynting vectors for the incident, reflected and transmitted rays are indicated by $\langle\hat{\mathbf{S}}_{inc}\rangle$, $\langle\hat{\mathbf{S}}_r\rangle$, $\langle\hat{\mathbf{S}}_o\rangle$ and $\langle\hat{\mathbf{S}}_e\rangle$, respectively.

We have derived concise vector equations in order to calculate the incident, reflected and refracted wave normals of both ordinary and extraordinary rays at an uniaxially anisotropic interface. These equations apply to arbitrary values of the indices n_o and n_e. However, Eqs. 3.10 and 3.13-3.16 only apply in the principal coordinate system. For these equations it is necessary to define the vectors $\langle \hat{\mathbf{S}}_{inc} \rangle$, $\hat{\mathbf{n}}$ and $\mathbf{p}_{tn}$ on the principal basis $\{\hat{\mathbf{u}}, \hat{\mathbf{v}}, \hat{\mathbf{w}}\}$. Moreover, Eq. 3.10 only applies if the basis $\{\hat{\mathbf{u}}, \hat{\mathbf{v}}, \hat{\mathbf{w}}\}$ is real. In addition, it can be concluded that all wave normals, together with the local normal vector $\hat{\mathbf{n}}$, are in the same plane: the plane of incidence. The optical axis does not necessarily lie in the plane of incidence: the optical indicatrix can have any arbitrary orientation in three-dimensional space. As a consequence, the Poynting vector does not necessarily lie in the plane of incidence.

3.2.3 Total reflection

In general, it is possible that Eq. 3.6 does not yield a real solution for the refracted wave normal. This can be the case if, for example, $|\mathbf{p}_{tn}|$ exceeds the ordinary index of refraction of the upper medium in Fig. 3.2. Then Eq. 3.11 yields

$$\mathbf{p}_o = \mathbf{p}_{tn} + ip_I \hat{\mathbf{n}}, \tag{3.17}$$

with

$$p_I = \sqrt{|\mathbf{p}_{tn}|^2 - n_o^2}. \tag{3.18}$$

The physical meaning of a complex wave normal can be explained as follows. Let us consider a plane wave given by

$$\mathbf{E}(\mathbf{r}, t) = \tilde{\mathbf{E}}(\mathbf{r}) e^{i(k_0 \mathbf{p} \cdot \mathbf{r} - \omega t)}.$$

When we substitute Eq. 3.17 into Eq. 3.2.3, we obtain

$$\mathbf{E}(\mathbf{r}, t) = \left[\tilde{\mathbf{E}}(\mathbf{r}) e^{-k_0 p_I \hat{\mathbf{n}} \cdot \mathbf{r}} \right] e^{i(k_0 \mathbf{p}_{tn} \cdot \mathbf{r} - \omega t)}.$$

This equation represents a plane wave propagating along the interface (orthogonal to the local normal vector $\hat{\mathbf{n}}$) in the plane of incidence. Moreover, the amplitude of this plane wave decreases exponentially with the normal distance from the interface (in the direction of $\hat{\mathbf{n}}$). The effective depth of penetration in the medium is of the order of $\frac{c}{\omega n} = \frac{\lambda}{2\pi}$, with λ the wavelength of light in the corresponding medium. As a result, the effective depth of penetration is in the order of the wavelength. The type of wave represented by Eq. 3.2.3 is called an evanescent wave.

When a refracted wave normal is of the form given by Eq. 3.17, the time average of the flow of energy across the interface vanishes. However, the preceding analysis is based on the assumption that the interface region and the wave front are of infinite extent (cf. [6], p. 47). For the moment, in the approximation that we use, which is the geometrical-optics approach, it is sufficient to assume that no energy will penetrate the second medium.

3.2.4 Fresnel coefficients

With the procedure derived in the previous subsection, we are able to calculate refracted and reflected wave normals at an anisotropic interface. The corresponding polarization vectors can be calculated with the equations derived in Section 2.6. The amplitude A and the phase term δ of the complex amplitude of a quasi-plane wave (see Eq. 2.13) can also be calculated in the interface region. For the remainder of this thesis, we define the electric or magnetic complex amplitude as the complex number a. Hence, a satisfies

$$a = A(\mathbf{r})e^{i\delta(\mathbf{r})}.$$

As a consequence, the electric and magnetic complex amplitude vectors can be written as

$$\begin{aligned} \tilde{\mathbf{E}} &= a\hat{\mathbf{E}}, & (3.19) \\ \tilde{\mathbf{H}} &= a\mathbf{H}, & (3.20) \end{aligned}$$

where $\mathbf{H} = \frac{1}{c\mu_0}\mathbf{p} \times \hat{\mathbf{E}}$. In order to calculate the complex amplitudes on both sides of an anisotropic interface, we apply boundary conditions. The boundary conditions for an electromagnetic field demand that across a boundary, the tangential components of the complex amplitude vectors $\tilde{\mathbf{E}}$ and $\tilde{\mathbf{H}}$ should be continuous (cf. [92], p. 18). This means that the vector components of $\tilde{\mathbf{E}}$ and $\tilde{\mathbf{H}}$ that are orthogonal to the local normal vector $\hat{\mathbf{n}}$ are identical on both sides of an interface. In order to calculate these vector components, we define two unit vectors $\hat{\mathbf{t}}_s$ and $\hat{\mathbf{t}}_p$ in such a way that they define a local orthonormal basis $\{\hat{\mathbf{t}}_s, \hat{\mathbf{t}}_p, \hat{\mathbf{n}}\}$. Moreover, the unit vector $\hat{\mathbf{t}}_s$ is defined orthogonal to the plane of incidence (senkrecht) and $\hat{\mathbf{t}}_p$ is defined in the plane of incidence (parallel). In terms of an incident wave normal $\mathbf{p}_{inc}$ and a normal vector $\hat{\mathbf{n}}$, the local unit vectors can be written as (cf. [56], p. 2375)

$$\begin{aligned} \hat{\mathbf{t}}_s &= \frac{\mathbf{p}_{inc} \times \hat{\mathbf{n}}}{|\mathbf{p}_{inc} \times \hat{\mathbf{n}}|}, & (3.21) \\ \hat{\mathbf{t}}_p &= \hat{\mathbf{n}} \times \hat{\mathbf{t}}_s. & (3.22) \end{aligned}$$

For a general approach, we consider the case for a boundary that forms an interface between two anisotropic media. Then the optical wave field at the interface consists of two reflected and two transmitted rays. In Fig. 3.1, these rays are denoted by the indices 1 and 2.

Application of the boundary conditions yields four linear equations given by (cf. [57], p. 2391)

$$\begin{aligned} \hat{\mathbf{t}}_s \cdot (\tilde{\mathbf{E}}_{t1} + \tilde{\mathbf{E}}_{t2}) &= \hat{\mathbf{t}}_s \cdot (\tilde{\mathbf{E}}_{inc} + \tilde{\mathbf{E}}_{r1} + \tilde{\mathbf{E}}_{r2}), & (3.23) \\ \hat{\mathbf{t}}_p \cdot (\tilde{\mathbf{E}}_{t1} + \tilde{\mathbf{E}}_{t2}) &= \hat{\mathbf{t}}_p \cdot (\tilde{\mathbf{E}}_{inc} + \tilde{\mathbf{E}}_{r1} + \tilde{\mathbf{E}}_{r2}), & (3.24) \\ \hat{\mathbf{t}}_s \cdot (\tilde{\mathbf{H}}_{t1} + \tilde{\mathbf{H}}_{t2}) &= \hat{\mathbf{t}}_s \cdot (\tilde{\mathbf{H}}_{inc} + \tilde{\mathbf{H}}_{r1} + \tilde{\mathbf{H}}_{r2}), & (3.25) \\ \hat{\mathbf{t}}_p \cdot (\tilde{\mathbf{H}}_{t1} + \tilde{\mathbf{H}}_{t2}) &= \hat{\mathbf{t}}_p \cdot (\tilde{\mathbf{H}}_{inc} + \tilde{\mathbf{H}}_{r1} + \tilde{\mathbf{H}}_{r2}), & (3.26) \end{aligned}$$

where the indices r and t denote the reflected and transmitted electromagnetic fields, respectively. Without loss of generality, we can define the incident electric and magnetic complex vectors $\tilde{\mathbf{E}}_{inc}$ and $\tilde{\mathbf{H}}_{inc}$ in such a way that a_{inc} is real and normalized. This means that $\delta_{inc} = 0$ and $A_{inc} = 1$ so that a_{inc} satisfies

$$a_{inc} = 1. \qquad (3.27)$$

When we substitute Eqs. 3.19, 3.20 and 3.27 into the boundary conditions and rearrange terms, we can rewrite the boundary conditions as a matrix equation according to

$$\begin{pmatrix} \hat{\mathbf{t}}_s \cdot \hat{\mathbf{E}}_{t1} & \hat{\mathbf{t}}_s \cdot \hat{\mathbf{E}}_{t2} & -\hat{\mathbf{t}}_s \cdot \hat{\mathbf{E}}_{r1} & -\hat{\mathbf{t}}_s \cdot \hat{\mathbf{E}}_{r2} \\ \hat{\mathbf{t}}_p \cdot \hat{\mathbf{E}}_{t1} & \hat{\mathbf{t}}_p \cdot \hat{\mathbf{E}}_{t2} & -\hat{\mathbf{t}}_p \cdot \hat{\mathbf{E}}_{r1} & -\hat{\mathbf{t}}_p \cdot \hat{\mathbf{E}}_{r2} \\ \hat{\mathbf{t}}_s \cdot \mathbf{H}_{t1} & \hat{\mathbf{t}}_s \cdot \mathbf{H}_{t2} & -\hat{\mathbf{t}}_s \cdot \mathbf{H}_{r1} & -\hat{\mathbf{t}}_s \cdot \mathbf{H}_{r2} \\ \hat{\mathbf{t}}_p \cdot \mathbf{H}_{t1} & \hat{\mathbf{t}}_p \cdot \mathbf{H}_{t2} & -\hat{\mathbf{t}}_p \cdot \mathbf{H}_{r1} & -\hat{\mathbf{t}}_p \cdot \mathbf{H}_{r2} \end{pmatrix} \begin{pmatrix} a_{t1} \\ a_{t2} \\ a_{r1} \\ a_{r2} \end{pmatrix} = \begin{pmatrix} \hat{\mathbf{t}}_s \cdot \hat{\mathbf{E}}_{inc} \\ \hat{\mathbf{t}}_p \cdot \hat{\mathbf{E}}_{inc} \\ \hat{\mathbf{t}}_s \cdot \mathbf{H}_{inc} \\ \hat{\mathbf{t}}_p \cdot \mathbf{H}_{inc} \end{pmatrix}. \tag{3.28}$$

The only unknowns in this matrix equation are the complex amplitudes a_{t1}, a_{t2}, a_{r1} and a_{r2}. These complex amplitudes are also known as the Fresnel coefficients. The matrix equation can be solved analytically or by any of the standard methods as e.g. described in Numerical Recipes (cf. [90], p. 22).

In this thesis, we apply the following notation. In uniaxially anisotropic media, the indices 1 and 2 are substituted by the indices o and e for the ordinary and extraordinary rays, respectively. In isotropic media, the electric and magnetic field vectors have an s-component and a p-component on the basis $\{\hat{\mathbf{t}}_s, \hat{\mathbf{t}}_p, \hat{\mathbf{n}}\}$. Then, the indices 1 and 2 are replaced by the indices s and p.

Consider for example an interface between an isotropic medium and an uniaxially anisotropic medium. For this type of interface, a_{r1} and a_{r2} are replaced by a_{rs} and a_{rp}, respectively. In addition, $\hat{\mathbf{E}}_{r1}$, $\hat{\mathbf{E}}_{r2}$, $\mathbf{H}_{r1}$ and $\mathbf{H}_{r2}$ are replaced by $\hat{\mathbf{E}}_{rs}$, $\hat{\mathbf{E}}_{rp}$, $\mathbf{H}_{rs}$ and $\mathbf{H}_{rp}$, respectively. Moreover, the electric polarization vector for the s-component is given by

$$\hat{\mathbf{E}}_{rs} = \hat{\mathbf{t}}_s, \tag{3.29}$$

and the electric polarization vector of the p-component satisfies

$$\hat{\mathbf{E}}_{rp} = \frac{\hat{\mathbf{E}}_{rs} \times \mathbf{p}_r}{|\hat{\mathbf{E}}_{rs} \times \mathbf{p}_r|}. \tag{3.30}$$

The polarization vectors for the transmitted ordinary and extraordinary rays are given by Eqs. 2.62 and 2.64, respectively.

For an anisotropic-isotropic interface, Eq. 3.29 and Eq. 3.30 apply as well, provided that the index r is replaced by the index t, resulting in the set of Fresnel coefficients a_{ts}, a_{tp}, a_{ro} and a_{re}. For isotropic-isotropic interfaces, Eq. 3.29 and Eq. 3.30 apply for both the index r and the index t, yielding a_{ts}, a_{tp}, a_{rs} and a_{rp}.

As a result, the electromagnetic field of, for example, a reflected quasi-plane wave in an isotropic medium is given by

$$\mathbf{E}(\mathbf{r}, t) = (a_{rs}\hat{\mathbf{E}}_{rs} + a_{rp}\hat{\mathbf{E}}_{rp})e^{i(k_0\psi_r - \omega t)}, \tag{3.31}$$

$$\mathbf{H}(\mathbf{r}, t) = \frac{1}{c\mu_0}(a_{rs}\mathbf{H}_{rs} + a_{rp}\mathbf{H}_{rp})e^{i(k_0\psi_r - \omega t)}, \tag{3.32}$$

while the electromagnetic field of a transmitted extraordinary quasi-plane wave is given by

$$\mathbf{E}(\mathbf{r},t) = a_{te}\hat{\mathbf{E}}_{te}e^{i(k_0\psi_{te}-\omega t)}, \tag{3.33}$$

$$\mathbf{H}(\mathbf{r},t) = \frac{1}{c\mu_0}a_{te}\mathbf{H}_{te}e^{i(k_0\psi_{te}-\omega t)}. \tag{3.34}$$

The Fresnel coefficients are complex numbers from which we can determine the phase shift of the refracted and reflected rays. Moreover, we can determine the polarization state of the rays from the complex amplitude vectors. In anisotropic media, the polarization state of light rays is in general elliptical. Only when the dielectric tensor is real and symmetric, the polarization state of light rays is linear. In isotropic media, the polarization state is, in general, elliptical.

3.2.5 Intensity transmittance and reflectance factors

From the electromagnetic field at an interface, we can calculate the time-averaged Poynting vector with Eq. 2.57. In addition, for an arbitrary type of interface, we can apply the law of conservation of energy flow in the direction of the local normal vector $\hat{\mathbf{n}}$. For an anisotropic-anisotropic interface, this yields

$$\begin{aligned}\hat{\mathbf{n}}\cdot\langle\mathbf{S}_{inc}\rangle &= \hat{\mathbf{n}}\cdot\langle\mathbf{S}_{t1}\rangle + \hat{\mathbf{n}}\cdot\langle\mathbf{S}_{t2}\rangle \\ &\quad - \hat{\mathbf{n}}\cdot\langle\mathbf{S}_{r1}\rangle - \hat{\mathbf{n}}\cdot\langle\mathbf{S}_{r2}\rangle.\end{aligned} \tag{3.35}$$

The minus sign appears since, for reflected rays, $\hat{\mathbf{n}}\cdot\langle\mathbf{S}_r\rangle \leq 0$. By dividing both sides of Eq. 3.35 by $\hat{\mathbf{n}}\cdot\langle\mathbf{S}_{inc}\rangle$, we obtain

$$\begin{aligned}1 &= \frac{\hat{\mathbf{n}}\cdot\langle\mathbf{S}_{t1}\rangle}{\hat{\mathbf{n}}\cdot\langle\mathbf{S}_{inc}\rangle} + \frac{\hat{\mathbf{n}}\cdot\langle\mathbf{S}_{t2}\rangle}{\hat{\mathbf{n}}\cdot\langle\mathbf{S}_{inc}\rangle} \\ &\quad - \frac{\hat{\mathbf{n}}\cdot\langle\mathbf{S}_{r1}\rangle}{\hat{\mathbf{n}}\cdot\langle\mathbf{S}_{inc}\rangle} - \frac{\hat{\mathbf{n}}\cdot\langle\mathbf{S}_{r2}\rangle}{\hat{\mathbf{n}}\cdot\langle\mathbf{S}_{inc}\rangle}.\end{aligned} \tag{3.36}$$

The electromagnetic field at an anisotropic interface has to satisfy Eq. 3.36. Each term on the left side of Eq. 3.36 represents either an intensity transmittance factor T or an intensity reflectance factor R. Consequently, Eq. 3.36 can be written as

$$1 = T_1 + T_2 + R_1 + R_2, \tag{3.37}$$

with

$$T_1 = \left|\frac{\hat{\mathbf{n}}\cdot\langle\mathbf{S}_{t1}\rangle}{\hat{\mathbf{n}}\cdot\langle\mathbf{S}_{inc}\rangle}\right|, \quad T_2 = \left|\frac{\hat{\mathbf{n}}\cdot\langle\mathbf{S}_{t2}\rangle}{\hat{\mathbf{n}}\cdot\langle\mathbf{S}_{inc}\rangle}\right|, \tag{3.38}$$

$$R_1 = \left|\frac{\hat{\mathbf{n}}\cdot\langle\mathbf{S}_{r1}\rangle}{\hat{\mathbf{n}}\cdot\langle\mathbf{S}_{inc}\rangle}\right|, \quad R_2 = \left|\frac{\hat{\mathbf{n}}\cdot\langle\mathbf{S}_{r2}\rangle}{\hat{\mathbf{n}}\cdot\langle\mathbf{S}_{inc}\rangle}\right|. \tag{3.39}$$

As usual, the indices 1 and 2 are replaced by o and e for uniaxially anisotropic media. For isotropic media, we obtain R_s, R_p, T_s and T_p.

In general, we can conclude that we are able to calculate the amplitude and phase terms (A and δ) of the optical wave field at an (an)isotropic interface through the calculation of the Fresnel coefficients. From the optical wave field, we can also calculate the intensity transmittance and reflectance factors at an interface. In the next section, we discuss how the classical theory discussed can be implemented into a computer program.

3.3 General ray-tracing procedure for anisotropic interfaces

The classical theory discussed enables the calculation of the optical wave field at an arbitrary interface between two anisotropic media. To calculate the optical properties of anisotropic interfaces numerically, we apply the classical theory into a numerical simulation program. This section describes the relevant subsequent steps that are necessary for a proper determination of the optical wave field at anisotropic interfaces.

First, we need to define the optical properties of the two media forming an anisotropic interface: the principal indices of refraction $n_u^{i,f}$, $n_v^{i,f}$ and $n_w^{i,f}$, the optical axes and the normal vector $\hat{\mathbf{n}}$ to the plane boundary. The indices i and f denote the incident and the final medium, respectively. With the definition of the principal indices of refraction it is possible to determine the type of interface. For example, when $n_u^i = n_v^i \neq n_w^i$ and $n_u^f \neq n_v^f \neq n_w^f$, the incident medium is uniaxially anisotropic and the final medium is biaxially anisotropic. In addition, we know that an incident light ray, defined by an incident wave normal $\mathbf{p}_{inc}$ in the incident medium, gives rise to in general two reflected rays and two refracted rays.

Next, we calculate the wave normals that correspond to the reflected and refracted rays. These are calculated with the help of the procedure described in Subsections 3.2.1 and 3.2.2. In this procedure, vectors are transformed from the Cartesian basis $\{\hat{\mathbf{x}}, \hat{\mathbf{y}}, \hat{\mathbf{z}}\}$ to the principal basis $\{\hat{\mathbf{u}}, \hat{\mathbf{v}}, \hat{\mathbf{w}}\}$ on which $\underline{\underline{\varepsilon}}$ is diagonal. The corresponding transformation matrix $\mathcal{T}$ is an orthogonal matrix which preserves the length of a vector. In the special case that the dielectric tensor is real and symmetric, the matrix $\mathcal{T}$ is given by a real orthogonal rotation matrix. Then the definition of the rotation matrix $\mathcal{T}$ depends on the orientation of the basis $\{\hat{\mathbf{u}}, \hat{\mathbf{v}}, \hat{\mathbf{w}}\}$ with respect to the basis $\{\hat{\mathbf{x}}, \hat{\mathbf{y}}, \hat{\mathbf{z}}\}$. In general, if we know the optical axes of both the incident and the final medium, we also know the bases $\{\hat{\mathbf{u}}, \hat{\mathbf{v}}, \hat{\mathbf{w}}\}^{i,f}$ and therefore the corresponding rotation matrices $\mathcal{T}^{i,f}$. Since the determination of the matrix $\mathcal{T}$ is a rather straightforward process, in particular when using technical computing software such as MatLab [93], we will not discuss this procedure further.

Finally, we calculate the Fresnel coefficients. Then we need to define the amplitude a_{inc} of an incident ray. Without loss of generality, we can define $a_{inc} = 1$ (see Eq. 3.27). In addition, we define the polarization vector $\hat{\mathbf{E}}_{inc}$ of the incident ray. Note that in general $\hat{\mathbf{E}}_{inc}$ can be complex. Furthermore, we need to calculate the polarization vectors using the appropriate vector equations presented in Section 2.6. From the polarization vectors, we obtain the polarization state of the individual rays. In order to calculate the polarization vectors, we use the reflected and refracted wave normals obtained in the procedure discussed above. Then we apply the matrix equation defined by Eq. 3.28 from which the Fresnel coefficients are calculated numerically. From the Fresnel coefficients we obtain the phase δ, the relative amplitude A (recall that $a_{inc} = 1$) and the transmittance and reflectance factors of the individual rays. In addition, the sum of the transmittance and reflectance factors should exactly add up to one (see Eq. 3.37). This condition is a good indicator for errors in the numerical simulation program.

At this point, we have obtained the optical wave field at an anisotropic interface of interest. From the results, we can proceed with the ray-tracing process in the bulk region. A procedure for the calculation of ray paths of light rays in the bulk region of inhomogeneous anisotropic media will be discussed in Chapter 4.

In what follows, we will calculate and analyze the optical properties of a number of (an)isotropic interfaces with the help of the classical theory and the numerical simulation program discussed above.

3.4 Modeling of anisotropic interfaces

In this section, we apply our computer program in order to calculate the optical properties of uniaxially anisotropic and biaxially anisotropic interfaces and investigate some interesting features. To this end, we aim to demonstrate the applicability of the classical theory derived in the preceding analysis. For the remainder of this chapter, we assume a real symmetric dielectric tensor.

3.4.1 Brewster angle of an air-calcite interface

In this example, we apply the classical theory to a plane interface between an isotropic and an uniaxially anisotropic medium. We define the isotropic medium to be air and the second anisotropic medium to be calcite. We analyze calcite with an ordinary index of refraction $n_o = 1.655$ and an extraordinary index of refraction $n_e = 1.485$ (negative birefringence). These values for the refractive indices are valid for light with a wavelength of 633 nm (cf. [66], p. 2766). The optical axis $\hat{\mathbf{w}}$ of the calcite is at an angle of 45° with the plane of incidence. The incident light has a linear polarization in the plane of incidence (p-polarization). As a function of the angle of incidence θ_{inc}, we calculate the transmittance factor T_o for the ordinary wave. Similarly, we calculate T_e, R_s and R_p. The results are depicted in Fig. 3.3. The sum of T_o, T_e, R_s and R_p is indicated by T_t and should result in 1 for any value of θ_{inc} (see Eq. 3.37).

It appears that the tilted optical axis generates both extraordinary and ordinary rays. In addition, the reflected light is mainly p-polarized (R_s is very small but not zero). The Brewster angle θ_B is defined as the incident angle where R_p vanishes. From Fig. 3.3, we can read a Brewster angle of 59.76°. In Lekner [66], the Brewster angle is calculated analytically. There, the reflection amplitudes result in a quartic equation of which one of the physical roots determines the Brewster angle. Lekner predicts a Brewster angle of 59.75° (cf. [66], Table 1, p. 2766).

Lekner also calculates the Brewster angle as a function of the angle Γ which the optical axis makes with the local normal vector $\hat{\mathbf{n}}$ [55]. In this case, the optical axis is defined in the plane of incidence. Fig. 3.4 shows the Brewster angle as a function of the square of the cosine of the angle Γ, denoted by γ^2. We can conclude that Lekner's results are well reproduced (cf. [55], Fig. 1, p. 2061).

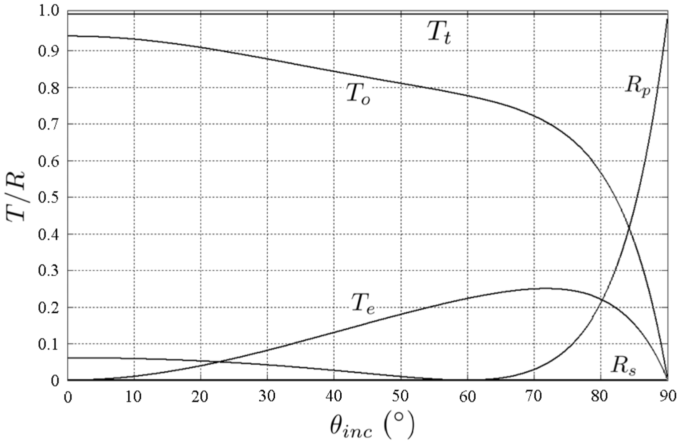

Figure 3.3: *Transmittance and reflectance factors as a function of the angle of incidence* θ_{inc} *for an air-calcite interface. The optical axis is at* $45°$ *with the plane of incidence.* T_o *and* T_e *are the ordinary and extraordinary transmittance factors, respectively.* R_s *and* R_p *are the reflectance factors for s- and p-polarized light, respectively.* T_t *is the sum of these factors and should result in 1 for any value of* θ_{inc}*. The Brewster angle* θ_B *is the angle where* R_p *vanishes and reads* $59.76°$.

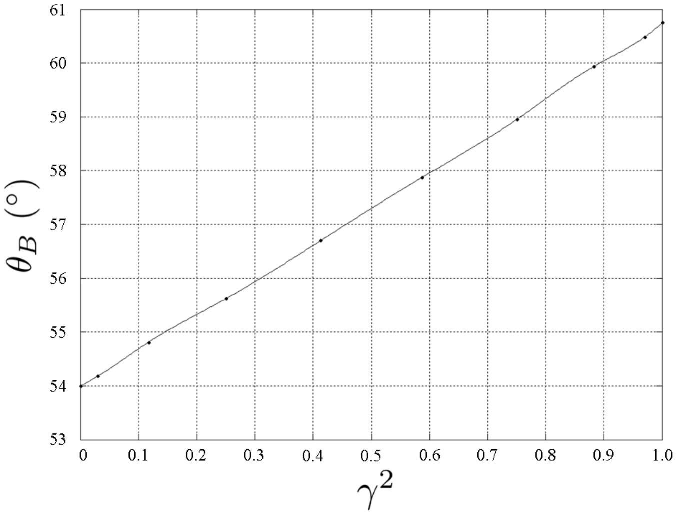

Figure 3.4: *Brewster angle* θ_B *for an air-calcite interface as a function of* γ^2*. The optical axis is in the plane of incidence. The parameter* γ *is the cosine of the angle* Γ *between the optical axis* $\hat{\boldsymbol{w}}$ *and the local normal vector* $\hat{\boldsymbol{n}}$.

3.4.2 Double total internal reflection

An interesting feature of an interface between an (an)isotropic and an anisotropic medium is that it can have two critical angles for total internal reflection. The possible existence of two critical angles is related to the duplicate character of the optical indicatrix.

We will investigate the optical properties of an interface between glass and crystalline chiolite ($Na_5Al_3F_{14}$). The ordinary and extraordinary index of refraction of uniaxial chiolite in a tetragonal crystal system are $n_o = 1.349$ and $n_e = 1.342$ at a wavelength of 589.3 nm (cf. [2], **4**-141). Since $n_o > n_e$, the crystal has a negative birefringence. We define the optical axis of the chiolite crystal at an angle of 45° with the plane of incidence. Moreover, the incident light in the glass medium ($n = 1.5$) is *p*-polarized in the plane of incidence.

Fig. 3.5 shows the intensity transmittance and reflectance factors as a function of the angle of incidence θ_{inc}. From the figure we can obtain the Brewster angle and two critical angles for total internal reflection. The Brewster angle reads $\theta_B = 42.21°$. The critical angle for the extraordinary polarization is $\theta_{ce} = 63.54°$ whereas the ordinary polarization has a critical angle $\theta_{co} = 64.08°$. Although the incident light is *p*-polarized, part of the light that is reflected by the chiolite crystal is *s*-polarized. This is due to the fact that the optical axis is at an angle with the plane of incidence. However, R_s is nonzero only in the neighborhood of the critical angles for total internal reflection.

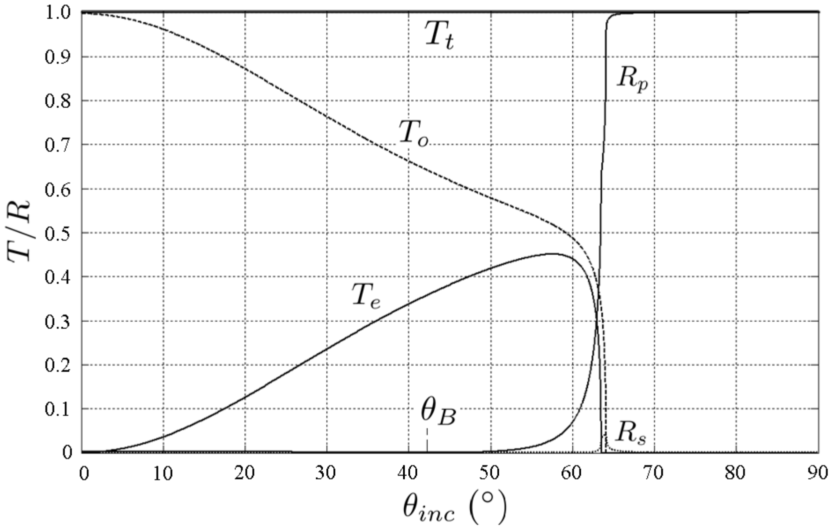

Figure 3.5: *Intensity transmittance and reflectance factors as a function of the angle of incidence θ_{inc} for a glass-chiolite interface. The curves for the ordinary and extraordinary transmittance factors T_o and T_e have different critical angles for total internal reflection. Although the incident light is p-polarized, the reflected light near the critical angles of reflection is s-polarized ($R_s \neq 0$). This is due to the fact that the optical axis is at an angle with the plane of incidence other than 90°.*

The number of critical angles that an anisotropic medium can have depends on the refractive indices and the direction of the optical axis at the interface. In general, an anisotropic medium can have two (but not more than two) critical angles for total internal reflection.

3.4.3 Amphoteric refraction

When an incident light ray has a direction of propagation that is perpendicular to a plane interface between isotropic media, the direction of the flow of energy will not change after transmission. For anisotropic interfaces, this is not necessarily the case. Then the direction of the Poynting vector after transmission depends on the direction of the local optical axis at the interface.

In general, when the tangential wave normal $\mathbf{p}_{tn} = 0$, the transmitted wave normal satisfies (see Eq. 3.6)

$$\mathbf{p} \propto \hat{\mathbf{n}}. \tag{3.40}$$

The direction of the corresponding Poynting vector depends on Eq. 3.40, but is not necessarily in the direction of $\hat{\mathbf{n}}$. This is because the Poynting vector of transmitted waves is perpendicular to the optical indicatrix, see Eq. 2.58. The orientation of the optical indicatrix depends on the direction of the local optical axis, i.e. on the definition of the local principal basis $\{\hat{\mathbf{u}}, \hat{\mathbf{v}}, \hat{\mathbf{w}}\}$. As a consequence, the energy flow, although at normal incidence, can be deflected at an anisotropic interface.

Fig. 3.6 shows three different cases of refraction at an anisotropic interface. In Fig. 3.6-(a), the incident and refracted Poynting vector are on the same side of the local normal vector $\hat{\mathbf{n}}$. This situation also applies to isotropic media and is called positive refraction. Fig. 3.6-(b) shows the situation where the incident and refracted Poynting vectors are on different sides of the local normal vector. This type of refraction is called negative refraction. Then the situation in Fig. 3.6-(c) is neither positive nor negative refraction. In general, when the type of refraction depends on the direction of propagation of the incident Poynting vector, we speak of amphoteric refraction [81].

We will investigate an example in which we show the type of amphoteric refraction illustrated in Fig. 3.6-(c).

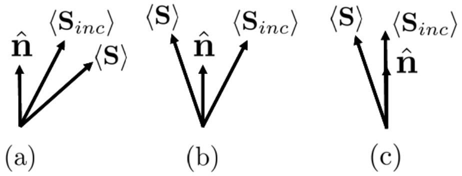

Figure 3.6: *Amphoteric refraction at an anisotropic interface. In (a), the incident and refracted Poynting vectors are on the same side of the local normal vector* $\hat{\boldsymbol{n}}$*. This type of refraction is called positive refraction. Negative refraction is illustrated in (b). In (c),* $\langle \boldsymbol{S} \rangle$ *and* $\hat{\boldsymbol{n}}$ *are parallel which corresponds neither to positive nor to negative refraction.*

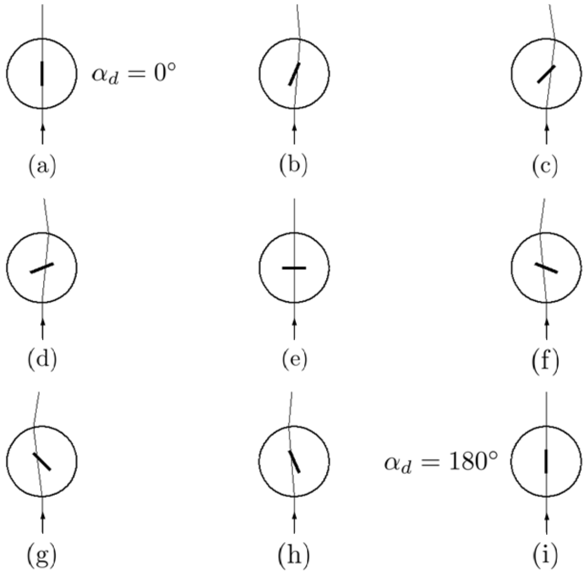

Figure 3.7: *Amphoteric refraction at an uniaxially anisotropic cylinder with* $n_o = 1.5$ *and* $n_e = 1.7$*. The angle between the vertical direction and the optical axis (indicated by the stripe inside the cylinder) is denoted by* α_d*. The cylinder is rotated over* 180° *with a step size of* 22.5°*.*

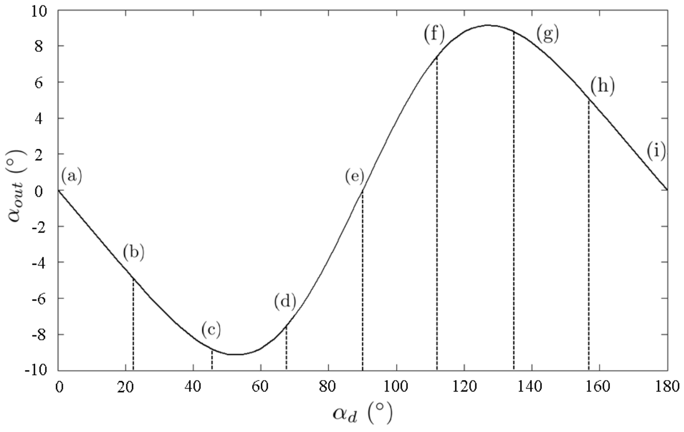

Figure 3.8: *Angle of deflection* α_{out} *as a function of the rotation angle* α_d*. The deflection angle lies approximately between* $-9°$ *and* 9°*. The situations that correspond to the illustrations in Fig. 3.7 are indicated in the graph. When* α_d *varies from* 0° *to* 180°*, the angle* α_{out} *has completed exactly one period. Apparently, the frequency of the swinging light ray (periods per second) is twice the frequency of the rotating cylinder (revolutions per second).*

We consider a homogeneous uniaxially anisotropic cylindrical rod with an optical axis perpendicular to the axis of symmetry. The cylinder is surrounded by air and has refractive indices $n_o = 1.5$ and $n_e = 1.7$. We define an incident light ray with direction of propagation parallel to the local normal vector $\hat{\mathbf{n}}$ of the cylinder. In addition, the incident ray is p-polarized orthogonal to the axis of symmetry. A cross section of the cylinder in the plane of incidence is depicted in Fig. 3.7-(a). The direction of the optical axis is indicated by the black stripe depicted inside the cylinder. The orientation of the optical axis with the vertical direction is denoted by the angle α_d.

In Fig. 3.7-(a), $\alpha_d = 0^\circ$ and the incident light ray is not deflected by the cylinder. In the remaining figures (b)-(i), the cylinder is rotated over 180° with a step size of 22.5°. From the illustrations we can conclude that amphoteric refraction occurs and the deflection of the light ray can be described by a periodic function of time. The angle under which the light ray is deflected after passing through the anisotropic cylinder is denoted by α_{out}. In Fig. 3.8 we have calculated the angle α_{out} as a function of the angle α_d. From the figure we conclude that one full revolution of the cylinder corresponds to two periods of the swinging light ray. Hence the frequency of the swinging light ray (periods per second) is twice the frequency of the rotating cylinder (revolutions per second).

If the incident light ray is s-polarized, the refracted ray is ordinary. Then the optical properties of the cylinder are equivalent to an isotropic medium with index n_o. Hence, s-polarized light is not deflected by the rotating anisotropic cylinder: $\alpha_{out}(\alpha_d) = 0^\circ$.

3.4.4 Conical refraction

We consider a linearly polarized beam of light which is refracted at a homogeneous biaxially anisotropic interface in the direction of one of the optical axes. Then the Poynting vector of a transmitted light ray, which is perpendicular to the optical indicatrix, is determined by the corresponding polarization vector of the light ray (see Fig. 2.3). At the position where the two sheets of the biaxial optical indicatrix touch each other (see Fig. 2.1-(d)), there exists an infinite number of possible polarization vectors. Each of these possible polarization vectors at the common point of intersection has a corresponding Poynting vector. Although the Poynting vectors of these eigenmodes are all different in direction, there is a common wave normal, which, on the principal orthonormal basis $\{\hat{\mathbf{u}}, \hat{\mathbf{v}}, \hat{\mathbf{w}}\}$, is given by (see also Eq. 2.40)

$$\mathbf{p} = \pm\sqrt{\frac{\varepsilon_w(\varepsilon_v - \varepsilon_u)}{\varepsilon_w - \varepsilon_u}}\hat{\mathbf{u}} + 0\hat{\mathbf{v}} \pm \sqrt{\frac{\varepsilon_u(\varepsilon_w - \varepsilon_v)}{\varepsilon_w - \varepsilon_u}}\hat{\mathbf{w}}. \tag{3.41}$$

Now let's consider an unpolarized beam of light which is refracted along the optical axis (with a wave normal given by Eq. 3.41) at the interface of a homogeneous biaxially anisotropic medium with principal indices $n_u = 1.3$, $n_v = 1.5$ and $n_w = 1.7$. Due to the optical properties described above, the incident beam of light is transformed to a hollow cone of light, see Fig. 3.9-(a). This is a phenomenon known as internal conical refraction (cf. [6], p. 688). Similarly, there is also a set of wave normals which have a common Poynting vector. In this case, an unpolarized incident beam of light, when refracted along the optical axis, is also transformed to a hollow cone by a biaxially anisotropic medium, see Fig. 3.9-(b). This phenomenon is known as external conical refraction.

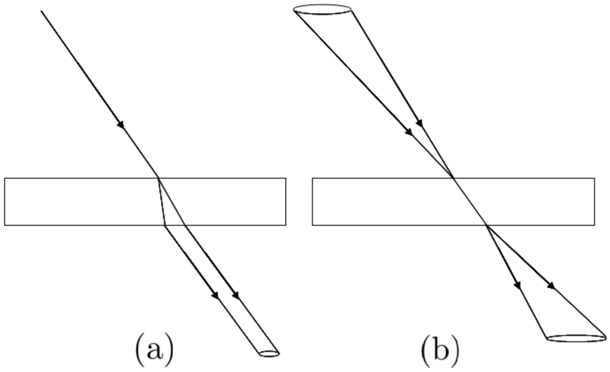

Figure 3.9: *When an unpolarized beam of light is refracted along the optical axis of a biaxially anisotropic medium, the light beam is transformed to a hollow cone of light, see Fig. (a). This phenomenon is known as internal conical refraction. The refracted light rays of the beam inside the biaxial medium have a common wave normal. In case the refracted light rays of the beam have a common Poynting vector, we observe external conical refraction, see Fig. (b).*

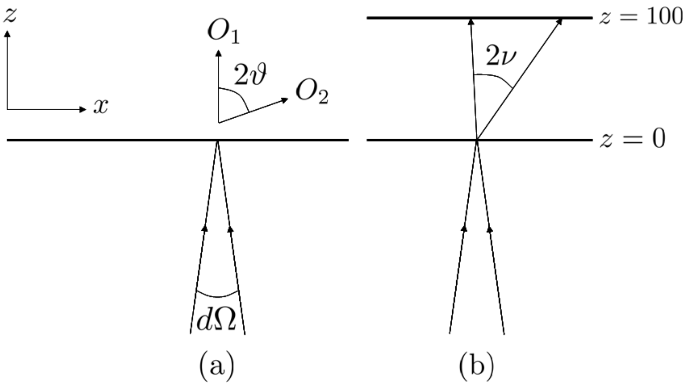

Figure 3.10: *An unpolarized beam of light incident to a biaxial medium where one of the optical axes (indicated by O_1 and O_2) is aligned with the vertical z-axis, see Fig. (a). Internal conical refraction occurs and the incident beam is transformed to a cone of light with semiangle ν. At $z = 100$ the light distribution is calculated, see Fig. (b).*

In the geometrical-optics approach, we can calculate the light distribution due to conical refraction with the procedure presented in Section 3.2. In what follows, we will simulate an example of internal conical refraction. Fig. 3.10-(a) shows an unpolarized incident beam of light with a solid angle $d\Omega$, propagating in the direction of the vertical z-axis. The light is refracted at the interface of a homogeneous biaxial medium. One of the optical axes of the biaxial medium is aligned with the z-axis. Due to the biaxial anisotropic properties, the incident light beam is transformed to a cone of light with semiangle ν, as depicted in Fig. 3.10-(b).

The incident light beam is defined by all light rays confined in the solid angle $d\Omega$. We define the initial position of the incident light beam at $(x, y, z) = (0, 0, 0)$. There, the incident light rays, which are randomly polarized, are refracted and split into two eigenmodes: the rays are bifurcated. We calculate the ray paths of these eigenmodes inside the homogeneous biaxial medium and the corresponding transmittance factors. At $z = 100$, we define a matrix in x and y which is used to bin the x- and y-coordinates of ray paths. The number of rays collected by each matrix element is a measure for the intensity. In this way, the intensity distribution at $z = 100$ is calculated. Fig. 3.11 shows the results for different solid angles. The number of rays that is traced for each image is 30000. In Fig. 3.11-(a), the incident beam of light has a solid angle of $1 \cdot 10^{-3}$ sr whereas in Fig. 3.11-(b) and 3.11-(c), the solid angles are $4 \cdot 10^{-3}$ sr and $9 \cdot 10^{-3}$ sr, respectively. The disc-like appearance of the light distributions changes with the solid angle: the disc edge increases with increasing $d\Omega$. In addition, the intensity decreases with increasing $d\Omega$ since the incident light is spread over a bigger area. The semiangle ν of the light cone can be expressed in terms of the principal indices of refraction of the biaxial medium, yielding (cf. [95], p. 291, Eq. 2.5)

$$\nu = \frac{\sqrt{(n_w - n_v)(n_v - n_u)}}{n_v}, \tag{3.42}$$

with the angle ν in radians. For the principal indices defined above, Eq. 3.42 yields $\nu = 7.63°$. In Fig. 3.11-(a), the semiangle ν is approximately 7.62°, which is in good agreement with Eq. 3.42.

Conical refraction only occurs when the incident light beam is accurately aligned with the optical axis of the biaxial medium. If the light beam is not aligned with the optical axis, we simply obtain two independent refracted eigenmodes for each individual light ray. Effectively, the incident light beam is split up into two beams, a phenomenon which is called double refraction. Fig. 3.12 shows three simulations of the light distribution at $z = 100$ for different angles of the optical axis in the xz-plane. The solid angle of the incident beam is $d\Omega = 1 \cdot 10^{-3}$ sr. In Fig. 3.12-(a), the optical axis is at 2.7° with the vertical z-axis. In this case we observe double refraction and the two resulting light beams are centered in the xz-plane. Fig. 3.12-(b) shows the result for the optical axis at 1.0° with the z-axis. Here, part of the light fulfills the conditions for conical refraction and we can already observe the formation of a hollow cone of light. Finally, in Fig. 3.12-(c), the optical axis is aligned with the z-axis and this image is equivalent to the situation in Fig. 3.11-(a). The simulated transition from double refraction to conical refraction depicted in Fig. 3.12 is in good agreement with observations as published in [94], p. 1631, Fig. 2.

In general, conical refraction contains both ray-optics and wave-optics effects [95]-[97]. Therefore, conical refraction is often termed conical diffraction. A full discussion

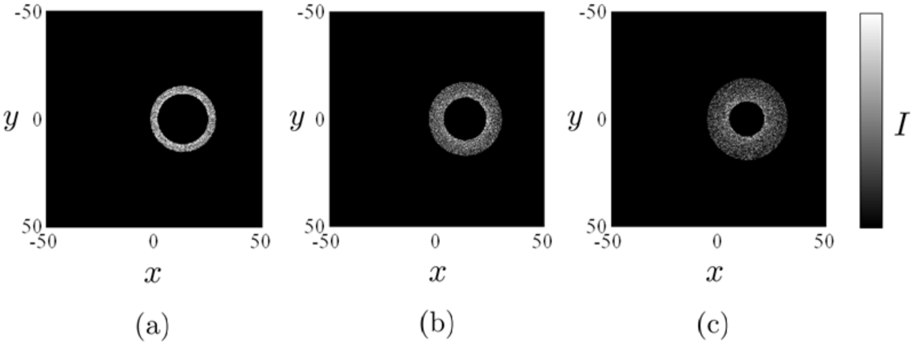

Figure 3.11: *Light intensity distribution I at* $z = 100$ *for different values of the solid angle* $d\Omega$*. For Fig. (a)-(c), the solid angles are* $1 \cdot 10^{-3}$ *sr,* $4 \cdot 10^{-3}$ *sr and* $9 \cdot 10^{-3}$ *sr, respectively. The unpolarized beam of light enters the biaxial medium at the origin. Apparently, the disc edge increases with increasing solid angle. In addition, the intensity decreases with increasing solid angle.*

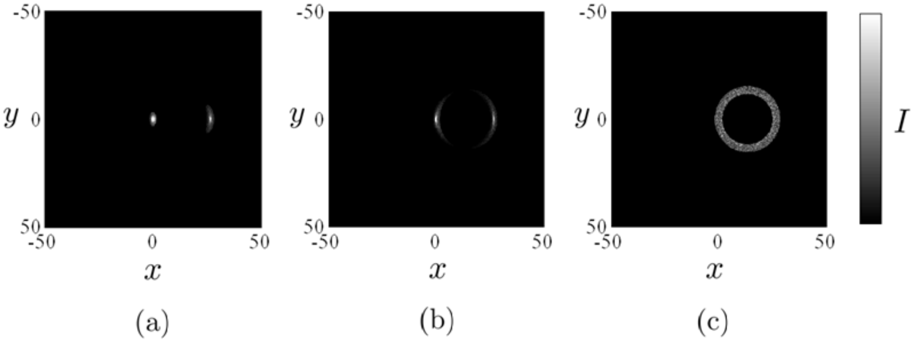

Figure 3.12: *Light intensity distribution I at* $z = 100$ *for different orientations of the optical axis. In Fig. (a)-(c), the angle between the optical axis and the vertical z-axis in the xz-plane is* $2.7°$, $1.0°$ *and* $0.0°$, *respectively. Fig. (a) shows double refraction, whereas Fig. (c) shows internal conical refraction. Fig. (b) is an intermediate state and shows how the two light beams are transformed to a hollow cone of light.*

would then also include optical properties due to the wave character of light, such as the Pogendorf rings [95]. However, this is beyond the scope of this treatise. For the moment, we conclude that conical refraction is an optical phenomenon due to a singularity in the surface of the biaxial optical indicatrix. More importantly, the optical effect of conical refraction can be simulated in the geometrical-optics approach with the theory presented in this chapter.

In a final example, we have investigated to what extend optical anisotropy can affect the resolving power of a last lens element in a photolithographic system (see Appendix B). From the calculations of a test case, we conclude that the resolving power in the perfect image point of a plano-convex lens with an a-spherical lens surface is highly sensitive to the effect of optical anisotropy. Therefore, we can conclude that high-index material last lens elements with birefringent properties are not suitable for immersion lithography as a resolution enhancement technique, unless the birefringence of the last lens element is compensated for.

3.5 Conclusions

With the help of the boundary conditions for an electromagnetic wave field at a surface of discontinuity, we have derived the classical theory for the optical wave field in the interface region of in general anisotropic media. The classical theory discussed is valid within the framework of geometrical optics. In addition, the equations are presented in complex notation, assuming a complex Hermitian permittivity tensor with optical axes. In geometrical optics, the optical wave field is constant in the bulk region of homogeneous media: the phase, amplitude, polarization state and direction of propagation do not change inside homogeneous media. Altogether, we can conclude that we are able to calculate the optical properties of homogeneous uniaxially and biaxially anisotropic media in the geometrical-optics approach.

In a number of didactical examples, we have demonstrated the applicability of the theory discussed. We have shown how the anisotropic properties at an interface determine the Brewster angle, the angles for total internal reflection and the transmissive and reflective properties. From the Fresnel coefficients at the interface, we are also able to calculate the phase shift and the polarization state of light rays. Moreover, we have discussed amphoteric refraction at a rotating uniaxially anisotropic cylinder and conical refraction at a biaxially anisotropic interface.

In the next chapter, we will discuss ray-optics analysis of inhomogeneous anisotropic media. We remark that the theory presented in this chapter also applies to anisotropic interfaces between inhomogeneous media, since locally the material properties at an interface are constant and independent of position.

Chapter 4

Ray-optics analysis of inhomogeneous anisotropic media

In general, the optical properties of an anisotropic medium depend on the position inside the medium. This means that the optical axis and the indices of refraction vary with position. These type of media are called inhomogeneous anisotropic media. Due to the position-dependent optical properties, ray paths inside inhomogeneous media are not necessarily straight lines, but can be curved. In this chapter, we derive novel ray-tracing equations to calculate the curved ray paths of light rays in the bulk region of inhomogeneous anisotropic media [102][103]. The optical properties in the interface region of inhomogeneous media can be calculated with the classical theory for the optical wave field at interfaces derived in Chapter 3. Recall that in the geometrical-optics approach, the optical properties in the bulk region should change slowly over the distance of a wavelength. If the properties change rapidly over the distance of a wavelength, we need to take into account the wave character of light. A further discussion on this topic can be found in Chapter 5.

4.1 Hamiltonian principle for inhomogeneous media

In this section we discuss a set of equations for the position $\mathbf{r}$ and the wave normal $\mathbf{p}$ of a ray in terms of the position-dependent optical indicatrix $\mathcal{H}(\mathbf{r},\mathbf{p})$. This approach is based on the so-called Hamiltonian principle introduced by Kline & Kay (cf. [75], p. 110-117). The Hamiltonian principle is the fundamental basis for the ray-tracing process in inhomogeneous media.

A light ray can be denoted by the parametric equations $x = x(\tau)$, $y = y(\tau)$ and $z = z(\tau)$, where the parameter τ can be considered as time. These parametric equations are defined on a fixed position-independent orthonormal basis $\{\hat{\mathbf{x}}, \hat{\mathbf{y}}, \hat{\mathbf{z}}\}$ in which the x-, y- and z-coordinates of a ray can vary with position. Recall that, since we are primarily interested in the energy transfer of a light ray, we have defined a ray to be an integral curve of the Poynting vector, given by Eq. 3.2. According to Eq. 2.58, the direction of the Poynting vector $\langle \mathbf{S} \rangle$ is parallel to the direction of $\nabla_p \mathcal{H}(\mathbf{r}, \mathbf{p})$. Hence, we can write a set of equations for the ray path given by

$$\frac{di}{d\tau} = \sigma \frac{\partial \mathcal{H}}{\partial p_i}, \quad i = x, y, z, \tag{4.1}$$

where the factor σ is an arbitrary function of τ and only depends on the choice for the parameter τ. As we move along the ray, the wave normal $\mathbf{p}$ also changes. Hence, the wave normal is also a function of τ. Likewise, we can derive a set of equations for the wave normal.

When we differentiate the optical indicatrix $\mathcal{H}(\mathbf{r}, \mathbf{p})$ with respect to x, we obtain

$$\frac{\partial \mathcal{H}}{\partial x} + \frac{\partial \mathcal{H}}{\partial p_x}\frac{\partial p_x}{\partial x} + \frac{\partial \mathcal{H}}{\partial p_y}\frac{\partial p_y}{\partial x} + \frac{\partial \mathcal{H}}{\partial p_z}\frac{\partial p_z}{\partial x} = 0. \tag{4.2}$$

When we use Eq. 4.1 in Eq. 4.2 we find

$$\sigma \frac{\partial \mathcal{H}}{\partial x} + \frac{\partial p_x}{\partial x}\frac{\partial x}{\partial \tau} + \frac{\partial p_y}{\partial x}\frac{\partial y}{\partial \tau} + \frac{\partial p_z}{\partial x}\frac{\partial z}{\partial \tau} = 0. \tag{4.3}$$

Recall that $\mathbf{p}(\mathbf{r}) = \nabla \psi(\mathbf{r})$, with $\psi(\mathbf{r})$ the optical path length function. Assuming that the scalar $\psi(\mathbf{r})$ is a twice continuously differentiable function of position, the derivatives of p_y and p_z satisfy

$$\frac{\partial p_y}{\partial x} = \frac{\partial^2 \psi}{\partial y \partial x} = \frac{\partial^2 \psi}{\partial x \partial y} = \frac{\partial p_x}{\partial y}, \tag{4.4}$$

$$\frac{\partial p_z}{\partial x} = \frac{\partial^2 \psi}{\partial z \partial x} = \frac{\partial^2 \psi}{\partial x \partial z} = \frac{\partial p_x}{\partial z}. \tag{4.5}$$

Hence, from Eq. 4.3 it follows that

$$\frac{dp_x}{d\tau} = -\sigma \frac{\partial \mathcal{H}}{\partial x}. \tag{4.6}$$

We can derive similar equations for the y- and z-components of the wave normal $\mathbf{p}$. As a result, the equations for the wave normal components are given by

$$\frac{dp_i}{d\tau} = -\sigma \frac{\partial \mathcal{H}}{\partial i}, \quad i = x, y, z, \tag{4.7}$$

where σ is the same parameter as in Eq. 4.1.

The next step is crucial, since we apply a classical-mechanical interpretation to the light rays: A mathematical light ray is considered the trajectory of a particle with coordinates $\mathbf{r} = (x, y, z)$ and generalized momentum $\mathbf{p} = (p_x, p_y, p_z)$, which satisfy Eqs. 4.1 and 4.7, respectively (cf. [75], p. 115). Moreover, this particle has the energy $\mathcal{H} = 0$. With this mechanical interpretation of a light ray, $\mathcal{H}(\mathbf{r}, \mathbf{p})$ represents a Hamiltonian system with canonical equations given by

$$\frac{d\mathbf{r}}{d\tau} = \sigma \nabla_p \mathcal{H}(\mathbf{r}, \mathbf{p}), \tag{4.8}$$

$$\frac{d\mathbf{p}}{d\tau} = -\sigma \nabla_r \mathcal{H}(\mathbf{r}, \mathbf{p}), \tag{4.9}$$

where the ray position $\mathbf{r}(\tau)$ and momentum $\mathbf{p}(\tau)$ are functions of the parameter τ. Eqs. 4.8 and 4.9 are also called the Hamilton equations. Eq. 4.8 describes the ray path of the Poynting vector. For each position $\mathbf{r}(\tau)$, there is a corresponding momentum $\mathbf{p}(\tau)$, determined by Eq. 4.9.

The Hamilton equations form a set of six coupled first-order differential equations with six unknowns: the vector components of the position $\mathbf{r}(\tau)$ and the momentum $\mathbf{p}(\tau)$. The inhomogeneous material properties are indirectly accounted for by the position-dependent optical indicatrix $\mathcal{H}(\mathbf{r}, \mathbf{p})$.

4.2 General ray-tracing equations for inhomogeneous anisotropic media

Although the Hamiltonian principle is the fundamental basis for the ray-tracing process in inhomogeneous media, it does not immediately provide a set of ray equations in which the position-dependent material properties are explicitly included. In that sense, the Hamilton equations discussed in Section 4.1 are incomplete. Building further on the Hamiltonian principle in this section, we introduce general ray-tracing equations that explicitly depend on the position-dependent material properties of anisotropic media. We assume a complex Hermitian permittivity tensor with optical axes and the ray-tracing equations are presented in complex notation. To the best of our knowledge, these equations are new and cannot be found in the literature.

4.2.1 The position-dependent optical indicatrix

In general, the inhomogeneous properties of an anisotropic medium can be ascribed to two effects: the position dependency of the principal dielectric values ε_u, ε_v and ε_w and the position dependency of the direction of the optical axes. For the moment, we assume that both effects are relevant. Since these properties are position dependent, so is the optical indicatrix. In Chapter 2, we have derived the optical indicatrix on the local principal basis $\{\hat{\mathbf{u}}(\mathbf{r}), \hat{\mathbf{v}}(\mathbf{r}), \hat{\mathbf{w}}(\mathbf{r})\}$. In what follows, we derive the position-dependent optical indicatrix with respect to a fixed position-independent orthonormal basis $\{\hat{\mathbf{x}}, \hat{\mathbf{y}}, \hat{\mathbf{z}}\}$ in which the optical properties can vary with position. In addition, we assume a Hermitian dielectric permittivity tensor.

From the macroscopic material equation we can derive the dielectric tensor as a function of the optical properties. The macroscopic material equation reads

$$\mathbf{D} = \varepsilon_0 \varepsilon_u \langle \mathbf{E}, \hat{\mathbf{u}} \rangle \hat{\mathbf{u}} + \varepsilon_0 \varepsilon_v \langle \mathbf{E}, \hat{\mathbf{v}} \rangle \hat{\mathbf{v}} + \varepsilon_0 \varepsilon_w \langle \mathbf{E}, \hat{\mathbf{w}} \rangle \hat{\mathbf{w}}, \tag{4.10}$$

where $\mathbf{D}$ is the electric flux density vector. This material equation can be written as $\mathbf{D} = \varepsilon_0 \underline{\underline{\varepsilon}} \mathbf{E}$, with $\underline{\underline{\varepsilon}}$ the dielectric tensor in terms of the vector components of the local unit vectors $\hat{\mathbf{u}}$, $\hat{\mathbf{v}}$ and $\hat{\mathbf{w}}$ and the principal indices ε_u, ε_v and ε_w.

Since we want to calculate ray paths of light rays in an inhomogeneous anisotropic bulk material, we now choose a fixed, position-independent orthonormal basis $\{\hat{\mathbf{x}}, \hat{\mathbf{y}}, \hat{\mathbf{z}}\}$. The elements of the tensor $\underline{\underline{\varepsilon}}$ on the fixed basis $\{\hat{\mathbf{x}}, \hat{\mathbf{y}}, \hat{\mathbf{z}}\}$ can be written as ε_{xx}, ε_{xy}, ε_{xz}

etc. Eq. 2.30 can then be written in terms of these tensor elements according to the matrix equation

$$\begin{pmatrix} \varepsilon_{xx} + |p_x|^2 - |\mathbf{p}|^2 & \varepsilon_{xy} + p_x p_y^* & \varepsilon_{xz} + p_x p_z^* \\ \varepsilon_{yx} + p_y p_x^* & \varepsilon_{yy} + |p_y|^2 - |\mathbf{p}|^2 & \varepsilon_{yz} + p_y p_z^* \\ \varepsilon_{zx} + p_z p_x^* & \varepsilon_{zy} + p_z p_y^* & \varepsilon_{zz} + |p_z|^2 - |\mathbf{p}|^2 \end{pmatrix} \tilde{\mathbf{E}} = 0. \tag{4.11}$$

Like Eq. 2.30, this equation only has nontrivial solutions if the determinant of the matrix vanishes. It follows from Eq. 2.32 that the determinant vanishes if

$$\begin{aligned} \mathcal{H}(\mathbf{r},\mathbf{p}) \quad = \quad & \Big(\varepsilon_u|\langle\mathbf{p},\hat{\mathbf{u}}\rangle|^2 + \varepsilon_v|\langle\mathbf{p},\hat{\mathbf{v}}\rangle|^2 + \varepsilon_w|\langle\mathbf{p},\hat{\mathbf{w}}\rangle|^2\Big)|\mathbf{p}|^2 \\ & + \varepsilon_u\varepsilon_v\Big[|\langle\hat{\mathbf{u}},(\mathbf{p}\times\hat{\mathbf{v}})\rangle|^2 - |\mathbf{p}|^2\Big] \\ & + \varepsilon_u\varepsilon_w\Big[|\langle\hat{\mathbf{u}},(\mathbf{p}\times\hat{\mathbf{w}})\rangle|^2 - |\mathbf{p}|^2\Big] \\ & + \varepsilon_v\varepsilon_w\Big[|\langle\hat{\mathbf{v}},(\mathbf{p}\times\hat{\mathbf{w}})\rangle|^2 - |\mathbf{p}|^2\Big] + \varepsilon_u\varepsilon_v\varepsilon_w = 0, \end{aligned} \tag{4.12}$$

where the unit vectors $\hat{\mathbf{u}}$, $\hat{\mathbf{v}}$ and $\hat{\mathbf{w}}$ are complex and all quantities depend on position $\mathbf{r}$. Eq. 4.12 is the biaxial position-dependent optical indicatrix. If we substitute $\hat{\mathbf{u}} = (1,0,0)$, $\hat{\mathbf{v}} = (0,1,0)$ and $\hat{\mathbf{w}} = (0,0,1)$, we obtain the biaxial optical indicatrix in the principal coordinate system as defined in Eq. 2.32.

If we set $\varepsilon_u = \varepsilon_v = \varepsilon_1$ and $\varepsilon_w = \varepsilon_2$, we obtain the optical indicatrix in the principal coordinate system for uniaxial anisotropy (see also Eq. 2.41):

$$\mathcal{H}(\mathbf{r},\mathbf{p}) = \Big(\varepsilon_1|\mathbf{p}|^2 + \triangle\varepsilon|\langle\mathbf{p},\hat{\mathbf{w}}\rangle|^2 - \varepsilon_1\varepsilon_2\Big)\Big(|\mathbf{p}|^2 - \varepsilon_1\Big) = 0, \tag{4.13}$$

with $\triangle\varepsilon = \varepsilon_2 - \varepsilon_1$ and all quantities depending on position $\mathbf{r}$. Eq. 4.13 can be written as $\mathcal{H} = \mathcal{H}_e\mathcal{H}_o = 0$, where $\mathcal{H}_e$ corresponds to extraordinary waves and $\mathcal{H}_o$ corresponds to ordinary waves.

4.2.2 Position-dependent optical axis

Inside an inhomogeneous anisotropic medium, the directions of the optical axis depends on the position. We call the position-dependent optical axis the director.

In case of an uniaxially anisotropic medium, we can derive an expression for the director. When $\mathbf{p} = \sqrt{\varepsilon_1}\hat{\mathbf{w}}$, we have $\mathcal{H}_o = \mathcal{H}_e = 0$ and then the wave normal is parallel to the optical axis. Let $\hat{\mathbf{d}}$ be a unit vector parallel to the optical axis. Then the director for uniaxially anisotropic media is given by

$$\hat{\mathbf{d}} = \hat{\mathbf{w}}, \tag{4.14}$$

with $\hat{\mathbf{w}}$ complex.

Inside an inhomogeneous biaxially anisotropic medium, there are two position-dependent directors $\hat{\mathbf{d}}_1$ and $\hat{\mathbf{d}}_2$. Recall that we have assumed that $\varepsilon_w > \varepsilon_v > \varepsilon_u$. Then if $\mathbf{p}$ is parallel to one of the two directors we have (see Eq. 2.40)

$$|p_u| = \sqrt{\frac{\varepsilon_w(\varepsilon_v - \varepsilon_u)}{(\varepsilon_w - \varepsilon_u)}},\ |p_v| = 0,\ |p_w| = \sqrt{\frac{\varepsilon_u(\varepsilon_w - \varepsilon_v)}{(\varepsilon_w - \varepsilon_u)}}, \tag{4.15}$$

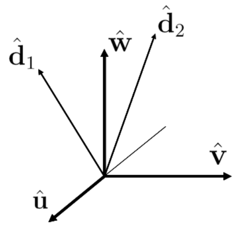

Figure 4.1: *Locally, a biaxially anisotropic medium is characterized by two position-dependent optical axes, indicated by* $\hat{\boldsymbol{d}}_1$ *and* $\hat{\boldsymbol{d}}_2$. *The corresponding principal coordinate system is defined by the local unit vectors* $\hat{\boldsymbol{u}}$, $\hat{\boldsymbol{v}}$ *and* $\hat{\boldsymbol{w}}$, *which can be expressed in terms of the local optical axes* $\hat{\boldsymbol{d}}_1$ *and* $\hat{\boldsymbol{d}}_2$.

and $|\mathbf{p}| = \sqrt{\varepsilon_v}$. Hence we can write $\mathbf{p} = |\mathbf{p}|\hat{\mathbf{p}} = \sqrt{\varepsilon_v}\hat{\mathbf{p}}$. On the complex basis $\{\hat{\mathbf{u}}(\mathbf{r}), \hat{\mathbf{v}}(\mathbf{r}), \hat{\mathbf{w}}(\mathbf{r})\}$, we then know $|\hat{\mathbf{p}}_u|$, $|\hat{\mathbf{p}}_v|$ and $|\hat{\mathbf{p}}_w|$, but the phases of the vector components of $\hat{\mathbf{p}}$ are unknown. In general, these phases follow directly from the linear transformation of $\hat{\mathbf{p}}$ from the fixed basis $\{\hat{\mathbf{x}}, \hat{\mathbf{y}}, \hat{\mathbf{z}}\}$ to the principle basis $\{\hat{\mathbf{u}}(\mathbf{r}), \hat{\mathbf{v}}(\mathbf{r}), \hat{\mathbf{w}}(\mathbf{r})\}$.

If the basis $\{\hat{\mathbf{u}}(\mathbf{r}), \hat{\mathbf{v}}(\mathbf{r}), \hat{\mathbf{w}}(\mathbf{r})\}$ is real, we have $\mathbf{p} = |p_u|\hat{\mathbf{u}} + |p_v|\hat{\mathbf{v}} + |p_w|\hat{\mathbf{w}}$. Then the directors in the upper half space satisfy (see Eq. 2.40)

$$\hat{\mathbf{d}}_1 = \sqrt{\frac{\varepsilon_w(\varepsilon_v - \varepsilon_u)}{\varepsilon_v(\varepsilon_w - \varepsilon_u)}}\hat{\mathbf{u}} + 0\hat{\mathbf{v}} + \sqrt{\frac{\varepsilon_u(\varepsilon_w - \varepsilon_v)}{\varepsilon_v(\varepsilon_w - \varepsilon_u)}}\hat{\mathbf{w}}, \tag{4.16}$$

$$\hat{\mathbf{d}}_2 = -\sqrt{\frac{\varepsilon_w(\varepsilon_v - \varepsilon_u)}{\varepsilon_v(\varepsilon_w - \varepsilon_u)}}\hat{\mathbf{u}} + 0\hat{\mathbf{v}} + \sqrt{\frac{\varepsilon_u(\varepsilon_w - \varepsilon_v)}{\varepsilon_v(\varepsilon_w - \varepsilon_u)}}\hat{\mathbf{w}}. \tag{4.17}$$

Fig. 4.1 shows two local directors and the local Cartesian principle coordinate system, defined by the real unit vectors $\hat{\mathbf{u}}$, $\hat{\mathbf{v}}$ and $\hat{\mathbf{w}}$. These unit vectors can be expressed in terms of the directors $\hat{\mathbf{d}}_1$ and $\hat{\mathbf{d}}_2$, according to

$$\hat{\mathbf{u}} = \frac{\hat{\mathbf{d}}_1 - \hat{\mathbf{d}}_2}{|\hat{\mathbf{d}}_1 - \hat{\mathbf{d}}_2|}, \tag{4.18}$$

$$\hat{\mathbf{v}} = \frac{\hat{\mathbf{d}}_2 \times \hat{\mathbf{d}}_1}{|\hat{\mathbf{d}}_2 \times \hat{\mathbf{d}}_1|}, \tag{4.19}$$

$$\hat{\mathbf{w}} = \frac{\hat{\mathbf{d}}_1 + \hat{\mathbf{d}}_2}{|\hat{\mathbf{d}}_1 + \hat{\mathbf{d}}_2|}. \tag{4.20}$$

In conclusion, if we know the local directors $\hat{\mathbf{d}}_1$ and $\hat{\mathbf{d}}_2$, we also know the real local principal basis $\{\hat{\mathbf{u}}, \hat{\mathbf{v}}, \hat{\mathbf{w}}\}$ and vice versa. If the basis $\{\hat{\mathbf{u}}, \hat{\mathbf{v}}, \hat{\mathbf{w}}\}$ is complex, then Eqs. 4.16 and 4.17 do not apply. Then the phases of $\hat{\mathbf{d}}_1$ and $\hat{\mathbf{d}}_2$ on the basis $\{\hat{\mathbf{u}}, \hat{\mathbf{v}}, \hat{\mathbf{w}}\}$ can be derived from the demand that $\mathbf{p}$ along the directions of $\hat{\mathbf{d}}_1$ and $\hat{\mathbf{d}}_2$ is real on the fixed basis $\{\hat{\mathbf{x}}, \hat{\mathbf{y}}, \hat{\mathbf{z}}\}$. However, in general, it is possible that for a complex Hermitian permittivity tensor this demand cannot be satisfied (see Appendix A). Then there is a complex vector $\mathbf{p}$ on the fixed basis $\{\hat{\mathbf{x}}, \hat{\mathbf{y}}, \hat{\mathbf{z}}\}$ along which $|\mathbf{p}|$ satisfies Eq. 4.15. In that case there is no optical axis and the two sheets of the optical indicatrix are separated for all directions of propagation. However, as mentioned in Chapter 2, we assume that the Hermitian permittivity tensor always gives rise to one or two optical axes.

The position-dependent biaxial optical indicatrix of Eq. 4.12 and the uniaxial optical indicatrix of Eq. 4.13 together with the position-dependent directors play a crucial role in the formulation of a ray-tracing process for inhomogeneous anisotropic media.

4.2.3 General ray-tracing equations for anisotropic media

The Hamiltonian principle and the formulas for the position-dependent optical indicatrix are the main ingredients for a general ray-tracing method for inhomogeneous anisotropic media defined by a Hermitian dielectric tensor. In what follows, we introduce general ray-tracing equations that depend explicitly on the position-dependent principal dielectric values, the director $\hat{\mathbf{d}}(\mathbf{r})$ and the principle unit vectors $\hat{\mathbf{u}}(\mathbf{r})$, $\hat{\mathbf{v}}(\mathbf{r})$ and $\hat{\mathbf{w}}(\mathbf{r})$.

From the position-dependent biaxial optical indicatrix given by Eq. 4.12 we calculate the gradients with respect to position $\nabla_r \mathcal{H}(\mathbf{r},\mathbf{p})$ and momentum $\nabla_p \mathcal{H}(\mathbf{r},\mathbf{p})$. On the fixed orthonormal basis $\{\hat{\mathbf{x}},\hat{\mathbf{y}},\hat{\mathbf{z}}\}$, the partial derivatives of $\mathcal{H}(\mathbf{r},\mathbf{p})$ with respect to position read

$$\begin{aligned}
\frac{\partial \mathcal{H}}{\partial i} = {} & \mathrm{Re}\Bigg\{ 2|\mathbf{p}|^2 \Bigg(\varepsilon_u \langle \mathbf{p}, \hat{\mathbf{u}} \rangle^* \langle \mathbf{p}, \frac{\partial \hat{\mathbf{u}}}{\partial i} \rangle + \varepsilon_v \langle \mathbf{p}, \hat{\mathbf{v}} \rangle^* \langle \mathbf{p}, \frac{\partial \hat{\mathbf{v}}}{\partial i} \rangle + \varepsilon_w \langle \mathbf{p}, \hat{\mathbf{w}} \rangle^* \langle \mathbf{p}, \frac{\partial \hat{\mathbf{w}}}{\partial i} \rangle \Bigg) \\
& + 2\varepsilon_u \varepsilon_v \left[\langle \frac{\partial \hat{\mathbf{u}}}{\partial i}, (\mathbf{p} \times \hat{\mathbf{v}}) \rangle + \langle \hat{\mathbf{u}}, (\mathbf{p} \times \frac{\partial \hat{\mathbf{v}}}{\partial i}) \rangle \right] \langle \hat{\mathbf{u}}, (\mathbf{p} \times \hat{\mathbf{v}}) \rangle^* \\
& + 2\varepsilon_u \varepsilon_w \left[\langle \frac{\partial \hat{\mathbf{u}}}{\partial i}, (\mathbf{p} \times \hat{\mathbf{w}}) \rangle + \langle \hat{\mathbf{u}}, (\mathbf{p} \times \frac{\partial \hat{\mathbf{w}}}{\partial i}) \rangle \right] \langle \hat{\mathbf{u}}, (\mathbf{p} \times \hat{\mathbf{w}}) \rangle^* \\
& + 2\varepsilon_v \varepsilon_w \left[\langle \frac{\partial \hat{\mathbf{v}}}{\partial i}, (\mathbf{p} \times \hat{\mathbf{w}}) \rangle + \langle \hat{\mathbf{v}}, (\mathbf{p} \times \frac{\partial \hat{\mathbf{w}}}{\partial i}) \rangle \right] \langle \hat{\mathbf{v}}, (\mathbf{p} \times \hat{\mathbf{w}}) \rangle^* \Bigg\} \\
& + h\Bigg(\frac{\partial \varepsilon_u}{\partial i}, \frac{\partial \varepsilon_v}{\partial i}, \frac{\partial \varepsilon_w}{\partial i} \Bigg), \quad i = x, y, z, \qquad (4.21)
\end{aligned}$$

where h is a function of the partial derivatives of the principle dielectric values with respect to position, given by

$$\begin{aligned}
h = {} & |\mathbf{p}|^2 \Bigg(\frac{\partial \varepsilon_u}{\partial i} |\langle \mathbf{p}, \hat{\mathbf{u}} \rangle|^2 + \frac{\partial \varepsilon_v}{\partial i} |\langle \mathbf{p}, \hat{\mathbf{v}} \rangle|^2 + \frac{\partial \varepsilon_w}{\partial i} |\langle \mathbf{p}, \hat{\mathbf{w}} \rangle|^2 \Bigg) \\
& + |\langle \hat{\mathbf{u}}, (\mathbf{p} \times \hat{\mathbf{v}}) \rangle|^2 \frac{\partial}{\partial i} (\varepsilon_u \varepsilon_v) \\
& + |\langle \hat{\mathbf{u}}, (\mathbf{p} \times \hat{\mathbf{w}}) \rangle|^2 \frac{\partial}{\partial i} (\varepsilon_u \varepsilon_w) \\
& + |\langle \hat{\mathbf{v}}, (\mathbf{p} \times \hat{\mathbf{w}}) \rangle|^2 \frac{\partial}{\partial i} (\varepsilon_v \varepsilon_w) \\
& + \frac{\partial}{\partial i} (\varepsilon_u \varepsilon_v \varepsilon_w), \quad i = x, y, z. \qquad (4.22)
\end{aligned}$$

The partial derivatives of $\mathcal{H}(\mathbf{r},\mathbf{p})$ with respect to the wave normal components yield

$$\frac{\partial \mathcal{H}}{\partial p_i} = \mathrm{Re}\Bigg\{ 2|\mathbf{p}|^2 \Bigg(\varepsilon_u \langle \mathbf{p}, \hat{\mathbf{u}} \rangle \hat{u}_i + \varepsilon_v \langle \mathbf{p}, \hat{\mathbf{v}} \rangle \hat{v}_i + \varepsilon_w \langle \mathbf{p}, \hat{\mathbf{w}} \rangle \hat{w}_i \Bigg)$$

$$+ 2p_i\Bigg(\varepsilon_u|\langle \mathbf{p}, \hat{\mathbf{u}}\rangle|^2 + \varepsilon_v|\langle \mathbf{p}, \hat{\mathbf{v}}\rangle|^2 + \varepsilon_w|\langle \mathbf{p}, \hat{\mathbf{w}}\rangle|^2 - \varepsilon_u\varepsilon_v - \varepsilon_u\varepsilon_w - \varepsilon_v\varepsilon_w \Bigg)$$

$$- 2\varepsilon_u\varepsilon_v\Bigg(\hat{\mathbf{u}}^* \times \hat{\mathbf{v}} \Bigg)_i \langle \hat{\mathbf{u}}, (\mathbf{p} \times \hat{\mathbf{v}})\rangle$$

$$- 2\varepsilon_u\varepsilon_w\Bigg(\hat{\mathbf{u}}^* \times \hat{\mathbf{w}} \Bigg)_i \langle \hat{\mathbf{u}}, (\mathbf{p} \times \hat{\mathbf{w}})\rangle$$

$$- 2\varepsilon_v\varepsilon_w\Bigg(\hat{\mathbf{v}}^* \times \hat{\mathbf{w}} \Bigg)_i \langle \hat{\mathbf{v}}, (\mathbf{p} \times \hat{\mathbf{w}})\rangle \Bigg\}, \quad i = x, y, z. \tag{4.23}$$

Eqs. 4.21-4.23 contain the principal dielectric values, $\hat{\mathbf{u}}(\mathbf{r})$, $\hat{\mathbf{v}}(\mathbf{r})$, $\hat{\mathbf{w}}(\mathbf{r})$ and their partial derivatives with respect to position. When we substitute these equations into the Hamilton equations (Eqs. 4.8 and 4.9) we obtain equations for the position $\mathbf{r}$ and wave normal $\mathbf{p}$ on the fixed basis, in which the position dependency of the biaxially anisotropic material properties is included explicitly.

In the case of uniaxial anisotropy, the gradient of $\mathcal{H}(\mathbf{r}, \mathbf{p})$ can in general be written as

$$\nabla\mathcal{H} = \nabla\Bigg(\mathcal{H}_e\mathcal{H}_o\Bigg) = \mathcal{H}_e\nabla\mathcal{H}_o + \mathcal{H}_o\nabla\mathcal{H}_e. \tag{4.24}$$

For extraordinary rays, $\mathcal{H}_e = 0$ and then Eq. 4.24 reduces to

$$\nabla\mathcal{H} = \mathcal{H}_o\nabla\mathcal{H}_e. \tag{4.25}$$

When we substitute Eq. 4.25 into the Hamilton equations, the factor $\mathcal{H}_o$ can be incorporated in the parameter σ. Then the Hamilton equations read

$$\frac{d\mathbf{r}}{d\tau} = \sigma\nabla_p\mathcal{H}_e(\mathbf{r}, \mathbf{p}_e), \tag{4.26}$$

$$\frac{d\mathbf{p}_e}{d\tau} = -\sigma\nabla_r\mathcal{H}_e(\mathbf{r}, \mathbf{p}_e). \tag{4.27}$$

With the help of Eqs. 4.13 and 4.14, the gradients of the extraordinary Hamiltonian $\mathcal{H}_e(\mathbf{r}, \mathbf{p}_e)$ with respect to position and momentum can be calculated. On the fixed orthonormal basis $\{\hat{\mathbf{x}}, \hat{\mathbf{y}}, \hat{\mathbf{z}}\}$, these are given by

$$\begin{aligned} \frac{\partial\mathcal{H}_e}{\partial i} &= \mathrm{Re}\Bigg\{ 2(\varepsilon_2 - \varepsilon_1)\langle \mathbf{p}_e, \hat{\mathbf{d}}\rangle^* \langle \mathbf{p}_e, \frac{\partial\hat{\mathbf{d}}}{\partial i}\rangle \Bigg\} \\ &+ \Bigg(|\langle \mathbf{p}_e, \hat{\mathbf{d}}\rangle|^2 - \varepsilon_1 \Bigg)\frac{\partial\varepsilon_2}{\partial i} \\ &+ \Bigg(|\mathbf{p}_e|^2 - |\langle \mathbf{p}_e, \hat{\mathbf{d}}\rangle|^2 - \varepsilon_2 \Bigg)\frac{\partial\varepsilon_1}{\partial i}, \end{aligned} \tag{4.28}$$

$$\frac{\partial\mathcal{H}_e}{\partial p_{ei}} = \mathrm{Re}\Bigg\{ 2\varepsilon_1 p_{ei} + 2(\varepsilon_2 - \varepsilon_1)\langle \mathbf{p}_e, \hat{\mathbf{d}}\rangle \hat{d}_i \Bigg\}, \quad i = x, y, z. \tag{4.29}$$

For ordinary rays $\mathcal{H}_o = 0$ and then the Hamilton equations can be written as

$$\frac{d\mathbf{r}}{d\tau} = \sigma\nabla_p\mathcal{H}_o(\mathbf{r}, \mathbf{p}_o), \tag{4.30}$$

$$\frac{d\mathbf{p}_o}{d\tau} = -\sigma\nabla_r\mathcal{H}_o(\mathbf{r}, \mathbf{p}_o), \tag{4.31}$$

where the factor $\mathcal{H}_e$ is incorporated into the parameter σ. In this case, the gradients $\nabla_r \mathcal{H}_o(\mathbf{r}, \mathbf{p}_o)$ and $\nabla_p \mathcal{H}_o(\mathbf{r}, \mathbf{p}_o)$ are

$$\frac{\partial \mathcal{H}_o}{\partial i} = -\frac{\partial \varepsilon_1}{\partial i}, \tag{4.32}$$

$$\frac{\partial \mathcal{H}_o}{\partial p_{oi}} = \mathrm{Re}\left\{ 2p_{oi} \right\}, \quad i = x, y, z. \tag{4.33}$$

As a result, the Hamilton equations for ordinary rays are given by

$$\frac{d\mathbf{r}}{d\tau} = \mathrm{Re}\left\{ 2\sigma \mathbf{p}_o \right\}, \tag{4.34}$$

$$\frac{d\mathbf{p}_o}{d\tau} = \sigma \nabla_r \varepsilon_1. \tag{4.35}$$

If we redefine τ such that $\sigma = \frac{1}{2}$, we obtain Eq. 3.1: the ordinary ray path is defined as the integral curve of the wave normal $\mathbf{p}_o$. This is because the wave normal and the corresponding time-averaged Poynting vector are always parallel for ordinary rays. The same conclusion applies to rays in isotropic media. Then ε_1 and $\mathbf{p}_o$ are replaced with ε and $\mathbf{p}$, respectively.

We can conclude that we have derived general ray-tracing equations in which the position dependency of the optical properties of anisotropic material properties is included explicitly. These ray-tracing equations apply for a Hermitian dielectric tensor and enable the calculation of the in general curved ray paths of light rays in the bulk region of inhomogeneous anisotropic media. Moreover, we have derived equations for both biaxially and uniaxially anisotropic media. In the next section, we apply the ray-tracing equations to a mathematical example.

4.2.4 Example: Hamilton equations applied to a normalized vector field

If we redefine τ such that $\sigma = 1$, we find

$$\frac{d\mathbf{r}(\tau)}{d\tau} = \nabla_p \mathcal{H}(\hat{\mathbf{d}}), \tag{4.36}$$

$$\frac{d\mathbf{p}(\tau)}{d\tau} = -\nabla_r \mathcal{H}(\hat{\mathbf{d}}), \tag{4.37}$$

with $\nabla_p \mathcal{H}$ and $\nabla_r \mathcal{H}$ as discussed previously. This set of six coupled first-order differential equations can be solved with for example the first-order Runge-Kutta method, also known as the Euler method (cf. [90], p. 704). If we start at an interface between two (an)isotropic media at 'time' $\tau = \tau_0$, the initial conditions for the set of first-order differential equations are given by

$$\mathbf{r}(\tau_0) = (x_0, y_0, z_0), \tag{4.38}$$

$$\mathbf{p}(\tau_0) = \mathbf{p}_0. \tag{4.39}$$

By taking steps $\triangle\tau$ in the time τ, the Runge-Kutta method can solve for the ray path $\mathbf{r}(\tau_0 + K\triangle\tau)$ and the corresponding wave normal $\mathbf{p}(\tau_0 + K\triangle\tau)$, with $K \in \mathbb{N}$ (see Appendix C). In this way, we can obtain the ray paths of in general curved rays in the bulk

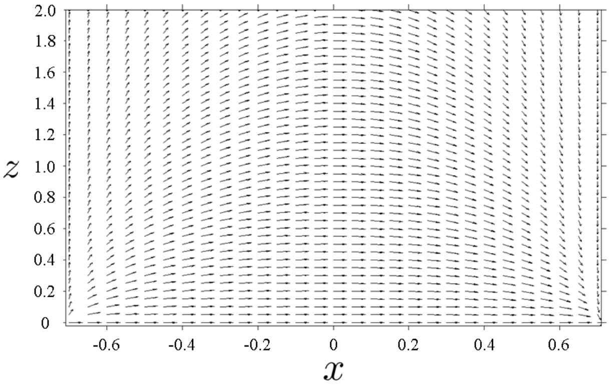

Figure 4.2: *The position-dependent director* $\boldsymbol{d} = \nabla F$ *in the plane* $y = 0$. *Note that the director is not normalized. The two-dimensional scalar function* F *is defined* $F(x, y, z) = xe^{-x^2-z^2}$, *where* $-\frac{1}{2}\sqrt{2} < x < \frac{1}{2}\sqrt{2}$, $y = 0$ *and* $z \geq 0$.

material of inhomogeneous anisotropic media.

In this example, we consider an inhomogeneous uniaxially anisotropic medium with $\varepsilon_1 = n_o^2$ constant, $\varepsilon_2 = n_e^2$ constant and the dielectric tensor real and symmetric, as in a nematic liquid crystal. Then the Hamilton equations for extraordinary rays are given by

$$\frac{di}{d\tau} = 2n_o^2 p_{ei} + 2(n_e^2 - n_o^2)(\mathbf{p}_e \cdot \hat{\mathbf{d}})\hat{d}_i, \tag{4.40}$$

$$\frac{dp_{ei}}{d\tau} = -2(n_e^2 - n_o^2)(\mathbf{p}_e \cdot \hat{\mathbf{d}})\left(\mathbf{p}_e \cdot \frac{\partial \hat{\mathbf{d}}}{\partial i}\right), \quad i = x, y, z. \tag{4.41}$$

For ordinary rays the Hamilton equations reduce to

$$\frac{d\mathbf{r}}{d\tau} = \mathbf{p}_o, \tag{4.42}$$

$$\frac{d\mathbf{p}_o}{d\tau} = 0. \tag{4.43}$$

Apparently, the ordinary wave normal $\mathbf{p}_o(\tau)$ is constant and the ray path $\mathbf{r}(\tau)$ is a straight line. In contrast with ordinary rays, the ray paths of extraordinary rays are curved in general.

As a specific example, we consider a position-dependent director $\hat{\mathbf{d}}(\mathbf{r})$ which is proportional to a gradient vector field $\nabla F(x, y, z)$ where the scalar function $F(x, y, z)$ satisfies

$$F(x, y, z) = xe^{-x^2-z^2}, \ -\frac{1}{2}\sqrt{2} < x < \frac{1}{2}\sqrt{2}, \ y = 0, \ z \geq 0. \tag{4.44}$$

Fig. 4.2 shows the vector field $\nabla F(x, y, z)$ in the domain defined in Eq. 4.44. However, in the Hamilton equations the director is normalized. Therefore the director $\mathbf{d}(x, y, z) =$

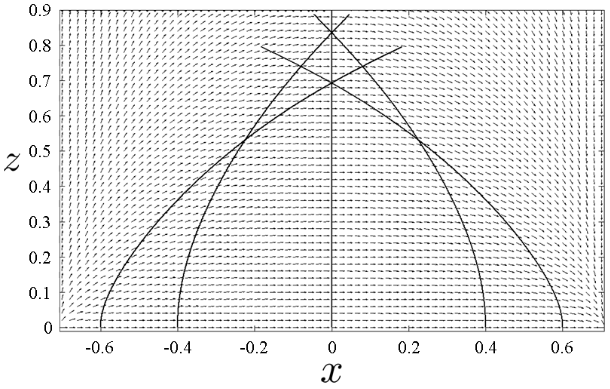

Figure 4.3: *Ray paths of five extraordinary rays incident orthogonal to the plane* $z = 0$*, where* $\hat{\boldsymbol{d}} = (1,0,0)$ *and* $\boldsymbol{p}(\tau_0) = (0,0,n_e)$*. The ray paths are calculated with the second-order Runge-Kutta method with step size* $\triangle\tau = 10^{-4}$ *and the number of steps* $K = 2000$*.*

$\nabla F(x,y,z)$ is given by

$$\hat{\mathbf{d}} = \frac{\nabla F(x,y,z)}{|\nabla F(x,y,z)|}. \tag{4.45}$$

For the chosen function F this implies:

$$\hat{\mathbf{d}}(x,y,z) = \frac{\Big(1-2x^2, 0, -2xz\Big)}{\sqrt{\Big(1-2x^2\Big)^2 + \Big(2xz\Big)^2}}. \tag{4.46}$$

With the director defined in Eq. 4.46, the partial derivatives of the director vector components with respect to y vanish. Only four terms are nonzero and these are given by

$$\frac{\partial \hat{d}_x}{\partial x} = \frac{-4xz^2(1+2x^2)}{|\mathbf{d}|^{\frac{3}{2}}}, \tag{4.47}$$

$$\frac{\partial \hat{d}_z}{\partial x} = \frac{2z(4x^4-1)}{|\mathbf{d}|^{\frac{3}{2}}}, \tag{4.48}$$

$$\frac{\partial \hat{d}_x}{\partial z} = \frac{-4zx^2(1-2x^2)}{|\mathbf{d}|^{\frac{3}{2}}}, \tag{4.49}$$

$$\frac{\partial \hat{d}_z}{\partial z} = \frac{-2x(1-2x^2)^2}{|\mathbf{d}|^{\frac{3}{2}}}. \tag{4.50}$$

With these definitions the only unknowns in the Hamilton equations are the position $\mathbf{r}(\tau)$ and the wave normal $\mathbf{p}(\tau)$ of a ray.

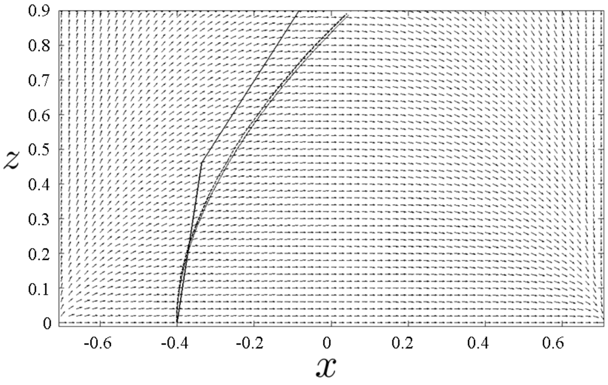

Figure 4.4: *Ray paths for four different values of $\triangle\tau$: from left to right the ray paths correspond to $\triangle\tau = 10^{-1}$, $\triangle\tau = 10^{-2}$, $\triangle\tau = 10^{-3}$ and $\triangle\tau = 10^{-4}$. In this particular example, a step size $\triangle\tau = 10^{-3}$ is sufficient for an accurate calculation of the ray paths.*

For the director defined in Eq. 4.46, we calculate the ray paths of five extraordinary rays incident orthogonal to the plane $z = 0$. In this plane the director satisfies $\hat{\mathbf{d}}(x, y, z) = (1, 0, 0)$. Then the initial conditions for the position and momentum are

$$\mathbf{r}(\tau_0) = (x_0, 0, 0), \tag{4.51}$$

$$\mathbf{p}(\tau_0) = (0, 0, n_e). \tag{4.52}$$

For x_0, we choose five different values: -0.6, -0.4, 0.0, 0.4 and 0.6. Furthermore, we investigate an anisotropic medium with $n_o = 1.0$ and $n_e = 1.5$. We calculate the extraordinary ray paths numerically by using the second-order Runge-Kutta method (see Appendix C): the step size $\triangle\tau = 10^{-4}$ and the number of steps is $K = 2000$. The results are depicted in Fig. 4.3. The ray at $x = 0$ propagates along the z-axis, while the other rays are curved in the plane $y = 0$. It is clear that the symmetry of the ray paths is due to the symmetry of the director $\hat{\mathbf{d}}(x, y, z)$ with respect to the z-axis: the position where a ray crosses the z-axis depends on $|x_0|$. Here we point out that the director profile induces a kind of lens effect. The lens effect generated by inhomogeneous liquid-crystal configurations will be discussed in Chapter 7.

In Fig. 4.4 we have calculated four extraordinary rays for $x_0 = -0.4$. Each ray corresponds to a different value for $\triangle\tau$. The ray that consists of two straight lines corresponds to $\triangle\tau = 10^{-1}$ (ray path on the left). Obviously, this step size is too large for an accurate calculation of the ray path. When $\triangle\tau = 10^{-2}$, the accuracy of the ray path has improved significantly (middle curve). A step size of $\triangle\tau = 10^{-3}$ results in another improvement (curve on the right). However, the ray paths calculated with step size $\triangle\tau = 10^{-3}$ and $\triangle\tau = 10^{-4}$ are essentially equal and cannot be distinguished from each other in Fig. 4.4. As a result, a step size of $\triangle\tau = 10^{-3}$ is sufficient for an accurate calculation of the ray paths in this particular example. In general, we conclude that for an accurate calculation of the ray paths the step size $\triangle\tau$ should be optimized accordingly.

With the mathematical example discussed we have shown that with a proper definition of the anisotropic properties we are able to calculate the (in general curved) ray paths of light rays in the bulk region of inhomogeneous anisotropic media.

Finally, we have investigated the ray-tracing equations for inhomogeneous anisotropic media when applied to an interface (see Appendix D). The interface is represented by a surface of discontinuity in the material properties. In theory, we can conclude that the Hamilton equations are not in contradiction with the rules of geometrical optics when applied to a surface of discontinuity in the bulk region of (in)homogeneous anisotropic media. However, the Hamilton equations alone cannot provide the wave normal $\mathbf{p}$ that satisfies $\mathcal{H} = 0$ on both sides of a discontinuity surface. To find the wave normals on either side of a discontinuity surface, we need the theory discussed in Chapter 3. Hence the Hamilton equations alone are not sufficient for the ray tracing of a light ray across a surface of discontinuity. These conclusions support the condition (mentioned in Section 2.3) that in the bulk region we only consider anisotropic media for which there are no discontinuities and condition 2.18 is satisfied.

In the next section, we investigate the optical properties of a nematic liquid-crystal configuration in both the interface region and the bulk region.

4.3 Simulations of a nematic liquid-crystal configuration

At this point we are able to calculate the optical properties of in general inhomogeneous anisotropic media in the geometrical-optics approach. Once we have defined the anisotropic material properties, we are able to calculate the optical properties in both the interface region and the bulk region. In this section we will show this for a number of three-dimensional liquid-crystal configurations [104]. Although we investigate rather academic liquid crystal configurations, this exercise has the purpose to show the potential of the general ray-tracing procedure that we now have at our disposal. In what follows, we will investigate both an uniaxially anisotropic and a biaxially anisotropic liquid crystal with a real symmetric dielectric tensor.

4.3.1 Point charge in an uniaxial liquid crystal

We consider a fixed Cartesian orthonormal basis $\{\hat{\mathbf{x}}, \hat{\mathbf{y}}, \hat{\mathbf{z}}\}$ in which the plane $z = 0$ is defined as a grounded conducting plate with electric potential $\Phi = 0$. Let there be a point charge in $(0, 0, Z_0)$, for some $Z_0 > 0$, with negative charge $-q$ (see Fig. 4.5). With the help of the method of images (cf. [92], p. 57), we can write the electric potential due to the charge $-q$ for $z \geq 0$ as

$$\begin{aligned} \Phi(x, y, z) \quad &= \quad \frac{q}{4\pi\varepsilon_0} \frac{1}{\sqrt{x^2 + y^2 + (z + Z_0)^2}} \\ &\quad - \frac{q}{4\pi\varepsilon_0} \frac{1}{\sqrt{x^2 + y^2 + (z - Z_0)^2}}. \end{aligned} \tag{4.53}$$

The corresponding static electric field is then given by $\mathbf{E}(x, y, z) = -\nabla\Phi(x, y, z)$. We define the space $z \geq 0$ to be filled with an uniaxially anisotropic medium with the material

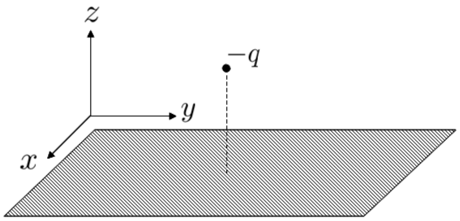

Figure 4.5: *Point charge $-q$ at a distance Z_0 above the origin. The plane $z = 0$ is defined a grounded conducting plate. As a result, there is an electric field in the half-space $z \geq 0$.*

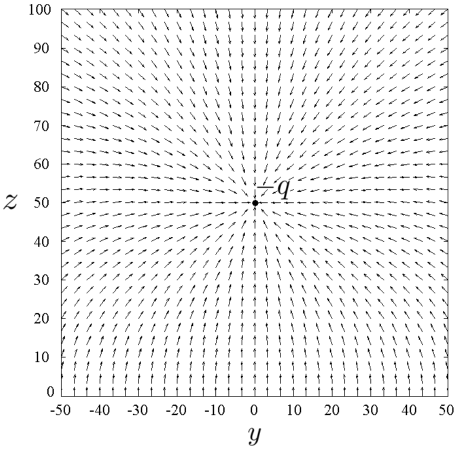

Figure 4.6: *The director profile (i.e. the normalized electric field due to the point charge $-q$) in the yz-plane for $Z_0 = 50$, $x \in [-50, 50]$ and $z \in [0, 100]$. The profile has azimuthal symmetry.*

properties of a liquid crystal. In addition, we will assume that the electric field strength is so high, that all directors follow the field direction. In other words, the electric energy is considered to be much higher than the elastic energy between the directors. Hence, the director profile due to the electric field of the point charge $-q$ is:

$$\hat{\mathbf{d}}(x, y, z) = \frac{\mathbf{E}(x, y, z)}{\big|\mathbf{E}(x, y, z)\big|}, \qquad z \geq 0. \tag{4.54}$$

Fig. 4.6 shows the director profile in the yz-plane for $Z_0 = 50$, $x \in [-50, 50]$ and $z \in [0, 100]$. The uniaxial liquid crystal in the upper half space $z \geq 0$ has an ordinary index of refraction $n_o = 1.5$ and an extraordinary index of refraction $n_e = 1.7$. These indices are constant and independent of position. The lower half space $z < 0$ is defined to be glass with an index of refraction $n_{glass} = 1.5$.

We define rays of light propagating in the z-direction incident on the (transparent) conducting plate. These rays are refracted at the conducting plate at $z = 0$, where $\hat{\mathbf{d}} = (0, 0, 1)$. Propagating along the z-direction, the refracted rays would be ordinary rays with an intensity transmittance factor $T_o = 1$. Then, according to the Hamilton

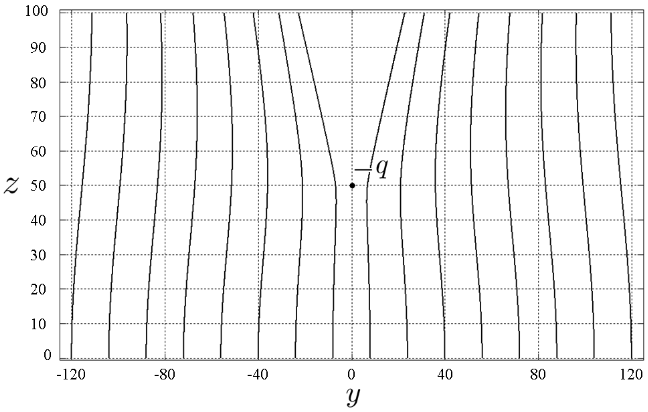

Figure 4.7: *Ray paths of several extraordinary rays at normal incidence to the plane $z = 0$, where the yz-plane is the plane of incidence. Note the 'curtain-like' behavior, allowing no light in the region above the point charge.*

equations for position-independent refractive indices, the rays in the bulk region would not be curved (see Eq. 4.42). To overcome this effect, we perturb the incident angle of the rays by 10^{-6} degrees in the yz-plane. Then the incident wave normal in the glass medium has a y- and a z-component. As a result, the plane of incidence is parallel to the yz-plane. In addition, we define a linear polarization parallel to the yz-plane. Then, by definition, the refracted rays are extraordinary rays with $T_e = 1$. In addition, the refractive indices are constant and as a result, we can apply the Hamilton equations given by Eqs. 4.40 and 4.41. By taking small steps in the 'time' τ, the position $\mathbf{r}(\tau)$ and momentum $\mathbf{p}_e(\tau)$ are calculated using the first-order Runge-Kutta method. Fig. 4.7 shows several ray paths of extraordinary rays in the bulk region of the liquid crystal configuration. Apparently, light rays are absent in the region above the point charge $-q$ and the ray paths seems to form a 'curtain-like' appearance.

An explanation for this phenomenon can be found in the fact that light bends towards regions of high refractive index. We will show this by examining the effective index of refraction n_{eff} of the liquid crystal in the yz-plane for light rays propagating in the vertical z-direction. In other words, we calculate the length of the extraordinary wave normal $|\mathbf{p}_e| = n_{eff}$ at position $\mathbf{r} = (0, y, z)$ for light rays with $\hat{\mathbf{p}}_e = (0, 0, 1)$. Since the director $\hat{\mathbf{d}}$ depends on the position in the yz-plane, so does $|\mathbf{p}_e|$. Fig. 4.8 shows the value of $|\mathbf{p}_e|$ as a function of position for $y \in [-50, 50]$ and $z \in [0, 100]$. We can clearly see that $|\mathbf{p}_e|$ has a maximum in the region of the location of the point charge. As a result, a light ray entering the liquid crystal at $z = 0$ will bend towards the region where the point charge is located. When the light ray approaches approximately $z = 50$, it will bend away from the region directly above the point charge since $|\mathbf{p}_e|$ increases with increasing distance from the vertical z-axis. This behavior is in agreement with the simulated ray paths depicted in Fig. 4.7.

At $z = 100$, we define a matrix in x and y that is used to collect the x- and y-coordinates of the extraordinary ray paths. The number of rays collected by each interval

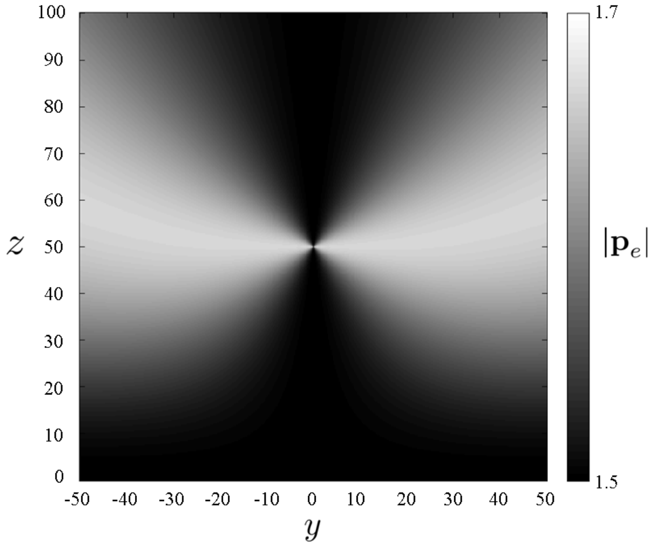

Figure 4.8: *The value of $n_{eff} = |\boldsymbol{p}_e|$ for $y \in [-50, 50]$ and $z \in [0, 100]$. In the region of the location of the point charge at $(y, z) = (0, 50)$, $|\boldsymbol{p}_e|$ has a maximum whereas $|\boldsymbol{p}_e|$ has a minimum along the y- and z-axes.*

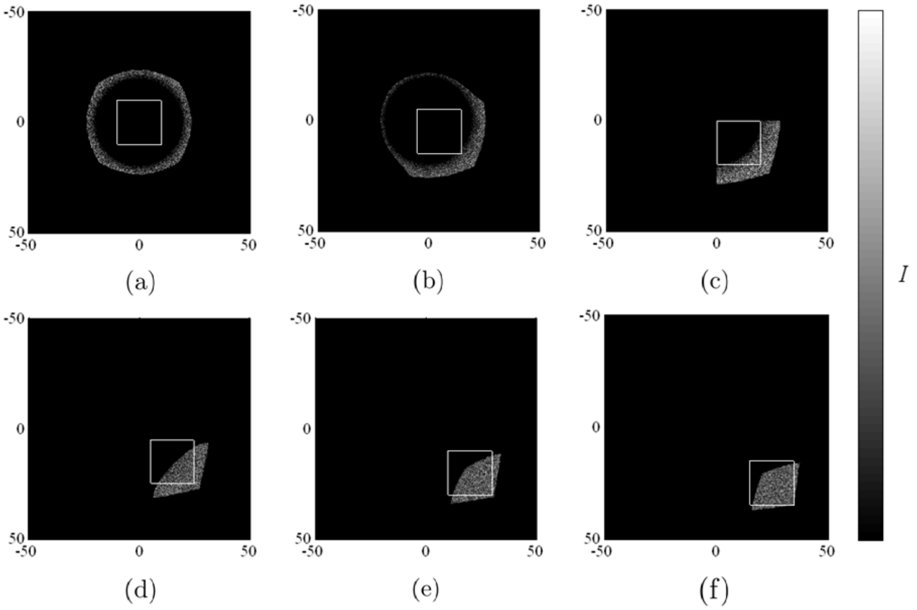

Figure 4.9: *Intensity distribution I at $z = 100$ for $x \in [-50, 50]$ and $y \in [-50, 50]$. The square (white) indicates the boundary in which the initial positions of the incident rays lie. This boundary is moved along the line $x = y$.*

is a measure to determine the intensity. Then the spatial intensity distribution I at $z = 100$ should give us an idea of the optical behavior. In order to obtain the spatial intensity distribution, we calculate the ray paths of $30,000$ extraordinary rays. The initial positions of these rays (x_0, y_0, z_0) randomly lie inside a square defined by $x_0 \in [-10, 10]$ and $y_0 \in [-10, 10]$.

Fig. 4.9-(a) shows the calculated intensity distribution I at $z = 100$. The white square indicates the boundary in which the initial positions (at $z = 0$) of the incident rays lie. Apparently, the square light source at $z = 0$ is transformed into a circular-like light distribution at $z = 100$. This is the case when the center of the square is exactly below the point charge. In the figures (b)-(f) this square is moved along the line $x = y$. From these figures it is clear that the intensity distribution changes with the position of the square. In Fig. 4.9-(f), the distortion of the square light source is only small, since the square is far away from the point charge.

4.3.2 Point charge in a biaxial liquid crystal

In the following exercise, we consider the same optical configuration except that now the half space $z \geq 0$ is filled with a nematic biaxially anisotropic liquid crystal. We will assume that the principal w-axis (see also Fig. 4.1) is parallel to the direction of the static electric field. Hence, on the fixed orthonormal basis $\{\hat{\mathbf{x}}, \hat{\mathbf{y}}, \hat{\mathbf{z}}\}$, the unit vector $\hat{\mathbf{w}}(x, y, z)$ satisfies

$$\hat{\mathbf{w}}(x, y, z) = \frac{\mathbf{E}(x, y, z)}{\left|\mathbf{E}(x, y, z)\right|}, \qquad z \geq 0, \tag{4.55}$$

where $\mathbf{E}(x, y, z)$ is the electric field due to the negative point charge $-q$. Fig. 4.10 shows $\hat{\mathbf{w}}(x, y, z)$ in the yz-plane for $Z_0 = 50$, $y \in [-50, 50]$ and $z \in [0, 100]$. In addition to this, we assume that the principal u-axis is in the direction of the vector $\hat{\mathbf{w}} \times \hat{\mathbf{z}}$. The principal v-axis is then in the direction of $\hat{\mathbf{w}} \times (\hat{\mathbf{w}} \times \hat{\mathbf{z}})$. The principal unit vectors $\hat{\mathbf{u}}$ and $\hat{\mathbf{v}}$ are also indicated in Fig. 4.10. In the special case that x and y are both zero $\hat{\mathbf{w}} = \pm\hat{\mathbf{z}}$ and hence the orthonormal unit vectors $\hat{\mathbf{u}}$ and $\hat{\mathbf{v}}$ can have any arbitrary orientation in a plane parallel to the plane $z = 0$.

The biaxial medium in the upper half space $z \geq 0$ is defined with constant position-independent principal indices of refraction $n_u = 1.3$, $n_v = 1.5$ and $n_w = 1.7$. Since ε_u, ε_v and ε_w are independent of position, $h = 0$ (see Eq. 4.22). The lower half space $z < 0$ is assumed to be glass with an index of refraction $n_{glass} = 1.5$.

We will use the theory discussed in Chapter 3 to calculate the directions of propagation and the intensity transmittance factors of the rays propagating from the glass into the biaxial liquid crystal. In general, there will be two refracted rays for each incident ray. Then we will use the Hamilton equations 4.21 and 4.23 ($h = 0$) to calculate the ray paths of the refracted rays in the bulk material. The initial positions of the rays (x_0, y_0, z_0) randomly lie inside a square defined by $x_0 \in [-10, 10]$ and $y_0 \in [-10, 10]$. These rays are refracted at the (transparent) conducting plate at $z = 0$, where $\hat{\mathbf{w}} = (0, 0, 1)$. The incident rays are linearly polarized parallel to the yz-plane and have an angle of incidence of 10° with the z-axis in a plane parallel to the yz-plane. By taking small steps in the 'time' τ, the position $\mathbf{r}(\tau)$ and momentum $\mathbf{p}(\tau)$ are calculated using the first-order Runge-Kutta method.

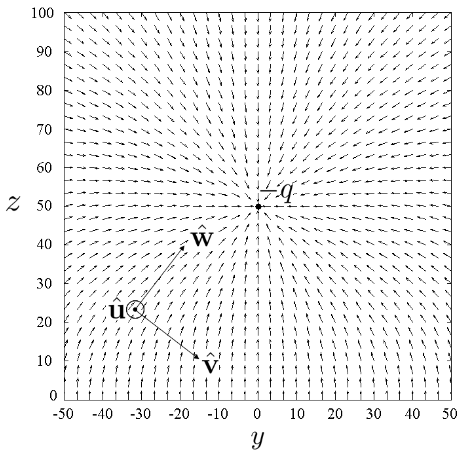

Figure 4.10: *The principal unit vector $\hat{\boldsymbol{w}}$ (i.e. the normalized electric field due to the point charge $-q$) in the yz-plane for $Z_0 = 50$, $x \in [-50, 50]$ and $z \in [0, 100]$. The corresponding principal unit vectors $\hat{\boldsymbol{u}}$ and $\hat{\boldsymbol{v}}$ are also indicated.*

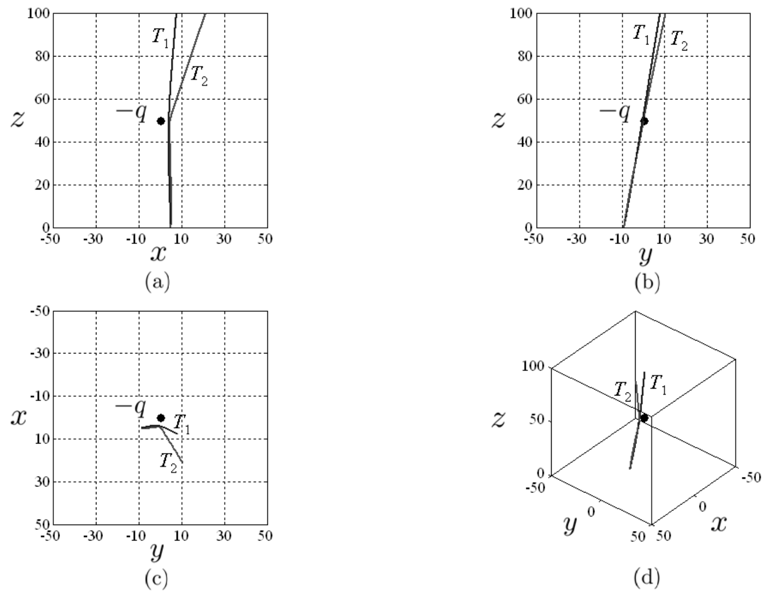

(a)

(b)

(c)

(d)

Figure 4.11: *Ray paths of two refracted rays incident at the position $(x_0, y_0, z_0) = (5, -9, 0)$. Fig. (a) and (b) show the image projections in the xz- and yz-plane, respectively. Likewise, Fig. (c) shows the top view of the two ray paths and Fig. (d) shows the ray paths in three-dimensional space. Apparently, both ray paths are curved and they are drawn away from the region above the point charge.*

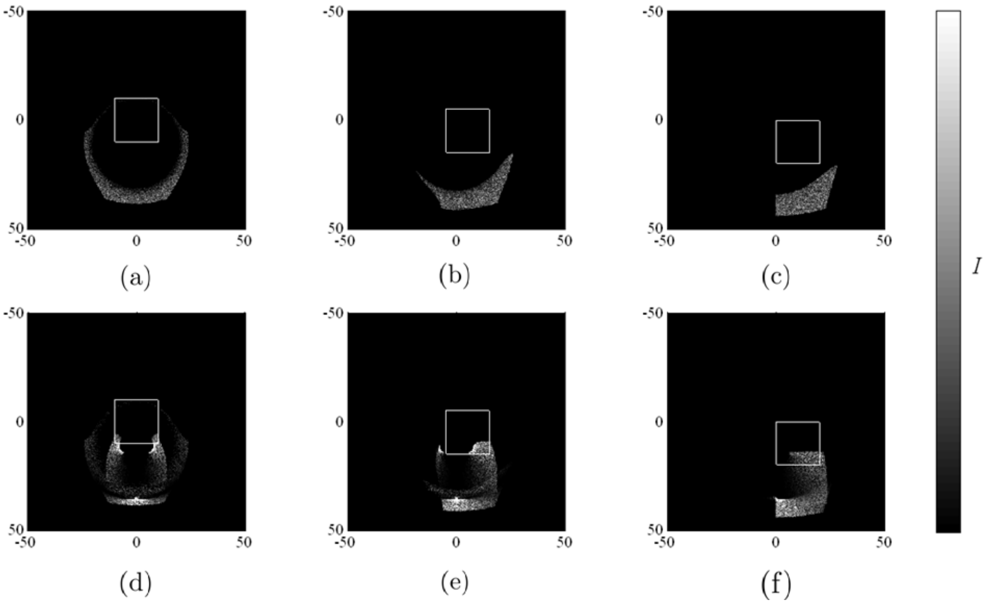

Figure 4.12: *Intensity distribution I at $z = 100$ for $x \in [-50, 50]$ and $y \in [-50, 50]$. Fig. (a)-(c) show the light distribution for the uniaxial liquid crystal ($n_o = 1.5$ and $n_e = 1.7$). Fig. (d)-(f) show the light distribution for a biaxial liquid crystal ($n_u = 1.3$, $n_v = 1.5$ and $n_w = 1.7$). The square (white) indicates the boundary in which the initial positions of the incident rays lie. The square is moved along the line $x = y$.*

Fig. 4.11 shows the ray paths of two refracted rays corresponding to a ray incident at the position $(x_0, y_0, z_0) = (5, -9, 0)$. Fig. 4.11-(a) and (b) show the image projections in the xz- and yz-plane, respectively. Fig. 4.11-(c) shows the top view of the two ray paths. Finally, Fig. 4.11-(d) shows an oblique projection of the two ray paths. Apparently, both ray paths are curved and they seem to be repelled from the region above the point charge. The ray paths correspond to intensity transmittance factors $T_1 = 0.2210$ and $T_2 = 0.7777$. The reflected ray in the glass ($z < 0$) has an intensity reflectance factor $R = 0.0013$. As expected, the sum of T_1, T_2 and R exactly adds up to 1.0000.

In Fig. 4.12 (a)-(c), we show the spatial intensity distribution I at $z = 100$ for the uniaxial liquid crystal with $n_o = 1.5$ and $n_e = 1.7$ (similar to the results presented in Fig. 4.9, but now with an angle of incidence of 10°). In Fig. 4.12 (d)-(f), the results are depicted for the biaxial liquid crystal. The number of rays that is traced for each individual image is 25000. The white square (at $z = 0$) indicates the boundary in which the initial positions of the incident rays lie. In Fig. 4.12-(a) and 4.12-(d), the center of the white square is exactly below the point charge. Fig. 4.12-(a) shows how the square light source at $z = 0$ is transformed to a ring-shaped light distribution. Clearly, we observe a different intensity distribution in Fig. 4.12-(d). In contrast with Fig. 4.12-(a), the biaxial anisotropic properties of the liquid crystal are responsible for a twofold light distribution. Moreover, the total light distribution shows three compact regions of high intensity, located above two corners of the white square and the (positive) y-axis.

In Fig. 4.12 (b)-(c) and 4.12 (e)-(f) the white square is moved from its initial position along the line $x = y$. It is clear that the intensity distribution changes with the position of the square. In the limit where the square is far away from the point charge, the image of the square light source at $z = 100$ is again a square.

4.3.3 Multiple point charges in an uniaxial liquid crystal

Up to this point, we have simulated the optical properties due to a single point charge inside a liquid crystal. In what follows, we will investigate the optical properties of the same optical system as in Subsection 4.3.1, but now with a configuration of nine point charges. The positions of the nine point charges are defined in a plane parallel to the xy-plane at $z = 50$, see Fig. 4.13. The distance between the individual point charges is indicated by u. In addition, the middle point charge is positioned exactly above the origin in $(x, y, z) = (0, 0, 50)$. In Fig. 4.13-(a), all the point charges are positively charged whereas in Fig. 4.13-(b), one point charge (upper right corner) is negatively charged.

We can use the method of images to calculate the electric potential $\Phi(x, y, z)$ for $z \geq 0$ due to multiple point charges. Then the electric potential due to nine point charges is given by

$$\Phi(x,y,z) \quad = \quad \Phi_1(x,y,z) + ... + \Phi_9(x,y,z), \tag{4.56}$$

where

$$\begin{aligned} \Phi_i(x,y,z) \quad = \quad & \frac{q_i}{4\pi\varepsilon_0} \frac{1}{\sqrt{(x-X_i)^2 + (y-Y_i)^2 + (z+Z_i)^2}} \\ & - \frac{q_i}{4\pi\varepsilon_0} \frac{1}{\sqrt{(x-X_i)^2 + (y-Y_i)^2 + (z-Z_i)^2}}, \end{aligned} \tag{4.57}$$

with $i = 1, ..., 9$ and the constants X_i, Y_i and Z_i the coordinates of the individual point charges. The corresponding electric field is then given by $\mathbf{E}(x, y, z) = -\nabla\Phi(x, y, z)$ and the resulting director profile $\hat{\mathbf{d}}$ is given by Eq. 4.54.

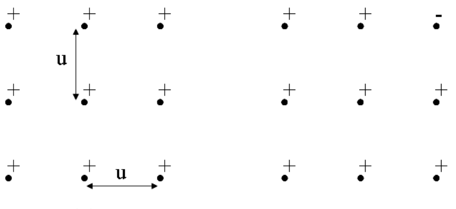

(a) (b)

Figure 4.13: *Positions of nine point charges in the plane $z = 50$. The distance between the individual point charges is indicated by u and the middle point charge is exactly above the origin at $(x, y, z) = (0, 0, 50)$. In figure (a), all the point charges are positively charged whereas in figure (b), one point charge is negatively charged.*

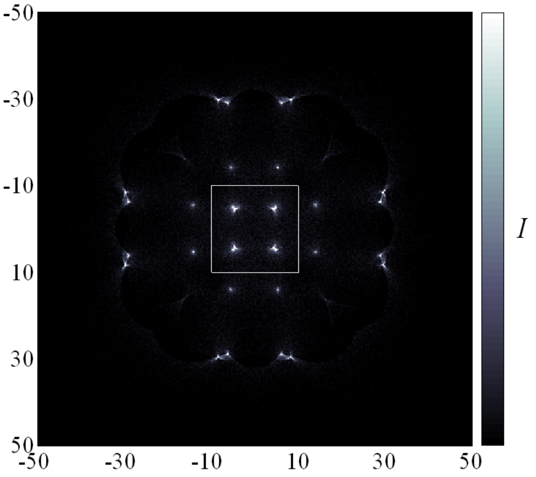

Figure 4.14: *Intensity distribution I for the configuration of Fig. 4.13-(a) at* $z = 100$ *for* $x \in [-50, 50]$ *and* $y \in [-50, 50]$ *and* $u = \frac{20}{3}$. *The square light source at* $z = 0$ *(indicated by the white square) is transformed to a configuration of light spots that lie on the grid points of a regular square grid.*

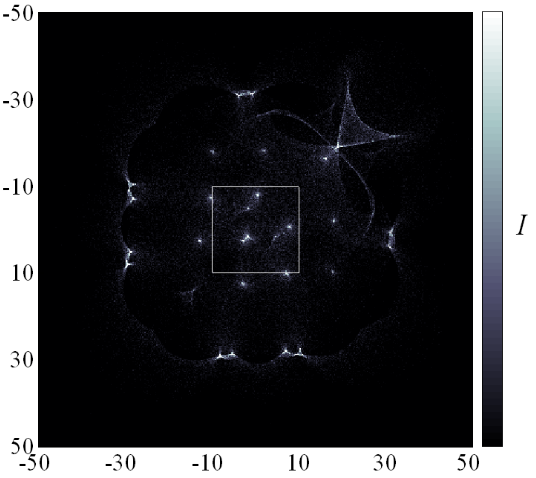

Figure 4.15: *Intensity distribution I for the configuration of Fig. 4.13-(b) at* $z = 100$ *for* $x \in [-50, 50]$ *and* $y \in [-50, 50]$ *and* $u = \frac{20}{3}$. *Although we define a different charge distribution of the point charges, we apply the same optical system used in Fig. 4.14. In this case, the intensity distribution I at* $z = 100$ *shows both light spots and blurring effects.*

We apply the Hamilton equations to calculate the ray paths of extraordinary rays in a liquid crystal with indices of refraction $n_o = 1.5$ and $n_e = 1.7$. The initial positions of the rays (x_0, y_0, z_0), propagating in the positive z-direction, randomly lie inside a square defined by $x_0 \in [-10, 10]$ and $y_0 \in [-10, 10]$. The rays are refracted at the liquid crystal interface at $z = 0$ and modulated by the liquid crystal in the half space $z > 0$. At $z = 100$, we calculate the spatial intensity distribution I.

Fig. 4.14 shows the intensity distribution I at $z = 100$ for the configuration depicted in Fig. 4.13-(a). In this case, $u = \frac{20}{3}$. The number of rays that is traced is 150000. The white square indicates the boundary in which the initial positions (at $z = 0$) of the incident rays lie. The center of the square is exactly at the origin. As can be seen from Fig. 4.7, the light rays are repelled in the neighborhood of a point charge. Hence, we can expect that light rays will converge in regions between multiple point charges with the same charge sign. Indeed in Fig. 4.14, we clearly see that the square light source at $z = 0$ is transformed into multiple light spots at $z = 100$. Moreover, this collection of light spots lies on the grid points of a regular square grid, similar (but not identical) to the configuration of point charges.

Fig. 4.15 shows the intensity distribution I at $z = 100$ for the configuration depicted in Fig. 4.13-(b). This configuration of point charges corresponds to the same optical system, but with a different charge sign distribution. Similar to the intensity distribution I in Fig. 4.14, the eight positive point charges converge the light rays to light spots at $z = 100$. On the other hand, the negatively charged point charge on the right side is responsible for a different optical response. Clearly, the combination of positive and negative point charges is responsible for a diverging effect. As a result, the square light source at $z = 0$ is transformed to a spatial light distribution which shows both light spots and blurring effects.

From these results we can conclude that point charges positioned on the grid points of a regular square grid in a liquid crystal can control the optical response of the optical system by controlling the distribution of positive and negative charges. Although the use of point charges is a rather artificial approach, it brings the idea of switchable gradient-index devices with multiple optical states to mind. In conventional applications, liquid crystal gradient-index devices are designed with a pattern of line electrodes that are able to switch a liquid crystal profile between two different optical states. In our simulations, we have investigated a configuration of multiple charges that introduces the possibility to increase the number of liquid crystal configurations with just one optical system.

In this section, we have investigated the optical properties of inhomogeneous liquid-crystal configurations for both uniaxial and biaxial anisotropy. Altogether, we have shown that the general ray-tracing method for inhomogeneous anisotropic media can be applied to assess the optical properties of arbitrary optical configurations in three dimensions.

4.4 Conclusions

In this chapter we have derived expressions for the position-dependent optical indicatrix for both uniaxial and biaxial anisotropy. With the help of these equations and the Hamiltonian principle, we have introduced novel ray-tracing equations for the, in general curved, ray paths in inhomogeneous anisotropic media. These equations comprise the position-dependent material properties explicitly: the position-dependent director and the principal indices of refraction. For the remainder of this thesis, we will be mainly concerned with the position-dependency of the director. Furthermore, the ray-tracing equations are given in complex notation and in general, these equations apply for media with a complex Hermitian dielectric tensor. In that sense, they define the state-of-the-art in the field of polarized ray tracing of (non-absorbing, optically inactive) inhomogeneous anisotropic media within the framework of geometrical optics. In Chapters 6, 7 and 8 we will study applications of liquid crystal defined by a real Hermitian dielectric tensor.

The ray-tracing equations introduced in this chapter are applied to an uniaxial and a biaxial liquid-crystal configuration with an inhomogeneous director profile. In this exercise we have shown the potential of the general ray-tracing procedure that we now have at our disposal. In general, we can conclude that the general ray-tracing equations for inhomogeneous anisotropic media can be applied to assess the optical properties of arbitrary optical configurations in three dimensions.

Chapter 5

On the applicability of geometrical optics to in-plane liquid-crystal configurations

Within the framework of geometrical optics, the material properties are allowed to change with position provided that condition 2.18 is satisfied. This condition implies that 1) the properties of the medium should change continuously with position and 2) the change in the material properties is sufficiently small over the distance of a wavelength.

In Chapter 4 and Appendix D, we have shown that the Hamilton equations can be applied in a bulk region where the material properties vary continuously with position, but fail at a surface of discontinuity. Therefore, we only consider bulk regions without any discontinuities in the material properties. The material properties in the interface region are discontinuous and then we can apply the classical theory discussed in Chapter 3.

One important question that has not received much attention so far is how much change in the material properties per unit wavelength is allowed in the geometrical optics. Kline & Kay, for example, remark that the derivation of geometrical optics from the Sommerfeld-Runge Ansatz (see Eqs. 2.11 and 2.12) offers little insight into the relationship between wave optics and geometrical optics which might be used to make some gradual transition from the one to the other (cf. [75], p. 13). In this chapter, we formulate a criterion for the applicability of geometrical optics to typical inhomogeneous in-plane liquid-crystal configurations. We do this because the optical properties of many liquid-crystal applications are determined by a characteristic in-plane director profile. To this end, we present advanced ray- and wave-optics simulations of the propagation of an incident plane wave to a two-dimensional director profile with special optical properties.

5.1 Beyond geometrical optics

Up to this point, we have discussed the propagation of light rays in anisotropic media within the framework of geometrical optics. In the geometrical-optics approach, light rays propagate independently and do not exchange energy with the (non-absorbing) medium in which they are propagating. These properties are called mode independency and adiabatic propagation (see also [105]), respectively, and are further discussed in Appendix E. The adiabatic propagation of light rays applies to media in which the material properties change continuously with position. This means that there is no reason whatsoever for a light ray to split into two or more light rays. On the other hand, at a surface of discontinuity, the total energy of a light ray is conserved, but is in general divided over two reflected and two refracted light rays (see Chapter 3). The mode independency and adiabatic propagation of light rays only apply in geometrical optics. In case geometrical optics is no longer valid, the wave character of light needs to be taken into account.

The classical theory of geometrical optics is based on the Maxwell equations in the limit where the wave number in vacuum k_0 becomes very large. For smaller values of k_0 the wave character of light has to be taken into account and the full Maxwell equations must be considered. Then a widely used approach consists of expanding the wave amplitude in terms of $\frac{1}{ik_0}$, called a Debye expansion (cf. [105], p. 7). When we substitute this expansion into the Maxwell equations and collect the coefficients of terms of equal power in $\frac{1}{ik_0}$, we obtain a set of first-order partial differential equations which are called the transport equations (see Appendix F). In the geometrical-optics approach, the optical wave field satisfies the zeroth-order transport equation. Therefore we say that in geometrical optics we only consider the lowest-order approximation of the optical wave field. The higher-order transport equations define the higher-order corrections to the zeroth-order wave field. These corrections can be applied beyond the validity region of geometrical optics.

The transport equations of higher order are difficult to solve and they do not provide additional physical insight into the modeling of anisotropic media. In that sense, the use of the transport equations does not form an attractive route to investigate the applicability of geometrical optics to inhomogeneous anisotropic media. Other criteria for the applicability of geometrical optics, such as Fresnel zones discussed by Kravtsov & Orlov (cf. [105], p. 80), are also difficult to apply in practice. In what follows, we apply a different approach to investigate the applicability of geometrical optics. We will consider a typical director profile of an in-plane liquid-crystal configuration, since they occur in many liquid-crystal applications.

5.2 Ray- and wave-optics simulations of a periodic director profile

A criterion for the application of geometrical optics in inhomogeneous media can be deduced from the following consideration. Consider an inhomogeneous anisotropic medium in which the director is rotated gradually by an angle of 90° over a distance L_d, see Fig. 1.8 in Subsection 1.3.2. Then L_d is the distance over which a maximum change in optical properties occurs (for fixed principal indices of refraction).

We define the dimensionless wavelength by $\frac{\lambda}{L_d}$, where λ is the wavelength of light. In the limit where $\frac{\lambda}{L_d} \to 0$, a medium has material properties that are independent of position: the medium is homogeneous. The limit where $\frac{\lambda}{L_d} \to \infty$ corresponds to a discontinuity in the material properties, i.e. at the interface between two different media. Then the boundary conditions for the electromagnetic field apply (see e.g. [57], p. 2390).

For sufficient small $\frac{\lambda}{L_d}$, the predictions of geometrical optics and wave optics agree. The main question is then up to what value of $\frac{\lambda}{L_d}$ approximately we are allowed to apply geometrical optics.

To answer this question, we study the effect of a director profile on the propagation of an incident plane wave.

5.2.1 Ray-tracing simulations

The periodic director profile lies in the xz-plane and represents an inhomogeneous uniaxially anisotropic medium (with a real symmetric permittivity tensor) and is given by

$$\hat{\mathbf{d}}(x,z) = \cos\theta(x,z)\hat{\mathbf{x}} + \sin\theta(x,z)\hat{\mathbf{z}}, \tag{5.1}$$

with the angle $\theta(x,z)$ defined by

$$\theta(x,z) = \frac{\pi}{4}\left[1 - \cos\left(\frac{2\pi x}{T}\right)\right]\sin\left(\frac{\pi z}{D}\right), \tag{5.2}$$

where D is the thickness and T is the period of the director profile. Three periods of the director profile $\hat{\mathbf{d}}(x,z)$ are depicted in Fig. 5.1 for $T = 20$ and $D = 20$. We choose this fictitious director profile, because it has the properties we are looking for: the director is gradually rotated by 90° over a distance $\frac{D}{2}$ in the z-direction halfway each period (e.g. at $x = 30$). In addition to this, the director is rotated by 90° twice each period in the x-direction at $z = \frac{D}{2}$. In this case, the gradual rotation of $\hat{\mathbf{d}}$ is defined by goniometric functions. The rotation can also be defined by e.g. linear functions, as long as they describe a gradual rotation over L_d. Finally, we see that the director is in the x-direction for $z = 0$, $z = D$ and $x = kT$, with $k \in \mathbb{N}$. The ordinary and extraordinary indices of refraction are taken $n_o = 1.5$ and $n_e = 1.7$, respectively. The surrounding medium ($z < 0$ and $z > D$) is isotropic with $n = 1.0$. We remark that this optical system is somewhat similar to that of an in-plane-switching liquid-crystal cell [106].

We will use the advanced ray-tracing procedure discussed in Chapters 3 and 4 to simulate how an incident plane wave propagating in the z-direction and polarized in the xz-plane is affected by the periodic director profile. The polarization of the incident plane wave is in the x-direction. Fig. 5.2 shows the curved ray paths of extraordinary light rays inside one period of the director profile. From the results we can conclude that the rays are diverging away from the center of the period T.

An explanation for this behavior can be found in the fact that light bends towards regions of high refractive index (see also Section 4.3.1). We can show this by examining an effective index of refraction n_{eff} at each position (x,z) of extraordinary light rays with propagation direction $\hat{\mathbf{p}}_e(x,z) = \hat{\mathbf{z}}$. Then we have

$$n_{\text{eff}} = \sqrt{\frac{n_o^2 n_e^2}{n_o^2 \sin^2(\frac{\pi}{2} - \theta) + n_e^2 \cos^2(\frac{\pi}{2} - \theta)}}, \tag{5.3}$$

with θ given by Eq. 5.2 and $|\mathbf{p}_e| = n_{\text{eff}}$. Since the director $\hat{\mathbf{d}}$ depends on the position in the (xz)-plane, so does n_{eff}, as can be seen in Fig. 5.3. We can clearly see that n_{eff} has a maximum in the periphery of one period of the director profile, since there $n_{\text{eff}} = n_e$. In the center we have $n_{\text{eff}} = n_o$. As a result, a light ray entering the director profile at

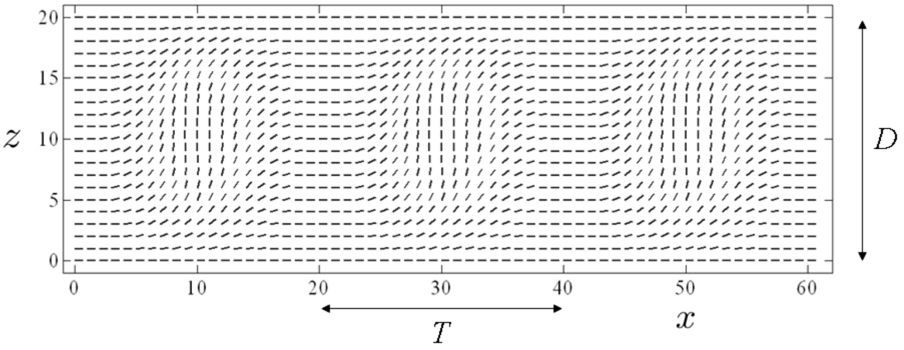

Figure 5.1: *Inhomogeneous periodic director profile with* $T = 20$ *and* $D = 20$. *The director profile represents an uniaxially anisotropic medium with* $n_o = 1.5$ *and* $n_e = 1.7$.

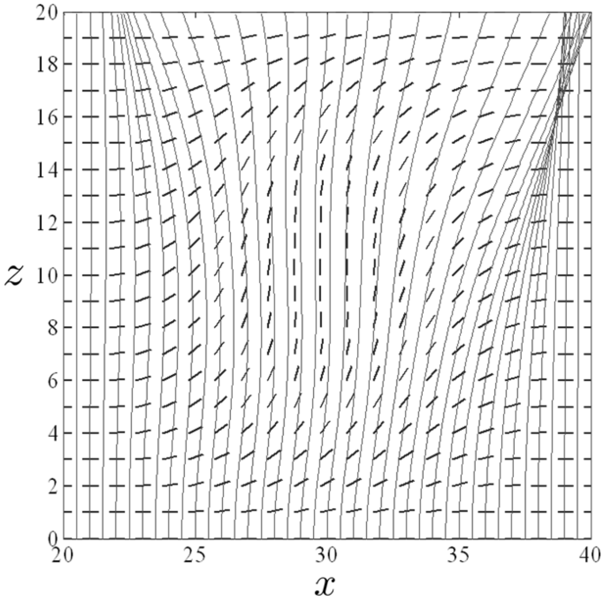

Figure 5.2: *Periodic director profile for* $x \in [T, 2T]$ *with the ray paths of extraordinary rays indicated by the curved lines. The light rays are at normal incidence with the plane* $z = 0$.

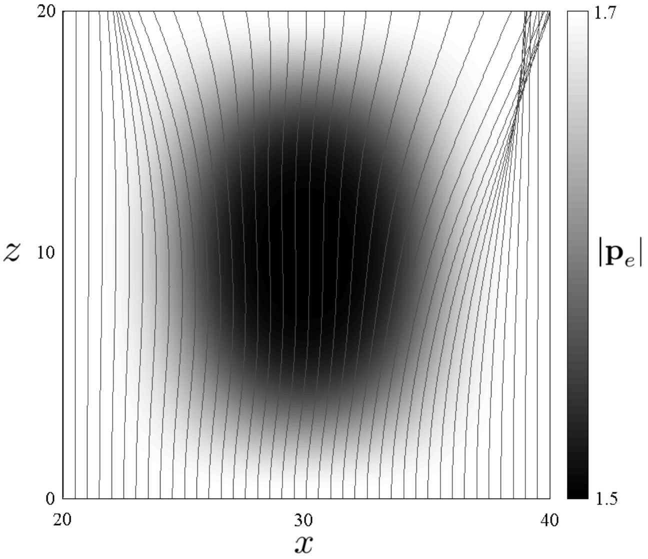

Figure 5.3: *The value of* $n_{\mathit{eff}} = |\boldsymbol{p}_e|$ *for* $x \in [20, 40]$ *and* $z \in [0, 20]$. *In the periphery of the square region* $|\boldsymbol{p}_e|$ *is approximately* 1.7 *whereas in the center* $|\boldsymbol{p}_e|$ *approaches* 1.5. *The curved ray paths of the extraordinary light rays are also depicted.*

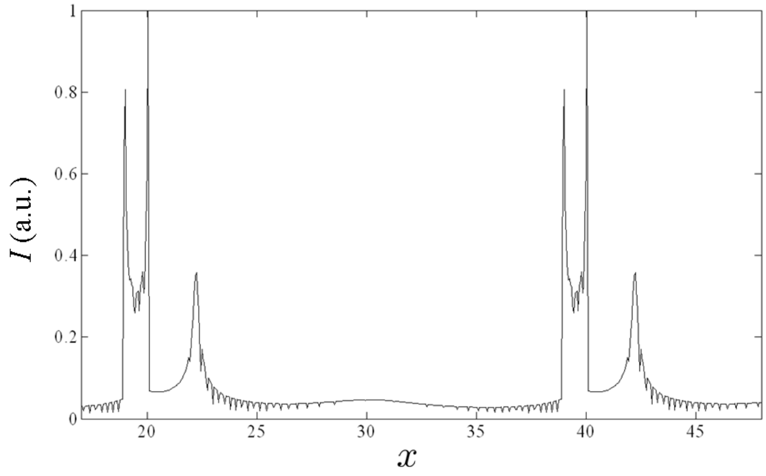

Figure 5.4: *The spatial (scaled) intensity distribution* I *at* $z = D$ *for the periodic director profile. Clearly, the intensity distribution is periodic with period* $T = 20$.

for example $x = 32$ penetrates the region of low refractive index in the center and then bends towards the nearby region of high refractive index at the right. The ray paths are seeking the fastest way towards the periphery and thus show a diverging effect.

At $z = D$ the extraordinary intensity transmittance factor T_e of the rays is calculated (taking into account single reflections):

$$T_e = \frac{S_z^t}{S_z^{inc}}, \tag{5.4}$$

with S_z^t the z-component of the transmitted Poynting vector and S_z^{inc} the z-component of the incident Poynting vector (see also Eq. 3.38). At $z = D$ the rays (a total number of $1.44 \cdot 10^6$, each having a weight factor T_e) are collected in intervals of length $\triangle x = 0.05$. Then the total number of rays collected by an interval is a measure for the intensity. Hence we obtain a (scaled) spatial intensity distribution I which is periodic with period T. The result is depicted in Fig. 5.4. Clearly we observe peak intensities near the edges of the period T and a low intensity in the middle.

5.2.2 FEM simulations

In what follows, we present results of wave-optics simulations according to an advanced rigorous in-house numerical simulation program based on the Finite Element Method developed jointly by Philips Research and Delft University of Technology [107]. This method enables in particular the numerical simulation of the electromagnetic field inside an inhomogeneous anisotropic medium. The computational domain is restricted because of memory constraints: the results are presented for dimensions up to 60×60 wavelengths.

In the FEM simulations, the wavelength λ of the incident plane wave in the surrounding medium (where $n = 1$) is 500 nm. The ratio of the period T and the thickness D is fixed: $\frac{T}{D} = 1$. The values of T and D are chosen in terms of the wavelength λ. The electromagnetic field of the propagating plane wave is calculated at $z = D$ after refraction at the interface between the director profile and the surrounding medium. There the ratio between the z-component of the transmitted and incident Poynting vector is calculated as a function of position x and the resulting spatial intensity distribution reads

$$I^{FEM}(x) = \frac{S_z^t}{S_z^{inc}}. \tag{5.5}$$

The FEM simulations are performed for different values of the period T. First, we take $T = D = 10\lambda$ and with $\lambda = 500$ nm, this corresponds to a computational domain of 5×5 μm. The spatial intensity distribution is depicted in Fig. 5.5 together with the scaled spatial intensity distribution obtained from the ray-tracing simulations. The results for $T = 20\lambda$, $T = 40\lambda$ and $T = 60\lambda$ are depicted in Fig. 5.6, 5.7 and 5.8, respectively.

From the results in general we can conclude that qualitatively, there is a match between the FEM simulations and the ray-tracing simulations. Quantitatively, there is a good match for $T = 40\lambda$ and $T = 60\lambda$ (see Figs. 5.7 and 5.8). However, the match is not perfect. This is because the FEM calculates the electromagnetic field whereas the ray-tracing simulations are based on counting rays. Hence the FEM simulations include diffraction effects. In this case, diffraction effects are likely to occur, especially in the

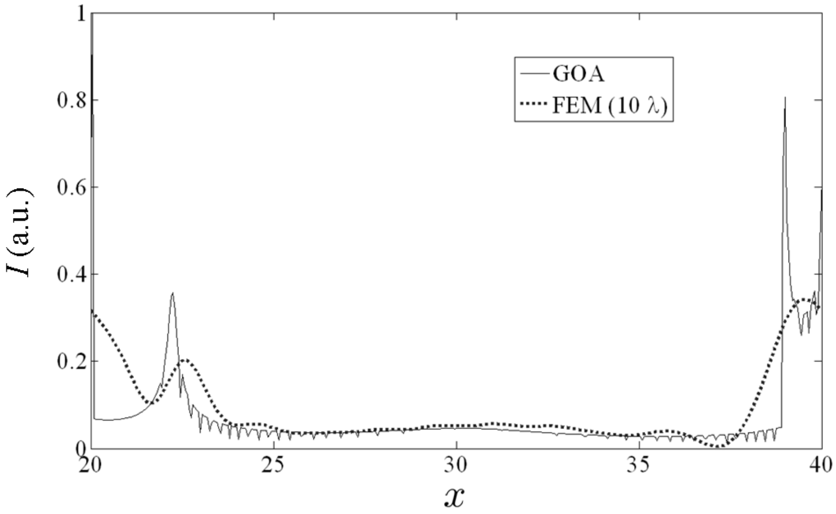

Figure 5.5: *Spatial intensity distribution according to the FEM simulations for* $T = 10\lambda$*. This corresponds to a computational domain of* 5×5 *μm. The (scaled) spatial intensity distribution according to the ray-tracing simulations (see Fig. 5.4) is also depicted (GOA).*

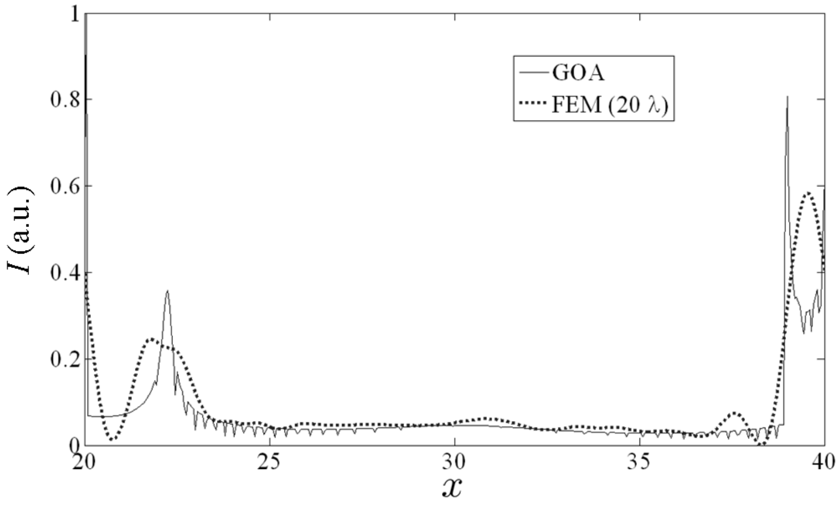

Figure 5.6: *Spatial intensity distribution according to the FEM simulations for* $T = 20\lambda$*. Then a period of the director profile corresponds to a computational domain of* 10×10 *μm.*

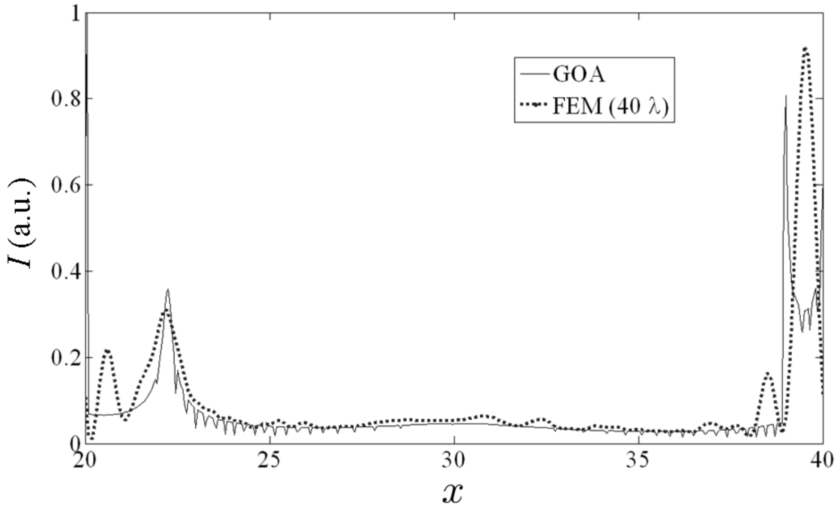

Figure 5.7: *Spatial intensity distribution according to the FEM simulations for* $T = 40\lambda$. *Now the computational domain of the FEM is* 20×20 μm.

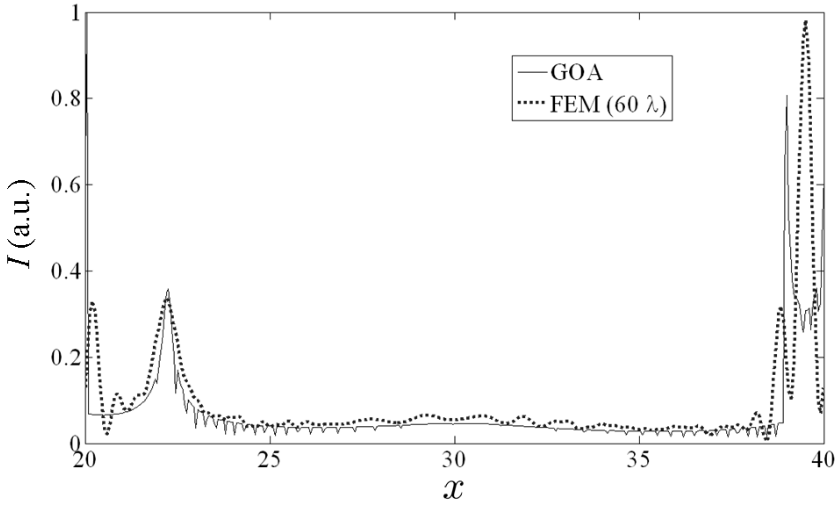

Figure 5.8: *Spatial intensity distribution according to the FEM simulations for* $T = 60\lambda$. *The computational domain of the FEM has reached a maximum of* 30×30 μm *due to memory constraints.*

Table 5.1: *Values for the period T, distance L_d and ratio $\frac{\lambda}{L_d}$ used in the simulations.*

T (λ)	L_d (λ)	L_d (μm)	$\frac{\lambda}{L_d}$
10	5	2.5	0.200
20	10	5.0	0.100
40	20	10.0	0.050
60	30	15.0	0.033

region where ray paths intersect one another. This can be seen in the right upper corner in Fig. 5.2, where the FEM simulations show an intensity distribution that resembles a diffraction pattern. This explains the incongruence between the FEM simulations and ray-optics simulations in this particular region.

We can see that the agreement between the FEM simulations and the ray-tracing simulations improves when T (and therefore D) increases. This observation is in line with what one would expect, since the ratio $\frac{\lambda}{L_d}$ decreases with increasing T. For the director profile discussed in this section, the distance $L_d = \frac{D}{2} = \frac{T}{2}$ (see Fig. 1.8 and Fig. 5.1). The values for the period T and the corresponding ratio $\frac{\lambda}{L_d}$ used in the simulations are listed in Table 5.1.

Based on the results, we formulate the following criterion. If $L_d > 20\lambda$ or $\frac{\lambda}{L_d} < 0.05$, ray- and wave-optics are in good agreement, both qualitatively and quantitatively. If $L_d < 20\lambda$, the correlation between ray- and wave-optics worsens. However, a qualitative agreement between ray- and wave-optics might still be established for values of L_d below 20 wavelengths. This criterion applies when L_d corresponds to a director rotation of 90°, and thus a maximum change in material properties. If L_d corresponds to a rotation of less than 90°, larger values for $\frac{\lambda}{L_d}$ are allowed.

5.3 Conclusions

In this chapter, we have studied the applicability of geometrical optics to typical in-plane liquid-crystal configurations. In particular, we have investigated how much change per unit wavelength in a two-dimensional director profile is approximately allowed within the geometrical-optics approach. To this end, we consider the ratio $\frac{\lambda}{L_d}$, where L_d is the distance over which the director is rotated by 90°. Then L_d is the distance over which a maximum change in optical properties occurs for fixed principal indices of refraction. The formulated criterion is based upon the results of ray- and wave-optics simulations of an uniaxially anisotropic medium with a periodic director profile with special properties. The approach described in this chapter can also be applied to biaxially anisotropic media, since they can have similar director variations and birefringence. From the results we conclude that if $\frac{\lambda}{L_d} < 0.05$, it is fair to say that ray- and wave-optics are in good agreement, both qualitatively and quantitatively. If L_d is smaller than 20 wavelengths, the agreement between ray- and wave-optics worsens. However, a qualitative agreement between ray- and wave-optics might still be established for values of L_d below 20 wavelengths. In Chapter 8, we present simulations of the liquid-crystal-based light guide structure (see Subsection 1.2.2) that support this statement.

Chapter 6

Switchable lenticulars for 3D displays

In the previous chapters we have discussed the classical electromagnetic theory and the ray-tracing procedures to model optically anisotropic media. In the chapters that will follow we apply the ray-tracing procedures to simulate the optical properties of novel liquid-crystal applications. In this chapter, we discuss liquid-crystal-based lenticulars for application in 3D displays.

In 2004, Philips Research has developed an innovative technique of creating auto-stereoscopic three-dimensional (3D) images by combining a multi-view lenticular-based 3D display technology with advanced computer graphics and image analysis techniques [25]-[27]. The display technology involved makes use of a liquid-crystal-based lenticular sheet that is able to switch between a conventional 2D mode and an auto-stereoscopic 3D mode. The lenticular sheet is an array of cylindrical lenses filled with liquid crystal. The liquid crystal can be switched between two optical states with the help of an electric field. As a result, the lens effect of the lenticular can be switched on and off. In this chapter, after a short introduction to lenticular-based 3D displays, we focus our attention to this part of the 3D display technology.

6.1 Multi-view auto-stereoscopic lenticular-based 3D displays

The design of a lenticular-based 3D display involves a number of important issues related to the display, such as resolution loss and pixel layout, and in particular to the optical design of the lenticular. In this section, we briefly discuss these issues and explain the working principle of a multi-view lenticular-based 3D display. In the discussion that follows we will consider the technical specifications of a nine-views 20 inch lenticular-based 3D display. Fig. 6.1 shows a picture of the 3D display involved. The display that is used is a liquid crystal display (LCD).

6.1.1 Resolution of a 3D display

In general, a multi-view 3D display suffers from a resolution loss, since the available (sub-)pixels of a display are used to generate multiple images. The resolution loss of each view in a multi-view 3D display is equal to a factor that is the total number of views.

Fig. 6.2 shows the schematic (sub-)pixel layout of a nine-views 3D display. The sub-pixel width and height are 0.085 mm and 0.255 mm, respectively. Hence the ratio between sub-pixel width and height is $\frac{1}{3}$. The numbers depicted in each sub-pixel correspond to one of the nine views. In addition, the diagonal lines indicate the position of the cylindrical lenses of the lenticular. These lenses are slanted with respect to the display by an angle $\arctan(\frac{1}{6})$. With this particular design, we can explain the construction of the individual views. For example, let us consider the sub-pixels with number five. These sub-pixels are all positioned equally with respect to the central axis of a cylindrical lens. This means that light from all sub-pixels with number five are collimated by the lenticular towards the same viewing direction. The same reasoning applies to the remaining sub-pixels. The result is an angular distribution of views imaged towards the viewer.

From the pixel layout depicted in Fig. 6.2 we can deduce that the total resolution loss is distributed equally in the horizontal and vertical direction. For example, we can show that the number of pixels that correspond to view one are equivalent in both the horizontal and vertical direction. As a result, the resolution loss factor observed by a viewer for the nine-views 3D display is only three, since the views are observed in the horizontal direction only (see also Fig. 1.6-(a)). In general, we can say that a multi-view 3D display with K views, has a total resolution loss factor of K. The resolution loss factor in the horizontal direction is $\sqrt{K}$, provided that the (sub-)pixel layout and the slant angle of the lenticular is adapted accordingly.

6.1.2 Uniformity and 3D performance

The use of a lenticular can introduce some imperfections in the performance of a multi-view 3D display. These imperfections can be described by two parameters: modulation depth and cross talk.

Modulation depth is defined a measure for the uniformity in the angular intensity distribution of a 3D display. One important reason that the angular intensity distribution can show a modulation (within a single view) is due to the presence of a black matrix in the pixel structure of a liquid crystal display. The black matrix is defined the area of the pixel structure in total that does not emit light. For the nine-views 3D display discussed, the black matrix of the pixel structure is 43% of the sub-pixel width in the horizontal direction and 31% of the sub-pixel height in the vertical direction. In a 3D display, the light from the pixel structure together with the black matrix is collimated by the lenticular towards a viewer. Hence, the collimated light originating from a 3D display is non-uniform and contains regions of higher and lower intensity. A viewer looking at the display will see each cylindrical lens from a slightly different angle and hence will see the black matrix only at certain positions on the screen. Effectively, a viewer perceives this effect as dark bands, as depicted in Fig. 6.3. This disturbing artifact is enhanced by the fact that the dark bands are moving across the screen when a viewer moves from side to side in front of a 3D display.

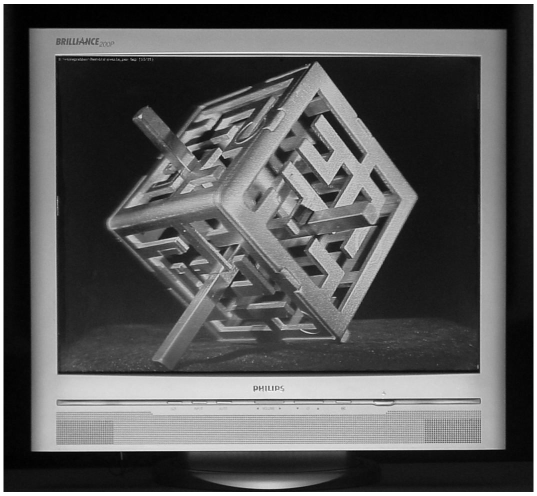

Figure 6.1: *Prototype (*20 *inch) of a nine-views lenticular-based autostereoscopic 3D display.*

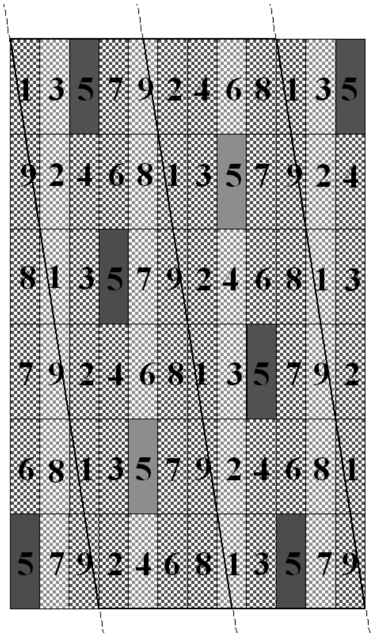

1	3	5	7	9	2	4	6	8	1	3	5
9	2	4	6	8	1	3	5	7	9	2	4
8	1	3	5	7	9	2	4	6	8	1	3
7	9	2	4	6	8	1	3	5	7	9	2
6	8	1	3	5	7	9	2	4	6	8	1
5	7	9	2	4	6	8	1	3	5	7	9

Figure 6.2: *Schematic sub-pixel layout of a nine-views lenticular-based 3D display. The diagonal lines indicate the position of the cylindrical lenses of the lenticular. The numbers depicted in the sub-pixels correspond to one of the nine views.*

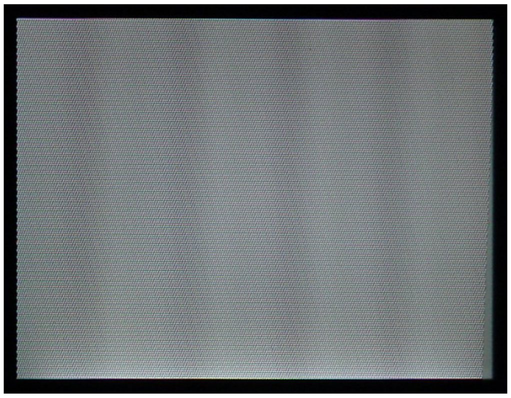

Figure 6.3: *When viewing a 3D display, a viewer can see dark bands.*

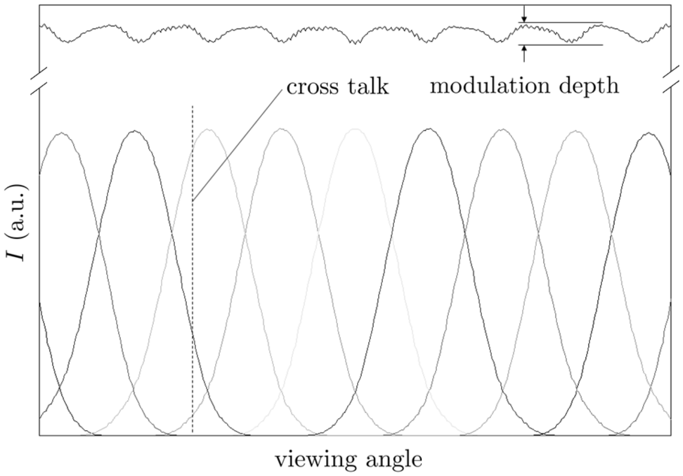

Figure 6.4: *Angular intensity distribution I for nine individual views. For the viewing angle indicated by the dashed line, three different views can be perceived by a viewer. A measure for the overlap between two neighboring views is defined cross talk. The modulation depth is a measure for the non-uniformity of the total angular intensity distribution.*

The 3D performance of a 3D display can be expressed in terms of a parameter called cross talk. Cross talk is a measure for the overlap between two neighboring views. Fig. 6.4 shows the angular intensity distribution of nine individual views. For one specific viewing angle, it is possible that a viewer can observe three views simultaneously. Moreover, one view is more visible than the others, since the intensities of the views for this viewing angle are all different. When the cross talk is too high, a viewer cannot perceive a three-dimensional image, since then multiple views can be seen by a single eye.

The cross talk of a multi-view 3D display also contributes to the non-uniformity in the angular intensity distribution. This can be seen in Fig. 6.4, where the modulation in the total angular intensity distribution can be described by two independent contributions: a small and large contribution. In this particular case, the large modulation is due to the cross talk between the views. This statement is verified by the fact that the intensity distribution has a maximum in between two neighboring views.

In general, for a good 3D performance, the cross talk of a 3D display should be minimized provided that the modulation depth is not too high.

The cross talk and modulation depth for a multi-view 3D display can be calculated with a ray-tracing program previously developed by Philips Research (cf. [108], p. 27). For example, we can calculate the cross talk and modulation depth for the optical system of the nine-views 3D display. Recall that the lenticular is slanted with respect to the pixel columns, as depicted in Fig. 6.2. Then a 3D display can either be investigated in a plane perpendicular to the pixel columns or perpendicular with respect to the orientation of the cylindrical lenses. Both approaches can be applied since effectively the optical properties merely depend on the relative orientation between pixel column and lenticular. In what follows, we will investigate the cross talk and modulation depth of the nine-views 3D display in the plane perpendicular to the orientation of the lenses.

According to Fig. 6.2, the width of a cylindrical lens in the horizontal direction is $4\frac{1}{2}$ sub-pixels corresponding to a width of $4\frac{1}{2} \cdot 0.085 = 0.383$ mm. Then the period of the lenticular is $0.383 \cdot \cos[\arctan(\frac{1}{6})] = 0.377$ mm. A cross section of the geometry of a nine-views lenticular-based 3D display is depicted in Fig. 6.5. For reasons that will become clear later in this chapter, the lenticular consists of a (polymer) lens plate that is filled with liquid crystal. The liquid crystal is homogeneously aligned in the direction parallel to the orientation of the cylindrical lenses. The refractive index of the lens plate is 1.550. The liquid crystal material is a TL213-type liquid crystal and has refractive indices $n_o = 1.527$ and $n_e = 1.766$. The light originating from the LCD is linearly polarized perpendicular to the plane of the drawing. Hence the effective index of refraction of the liquid crystal material is 1.766 which gives rise to a positive lens effect. The index of refraction of the glass material is 1.500.

Fig. 6.6 shows the cross talk and modulation depth as a function of the radius of curvature R_{cl} of the cylindrical lenses. The modulation depth is defined

$$M = \frac{\overline{SD(I_{tot})}}{\overline{I_{tot}}}, \tag{6.1}$$

with $\overline{SD(I_{tot})}$ the average Standard Deviation in the total angular intensity distribution and $\overline{I_{tot}}$ the average total angular intensity distribution. In addition, the cross talk is

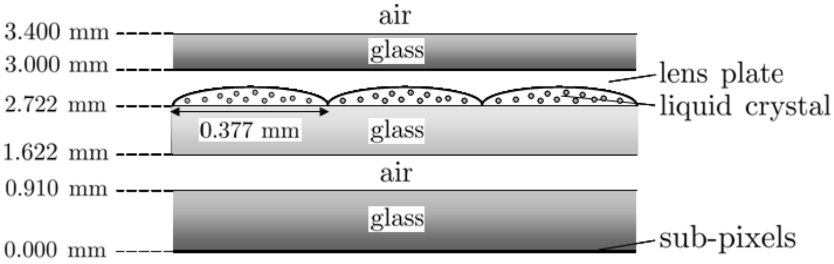

Figure 6.5: *Cross section of the geometry of a nine-views lenticular-based 3D display. For reasons that will become clear later, the lens plate is filled with liquid crystal.*

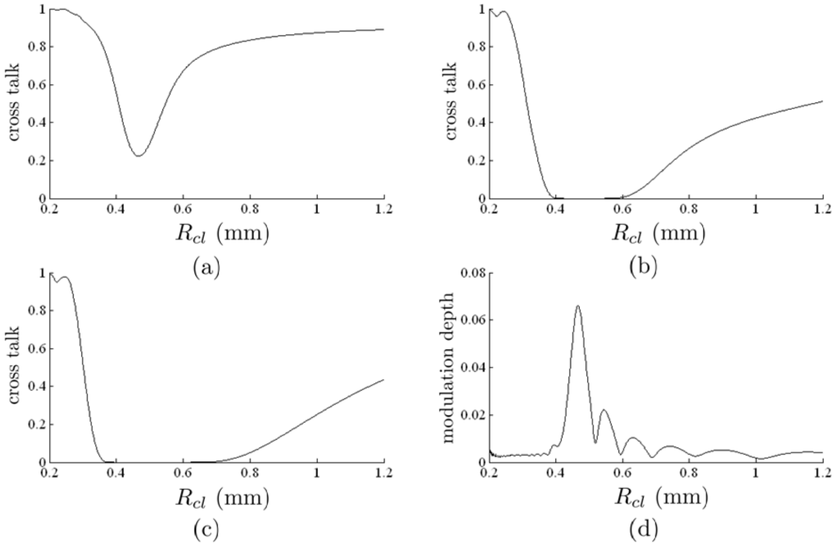

Figure 6.6: *Cross talk and modulation depth as a function of the radius of curvature R_{cl} of the cylindrical lenses. In (a), the cross talk between two adjacent views is calculated. In (b) and (c), the cross talk between two next neighboring views and two next next neighboring views are calculated, respectively. Figure (d) shows the modulation depth. Apparently, the modulation depth is high in a region where the cross talk is low.*

defined

$$O = \frac{\int F \times G}{\int F \times \int G}, \tag{6.2}$$

where F and G represent the angular intensity distribution of two individual views. Fig. 6.6-(a) shows the cross talk of two neighboring views, whereas Fig. 6.6-(b) shows the cross talk of two next neighboring views, for example, between view number 1 and 3. Fig. 6.6-(c) shows the cross talk between two next next neighboring views. The cross talk of two next neighboring views is much smaller than the cross talk between two adjacent views, as expected. According to Fig. 6.6-(d), the modulation depth is large in the region where the cross talk is low. In general, we are looking for a radius of curvature for which the balance between modulation depth and cross talk is acceptable. For example, $R_{cl} = 0.422$ mm results in a cross talk of 38.6% and a modulation depth of 1.3% and $R_{cl} = 0.519$ mm results in a cross talk of 37.3% and a modulation depth of 0.8%. When the non-uniformity is approximately below 1%, the dark bands on a 3D display are hardly noticeable for a viewer. These are typical values for the radius R_{cl}, the cross talk and modulation depth when considering the design of a nine-views lenticular-based 3D display.

By adjusting the radius of curvature of the cylindrical lenses, the focal strength is adjusted as well. For the values of R_{cl} discussed above, the lenses are slightly out of focus with the pixel plane. Then the angular intensity distribution of the collimated individual pixels is broadened, resulting in a reduced modulation depth in the total angular intensity distribution.

The uniformity of a multi-view lenticular-based 3D display can be further improved by using fractional views [109]. The pixel layout in Fig. 6.2 is designed in such a way that the sub-pixels corresponding to nine views are positioned below one cylindrical lens. A 3D display with fractional views has a pixel layout where the sub-pixels corresponding to the views are distributed over multiple lenses. With this layout, the individual contributions of the lenses to the non-uniformity of the display are averaged to a heavily reduced modulation depth.

We can conclude that the cross talk and modulation depth of a multi-view lenticular-based 3D display can be optimized to obtain a good 3D performance and a highly uniform intensity distribution. Two important ways to optimize the performance of a 3D display are the fine tuning of the radius of curvature of the cylindrical lenses in a lenticular and the use of fractional views.

6.2 Switchable 2D/3D displays based on liquid-crystal lenses

A display imaging a normal two-dimensional image with a lenticular placed in front of the display introduces a problem in the image quality. The lens effect created by the lenticular makes text difficult to read and fine textures will not be displayed correctly. This can be clearly seen in Fig. 6.7. The picture on the left shows the image of a liquid crystal display without lenticular and the picture on the right shows the same image with lenticular. As a result, a 3D display is not suitable for conventional monitor applications.

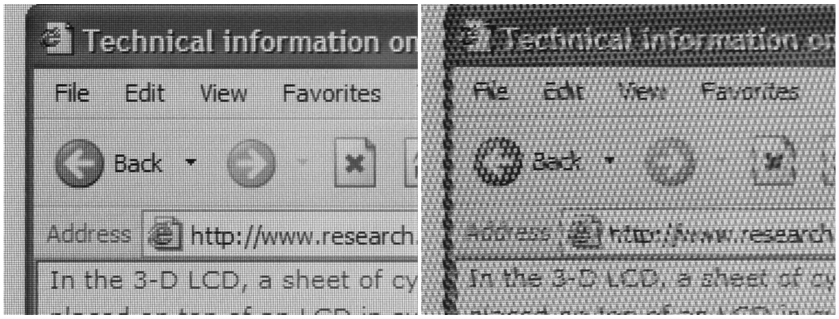

Figure 6.7: *The left picture shows the image of a liquid crystal display (LCD) without lenticular and the picture on the right shows the same image with a lenticular placed in front of the LCD. Clearly, the image quality on the right is not acceptable for conventional monitor applications.*

However, if the lens effect of the lenticular could somehow be switched on and off, a 3D display could be used for both 2D and 3D applications.

An elegant solution is the construction of a lenticular filled with liquid crystal that can be switched electronically between two optical modes: a 2D mode without lens effect (approximately) and a 3D mode with a lens effect. In 2004, Philips Research succeeded in manufacturing a switchable 2D/3D display based on LCDs equipped with liquid-crystal lenses [25][26].

Fig. 6.8 shows the cross section of a lenticular that contains liquid crystal. The lenticular consists of two glass plates that are equipped with a transparent conducting ITO (Indium Tin Oxide) layer. In between is a polymer lens plate that contains a negative lens structure, manufactured by means of replication techniques. The remaining space is filled with liquid crystal. On the lens plate and the lower glass plate a layer of poly-imide (PI) is applied. Rubbing of the PI surface is an effective way of achieving a preferred orientation of the PI molecules. The liquid-crystal molecules align themselves along the rubbing direction of the PI layer, occupying the lowest energy state.

Fig. 6.8-(a) shows the 3D mode of the switchable lenticular. No voltage is applied to the ITO electrodes. The rubbing direction of the lens plate and the lower glass plate are in the x-direction. As a result, the liquid crystal is aligned in the x-direction. Moreover, the linear polarization of the light coming from the LCD is also in the x-direction. As a result, the lens, although being optically birefringent, can be interpreted as an isotropic lens with index of refraction n_e. When $n_e > n^{lp}$, with n^{lp} the refractive index of the lens plate, the lenticular has a positive lens effect in the 3D mode.

Fig. 6.8-(b) shows the 2D mode of the switchable lenticular. A voltage is applied to the ITO electrodes creating an electric field in the z-direction. The director will align along the electric field lines, occupying the lowest possible energy state. If the applied voltage is high enough (100 V), it is a good approximation to assume a homogeneous vertical alignment [27]. As mentioned above, the light originating from the LCD is linearly polarized in the x-direction. Then the lenticular can be interpreted as an isotropic lens with index of refraction n_o. In the ideal case there is an index match between the

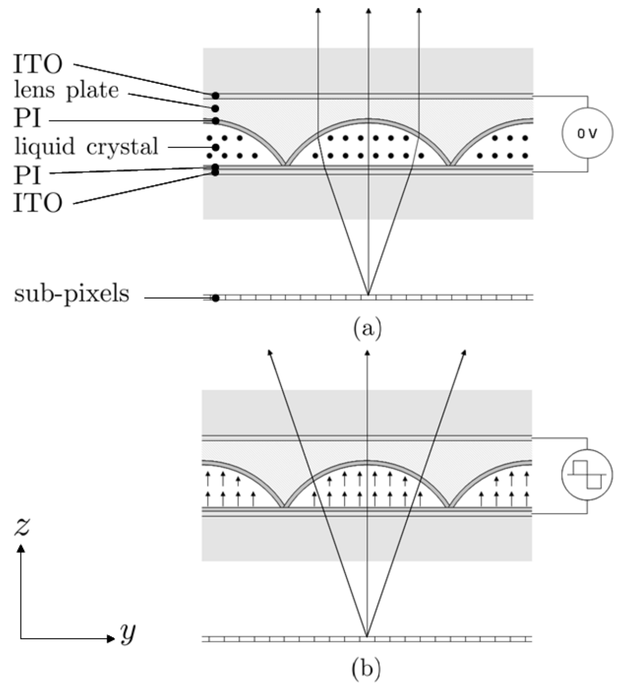

Figure 6.8: *Two optical modes of a switchable lenticular. The light originating from the underlying display is linearly polarized in the x-direction. In (a), no voltage is applied to the ITO electrodes. This optical state of the switchable lenticular is called the 3D mode. In the 3D mode, the lenticular has a (positive) lens effect. In (b), a voltage is applied to the ITO electrodes. Then the lenticular is in the 2D mode. When the ordinary refractive index of the liquid crystal and the refractive index of the lens plate match, the 2D mode has no lens effect.*

lens and the lens plate: $n_o = n^{lp}$. Then the light will not be refracted. Consequently, there is no lens effect.

With the possibility to switch a lenticular between a 2D mode and a 3D mode, a 3D display is capable to regain the full native 2D resolution of the underlying display. However, there are some issues concerning the image quality in the 2D mode of a switchable 2D/3D display. These issues will be discussed in the next section.

6.3 Residual lens effects in the 2D mode

When viewing a switchable 2D/3D display in the 2D mode at normal incidence, the image quality is acceptable for conventional monitor applications. However, at oblique viewing angles, there appears to be a residual lens effect. Apparently, the lens effect of the lenticular in the 2D mode depends on the viewing angle. For a certain viewing angle,

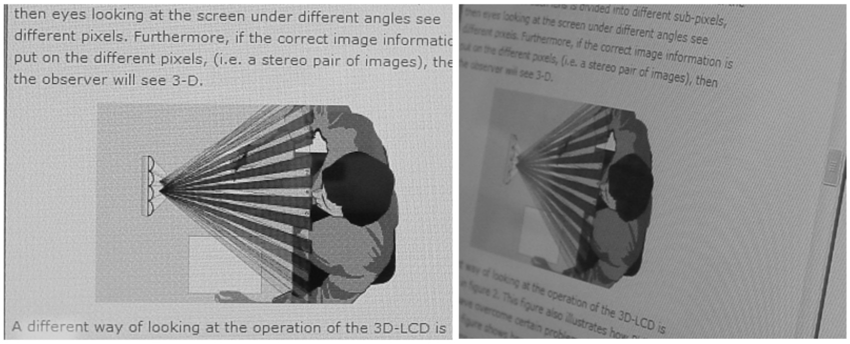

then eyes looking at the screen under different angles see
different pixels. Furthermore, if the correct image informatic
put on the different pixels, (i.e. a stereo pair of images), the
the observer will see 3-D.

A different way of looking at the operation of the 3D-LCD is

is divided into different sub-pixels,
then eyes looking at the screen under different angles see
different pixels. Furthermore, if the correct image information is
put on the different pixels, (i.e. a stereo pair of images), then
he observer will see 3-D.

way of looking at the operation of the 3D-LCD is
n figure 2. This figure also illustrates how
we overcome certain proble
figure shows h

Figure 6.9: *The left picture shows an image of a nine-views 20 inch lenticular-based switchable 2D/3D display in the 2D mode. The picture at the right shows the same image when viewing the display under an angle. Apparently, the image quality decreases due to residual lens effects.*

the focal point of the lenticular is exactly at the pixel structure of the underlying LCD. As a result, the black matrix is imaged at infinity, generating a large modulation depth at the viewing area. Fig. 6.9 shows the effect of residual lens effects when viewing the display at an oblique angle. In the 2D mode, it are these residual lens effects that we would like to get rid of.

The residual lens effects discussed are due to the anisotropic properties of the lenticular. In what follows, we will explain how the anisotropic properties of the 2D mode of a switchable lenticular can give rise to a residual lens effect.

In general, the polarization direction of the light coming from the underlying LCD is not parallel to the orientation of the lenticular. This is because the direction of the lenticular is adapted to the pixel layout (see Fig. 6.2) and not to the polarization direction of the LCD. Then the light propagating through the liquid crystal contains both ordinary and extraordinary polarization components. To overcome this problem, the following solution is applied to the lenticular.

The rubbing direction of the PI on the lower glass plate of the lenticular is matched with the polarization direction of the light coming from the LCD. At the same time, the rubbing direction of the lens plate is parallel to the long axis of the cylindrical lenses. As a result, in the 3D mode, the liquid crystal is twisted inside the lenticular. The linear polarization direction of the incident light is rotated along with the twist of the liquid-crystal molecules. This effect is called strong guiding or waveguiding (cf. [5], p. 122) and is not to be confused with optical activity. At any local position inside the liquid crystal, the polarization direction is parallel to the director. Consequently, the effective index of refraction of the lenticular in the 3D mode is the extraordinary index of refraction n_e. Then the lenticular has the same (positive) lens effect as defined in Fig. 6.8-(a).

For the 2D mode of the lenticular, the optical properties are now different from the situation in Fig. 6.8-(b). The director is still in the z-direction, but the polarization direction is now at an angle with the yz-plane other than 90° and not in the x-direction. Hence the light at oblique angles inside the liquid crystal of the lenticular in the 2D mode has both ordinary and extraordinary components. The effective index of refraction for extraordinary light depends on the direction of propagation and therefore the focal strength of the lenticular will depend on the viewing angle. As a result, the lenticular in the 2D mode has residual lens effects for light with extraordinary anisotropic properties.

Moreover, the refractive index of the lens plate is in general not equal to the ordinary index of refraction of the liquid crystal: $n_o \neq n^{lp}$. Hence, due to an index mismatch, there can also be a residual lens effect for light with ordinary polarization components.

In general, we conclude that in the 2D mode of a switchable lenticular the light has both ordinary and extraordinary polarization components. For these polarization components, there can be residual lens effects. Moreover, these residual lens effects depend on the viewing angle. In what follows, we will investigate the optical properties of the switchable lenticular in the 2D mode with the help of polarized ray tracing.

6.4 Polarized ray tracing of the 2D mode

In the 2D mode of a switchable lenticular, we assume that we are dealing with a homogeneous liquid-crystal alignment. Then for the anisotropic properties of the lenticular, we can apply the polarized ray-tracing method discussed in Chapter 3. For the ray tracing of the switchable lenses in the 2D mode, we have implemented the ray-tracing procedure for homogeneous anisotropic media into the ray-tracing program developed by Philips Research. The (optical) properties of the lenticular and the LCD are defined as discussed in Sections 6.1 and 6.2.

In the ray-tracing process, we trace rays for which the initial position is randomly defined, provided that the initial position is on one of the sub-pixels of the underlying LCD. Fig. 6.10 shows five thousand dots that indicate the initial positions of rays for five sub-pixels: one thousand dots per sub-pixel. Recall that the non-emitting part of a sub-pixel is defined 43% in the horizontal direction and 31% in the vertical direction. Hence the area without dots represents the black matrix of the LCD. The black lines indicate the boundaries of one cylindrical lens. The width of this cylindrical lens is 0.377 mm, and the geometry of the entire optical system is defined as shown in Fig. 6.5. The sub-pixels are slanted with respect to the orientation of the cylindrical lenses by an angle of $\arctan(\frac{1}{6})$. To verify the correct pixel layout, we can consider Fig. 6.2 and compare the sub-pixels numbered by 1, 3, 5, 7 and 9 and their position with respect to the lenticular with the layout depicted in Fig. 6.10.

In what follows, we calculate the angular intensity distribution of the switchable display in the 2D mode due to one sub-pixel only, namely the middle sub-pixel depicted in Fig. 6.10. This is because we like to investigate the qualitative properties of the switchable lenticular in the 2D mode rather than the total intensity distribution resulting from all the sub-pixels of the LCD. In the ray-tracing process, we trace two million rays originating from the central sub-pixel. All these rays are propagating in a plane parallel to the plane $x = 0$. Subsequently, the rays are projected to the yz-plane. The reason why we are allowed to do this is because the width of the image of the sub-pixel is approximately as wide as the (light-emitting) sub-pixel height (69% of 0.255 mm) and can be neglected when compared to a 20 inch 3D display. The ray-tracing process is applied to rays with a polarization in the x-direction (ordinary rays) and rays with a

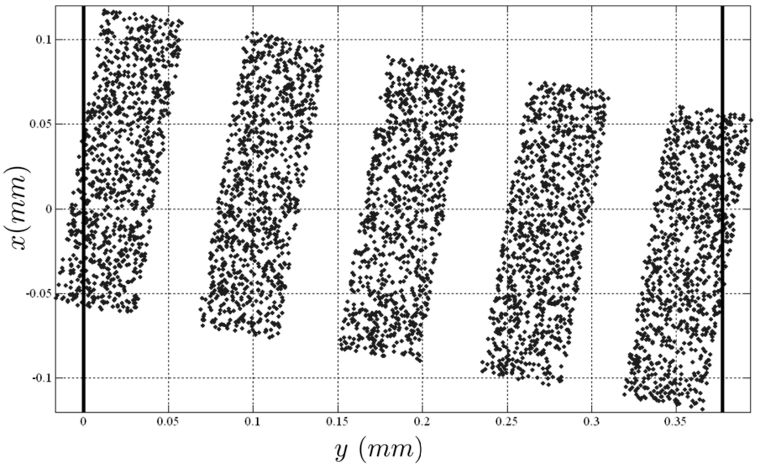

Figure 6.10: *Sub-pixel layout and dimensions of a nine-views lenticular-based 3D display. The dots indicate the initial positions of one thousand rays per sub-pixel. The area without dots represents the black matrix of the LCD. The black lines indicate the position of a cylindrical lens. The period of the lenticular is* 0.377 *mm.*

polarization direction in the yz-plane (extraordinary rays).

Fig. 6.11 shows the angular intensity distribution of the 2D mode for both ordinary and extraordinary rays [110]. The ordinary intensity distribution is represented by the dashed curve whereas the extraordinary intensity distribution is represented by the solid curve. For small viewing angles, the ordinary and extraordinary angular intensity distribution are identical. This is because for small viewing angles, the direction of propagation is approximately parallel to the liquid crystal director. Then the wave normal for both ordinary and extraordinary rays satisfies $|\mathbf{p}| \approx n_o$.

For the ordinary light rays there is always a residual negative lens effect, regardless of the viewing angle. This is because the index of refraction of the lens plate is 1.550 and the ordinary index of refraction of the liquid crystal is 1.527. This residual lens effect reveals itself through the peaks in the angular intensity distribution.

For extraordinary rays, the effective index of refraction depends on the viewing angle and lies between $n_o = 1.527$ and $n_e = 1.766$. Since $n_o < n^{lp} < n_e$, there is a negative lens effect for small viewing angles and a positive lens effect for large viewing angles. The transition from negative to positive lens effect occurs at approximately $\pm 30^\circ$. At this viewing angle, the peaks transform to ‘grooves’ in the extraordinary intensity distribution.

As mentioned before, there is a viewing angle for which the focal point of the lenticular is exactly on the pixel structure of the LCD. Then the black matrix is imaged at infinity, generating a large modulation depth in the angular intensity distribution. This observation is confirmed by the extraordinary angular intensity distribution of Fig. 6.11. The solid curve shows a large peak at approximately 60°. Alongside this intensity peak, there are intervals of zero intensity. The interval containing the zero and peak intensities

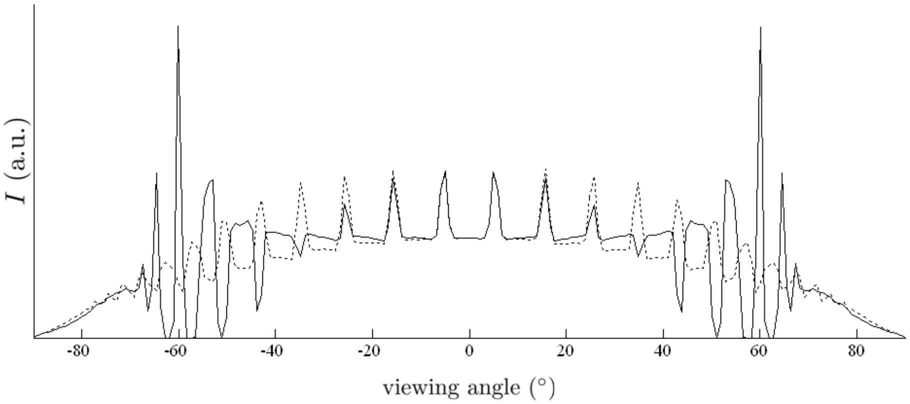

Figure 6.11: *Ordinary (dashed curve) and extraordinary (solid curve) angular intensity distribution I for a nine-views switchable 3D display in the 2D mode. The intensity distribution is the result of one light-emitting sub-pixel only.*

indicate the viewing angles for which the black matrix and the sub-pixels, respectively, are imaged at infinity.

We can conclude that the ray-tracing results for the nine-views switchable 3D display in the 2D mode confirm significant residual lens effects of the lenticular for large viewing angles. The residual lens effects are due to an index mismatch between the lens plate and the ordinary index of refraction of the liquid crystal and due to the anisotropic properties of the switchable lenticular. The simulations show a large modulation depth at a viewing angle of approximately 60°. In the next section, we propose a solution to get rid of these residual lens effects.

6.5 Anisotropic lens plates

The residual lens effects in the 2D mode of a switchable lenticular can decrease the image quality of the underlying LCD. Therefore, it is desired to minimize the difference in optical properties between the lens plate and the liquid crystal material. In the ideal case, the optical properties of the lens plate are equivalent to the optical properties of the liquid crystal in the 2D mode. However, when a different material is to be used for the lens plate, the 3D performance of the 3D display should not be affected. In what follows, we provide a solution to this problem and present ray-tracing simulations that support the proposed solution.

Let us consider a lens plate with homogeneous anisotropic properties. The optical axis of the lens plate is in the z-direction, see Fig. 6.12. The ordinary and extraordinary index of refraction of the lens plate are defined $n_o^{lp} = 1.527$ and $n_e^{lp} = 1.700$, respectively. Hence, there is an index match between the ordinary refractive index of the liquid crystal and the lens plate: $n_o = n_o^{lp}$. Otherwise, the optical properties of the 3D display are the

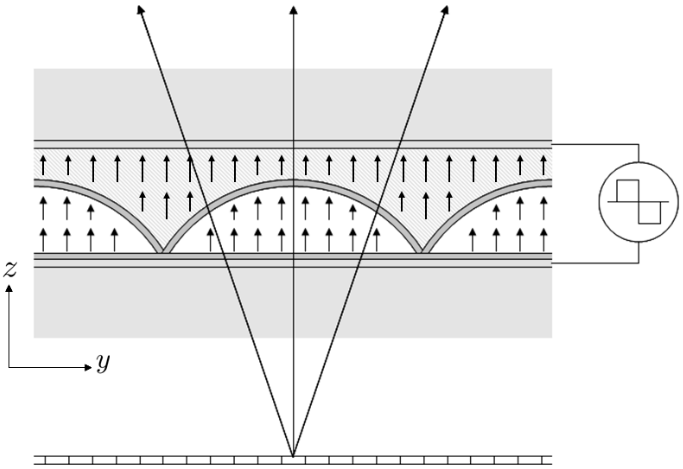

Figure 6.12: *2D mode of a switchable lenticular with an anisotropic lens plate. The anisotropic properties of the lens plate are homogeneous and the optical axis is parallel to the optical axis of the liquid crystal. In the ideal case, the optical properties of the lens plate and liquid crystal are the same and then there are no residual lens effects.*

same as discussed previously.

When we apply the same ray-tracing procedure as discussed in Section 6.4, we obtain the angular intensity distribution depicted in Fig. 6.13. For small viewing angles, there is an index match for both ordinary and extraordinary light rays since $n_o = n_o^{lp}$. As a result, the angular intensity distribution for ordinary and extraordinary light rays is the same when viewing the 3D display at normal incidence.

The angular intensity distribution for ordinary light (dashed curve) shows neither peaks nor grooves for all viewing angles: there are no residual lens effects for ordinary light rays. On the other hand, the extraordinary intensity distribution (solid curve) shows a positive lens effect for all viewing angles. This can be explained from the fact that the effective index of refraction of the liquid crystal always exceeds the effective index of refraction of the lens plate for all viewing angles since $n_e > n_e^{lp}$. This statement is confirmed by the fact that the extraordinary intensity distribution only contains grooves. In addition, the solid curve shows a large modulation depth for large viewing angles. This time, the black matrix is imaged at infinity for a viewing angle at approximately 70°. This is a larger viewing angle than the viewing angle of 60° for the 2D mode obtained in Section 6.4. This is because for all viewing angles, the lens strength of the lenticular with the anisotropic lens plate is weaker than the lens strength of the lenticular in Section 6.4. This can be explained by the fact that the difference between n_e and n_e^{lp} is smaller than the difference between n_e and n^{lp} (for large viewing angles). The results discussed above are a direct consequence of the anisotropic properties of the lenticular.

When $n_o = n_o^{lp}$ and $n_e = n_e^{lp}$, there is a perfect index match between the liquid crystal and the anisotropic lens plate. Then the extraordinary angular intensity distributions will transform to the dashed curve, resulting in a smooth intensity distribution. In that case, there are no residual lens effects for both ordinary and extraordinary light rays for

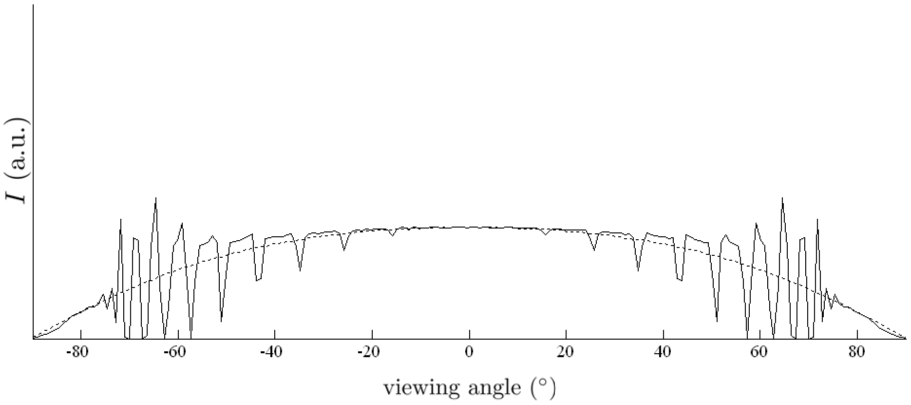

Figure 6.13: *Ordinary (dashed curve) and extraordinary (solid curve) angular intensity distribution I for a nine-views switchable 3D display with an anisotropic lens plate in the 2D mode. The refractive indices of the lens plate are* $n_o^{lp} = 1.527$ *and* $n_e^{lp} = 1.700$.

all viewing angles.

An important question is whether an anisotropic lens plate does affect the 3D performance of the 3D display. In the 3D mode, the effective index of refraction of the liquid crystal is n_e. The light that propagates through the anisotropic lens plate, where the optical axis is in the z-direction, is linearly polarized in the x-direction. Hence the light in the anisotropic lens plate is ordinary and then the lens plate can be considered a medium with refractive index n_o^{lp}. Since $n_e > n_o^{lp}$, there is a positive lens effect, similar to the situation depicted in Fig. 6.8-(a). In general, n_o^{lp} should be chosen carefully since the lens strength does affect the modulation depth and cross talk in the 3D mode of a 3D display (and so does the radius of curvature R_{cl}).

We can conclude that the residual lens effects of a multi-view switchable 3D display in the 2D mode can be reduced substantially when the lens plate is replaced by an anisotropic lens plate [111]. The optical properties of the anisotropic lens plate should resemble the optical properties of the liquid crystal. In the ideal case, the optical properties of the anisotropic lens plate match the optical properties of the liquid crystal. At the same time, the 3D performance of the 3D display is not necessarily affected provided that the refractive indices and the radius of curvature R_{cl} of the cylindrical lenses are chosen in such a way that the modulation depth and cross talk of the 3D mode are acceptable.

6.6 Conclusions

The use of a liquid-crystal-based switchable lenticular in an auto-stereoscopic 3D display enables to switch between a 2D mode and a 3D mode. In the 2D mode, a 3D display is capable to regain the full native 2D resolution of the underlying display. However, there are some issues concerning the image quality in the 2D mode of a switchable

2D/3D display. The light propagating in the 2D mode of a switchable lenticular has both ordinary and extraordinary polarization components. For these polarization components, there can be residual lens effects which depend on the viewing angle.

We have used our ray-tracing method for anisotropic media to simulate the optical properties of a switchable lenticular of a nine-views switchable 2D/3D display in the 2D mode. The ray-tracing results confirm significant residual lens effects of the lenticular for large viewing angles. The residual lens effects are due to an index mismatch between the lens plate and the ordinary index of refraction of the liquid crystal and due to the anisotropic properties of the switchable lenticular.

In view of these insights, we have proposed a solution to get rid of the residual lens effects. The improved lens design involved is filed in a patent application of which the author is co-inventor [111]. The residual lens effects of a multi-view switchable 2D/3D display in the 2D mode can be reduced substantially when the lens plate is optically anisotropic. Ideally, the optical properties of the anisotropic lens plate match the optical properties of the liquid crystal. In this case, the residual lens effects disappear completely. At the same time, the 3D performance of the 3D display is not affected by the anisotropic lens plate provided that the properties of the cylindrical lenses are chosen in such a way that the modulation depth and cross talk of the 3D mode are acceptable.

Chapter 7

Gradient-index lenses for 3D displays

In Chapter 6, we have discussed auto-stereoscopic multi-view switchable 2D/3D displays based on liquid-crystal lenticulars. In a switchable lenticular, the geometry of the lens plate is responsible for the lens effect in the 3D mode and the liquid crystal enables to switch between a 2D mode and a 3D mode. In a good approximation, the liquid-crystal material is homogeneously aligned in both the 2D and the 3D mode. It is also possible to apply an inhomogeneous configuration in which the liquid-crystal material itself is responsible for the desired lens effect in the 3D mode [112][113]. If this is the case, there is no need for a lens plate in the first place.

When a special gradient is induced inside a liquid-crystal layer, it is possible to obtain a lens effect. The type of lens associated with a gradient in the material properties is called a gradient-index lens. The advantage of gradient-index lenses based on liquid crystal can be found in size reduction and manufacturing costs when compared to switchable lenticulars. However, the optical design of an anisotropic gradient-index lens involves a much more complicated process. This is mainly because we are dealing with inhomogeneous anisotropic liquid-crystal material properties.

In contrast with isotropic lenses, the lens effect of a liquid-crystal gradient-index lens is difficult to model. Firstly, the inhomogeneous liquid-crystal profile of an electro-optical configuration needs to be simulated using software programs like LCD Master [114] or 2dimMOS [115]. Secondly, the optical properties of the obtained liquid-crystal profile need to be calculated. This means that the optical design of a liquid-crystal gradient-index lens involves a process characterized by trial and error.

Pioneering studies on liquid-crystal gradient-index (GRIN) lenses were done in the 1970s by Sato [116] and Berreman [117]. GRIN lenses based on liquid crystal appear in many forms and form a subject widely discussed in the literature [118]-[124]. There are many methods available to calculate the optical properties of liquid-crystal GRIN lenses. For example, in [123] a ray-tracing algorithm is introduced to trace ray paths in inhomogeneous uniaxially anisotropic media and applied to a liquid-crystal lens. This method is based on an eikonal equation which is solved using a so-called ray-bundle method to estimate the spatial derivatives of the wave normal $\mathbf{p}(\mathbf{r})$. Although the method appears to be accurate, the ray-tracing procedure involves a much more complicated process than the Hamiltonian principle. Another simple but effective method is the so-called Huygens method based on the Huygens principle [106], although it does not fully take into account the inhomogeneous properties of the liquid-crystal material. In addition to the Huygens method, other methods (including diffraction effects) that enable the modeling of liquid-crystal GRIN lenses have been discussed in the paper by Kraan et al. [106]. To account for the fact that ray paths are curved inside inhomogeneous media, Kraan uses a similar form of the Hamilton equations for inhomogeneous uniaxially anisotropic media as discussed in Chapter 4. However, the gradient-index lens discussed by Kraan is a different type of lens (beam-steering lens) than the one we are interested in. Moreover, light at normal incidence was considered, while the angular-dependent behavior of a gradient-index lens is important, in particular for auto-stereoscopic multi-view 3D displays.

In this chapter, after a short introduction, we will focus our attention to two different approaches to model liquid-crystal GRIN lenses: the Huygens principle and the Hamiltonian principle. We will discuss the differences and apply both principles to investigate the angular-dependent optical properties of an advanced liquid-crystal GRIN lens.

7.1 Liquid-crystal-based gradient-index lens

A liquid-crystal-based gradient-index lens is an optical system that enables a lens effect due to an imposed gradient in the director profile of a liquid-crystal layer. In what follows, we discuss the optical design of a liquid-crystal GRIN lens for application in multi-view auto-stereoscopic switchable 3D displays. In particular, we describe the optical design of a liquid-crystal GRIN sample of which the optical properties have been investigated in an experimental study at Philips Research by Herzog in 2008 [125].

7.1.1 Working principle

Fig. 7.1-(a) shows a schematic cross section of a liquid-crystal GRIN lens integrated in a 3D display. The optical configuration consists of two parallel transparent substrates with a liquid-crystal layer in between placed in front of a display. Recall that in a 3D display the distance between the lenses and the pixel plane of the display should be approximately the focal length of the lenses (see also Fig. 1.6-(b)). Both substrates are provided with a poly-imide (PI) layer (see also Section 6.2) to obtain the preferred alignment of the liquid-crystal material in the absence of an electric field: the y-direction. One of the substrates is provided with a transparent (ITO) electrode structure. This electrode structure consists of line electrodes with their long axis in the x-direction. When a voltage is applied to the electrodes, there is an electric field inside the liquid-crystal layer in the yz-plane. As a consequence, the liquid-crystal molecules align along the (curved) electric field lines, occupying the lowest possible energy state. As a result, there is a gradient in the liquid-crystal profile.

When a collimated beam of light (polarized in the yz-plane) enters the liquid-crystal layer, light rays are deflected from their original direction of propagation. The light rays are converging and we observe a positive lens effect. This is because we consider liquid crystal with positive anisotropy, i.e. $n_e > n_o$. To understand this, we consider the effective index of refraction corresponding to a light ray propagating in the vertical z-direction. The effective index of refraction is defined as the wave normal amplitude

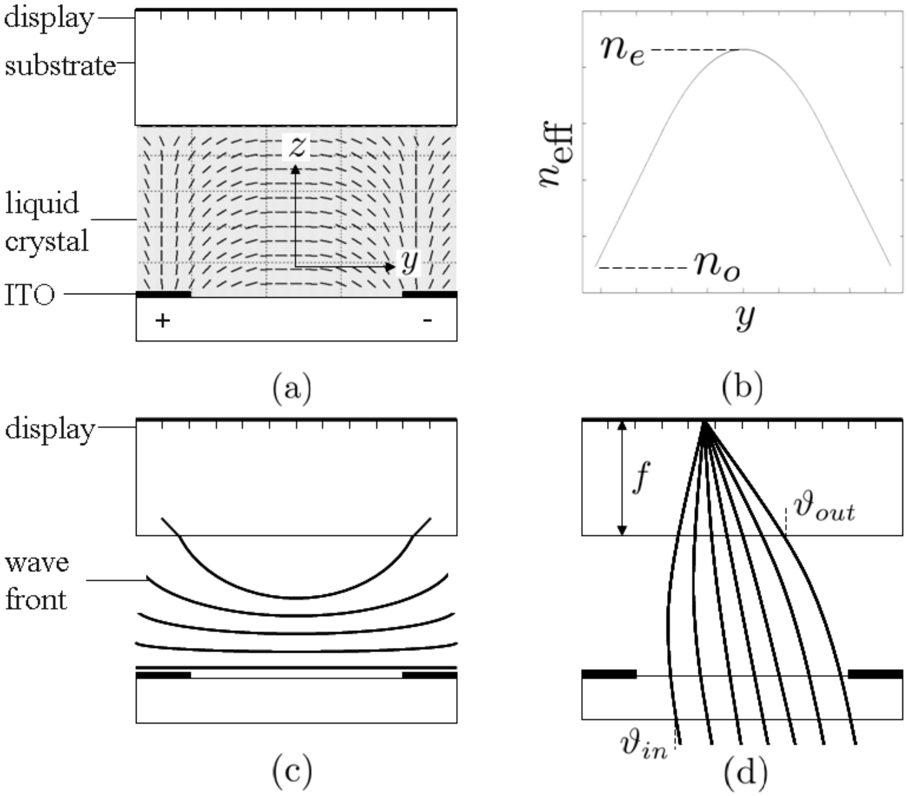

Figure 7.1: *Schematic working principle of a liquid-crystal GRIN lens integrated in a 3D display. Fig. (a) shows a liquid-crystal layer between two transparent substrates. The figure shows one unit cell, which is repeated in the y-direction (see also Fig. 1.6). An ITO electrode structure induces an electric field along which the liquid crystal molecules align (indicated by the black stripes). In (b), we show how the effective index of refraction typically varies with position between n_o and n_e, with $n_e > n_o$. The propagating wave front of an incident plane wave (polarized in the yz-plane) is depicted in (c). The ray paths that correspond to these wave fronts are depicted in (d). Ideally, the ray paths focus at a distance f in the pixel plane of the display.*

$|\mathbf{p}|$ of a light ray inside the liquid crystal (see also Eq. 2.33). Fig. 7.1-(b) shows how the effective index of refraction ($n_{\text{eff}} = |\mathbf{p}|$) typically varies with the position y. Since n_{eff} changes with position, an incident plane wave front is transformed to a curved wave front, as can be seen in Fig. 7.1-(c). Since $n_e > n_o$, the portion of the wave front in the center of the lens is delayed with respect to portions of the wave front further away from the center. As a result, the corresponding light rays are converging towards a focal point, as depicted in Fig. 7.1-(d). In the ideal case, all light rays intersect at the focal distance f in the pixel plane of the display and then the angle of refraction ϑ_{out} satisfies

$$\tan \vartheta_{out} = \frac{y}{f}, \tag{7.1}$$

where $y = 0$ is defined at the center of the lens. Note that if $\vartheta_{out} \ll 1$, it is a linear function of the position y. In multi-view 3D displays, the lenses are designed slightly out of focus with the pixel plane. This is desired to obtain a uniform angular light intensity distribution of the display, without compromising the 3D performance (see also [27], p. 3).

7.1.2 Experimental results of an advanced GRIN lens structure

At Philips Research, a number of attempts have been made to construct liquid-crystal GRIN lens structures. These structures consist of an array of GRIN lenses that should resemble the functionality of a switchable lenticular, discussed in Chapter 6. In what follows, we will discuss experimental results obtained by Herzog [125] of the optical properties of an advanced GRIN lens structure.

A schematic cross section of the liquid-crystal GRIN lens structure is depicted in Fig. 7.2. This advanced optical design (patented in [126]) of the GRIN lens structure is based on the results of previous studies on GRIN lenses (cf. [112], p. 852). One important issue investigated in these studies is the optimization of the active liquid-crystal region between two neighboring line electrodes that produces a desired lens effect. The problem is that in the neighborhood of the electrodes the liquid crystal does not align properly along the electric field lines. Hence the liquid crystal in these particular regions does not contribute to the desired lens action. In [127], it is concluded that the active region of a liquid-crystal GRIN lens is increased if 1) the distance between the electrodes and the liquid-crystal layer is increased by adding an extra dielectric transparent layer and 2) a grounded ITO electrode layer is added parallel to the electrode wire structure on top of a second dielectric transparent layer (see Fig. 7.2). These features improve the electric field distribution inside the liquid-crystal layer and thus the lens performance. In [128], it is investigated how the performance of such a GRIN lens depends on various parameters. There it is concluded that the relative dielectric permittivity of the two dielectric layers should be in the range of common glass ($3.0 \leq \varepsilon_r \leq 5.0$). In addition, for a lens pitch of 166 μm, the thickness of the two dielectric layers should be in the order of 50 μm. The width of the ITO electrodes is 10 μm.

With the advanced optical design discussed above, the active region of a GRIN lens is approximately 60% of the lens pitch (100 μm) with a focal distance f of approximately 1.8 mm in glass. Then the optical properties are close to the desired performance for application in an auto-stereoscopic 3D display.

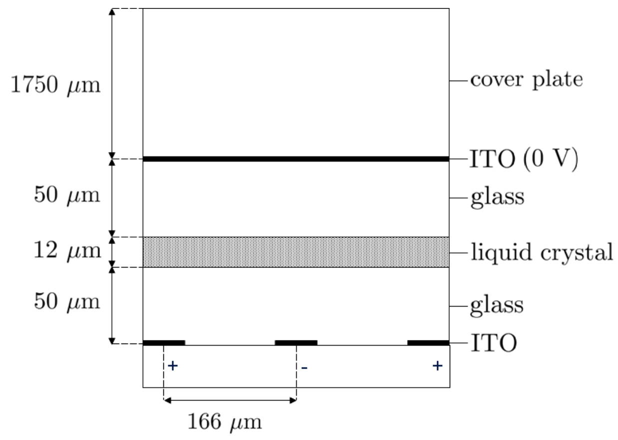

Figure 7.2: *Schematic cross section of the advanced design of a liquid-crystal GRIN lens structure. The liquid crystal that is used is TL213, for which* $n_o = 1.5271$ *and* $n_e = 1.7659$*.*

The angle of refraction ϑ_{out} (see Eq. 7.1) for light at normal incidence has been measured in an experiment [125]. These measurements will be discussed to show the working principle and provide a reference for the lens action for light at normal incidence.

In the experimental setup, a focussed laser beam scans the lens pitch of the liquid-crystal GRIN structure (y-direction in Fig. 7.1). Then the position and intensity of the refracted laser light is detected by a CCD camera. From these data the desired angle of refraction ϑ_{out} is calculated. The spot size in the waist of the focussed laser beam is (24 ± 5) μm while the pitch of the lens is 166 μm. This means that close to a line electrode between two GRIN lenses the laser beam can be split into two beams with different directions. Moreover, as discussed above, the liquid-crystal profile close to the line electrodes does not contribute to the desired lens effect. Then the light spot on the CCD camera is too wide to accurately determine the corresponding position. Because of these effects, the measurements near the line electrodes produce inaccurate results.

Fig. 7.3 shows the measured angle of refraction ϑ_{out} as a function of position for an angle of incidence $\vartheta_{in} = 0°$. In the experiment a voltage of approximately 100 V (AC) is applied to the electrodes. From the figure we can see that in the region where $|y| \leq 45$ μm, ϑ_{out} is approximately a linear function of y. This result is in agreement with Eq. 7.1, since $\vartheta_{out} \ll 1$ radians. The linearity is indicated by the dashed line for which $\vartheta_{out} = -0.85$ mrad/μm. In the region where $|y| > 45$ μm, ϑ_{out} is inaccurate because close to the electrodes light is scattered in various directions. For simplicity, the angle ϑ_{out} will be approximated by an average: $\vartheta_{out} = \pm 38.25$ mrad. Fig. 7.4 shows the experimental results for different angles of incidence ϑ_{in}. Here the difference $\vartheta_{out} - \vartheta_{in}$ (in air) is plotted against the position y for $\vartheta_{in} = 0°, ..., 40°$ with a step size of 10°. From the results we can conclude that the linearity of ϑ_{out} decreases with increasing ϑ_{in}.

In the following sections, we will investigate the angular dependence of the lens effect of the liquid-crystal GRIN structure discussed. We will do this with the help of our Hamiltonian method and the Huygens method. First, we will briefly discuss the Huygens

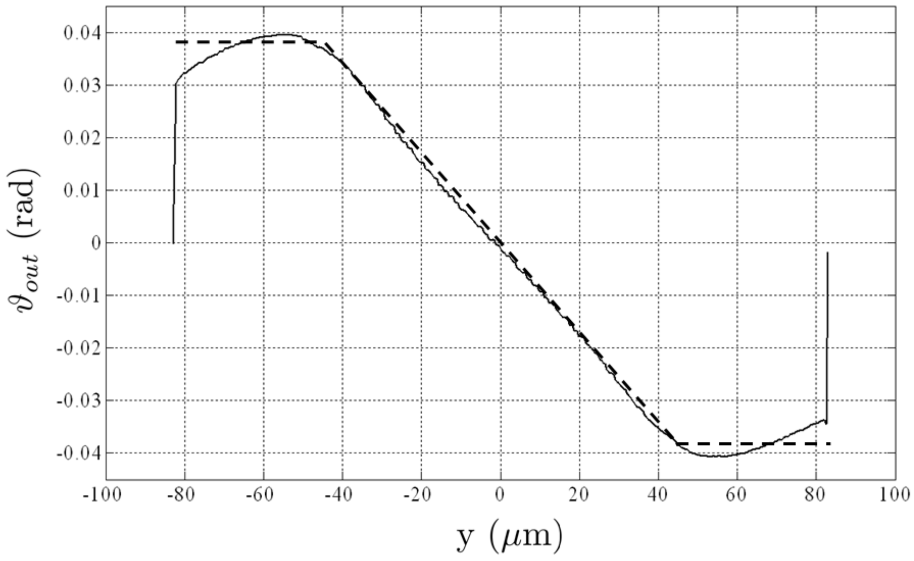

Figure 7.3: *Measured angle of refraction ϑ_{out} (in air) as a function of the position y (solid curve) [125] for the GRIN lens defined in Fig. 7.2. In the region where $|y| \leq 45$ μm, ϑ_{out} is approximately a linear function of y: $\vartheta_{out} = -0.85$ mrad/μm (dashed line). In the region where $|y| > 45$ μm, the measurement is inaccurate.*

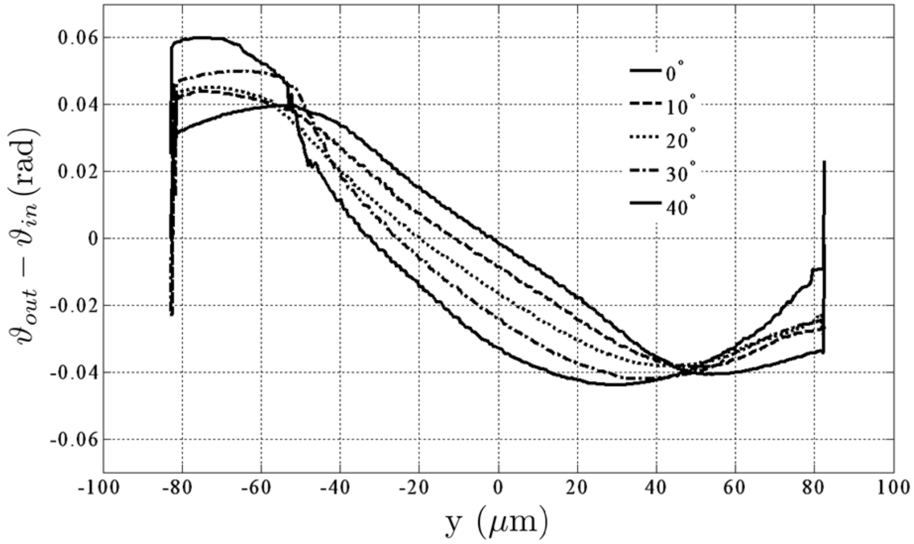

Figure 7.4: *Measured angle of refraction ϑ_{out} as a function of the position y [125] for different angles of incidence ϑ_{in} ($0° - 40°$).*

method.

7.2 Huygens method

The Huygens principle applied to an anisotropic liquid-crystal layer is derived in the paper of Kraan [106]. In this section, we will discuss the basic principle of the Huygens method and refer to the paper of Kraan for further details.

In the Huygens method the propagation of light rays in the lateral y-direction is assumed negligible inside the liquid-crystal layer. This means that effectively, the thickness of the liquid-crystal layer is assumed to approach zero. This is a fair approximation, since the ratio between the thickness and lens pitch of the liquid-crystal layer is ($\frac{12}{166} =$) 0.072. The method attributes an effective index of refraction to each position y of the liquid-crystal layer. This is achieved by averaging the effective index of refraction over the vertical z-direction for each position y. As a result, the Huygens method does not take into account the inhomogeneous material properties in the vertical z-direction. In principle, the Huygens method discussed is an extension of Snell's law for application to liquid-crystal GRIN lenses.

For each position $\mathbf{r}$ inside the liquid crystal there is a director $\hat{\mathbf{d}}$. We assume that

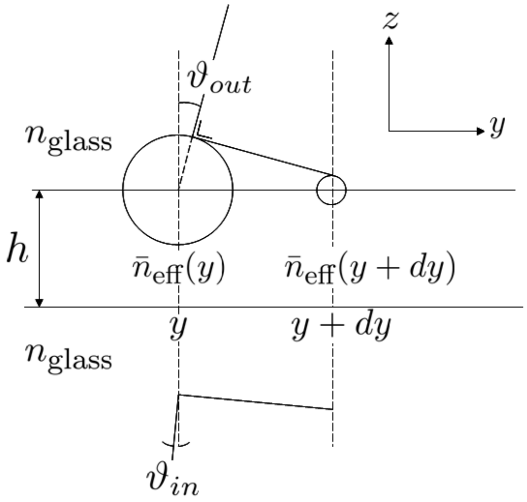

Figure 7.5: *Evolution of the Huygens spheres in a liquid-crystal layer. The Huygens spheres evolve differently at the positions* y *and* $y + dy$ *since at these positions the averaged effective index of refraction* $\bar{n}_{eff}(y)$ *varies over the distance* dy*. The figure shows an incident plane wave with an angle of incidence* ϑ_{in} *and the corresponding emerging plane wave with an angle of refraction* ϑ_{out}*. Here it is assumed that* $\bar{n}_{eff}(y) < \bar{n}_{eff}(y + dy)$*. The liquid-crystal layer has a thickness* h *and the index of refraction of the two glass substrates is indicated by* n_{glass}*.*

the director, the direction of propagation and the polarization of the light are all parallel to the yz-plane. Hence light rays inside the liquid crystal are extraordinary. For extraordinary rays, we have (see Eq. 4.13)

$$\mathcal{H}_e(\mathbf{r},\mathbf{p}) = n_o^2|\mathbf{p}|^2 + (n_e^2 - n_o^2)(\mathbf{p},\hat{\mathbf{d}})^2 - n_e^2 n_o^2 = 0. \tag{7.2}$$

With $\mathbf{p} = |\mathbf{p}|\hat{\mathbf{p}} = n_{\text{eff}}\hat{\mathbf{p}}$, Eq. 7.2 gives the effective index of refraction

$$n_{\text{eff}}(\mathbf{r},\mathbf{p}) = \sqrt{\frac{n_o^2 n_e^2}{n_o^2\Big[1-(\hat{\mathbf{p}},\hat{\mathbf{d}})^2\Big] + n_e^2(\hat{\mathbf{p}},\hat{\mathbf{d}})^2}}. \tag{7.3}$$

Note that $\hat{\mathbf{p}}$ denotes the direction of propagation inside the liquid-crystal layer. For a fixed position y and direction of propagation $\hat{\mathbf{p}}$, we can average the effective index of refraction over the vertical direction z. Then the average effective index of refraction is given by

$$\bar{n}_{\text{eff}}(y) = \frac{1}{h}\int_0^h n_{\text{eff}}(\mathbf{r})dz, \tag{7.4}$$

where h is the thickness of the liquid-crystal layer.

Fig. 7.5 shows the geometry of a liquid-crystal GRIN lens with the relevant parameters indicated. We consider an incident plane wave with an angle of incidence ϑ_{in}. The figure shows the Huygens spheres at position y and $y + dy$. The Huygens spheres evolve differently at these two positions since the effective index of refraction varies over the distance dy. The emerging plane wave has an angle of refraction ϑ_{out}. A temporal analysis of the evolution of the Huygens spheres leads to a relation between the angles ϑ_{in} and ϑ_{out} (cf. [106], p. 3469, Eq. 8):

$$n_{\text{glass}}\sin\vartheta_{out} = n_{\text{glass}}\sin\vartheta_{in} + h\frac{d\bar{n}_{\text{eff}}(y)}{dy}, \tag{7.5}$$

where n_{glass} is the index of refraction of the top and bottom glass substrates. The second term in Eq. 7.5 is an additional term to Snell's law in the presence of a gradient in the index of refraction in the y-direction. In addition, we remark that $\bar{n}_{\text{eff}}(y)$ is a function of ϑ_{in}. This is because the direction of propagation $\hat{\mathbf{p}}$ inside the liquid crystal is a function of the angle of incidence ϑ_{in}. With the help of the theory at anisotropic interfaces discussed in Chapter 3, we calculate $\hat{\mathbf{p}}$ inside the liquid crystal and solve Eq. 7.5.

In the following sections, we will use the Huygens method to investigate the angular-dependent properties of the GRIN lens structure presented in Fig. 7.2.

7.3 Ray-tracing simulations based on experimental results

In this section, we first calculate the liquid-crystal director profile from the measurement presented in Fig. 7.3. We will do this with the help of the (reverse) Huygens method discussed in the previous section. Then the resulting director profile is inhomogeneous in the lateral y-direction, but not in the vertical z-direction. Secondly, using the calculated director profile, we will investigate the angular-dependent optical properties of the GRIN lens structure. We will do this with the help of the Huygens method and the Hamiltonian method. At first sight it may seem strange to use the Hamiltonian method with a profile obtained with the Huygens method. However, the Hamiltonian method allows light rays to be curved inside the liquid-crystal layer whereas the Huygens method does not take into account this effect.

7.3.1 Averaged director profile

With the help of the Huygens method and the experimental result depicted in Fig. 7.3, we will calculate the liquid-crystal director profile of the GRIN lens structure.

First, we calculate $\bar{n}_{\text{eff}}(y)$ using Eq. 7.5 and $\vartheta_{out}(y)$. Note that $\vartheta_{out}(y)$ in Fig. 7.3 applies in air. Then, with the help of Snell's law, Eq. 7.5 is rewritten for light at normal incidence ($\vartheta_{in} = 0$) in air ($n_{\text{air}} = 1$):

$$\frac{\sin \vartheta_{out}(y)}{h} = \frac{d\bar{n}_{\text{eff}}(y)}{dy}. \tag{7.6}$$

The averaged effective index of refraction $\bar{n}_{\text{eff}}(y)$ can be obtained by integrating Eq. 7.6 on both sides. Then, for $\vartheta_{in} = 0^\circ$, we have

$$\bar{n}_{\text{eff}}(y) = \frac{1}{h} \int_0^y \sin \vartheta_{out}(y) dy + n_e, \tag{7.7}$$

since at the position $y = 0$ we have $\bar{n}_{\text{eff}}(0) = n_e$ (see Fig. 7.1-(b)). Fig. 7.6 shows $\bar{n}_{\text{eff}}(y)$ in case $\vartheta_{out}(y)$ is given by the dashed line in Fig. 7.3: $\vartheta_{out}(y) = -0.85$ mrad/μm for $|y| \leq 45$ μm and $\vartheta_{out}(y) = \pm 38.25$ mrad for $|y| > 45$ μm. In addition, we consider a liquid crystal with indices $n_o = 1.5271$ and $n_e = 1.7659$.

Secondly, we calculate the averaged director $\hat{\mathbf{d}}(y)$ using Eq. 7.3. Since we consider light at normal incidence, $\hat{\mathbf{p}}$ is in the vertical z-direction (both in air and in the liquid-crystal layer). Then the inner product between $\hat{\mathbf{p}}$ and $\hat{\mathbf{d}}(y)$ satisfies

$$(\hat{\mathbf{p}}, \hat{\mathbf{d}}) = (\hat{\mathbf{z}}, \hat{\mathbf{d}}) = \cos \alpha, \tag{7.8}$$

with α the angle between the vertical direction $\hat{\mathbf{z}}$ and the director $\hat{\mathbf{d}}$. Hence for a certain value of $\bar{n}_{\text{eff}}$ we calculate the corresponding value for α satisfying Eq. 7.3. The calculation is performed numerically with the Newton-Raphson method (cf. [90], p. 355). The result is depicted in Fig. 7.7. Then the averaged director is given by $\hat{\mathbf{d}}(y) = (0, \sin \alpha, \cos \alpha)$.

With the help of the calculated averaged director profile we will investigate the angular-dependent optical properties of the liquid-crystal GRIN lens structure. In what follows, we will present the results obtained from the Huygens method and the Hamiltonian method.

7.3.2 Huygens method

With the help of the director profile $\hat{\mathbf{d}}(y)$ (see Fig. 7.7) and the Huygens method we calculate the angle $\vartheta_{out}(y)$ in air for an incident plane wave at different angles of incidence

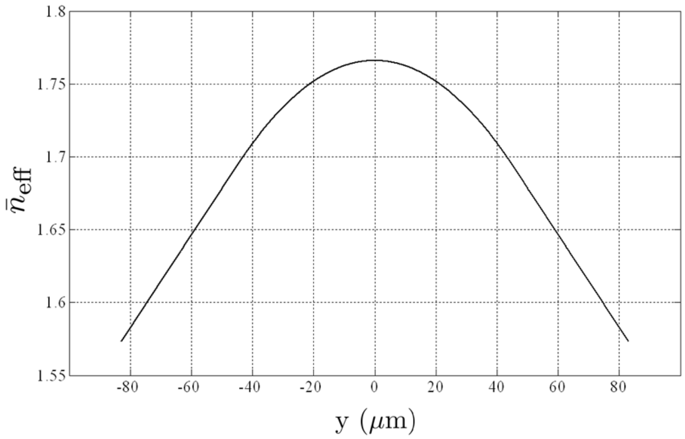

Figure 7.6: *$\bar{n}_{eff}$ as a function of y calculated from the experimentally obtained result depicted in Fig. 7.3. At the position $y = 0$, the value for $\bar{n}_{eff}$ is the extraordinary index of refraction $n_e = 1.7659$.*

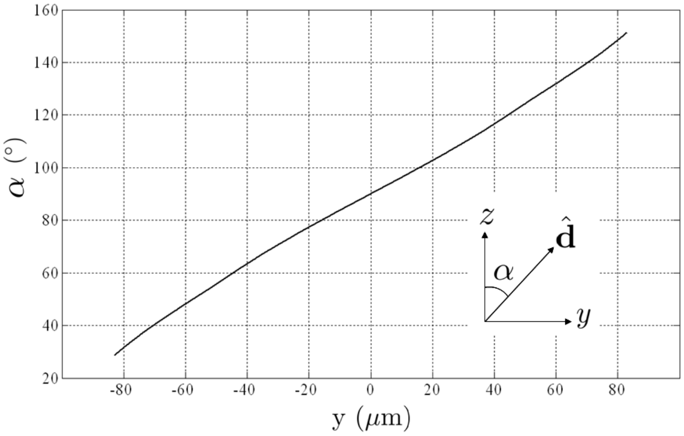

Figure 7.7: *The angle α (in degrees) between the director $\hat{\boldsymbol{d}}$ and the vertical z-direction (i.e. the direction of propagation $\hat{\boldsymbol{p}}$) as a function of the position y. Then the director is given by $\hat{\boldsymbol{d}} = (0, \sin\alpha, \cos\alpha)$.*

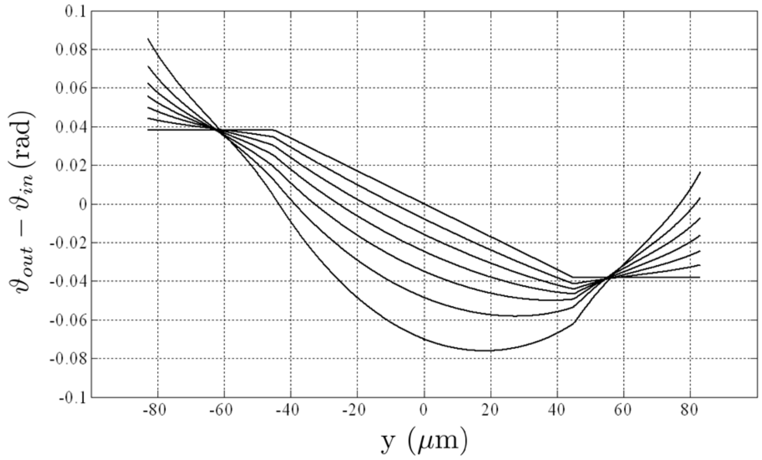

Figure 7.8: *Ray-tracing results of the Huygens method for $\vartheta_{out}(y) - \vartheta_{in}$ for $\vartheta_{in} = 0°, ..., 60°$ with steps of 10°. Clearly, the linearity of ϑ_{out} decreases with increasing ϑ_{in}. The angle ϑ_{out} for $\vartheta_{in} = 0°$ perfectly matches the dashed line depicted in Fig. 7.3. This is because the averaged director $\hat{\mathbf{d}}(y)$ used in the calculations is derived from the Huygens method itself.*

ϑ_{in}. Note that the position y indicates the position where the light enters the liquid-crystal layer between two line electrodes. Fig. 7.8 shows the result for $\vartheta_{in} = 0°, ..., 60°$ with steps of 10°. As expected, the simulated and experimental $\vartheta_{out}(y)$ (see Fig. 7.3) match perfectly for $\vartheta_{in} = 0°$. This is because the averaged director $\hat{\mathbf{d}}(y)$ used in the simulations is derived from the Huygens method itself. With ϑ_{in} increasing, the linearity of the angle ϑ_{out} with the lateral position y gets weaker. As a result, the incident light is not focussed properly for high values of ϑ_{in}. In other words, the light emerging from the pixel plane of a 3D display is not perfectly collimated as depicted in Fig. 7.1-(d). The imperfections discussed are not a problem for the performance of a 3D display. Recall that in Subsection 6.1.2, we concluded that a lenticular slightly out of focus with the pixel plane results in a reduced modulation depth in the total angular intensity distribution of a 3D display. However, the pixel plane should not be too much out of focus, since then the 3D performance will decrease. In Fig. 7.8 the lens effect appears to be acceptable for viewing angles less than 30°. This will be discussed further later in this chapter.

7.4 Ray-tracing simulations based on a simulated director profile

In the following exercise, we simulate the director profile to calculate the angular-dependent optical properties of the GRIN lens structure depicted in Fig. 7.2. The resulting numerical director profile is inhomogeneous in both the y- and z-direction. In this section, we investigate the angular-dependent behavior of the liquid-crystal lens structure in three different cases: 1) the Hamiltonian method applied to the simulated director profile $\hat{\mathbf{d}}(y,z)$, 2) the Hamiltonian method applied to the averaged simulated director profile $\hat{\mathbf{d}}(y)$ and 3) the Huygens method applied to the averaged director profile.

7.4.1 Simulated director profile

With the definition of the optical configuration depicted in Fig. 7.2, we simulate the director profile of the liquid-crystal layer between two line electrodes. The director profile is calculated numerically with the optical analysis software program LCD Master [114]. It was found that in the simulations a voltage of 200 V is needed to produce the same lens action as obtained in the experiment at 100 V. The explanation for this is subject to debate. However, the main result here is that we now have a director profile for the specific optical configuration of Fig. 7.2 that produces a lens action verified by experimental results. The properties of the liquid crystal (TL213 mixture) that we use in the simulations are listed in Table 1.1. There the values of the elastic constants K_{11}, K_{33}, the static dielectric permittivity $\triangle\varepsilon = \varepsilon_{||} - \varepsilon_{\perp}$ and the viscosity γ of the liquid crystal are indicated. These material properties are important input parameters for the LCD Master program.

The resulting numerical director profile is depicted in Fig. 7.9. Clearly, the director profile is inhomogeneous in both the y- and z-direction. Note that the director is forced to align in the y-direction along the interfaces at $z = 0$ μm and $z = 12$ μm.

When we average the director profile over the thickness h of the liquid-crystal layer, we obtain the profile depicted in Fig. 7.10. Note that the profile is inhomogeneous in the

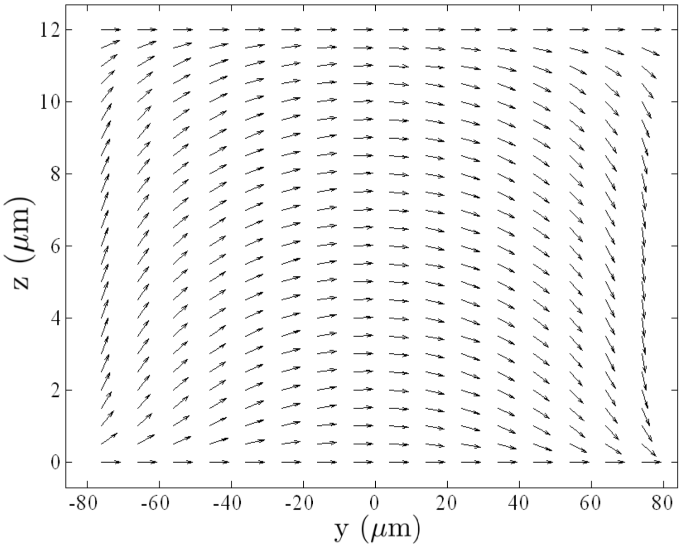

Figure 7.9: *Simulated director profile $\hat{\mathbf{d}}(y,z)$ of the liquid-crystal layer defined by the optical configuration depicted in Fig. 7.2. The result is obtained using the simulation program LCD Master [114]. The director profile is inhomogeneous in both the y- and z-direction and can be used for the Hamiltonian method.*

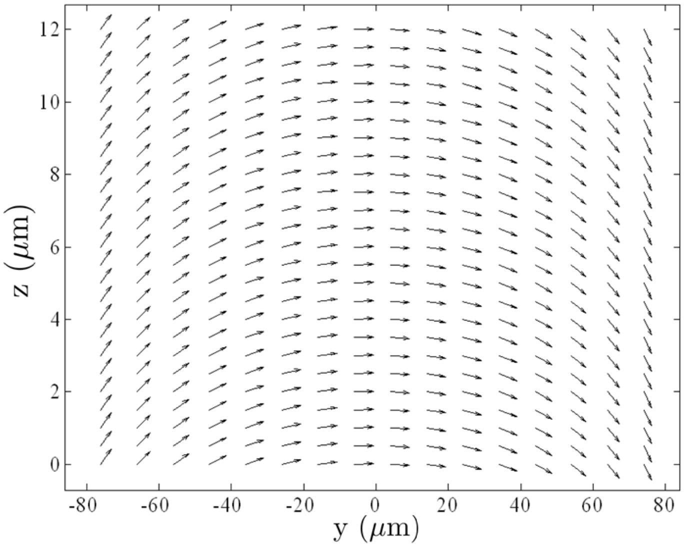

Figure 7.10: *The resulting director profile $\hat{\mathbf{d}}(y)$ when averaged over the vertical z-direction. This director profile can be used for both the Hamiltonian method and the Huygens method.*

y-direction but not in the z-direction. Moreover, the director is no longer aligned along the interfaces.

7.4.2 Huygens method

In this subsection, we apply the Huygens method to the numerical director profile $\hat{\mathbf{d}}(y)$ depicted in Fig. 7.10. First, we calculate the refracted wave normal in the liquid-crystal layer with the help of the classical theory on anisotropic interfaces discussed in Chapter 3. Then we use Eqs. 7.3 and 7.4 to calculate $\bar{n}_{\text{eff}}(y)$ and apply Eq. 7.5. Fig. 7.11 shows the result for $\vartheta_{out}(y)$ for $\vartheta_{in} = 0°, ..., 50°$, with steps of 10°. The figure also shows the experimental result for $\vartheta_{in} = 0°$ (dashed line). From the figure we conclude that for $\vartheta_{in} = 0°$ in the region of $y = 0$ μm the slope (angular change per unit length) of $\vartheta_{out}(y)$ is slightly smaller than the slope of the experimentally obtained result. In other words, the Huygens method predicts a lens effect that is slightly weaker than the lens effect obtained from the experimental characterization.

Finally, Fig. 7.12 shows the averaged effective index of refraction for various values of ϑ_{in}. Clearly, the maximum of the parabolic curve is shifted to the left for increasing angle of incidence. In fact, the position y in Fig. 7.12 for which $\bar{n}_{\text{eff}} = n_e$ is equivalent to the position y in Fig. 7.11 for which $\vartheta_{out} - \vartheta_{in} = 0$.

7.4.3 Hamiltonian method applied to averaged director profile

Next, we apply the Hamiltonian method to the averaged director profile $\hat{\mathbf{d}}(y)$ depicted in Fig. 7.10. After we have calculated the refracted wave normal at the liquid-crystal interface at $z = 0$ μm we use the Hamiltonian method to calculate the curved ray path

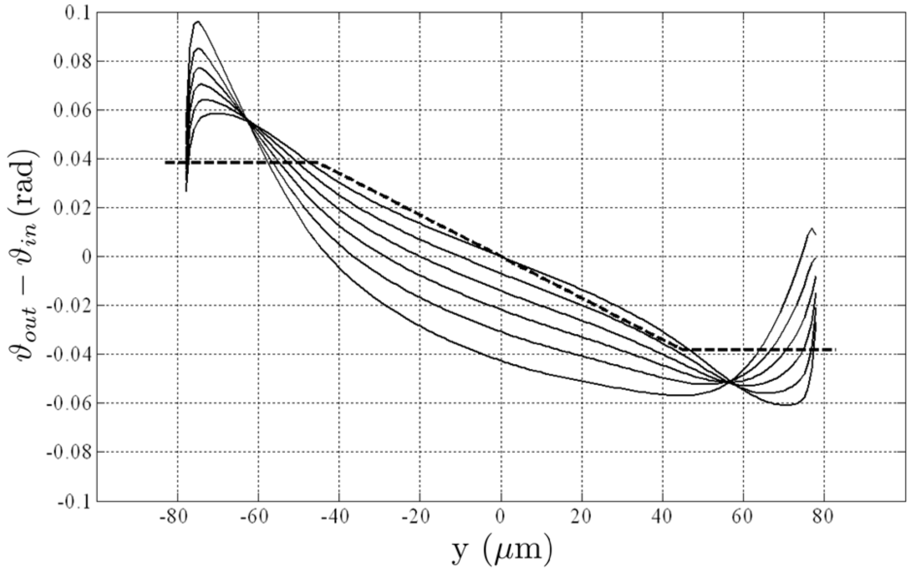

Figure 7.11: *Ray-tracing results of the Huygens method for* $\vartheta_{in} = 0°, ..., 50°$, *with steps of* $10°$. *The experimental result for* $\vartheta_{in} = 0°$ *is also depicted (dashed line).*

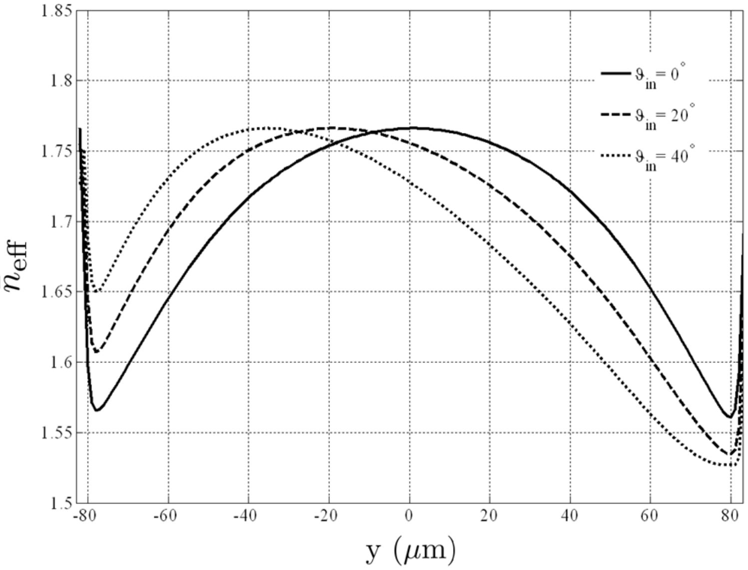

Figure 7.12: *The averaged effective index of refraction* $\bar{n}_{eff}$ *as a function of* y *for* $\vartheta_{in} = 0°$, $20°$ *and* $40°$.

inside the liquid-crystal layer. At $z = 12$ μm we calculate the refracted wave normal and the angle ϑ_{out}. The ray-tracing results are depicted in Fig. 7.13 (solid curves) together with the results of Fig. 7.11 (dashed curves). Similar to the conclusion for the Huygens method, the lens effect according to the Hamiltonian method for $\vartheta_{in} = 0°$ is slightly weaker than the lens effect observed in the experimental characterization. In addition, the Huygens method and the Hamiltonian method produce similar results. However, we can see that the difference between the Hamiltonian method and the Huygens method increases if ϑ_{in} increases. The reason for this can be explained as follows.

When we apply the Hamiltonian method the ray paths of light rays are curved inside the liquid-crystal layer. Then the deflection of light rays from their original direction of propagation (at $z = 0$ μm) increases with the optical path length inside the liquid-crystal layer and thus with the angle ϑ_{in}. This can be seen when we compare the curves in Fig. 7.13 for $\vartheta_{in} = 50°$. These curves have a minimum at approximately $y = 40$ μm. The minimum for the Hamiltonian method is -0.06 radians whereas the minimum for the Huygens method has a value above -0.06 radians. Moreover, the slope of the curve obtained from the Hamiltonian method exceeds the slope of the curve obtained from the Huygens method. Then we conclude that the Hamiltonian method predicts a stronger lens action than the Huygens method.

For an angle of incidence ϑ_{in} smaller than approximately 40°, we conclude that the results of both the Huygens and the Hamiltonian method are equivalent. In addition to this, we conclude that the Hamiltonian method predicts a stronger lens effect than the Huygens method for angles of incidence approximately above 40°.

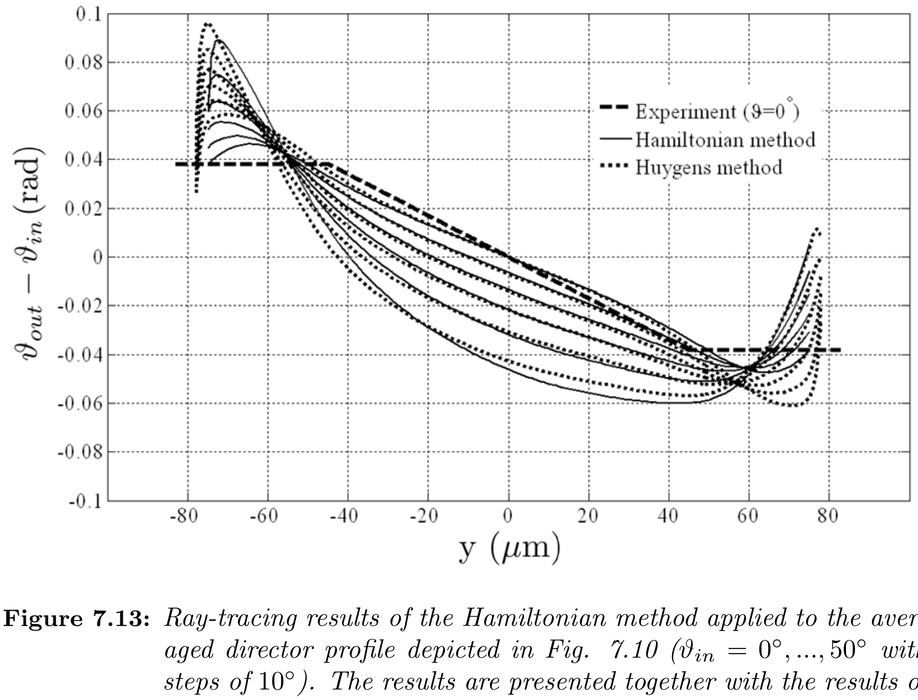

Figure 7.13: *Ray-tracing results of the Hamiltonian method applied to the averaged director profile depicted in Fig. 7.10 ($\vartheta_{in} = 0°, ..., 50°$ with steps of $10°$). The results are presented together with the results of Fig. 7.11. The experimental result for $\vartheta_{in} = 0°$ is also depicted.*

7.4.4 Hamiltonian method

Finally, we apply the Hamiltonian method to the simulated director profile $\hat{\mathbf{d}}(y, z)$ depicted in Fig. 7.9. This time, for $\vartheta_{in} = 0°$, there is a good match between the experimental lens effect and the lens effect according to the ray-tracing results, as can be seen in Fig. 7.14. For approximately $\vartheta_{in} \geq 10°$, the lens effects depicted in Fig. 7.14 (solid curves) are significantly stronger than the lens effects obtained from the averaged director profile (dashed curves). This is due to the fact that the numerical director profile in Fig. 7.9 is inhomogeneous in both the y- and z-direction. This means that locally, the gradients in the index profile of the liquid crystal are higher and ray paths of light rays are converged more strongly.

Fig. 7.15 and Fig. 7.16 show $\vartheta_{out}(y)$ according to the experimental characterization, the Huygens method and the Hamiltonian method for $\vartheta_{in} = 20°$ and for $\vartheta_{in} = 40°$, respectively. From the results we can conclude that both the Huygens and the Hamiltonian method are in good agreement with the experimental results in the region where $|y| \leq 45$ μm (active region of the GRIN lens). However, the discrepancies between model and experiment increase with the distance from the center ($y = 0$ μm). The discrepancies between model and experiment also increase with increasing ϑ_{in}. This is because for high values of ϑ_{in}, light rays entering the active region of the liquid-crystal GRIN lens ($|y| \leq 45$ μm) can penetrate the region close to the line electrodes ($|y| > 45$ μm). These observations can be explained in view of two effects. On the one hand, the properties

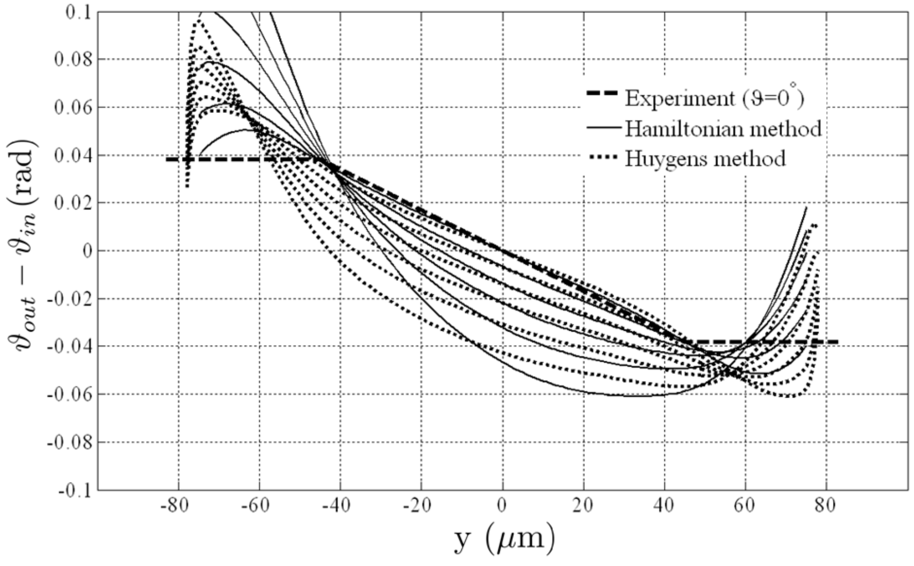

Figure 7.14: *Ray-tracing results of the Hamiltonian method applied to the director profile* $\hat{\mathbf{d}}(y, z)$ *depicted in Fig. 7.9 for* $\vartheta_{in} = 0°, ..., 50°$, *with steps of* 10°. *The results are presented together with the results of Fig. 7.11. The experimental result for* $\vartheta_{in} = 0°$ *is also depicted. Clearly, the Hamiltonian method predicts a stronger lens effect than the Huygens method does.*

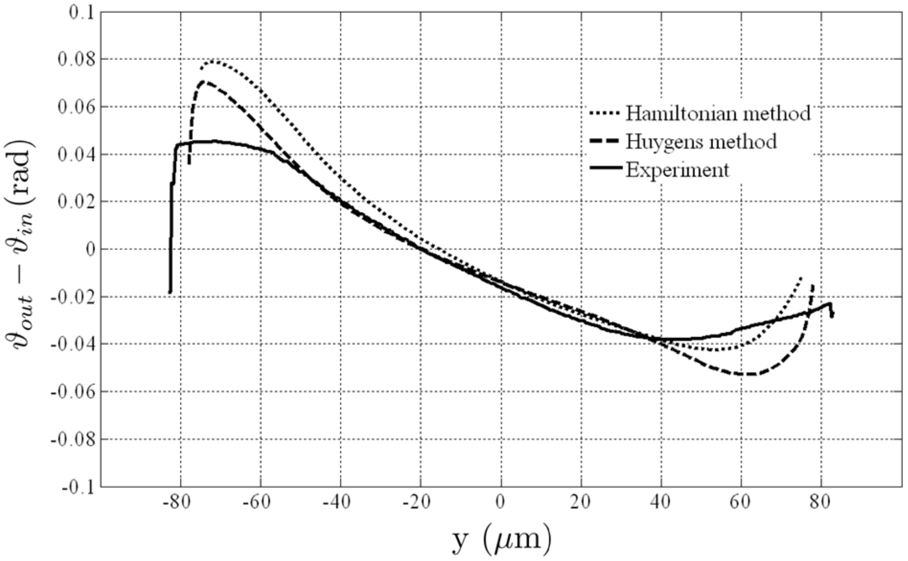

Figure 7.15: *Ray-tracing results of the Hamiltonian method and the Huygens method compared with the experimental result for* $\vartheta_{in} = 20°$.

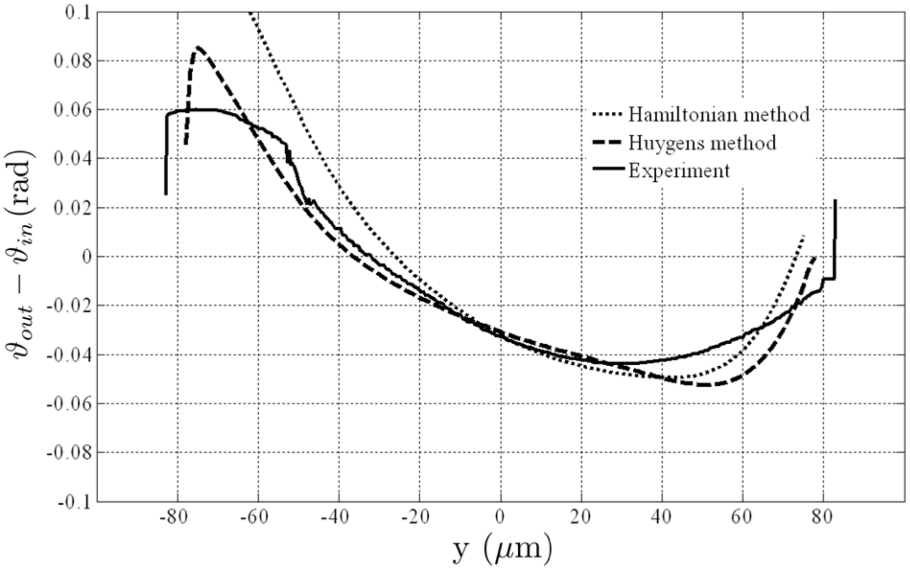

Figure 7.16: *Ray-tracing results of the Hamiltonian method and the Huygens method compared with the experimental result for* $\vartheta_{in} = 40°$.

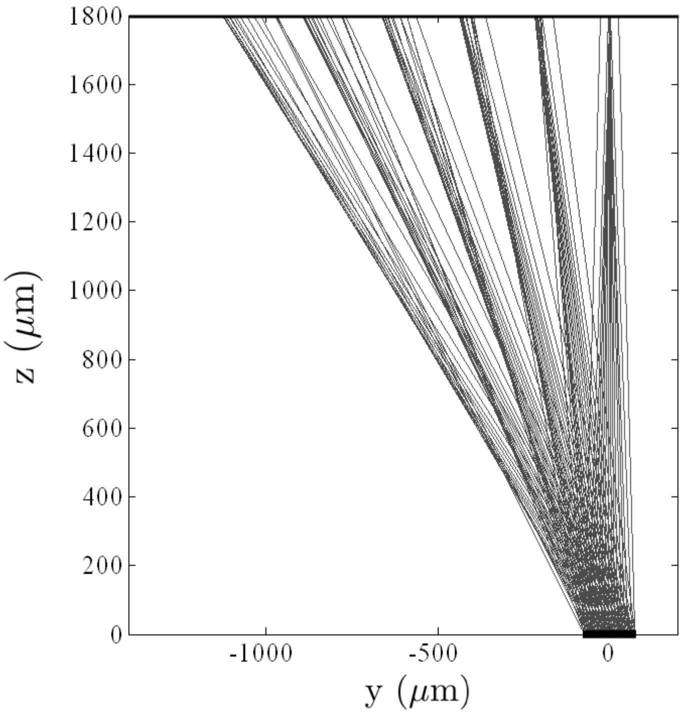

Figure 7.17: *Ray paths of light rays in the glass cover plate for incident plane waves with* $\vartheta_{in} = 0°, ..., 50°$ *with steps of* 10°. *The light rays for* $\vartheta_{in} = 0°$ *are focussed in the pixel plane at approximately* $z = 1800$ μ*m. The lens action for oblique angles of incidence decreases with* ϑ_{in}.

of the liquid crystal in the region of the line electrodes are not well defined, since the liquid crystal does not align properly along the electric field lines. On the other hand, the simulated director profile is prone to errors close to the line electrodes, since there the electric field changes rapidly per unit length.

From these conclusions, we cannot immediately deduce how the lens performance affects the 3D performance. Therefore, we have simulated the optical performance of the GRIN lens structure near the pixel plane of the underlying display. Fig. 7.17 shows the ray paths of light rays for $\vartheta_{in} = 0°, ..., 50°$ with steps of 10°. The light rays for $\vartheta_{in} = 0°$ are deflected by the GRIN lens structure and are focussed in the pixel plane at approximately $z = 1800$ μm. Clearly, the lens action of the GRIN structure decreases with the angle of incidence: for angles of approximately 30° and higher, the lens action has become significantly weaker. At 30°, the light spot at the pixel plane is 100 μm while the width of a sub-pixel is typically 85 μm. Then the light spot at the pixel plane partially covers two neighboring pixels of the LCD. As a result, for viewing angles larger than approximately 30° two neighboring views (see Figs. 6.2 and 6.4) have too much overlap compromising the 3D performance.

7.5 Conclusions

We have investigated the angular-dependent optical behavior of an advanced liquid-crystal GRIN lens structure. This GRIN lens structure is designed for application in switchable auto-stereoscopic 3D displays and is equivalent to the functionality of a switchable lenticular.

To model the angular-dependent optical properties of the liquid-crystal GRIN lens structure, we have used the Huygens method and the Hamiltonian method. The Huygens method is based on a one-dimensional approach: it only accounts for the inhomogeneous material properties in the lateral direction. This is a fair approximation since the ratio between the thickness and the lens pitch is much smaller than one (0.07). In contrast with the Huygens method, the Hamiltonian method takes into account the full inhomogeneous material properties of the liquid crystal.

The director profile of the advanced liquid-crystal GRIN lens structure has been calculated in two different ways. First, an averaged director profile has been calculated from experimental results. This has been done by applying the Huygens method in reverse. Then the resulting director profile only varies in the lateral direction of the GRIN lens. Secondly, a numerical director profile has been simulated using LCD Master. This numerical director profile is inhomogeneous in two dimensions. The resulting director profiles have been used for the Huygens method and the Hamiltonian method.

Based on the ray-tracing simulations, we conclude that the lens action of the advanced GRIN lens structure decreases with increasing angle of incidence. Moreover, the difference between the Hamiltonian method and the Huygens method increases with increasing angle of incidence. This is due to the fact that in contrast with the Huygens method, the Hamiltonian method incorporates the fact that ray paths of light rays are curved.

The regions near the line electrodes have relatively high gradients in the liquid-crystal profile. In theory, these regions are appropriate to visualize the difference between the Huygens method and the Hamiltonian method. However, in these specific regions, the liquid crystal inside the GRIN lens structure does not align properly along the electric field lines. As a result, the liquid crystal does not contribute to the desired lens action above the line electrodes. In addition, the simulated numerical director profile is prone to errors in the region of the line electrodes. Therefore both the theoretical and experimental results are inaccurate in these regions.

From the ray-tracing results we conclude that for small viewing angles in a 3D display, the light from the pixel plane is well collimated by the GRIN lens structure. For large viewing angles of approximately 30° and higher, the lens action of the GRIN lens is significantly weaker. At 30°, the light spot at the pixel plane is 100 μm while the width of a sub-pixel is 85 μm. Then the 3D performance of the 3D display is compromised. This is an important reason why the application of liquid-crystal GRIN lenses in 3D displays for high viewing angles is still in need of further research. The general approach and advanced ray-optics analysis procedures presented in this paper form a useful tool in the search for improvements and enable a better understanding of the liquid-crystal technology discussed.

Chapter 8

Ray-tracing simulations and applications of liquid-crystal beam control devices

The Hamilton equations and the ray-tracing procedure discussed in Chapters 3 and 4 enables the calculation of the optical properties of arbitrary inhomogeneous anisotropic optical systems within the geometrical-optics approach. The ray-tracing formulas discussed can be applied once the properties of a medium are defined. In addition, the ray-tracing procedure is easy to implement in a ray-tracing simulation program. In this chapter, we will show that the Hamiltonian ray-tracing procedure implemented in a simulation program facilitates the modeling of complex inhomogeneous anisotropic optical systems. We focus our attention to inhomogeneous liquid-crystal configurations and discuss two intriguing examples.

First we will introduce simulations of a novel liquid-crystal-based electro-optical device that enables a switching effect due to a back reflection phenomenon [129]. In the simulations, we exploit the optical properties of a liquid-crystal configuration with a special director profile. We will show that a two-dimensional gradient in a liquid-crystal layer applied between two parallel mirrors enables a back reflection phenomenon in which the direction of propagation of extraordinary light rays is reversed. Possible applications of the liquid-crystal device can be found in, but are not restricted to, optical communication systems and lighting applications.

In a second example, we investigate the optical properties of the liquid-crystal-based optical element discussed in Subsection 1.2 [130]. This optical system enables the active control of guiding and local extraction of polarized light.

8.1 Ray-tracing simulations of a liquid-crystal-based electro-optical switch

In this section we present ray-tracing simulations of a novel electro-optical device that enables a back reflection phenomenon. The back reflection phenomenon occurs when light is propagating in a special liquid-crystal configuration. This liquid-crystal configuration is a Freéderickz alignment. As an introduction, we discuss the Freéderickz alignment and its mathematical formulation. Then we apply the Freéderickz alignment in a special liquid-crystal configuration and present ray-tracing simulations that support the working principle of the electro-optical device.

8.1.1 The Freéderickz alignment

Liquid crystal can be controlled by external electric (and magnetic) fields. Interactions between boundaries and liquid crystal also have a large controlling effect. Often, the influence of the boundaries opposes the response to an electric field. The result is a threshold phenomenon called the Freédericksz transition. Fig. 8.1 shows a Freédericksz alignment of a liquid crystal layer in which the local optical axis (indicated by the director $\hat{\mathbf{d}}$) is rotated towards the direction of an external electric field E. In what follows, we discuss Freédericksz alignments that show bend and splay deformations and no twist deformations of liquid crystal.

We consider a simple geometry, defined by two parallel glass plates, separated by a distance h, as depicted in Fig. 8.1. The space between the glass plates is filled with liquid crystal. In the xz-plane, the director $\hat{\mathbf{d}}$ tends to align itself in the x-direction parallel to the glass surfaces. When an electric field is applied in the z-direction the liquid crystal deforms. In order to describe the deformation profile of the liquid crystal, we will minimize the total free energy of the liquid crystal in the presence of an electric field.

The free elastic energy density of a deformed nematic liquid crystal in terms of the director $\hat{\mathbf{d}}$ is given by (cf. [9], p. 32)

$$U = \frac{1}{2}K_{11}(\nabla \cdot \hat{\mathbf{d}})^2 + \frac{1}{2}K_{22}(\hat{\mathbf{d}} \cdot \nabla \times \hat{\mathbf{d}})^2 + \frac{1}{2}K_{33}(\hat{\mathbf{d}} \times \nabla \times \hat{\mathbf{d}})^2, \tag{8.1}$$

where K_{11}, K_{22} and K_{33} are elastic constants with which the associated splay, twist and bend deformation energies scale. The total free energy per unit volume between the glass plates is the sum of the deformation (no twist: $K_{22} = 0$) and electric field energies and is given by (cf. [9], p. 200)

$$U = \frac{1}{2}K_{11}(\nabla \cdot \hat{\mathbf{d}})^2 + \frac{1}{2}K_{33}(\hat{\mathbf{d}} \times \nabla \times \hat{\mathbf{d}})^2 - \frac{1}{2}\varepsilon_0 \triangle\varepsilon(\mathbf{E} \cdot \hat{\mathbf{d}})^2, \tag{8.2}$$

where $\triangle\varepsilon = \varepsilon_{||} - \varepsilon_{\perp}$ and $\mathbf{E}$ represents the electric field vector. It is convenient to write the director vector components as $\hat{d}_x = \cos\theta(z)$, $\hat{d}_y = 0$ and $\hat{d}_z = \sin\theta(z)$, where $\theta(z)$ is the angle between $\hat{\mathbf{d}}$ and the x-axis. As a result, we can write Eq. 8.2 as

$$U = \frac{1}{2}\left[K_{11}\cos^2\theta(z) + K_{33}\sin^2\theta(z)\right]\left(\frac{d\theta}{dz}\right)^2 - \frac{1}{2}\varepsilon_0 \triangle\varepsilon E^2 \sin^2\theta(z). \tag{8.3}$$

By minimizing the free energy, it can be shown that $\theta(z)$ must satisfy the Euler equation (cf. [9], p. 205). Substituting Eq. 8.3 into the Euler equation yields

$$K_{11}\frac{d^2\theta}{dz^2} + \varepsilon_0 \triangle\varepsilon E^2 \sin\theta(z)\cos\theta(z) = 0, \tag{8.4}$$

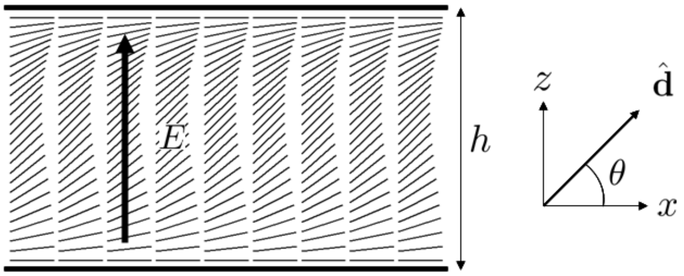

Figure 8.1: *Freédericksz alignment of a liquid-crystal layer applied between two parallel glass plates separated by a distance h. The director* $\hat{\mathbf{d}}$ *is rotated by an angle* θ *towards the direction of the electric field E. The deformation of the liquid crystal is opposed by the influence of the boundaries.*

where we only have considered the dominant terms (assuming $\frac{K_{33}-K_{11}}{K_{11}} \ll 1$ and $(\frac{d\theta}{dz})^2 \ll 1$). Apparently, the distortion of the liquid crystal is dominated by splay deformation. By introducing the variable $\zeta = \frac{z}{h}$, Eq. 8.4 can be written as

$$\xi_h^2 \left(\frac{d^2\theta}{d\zeta^2} \right) + \sin\theta(\zeta)\cos\theta(\zeta) = 0, \tag{8.5}$$

where ξ_h is given by

$$\xi_h^2 = \frac{K_{11}}{h^2 \varepsilon_0 \triangle\varepsilon E^2}. \tag{8.6}$$

Eq. 8.5 is a differential equation of which the solution $\theta(\zeta)$ can be expressed in terms of an elliptic integral. Since $\frac{d\theta}{d\zeta} = 0$ at $\zeta = \frac{1}{2}$, we define θ_m as the maximum value of θ at $\zeta = \frac{1}{2}$. In addition, $\mathcal{K}(m)$, with elliptic modulus $m = \sin^2\theta_m$, is the complete elliptic integral of the first kind. With these definitions, we can calculate the electric field E between the glass plates. From this, we calculate the potential difference, simply by multiplying E with the distance h. Then the potential difference across the liquid crystal layer is given by (cf. [9], p. 207)

$$V = 2\mathcal{K}(m)\sqrt{\frac{K_{11}}{\varepsilon_0 \Delta\varepsilon}}. \tag{8.7}$$

Also, there is a threshold voltage below which the liquid crystal remains undistorted, given by

$$V_{th} = \pi\sqrt{\frac{K_{11}}{\varepsilon_0 \Delta\varepsilon}}. \tag{8.8}$$

Above this threshold voltage, the director starts to rotate from its undistorted configuration towards the direction of the electric field. Note that the threshold voltage is independent of the distance h.

Finally, we use the incomplete elliptic integral of the first kind to calculate $\theta(\zeta)$: the Freédericksz alignment. This integral is defined as $F(\phi, m) = 2\mathcal{K}(m)\zeta$, where ϕ is the

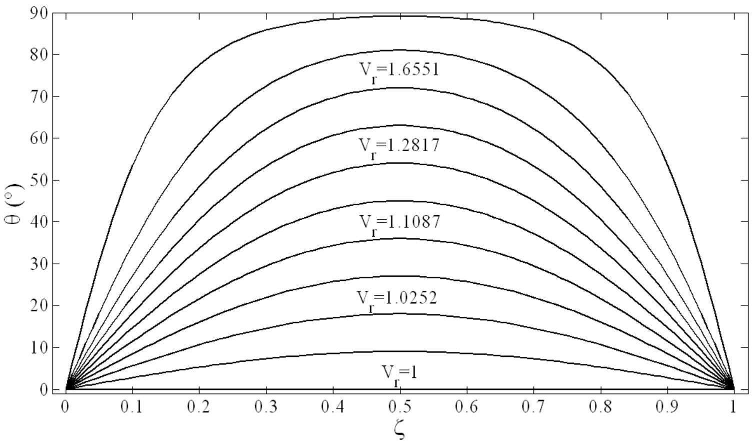

Figure 8.2: *Deformation angle $\theta(\zeta)$ for several values of $V_r = \frac{V}{V_{th}}$. K_{11} is estimated* 10 *pN and $\Delta\varepsilon$ is estimated* 10 *(at room temperature). In this case, the threshold voltage V_{th} is* 1.0558 *V.*

Jacobi amplitude (cf. [9], p. 208). Given the Jacobi amplitude $\phi(\zeta)$, the angle $\theta(\zeta)$ can be written as

$$\theta(\zeta) = \arcsin\Bigg(\sin\phi\sin\theta_m\Bigg). \tag{8.9}$$

Fig. 8.2 shows $\theta(\zeta)$ for different voltages, expressed in terms of $V_r = \frac{V}{V_{th}}$. If $V_r = 1$, $\theta(\zeta) = 0°$, whereas $\theta(\zeta) = 90°$ if $V_r \to \infty$. It is important to realize that the liquid-crystal profile depends on the dimensionless coordinate $\zeta = \frac{z}{h}$ only. The results are calculated for a liquid crystal with $K_{11} = 10$ pN and $\Delta\varepsilon = 10$. These values are realistic estimates and yield a threshold voltage of 1.0558 V.

In the next subsection, we use the mathematical formulation of the Freédericksz alignment to define a special liquid-crystal configuration that can be switched electrically between two optical states.

8.1.2 Back reflection phenomenon in a liquid-crystal layer between two parallel mirrors

The Freédericksz alignment can be designed in such a way that it enables a back reflection phenomenon when applied between two parallel mirrors. The concept discussed is novel and in what follows, we will discuss the optical configuration and present ray-tracing simulations confirming the back reflection phenomenon.

Before we go into details, a few instructive remarks on the subject of light guides is in place. In general, a light guide is an optical device which has the ability to 'guide' light. For example, optical fibers are light guides designed to guide light along its length. Also, gradient-index fibers are optical fibers whose core has a refractive index that decreases with increasing radial distance from the fiber axis. Gradient-index fibers are designed in

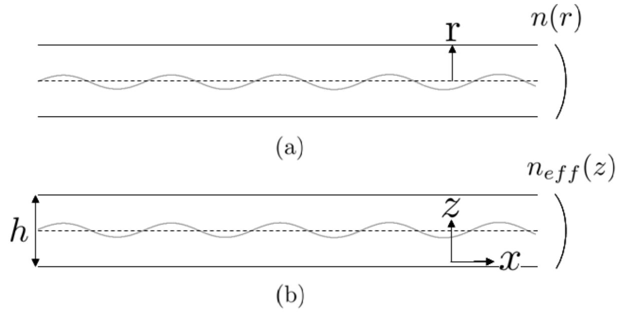

Figure 8.3: *Principle of gradient-index fibers. In (a), the optical properties are inhomogeneous isotropic. Here the index of refraction decreases with increasing distance from the fiber axis. In (b), the optical properties are inhomogeneous anisotropic according to the director profile depicted in Fig. 8.1. In both optical systems, light rays follow oscillatory ray paths down the fiber.*

such a way that light rays follow oscillatory ray paths down the fiber, as depicted in Fig. 8.3-(a). Fig. 8.3-(b) also shows a gradient-index fiber, but this time the optical properties are anisotropic according to the director profile depicted in Fig. 8.1 (the Freédericksz alignment). For light rays polarized in the xz-plane, the effective index of refraction is similar to the index profile of the isotropic gradient-index fiber depicted in Fig. 8.3-(a). Hence the functionality of the anisotropic gradient-index lens is the same and light rays follow oscillatory ray paths down the fiber. Finally, we remark that in contrast with the optical fiber depicted in Fig. 8.3-(a), the anisotropic optical fiber is not cylindrical.

We consider the liquid-crystal layer of Fig. 8.1. We assume that the thickness h is at least in the order of 20 wavelengths or more. Then the properties of the liquid crystal change slowly over the distance of a wavelength and the use of the Hamiltonian method is justified. An incident light ray is linearly polarized in the xz-plane (TM mode) and propagates in the positive x-direction. At $(x, z) = (0, \frac{h}{2})$ the light ray is injected in the liquid-crystal layer. Hence, the resulting light ray in the liquid-crystal layer is extraordinary and then the Hamilton equations given by Eqs. 4.26-4.29 can be applied. We simulate a nematic liquid crystal with $n_o = 1.5266$ and $n_e = 1.8181$ (Merck BL009 mixture). We estimate $K_{11} = 10$ pN and $\Delta\varepsilon = 10$, yielding $V_{th} = 1.0558$ V. We define $h = 5$ and the ray path is calculated with the first-order Runge-Kutta method with step size $\Delta\tau = 0.001$. Fig. 8.4 shows the result for the extraordinary ray path for four different values of $V_r = \frac{V}{V_{th}} = \frac{2}{\pi}\mathcal{K}(m)$. For example, the ray path for $V_r = 1$ in Fig. 8.4-(a) corresponds to a potential difference of $V = V_{th}$ and $\theta_{max} = 0$ radians whereas $V_r = 1.1803$ in Fig. 8.4-(d) corresponds to a potential difference of $V = 1.2461$ V and $\theta_{max} = \frac{\pi}{4}$ radians.

From Fig. 8.4 we can conclude that the ray path is oscillatory: the optical system shows a light-guiding behavior. Moreover, the angle at which the light is refracted at $(x, z) = (0, \frac{h}{2})$ increases with V_r since θ_m increases with V_r. As a result, we can expect that the period of the ray path decreases with increasing V_r. Fig. 8.4 shows that this expectation is confirmed by the simulations.

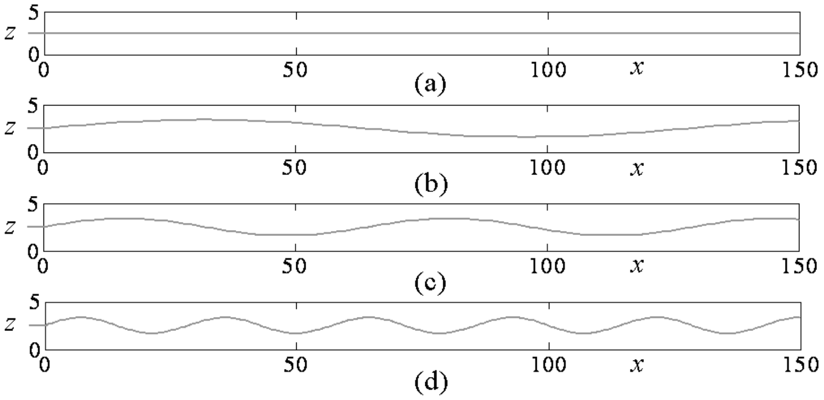

Figure 8.4: *Ray paths of extraordinary rays for four different values of* V_r. *In (a),* $V_r = 1$. *Here, the liquid crystal is homogeneous and the ray path is a straight line. In (b), (c) and (d),* V_r *increases to* 1.0062, 1.0252 *and* 1.1803, *respectively. The ray paths are oscillatory and the period decreases with increasing* V_r.

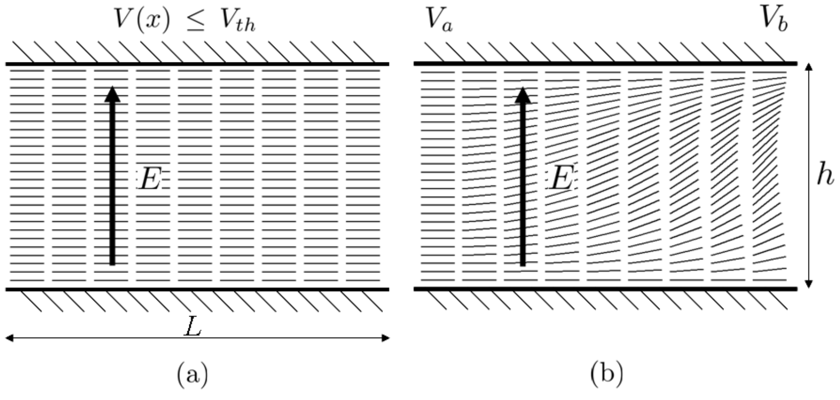

Figure 8.5: *Liquid crystal layer applied between two ideal parallel mirrors, separated by a distance* h. *In (a),* $V(x) \leq V_{th}$ *and* $\hat{\boldsymbol{d}} = (1,0)$. *In (b),* $V(x) = V_{th} + \frac{x}{L}(V_b - V_{th})$, *where* $L = 150$ *is the total length of the optical system and* $V_b > V_a$.

The light rays in Fig. 8.4 are modulated in the vertical z-direction, but not in the horizontal x-direction due to the absence of a gradient in the x-direction in the director profile. We can expect that a light ray is modulated both in the vertical and horizontal direction if we induce an additional horizontal gradient. In what follows below, we will show that these expectations are confirmed by our simulations.

Now let us consider a liquid-crystal layer applied between two parallel ideal mirrors (100% reflectance). Similar to the configuration in Fig. 8.1, the corresponding director profile $\hat{\mathbf{d}}(x, z)$ is a Freédericksz alignment. This time, however, we apply a horizontal gradient in the potential difference $V = V(x)$ across the liquid-crystal layer. This can be achieved with e.g. the application of a resistive electrode structure. As a result, the director profile has an additional gradient in the horizontal direction. In Fig. 8.5, the proposed optical design is depicted in two different situations. Fig. 8.5-(a) shows the situation where $V(x) \leq V_{th}$ and $\hat{\mathbf{d}}(x, z) = (1, 0)$. Hence, the properties of the liquid-crystal layer are homogeneous. On the other hand, in Fig. 8.5-(b) we show the director profile for which $V(x) = V_a + \frac{x}{L}(V_b - V_{th})$, where $L = 150$ is the total length of the optical system, $V_a = V_{th} = 1.0558$ V and $V_b = 1.2461$ V, corresponding to $\theta_{max} = \frac{\pi}{4}$ radians. In this case, the director profile has a gradient both in the vertical and the horizontal direction.

First, we will investigate the situation in Fig. 8.5-(a), where, at $x = 0$, an incident extraordinary ray enters the liquid crystal at approximately 12° with the vertical z-direction. This extraordinary ray is repeatedly reflected by the two ideal parallel mirrors and propagates in the positive x-direction. Since the director profile $\hat{\mathbf{d}}(x, z) = (1, 0)$, the ray path of the light ray consists of straight lines. Fig. 8.6-(a) shows the ray path of the extraordinary light ray inside the liquid crystal. Fig. 8.6-(b) shows the angle of reflection φ inside the optical system as a function of the number of reflections. As expected, φ is constant throughout the system. After approximately 145 reflections, the light ray leaves the system at $x = 150$.

Secondly, we examine the configuration of Fig. 8.5-(b), where the light ray enters the liquid crystal again at $x = 0$ at 12°. The result is depicted in Fig. 8.7. The light ray is reflected by the two ideal parallel mirrors and initially propagates in the positive x-direction. Since in this case the director profile $\hat{\mathbf{d}}(x, z)$ is inhomogeneous, the ray path of the light ray is curved and affected in the horizontal direction. Due to the presence of a lateral gradient in the liquid-crystal profile and the well-known fact that light bends towards regions with high refractive index, φ decreases after each reflection, see Fig. 8.7-(b). After 120 reflections ($x \approx 75$), φ is reduced to negative values. These negative values for φ imply that the ray is now propagating in the negative x-direction. After 240 reflections, the light ray leaves the system at $x = 0$, as can be seen in Fig. 8.7-(a). From these observations, we can conclude that the horizontal direction of propagation of the ray is back reflected due to the lateral gradient in the director profile.

To realize an acceptable efficiency in a real application, we suggest the following measures. For a high reflectivity of the mirrors, we suggest the use of dielectric stacks with a reflectivity of 99.9 %, similar to mirrors used in laser cavities. Then, after 240 reflections, the total reflectivity is reduced to 78 % versus a reduction to below 1 % for mirrors with 90 % reflectance. To minimize absorption and scattering, electrode structures could be fabricated outside the liquid-crystal layer on top of the dielectric stack. To optimize the optical response and minimize the number of reflections, the birefringence $\Delta n = |n_e - n_o|$ of the liquid crystal should be approximately 0.3 or higher.

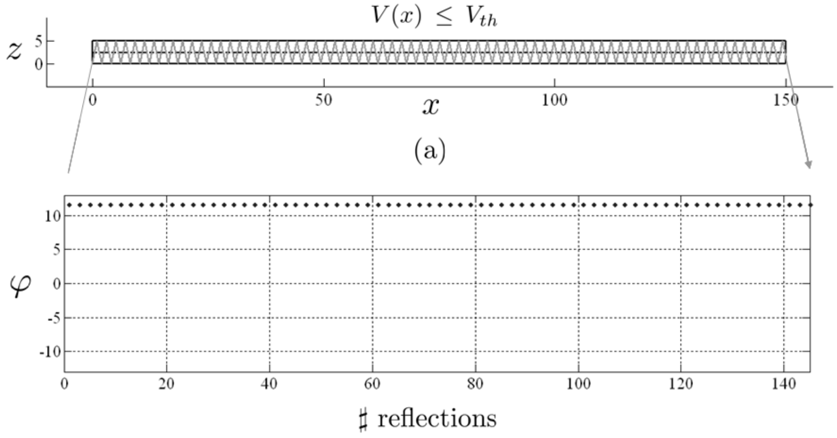

(a)

(b)

Figure 8.6: *In (a), the ray path of the extraordinary light ray is depicted inside the liquid-crystal layer as defined in Fig. 8.5-(a). In (b) the angle of reflection φ of the ray path is constant. Eventually, the ray leaves the system at $x = 150$.*

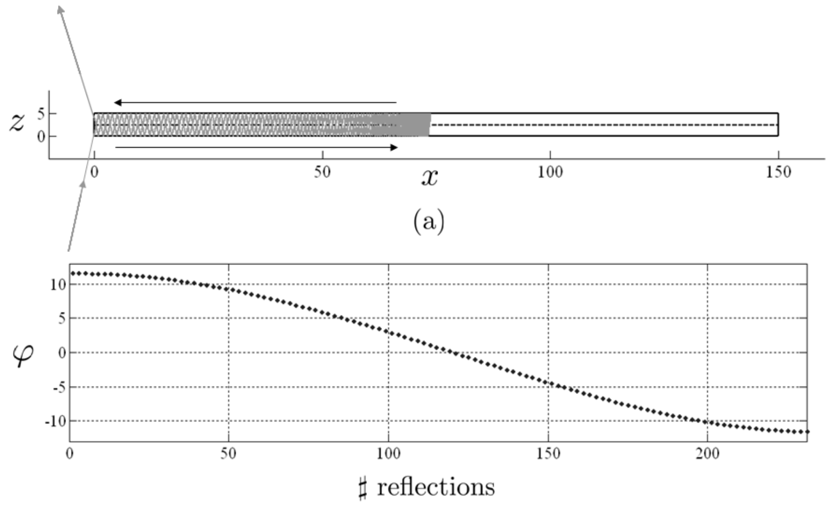

(a)

(b)

Figure 8.7: *In (a), the ray path of the extraordinary light ray is depicted inside the liquid-crystal layer as defined in Fig. 8.5-(b). From (b), we conclude that the angle of reflection φ decreases along the ray path: the direction of propagation is reversed and the light ray leaves the system at $x = 0$.*

Moreover, the gradients in the liquid crystal can be optimized with the thickness h and the voltage $V(x)$. With these suggestions, we believe that a total efficiency of 10 % or higher is feasible.

In a three-dimensional design, the director is parallel to the xz-plane. Since the director has no gradient in the y-direction, light is not affected by the liquid crystal in the y-direction. Therefore, the idea of multiple switches in parallel is possible and mainly depends on the collimation of a light source and any residual scattering effects. In view of this discussion, we point out the self confinement of spatial optical solitons in nematic liquid crystal cells: in [131] simulations reveal an oscillatory self-confined light beam in a 75 μm thick liquid-crystal cell, similar to the behavior presented in Fig. 8.4.

We have shown that a two-dimensional gradient in a liquid-crystal layer with a Freédericksz alignment applied between two parallel mirrors enables a back reflection phenomenon in which the direction of propagation of extraordinary light rays is reversed. As a result, the propagation direction of light in the proposed optical system can be switched by means of an external electric field. Hence, the optical system behaves like an electro-optical switch.

8.2 Ray-tracing simulations of a liquid-crystal-based light guide structure

In this section, we discuss the working principle of a liquid-crystal-based light guide structure. This liquid crystal light guide structure enables a controlled extraction of polarized light by selectively applying a voltage to electrode structures. In addition, we present ray-tracing results of the simulated optical properties of the liquid crystal light guide structure. These results are intended to give the reader a first impression of the optical behavior and potential use of the device discussed. In particular, our goal is to show that the Hamiltonian method provides us with a tool to obtain an understanding of the optical behavior of such a complex optical system.

8.2.1 Device principle

A schematic cross section of the device is depicted in Fig. 8.8 (xz-plane). The device consists of two parallel glass plates with a liquid-crystal layer in between. The bottom glass plate is equipped with a pattern of transparent conducting ITO (Indium Tin Oxide) line electrodes with their long axis perpendicular to the plane of the figure (y-direction). The glass plates are covered with alignment layers that orient the liquid crystal in the y-direction, i.e. when there is no voltage applied to the electrodes. Then the optical properties of the liquid crystal profile are homogeneous and the local optical axis of the liquid crystal, indicated by the unit vector $\hat{\mathbf{d}}(x, y, z)$ (the director), is given by $\hat{\mathbf{d}} = (0, \pm 1, 0)$. From the left the liquid-crystal device is illuminated by an unpolarized light source. There, light is injected into the liquid-crystal layer and the glass plates. Due to total internal reflection at the top and bottom glass-air interfaces, the injected light is trapped and guided in the positive x-direction. In conclusion, when no voltage is applied to the electrodes, the liquid-crystal device behaves like a light guide.

When a low voltage is applied to the electrodes, the liquid crystal aligns along the

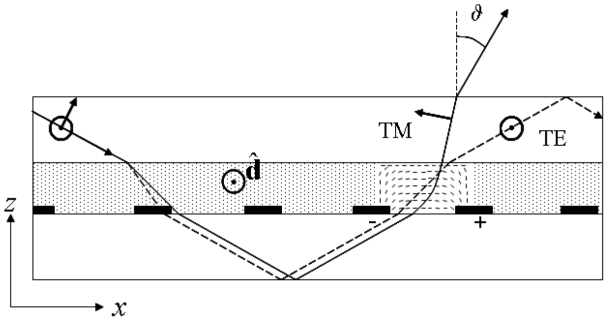

Figure 8.8: *Working principle of the liquid-crystal light guide structure. When a voltage is locally applied to the electrodes, the director* $\hat{\mathbf{d}}$ *aligns along the electric field lines. TM-polarized light is affected by the resulting local gradients in the liquid crystal and is extracted from the device. TE-polarized light remains inside the device due to a light guiding effect.*

electric field lines and the director lies in the xz-plane (see Fig. 8.8). Then, the optical properties of the liquid-crystal profile are inhomogeneous, i.e. the director $\hat{\mathbf{d}}$ depends on the position inside the liquid-crystal layer. As a result, the light paths of light rays inside the liquid crystal are curved. This is due to the fact that light bends towards regions with high refractive index. However, the two-dimensional gradient in the liquid crystal only affects light with a linear polarization in the xz-plane (TM polarization): only extraordinary light rays are curved. Extraordinary light rays are deflected from the linear trajectory in the liquid-crystal layer and can be extracted from the top and bottom glass plates of the device. Ordinary light rays with a linear polarization in the y-direction (TE polarization) are not affected by the gradients in the optical properties. Hence the corresponding light paths are always straight lines. Similar to the case in which $\hat{\mathbf{d}} = (0, \pm 1, 0)$ (homogeneous alignment), ordinary light rays are trapped and guided by the liquid-crystal device.

For the type of application we are interested in, the light guiding of ordinary rays is not a desired effect when a voltage is applied to the electrodes. This problem can be overcome if the ordinary rays are somehow recycled and transformed into polarization sensitive light. This can be achieved by using, for example, depolarizing diffusing reflectors at one or more sides of the liquid-crystal device. However, for simplicity, we do not take this scenario into account and focus our attention to the optical response of extraordinary light rays.

Summarizing, the liquid crystal light guide structure enables a controlled extraction of TM-polarized light by selectively applying a voltage to the electrode structures. As a result, the device enables local dimming and highlighting, a feature that is desired for applications such as polarized backlight architectures [28].

8.2.2 Modeling aspects of the light guide structure

In order to model the optical properties of the liquid-crystal-based light guide structure, we apply the Hamilton equations for extraordinary rays. Before the Hamilton equations

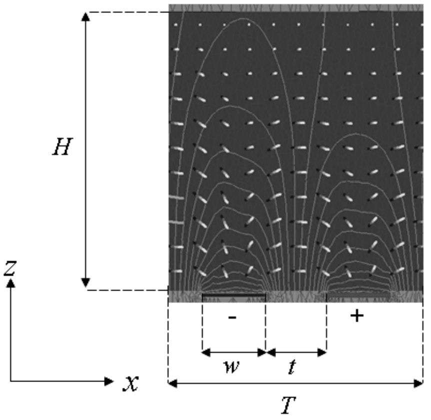

Figure 8.9: *Typical result of a director profile calculated by 2dimMOS. The director is indicated by the bars and the contour lines represent the equipotential lines. The director at the top is aligned in the* y*-direction, whereas the director is in the* xz*-plane at the bottom of the liquid-crystal cell. The period and height of the liquid-crystal region are indicated by* T *and* H*, respectively. The width of the electrodes and the inter-electrode distance are indicated by* w *and* t*, respectively. In this particular case,* $T = 12\mu m$*,* $H = 6.4\mu m$*,* $w = 3\mu m$ *and* $t = 3\mu m$*.*

can be applied, the director profile $\hat{\mathbf{d}}$ of the liquid crystal needs to be calculated. Numerical director profiles are produced by optical analysis software programs, like LCD Master [114] or 2dimMOS [115]. We calculated the liquid-crystal profile obtained for one period of the electrode structure. This period is defined as the liquid-crystal profile induced by two electrodes: one electrode with a positive voltage and one with a negative voltage. Fig. 8.9 shows a typical numerical director profile calculated by 2dimMOS. The dimensions of the simulated liquid-crystal region are also indicated. The period and height are indicated by T and H, respectively. The width of the electrodes and the inter-electrode distance correspond to w and t, respectively. The periodical director profile is repeated in the horizontal direction, hence producing a liquid-crystal cell as depicted in Fig. 8.9.

To simplify the modeling aspects, we assume that the electric field is strong enough to induce a twist of 90° in the xy-plane: the director lies in the xz-plane. The assumption that the director lies in the plane of the drawing is in good agreement with the numerical results depicted in Fig. 8.9. The upper region of the director profile clearly shows a twist and there the director has a component perpendicular to the plane of the drawing. However, the gradients of the director in this region of the liquid-crystal layer are not expected to affect the ray paths of light rays significantly. Therefore, in a good approximation, the director can be assumed in the plane of the drawing: $\hat{d}_y = 0$. For the moment, a two-dimensional approach is sufficient in order to obtain a good understanding of the optical properties.

The illumination of the light guide structure is simulated by the injection of light rays with initial positions and directions of propagation along the vertical edge: we define a

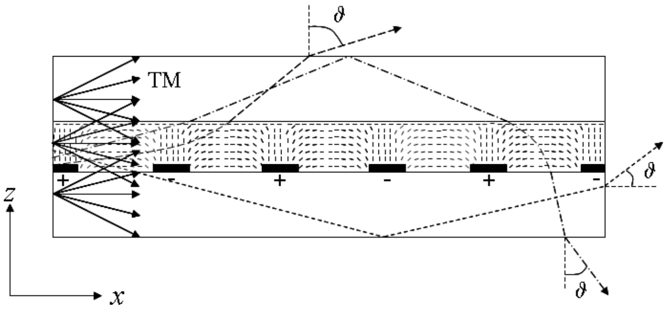

Figure 8.10: *The illumination is simulated by the injection of TM-polarized light rays into the left side. The light rays exit the liquid-crystal cell through the top, bottom and right side of the device. The angle of refraction is indicated by the angle ϑ.*

discrete set of initial values for the position and direction, as can be seen in Fig. 8.10. In order to simulate the optical properties of the device we trace a sufficient number of TM-polarized rays through the glass and liquid-crystal layer when a voltage is applied to the electrodes. In the ray-tracing simulations, we also include the possibility that rays can be totally reflected at the top and bottom glass-air interfaces (total internal reflection). When this is the case, the ray tracing continues until the rays finally enter the exterior of the device. In particular, we calculate the angle ϑ under which the light is transmitted at the top and bottom glass-air interfaces of the liquid-crystal device (see Fig. 8.10). In addition, we also calculate the light output from the side at the right. The number of transmitted rays obtained for a certain angular range is a measure for the light intensity. In this way, we obtain angular intensity distributions for the top, bottom and right side of the device.

8.2.3 Ray-tracing results

In order to obtain an understanding of the optical behavior, we calculate the ray paths of a number of rays when a voltage is applied to the electrode structure. In the ray-tracing simulations we define an un-collimated light source that illuminates the light guide structure from the left. This light source is modeled by injecting (TM-polarized) light rays into the device at certain angles and positions. For each initial position $\mathbf{r}(\tau_0)$ five rays are defined with an angle of incidence with respect to the horizontal axis at 60°, 30°, 0°, −30° and −60° (see also Fig. 8.10). The initial positions of the rays (and the corresponding vectors $\mathbf{p}_e(\tau_0)$) are distributed along the vertical rim of the device at 300 equidistant positions. The total amount of rays injected into the glass and the liquid crystal is therefore 1500.

The position $\mathbf{r}(\tau)$ and the vector $\mathbf{p}_e(\tau)$ of the rays inside the liquid crystal are calculated with the first-order Runge-Kutta method. For an arbitrary interval $[\tau_K, \tau_K + \Delta\tau]$, with $K \in \mathbb{N}$, the x- and z-components of the position and extraordinary phase velocity vector are given by

$$x(\tau_K + \Delta\tau) = x(\tau_K) + \triangle\tau \frac{\partial \mathcal{H}_e}{\partial p_{ex}}(\tau_K), \tag{8.10}$$

$$z(\tau_K + \Delta\tau) = z(\tau_K) + \triangle\tau \frac{\partial \mathcal{H}_e}{\partial p_{ez}}(\tau_K), \tag{8.11}$$

$$p_{ex}(\tau_K + \Delta\tau) = p_{ex}(\tau_K) - \triangle\tau \frac{\partial \mathcal{H}_e}{\partial x}(\tau_K), \tag{8.12}$$

$$p_{ez}(\tau_K + \Delta\tau) = p_{ez}(\tau_K) - \triangle\tau \frac{\partial \mathcal{H}_e}{\partial z}(\tau_K), \tag{8.13}$$

with the partial derivatives of $\mathcal{H}_e$ given by Eqs. 4.28 and 4.29. The step size $\triangle\tau$ that is used in the simulations is 0.05.

The properties of the liquid-crystal material that we use in the simulations are listed in Table 1.1. In this case, a BL009 mixture is used. Table 1.1 lists the elastic constants K_{11}, K_{22} and K_{33}, the static dielectric permittivity $\triangle\varepsilon = \varepsilon_{||} - \varepsilon_{\perp}$ and the viscosity γ of the liquid crystal.

The thickness of the glass substrates is defined to be only 2 μm. This order of magnitude is not realistic for the thickness of a glass substrate. However, in the first approximations that we use, this is of little importance for the simulations since, for the moment, we are mainly interested in the angular optical response of the device and not so much in the position-dependent optical properties.

The numerical director profile $\hat{\mathbf{d}}$ calculated by 2dimMOS is given on the grid points of a regular two-dimensional grid (see Fig. 8.9). In the simulations, the grid represents a matrix of 7993 columns, corresponding to a length of 28 μm, and 321 rows, corresponding to a height H of 6.4 μm. The width w of the electrodes and inter-electrode distance t on the bottom glass substrate are both defined to be 4 μm. The voltage applied to the electrodes is 5 V. The spatial resolution of the grid is limited and for an accurate calculation of the ray path inside the liquid crystal, it is necessary to apply interpolation techniques in order to obtain the director in intermediate space. Note that the order for the interpolation of the director profile in intermediate space must be the order of the Runge-Kutta method.

As mentioned before, we calculate the angular intensity distribution of the top, bottom and right side of the light guide structure. The angular intensity distribution I for the top side is depicted in Fig. 8.11-(a). The results are presented by a histogram: each angular interval $\triangle\vartheta = 1°$ corresponds to a number of collected rays. From these results we can conclude that the majority of the light that is transmitted at the top side propagates at angles larger than 60°. The remaining light is transmitted towards lower angles. Moreover, for some light rays the angle ϑ is even negative. A negative value for ϑ means that light rays are propagating in the negative x-direction. Although physically possible, these kind of light rays rarely occur in the ray-tracing simulations.

The angular intensity distribution for the bottom side is depicted in Fig. 8.11-(b). The light transmitted from the bottom glass substrate is primarily propagating between $-10°$ and $-60°$. The negative values for the angle ϑ correspond to a direction of propagation in the positive x-direction. Apparently, the angular intensity distributions of the top and bottom side do not resemble each other. Hence, we can conclude that, according to the ray-tracing simulations, the optical response of the liquid crystal light guide structure is different for the top and bottom sides. In particular, the intensity profile

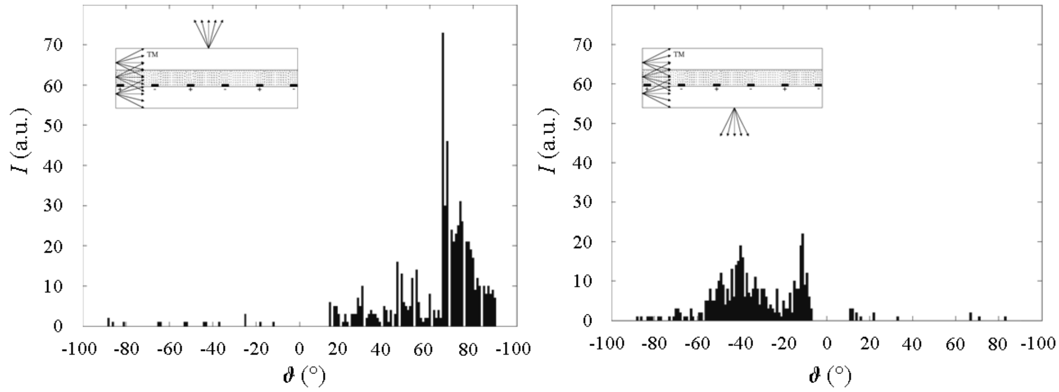

(a)

(b)

Figure 8.11: *(a) Angular intensity distribution I for the top side of the liquid crystal light guide structure. The histogram shows the number of collected rays for each angular interval $\Delta\vartheta = 1°$. Most of the light rays are collected in the range between approximately 65° and 80°. (b) Angular intensity distribution I for the bottom side of the liquid-crystal beam control device. The negative values for ϑ correspond to rays propagating in the positive x-direction.*

of the top side is confined in a smaller angular range than the intensity profile for the bottom side.

Only an insignificant part of the (TM-polarized) light is guided by the liquid-crystal device and transmitted through the right side. Almost all of the incident light is transmitted through the top and bottom glass substrates. Therefore, the simulations support the idea of a controlled extraction of light when a voltage is applied to the electrode structure.

In general, we can conclude that the preliminary ray-tracing simulations support the working principle of the liquid crystal light guide structure. Moreover, the optical response at the top side shows an angular intensity distribution that is confined in a relatively narrow angular range. This angular range lies approximately between 65° and 80°.

8.2.4 Comparison with experimental results

To verify some of the simulation results, the angular intensity distribution emerging from the top glass substrate of a liquid crystal cell has been measured. A liquid-crystal cell is characterized with design parameters resembling the configuration used in our simulations: the thickness H of the liquid-crystal layer is 5 μm and the width of the electrodes and the inter-electrode distance is 4 μm. The voltage applied to the electrodes is 5 V.

The liquid-crystal cell was placed in a side-lit configuration directly in contact with a cold-cathode fluorescence lamp (CCFL). The angular luminance was measured with an EZContrast 160 conoscope from Eldim S.A. [132]. Fig. 8.12-(a) shows a typical result of

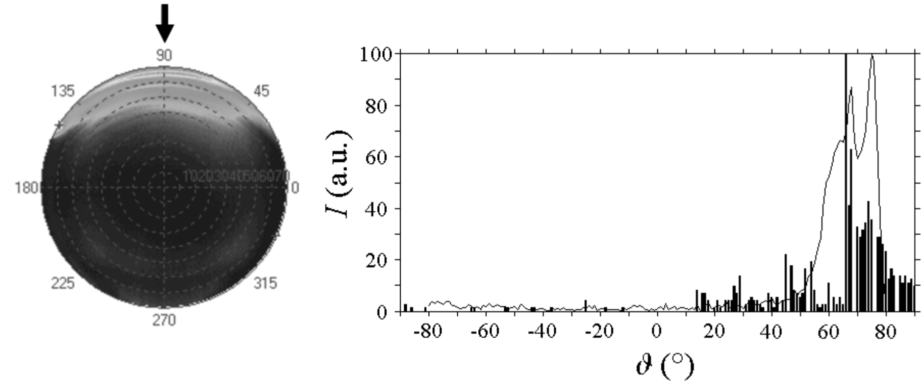

(a) (b)

Figure 8.12: *(a) Polar coordinate plot of a typical light profile measured by the EZContrast 160 conoscope. Note that the transmitted light is confined in the angular range for* ϑ *approximately above* 60°. *The plane which corresponds to the plane* $y = 0$ *in the model and the simulations is indicated by the arrow. (b) The experimental results (curve) and the numerical results (histogram) for the top side depicted in one diagram. The angular region where the simulated light intensity is maximal lies approximately between* 65° *and* 80°. *This observation is confirmed by the experimental results.*

such an analysis. These results clearly resemble the angular characteristics obtained by the ray-tracing simulations (see Fig. 8.11-(a)): the light is typically confined in the angular range for ϑ approximately above 60°. The plane which corresponds to the xz-plane in the model ($y = 0$) is indicated in Fig. 8.12-(a) by the arrow. The angular intensity distribution measured in this plane can be compared with the two-dimensional simulations of Fig. 8.11-(a). For an accurate comparison between simulations and experiment, the measured luminance (cd/m^2) is scaled by a factor $\cos(\vartheta)$ to obtain the relative luminance intensity (cd).

Fig. 8.12-(b) shows the simulated intensity distribution (histogram) depicted in Fig. 8.11-(a) together with the experimental intensity distribution for $y = 0$. We can see that the theoretical results and the experimental results are in a fair agreement: the high intensity region between approximately 65° and 80° is confirmed by the experimental results. The rapid decrease in the measured angular intensity at 80° is explained by the limited angular range of the conoscope that lies between $-80°$ and 80°.

On the other hand, the results do not match quantitatively. The correspondence between model and experiment is limited by, for example, the computational power of the ray-tracing simulation program, i.e. the number of rays. Another reason for a mismatch between theory and experiment can be due to the fact that near the electrode structures of the light guide the material properties of the liquid crystal can change rapidly with respect to the wavelength of light. On the other hand, the Hamiltonian method is based on the assumption that the properties of a medium change slowly over the distance of a wavelength. As a consequence, not all ray paths calculated in the simulations necessarily represent physical light rays. In addition to this, yet another explanation for the discrepancy can be ascribed to the fact that the ray-tracing simulations are performed in two dimensions, whereas the experiment has a three-dimensional character, including diffraction effects. In addition, light can be scattered by the pollution of the glass surfaces and absorbed by the transparent conducting ITO electrode structures. Because of these imperfections, the ray-tracing results presented in this section should be considered as a first approximation of the actual optical properties of the liquid-crystal-based light guide structure.

8.3 Conclusions

We have shown that the Hamiltonian method enables the modeling of the optical properties in the geometrical-optics approach of inhomogeneous anisotropic optical systems. In particular, we have investigated the optical properties of two inhomogeneous liquid-crystal-based optical configurations.

In a first example, we have shown that a two-dimensional gradient in a liquid-crystal layer with a Freédericksz alignment applied between two parallel mirrors enables a back reflection phenomenon in which the direction of propagation of extraordinary light rays (TM mode) is reversed. The propagation direction of light in the optical system discussed can be switched by means of an external electric field. As a result, the optical system behaves like an electro-optical switch. This result is new and, besides the publication of our letter [129], cannot be found in the literature. For this optical configuration, the use of the Hamiltonian method is justified since we have assumed an inhomogeneous liquid-crystal layer with a thickness of at least 20 wavelengths. In an attempt to demonstrate this novel optical effect, we have succeeded in constructing a sample with a 100 μm thick liquid-crystal layer with a Freédericksz alignment. However, we failed to reproduce the back reflection phenomenon due to imperfections in the optical design. From this exercise, we conclude that the effect might be obtained experimentally by minimizing losses in the optical system and optimizing the gradients of the liquid crystal.

In a second example, we have simulated the optical properties of a liquid-crystal-based light guide structure which enables a controlled extraction of TM-polarized light when a voltage is applied to electrode structures. From ray-tracing simulations we can conclude that the numerical results support the working principle of the liquid-crystal device. The ray-tracing simulations show that the angular intensity distribution for the top side is confined in a relatively narrow angular range. This angular range lies approximately between 65° and 80°. Qualitatively, this result is in good agreement with experimental results. However, the quantitative correspondence between model and experiment is limited by the computational power of the ray-tracing simulation program, i.e. the number of rays. To improve this, the simulation program needs further optimization. In addition, the liquid crystal contains regions where the material properties change rapidly over the distance of a wavelength, which is in contradiction with the rules of geometrical optics. Finally, the ray-tracing simulations are performed in two dimensions, whereas the experiment has a three-dimensional character, including diffraction effects, absorption and scattering of the light. Because of these imperfections, the ray-tracing results presented for the liquid-crystal-based light guide structure should be considered a first approximation of the actual optical properties. However, the observation that the results are in agreement with experimental results in terms of quality rather than quantity is not in contradiction with the conclusions drawn in Chapter 5. Recall that there it is concluded that for values of L_d below 20 wavelengths a qualitative agreement between ray- and wave-optics (i.e. the experimental results) might still be established.

It has been shown that, given an arbitrary director profile, our polarized ray-tracing method can be applied to calculate curved ray paths of light rays in inhomogeneous anisotropic media. With the implementation of the method in a ray-tracing simulation program, we are able to assess the optical properties of complex anisotropic optical systems.

Chapter 9

Conclusions and outlook

In this thesis, we have presented the electromagnetic theory for inhomogeneous anisotropic media with a complex Hermitian permittivity tensor in the geometrical-optics approach. The theory is discussed for general anisotropy, including both uniaxial and biaxial anisotropy, and provides a general overview of the propagation of light in (non-absorbing, optically inactive) inhomogeneous anisotropic media. One important conclusion is that light rays in anisotropic media with a complex Hermitian permittivity tensor are in general elliptically polarized and do not necessarily have an optical axis. In the special case of a real symmetric tensor, light rays are linearly polarized by definition and always have an optical axis. In addition, we have derived general ray-tracing equations for inhomogeneous anisotropic media. In geometrical optics, these ray-tracing equations define the state-of-the-art in the field of polarized ray tracing. They are derived from the Hamiltonian principle, are formulated in complex notation and explicitly include the position-dependent material properties. In other words, we have established the general relation between the material properties and the curved ray paths of light rays in anisotropic media. In this thesis, the ray-tracing equations are applied to study liquid-crystal applications that have been under development at Philips Research. For the liquid-crystal material discussed, the dielectric permittivity tensor is real and symmetric.

In geometrical optics, the material properties are allowed to change with position, as long as the change per unit length is sufficiently small. We have investigated how much the anisotropic material properties are allowed to change over the distance of a wavelength in the geometrical-optics approach. We have shown for the first time that a criterion for typical in-plane liquid-crystal configurations can be found based on advanced ray- and wave-optics simulations. These simulations are applied to an anisotropic medium with a two-dimensional periodic director profile. In this director profile, the director is rotated by 90° over a distance L_d. Then L_d is the distance over which a maximum change in optical properties occurs for fixed principal indices of refraction. Based on the results of the simulations, we have concluded that if $\frac{\lambda}{L_d} < 0.05$, it is fair to say that ray- and wave-optics are in good agreement, both qualitatively and quantitatively. If L_d is smaller than 20 wavelengths, the agreement between ray- and wave-optics worsens. However, a qualitative agreement between ray- and wave-optics might still be established for values of L_d below 20 wavelengths. This statement is verified by the ray-tracing simulations of a liquid-crystal light guide structure discussed in Chapter 8.

A significant part of this thesis is devoted to the application of liquid crystal in switchable auto-stereoscopic 2D/3D displays. For lenticular-based 3D displays, we have proposed an improved lens design. This lens design makes use of an anisotropic lens plate to minimize any residual lens action in the 2D mode, without compromising the performance of the 3D mode. In 2008, Philips Research succeeded in making samples of anisotropic lens plates. This lens plate consists of a special liquid-crystal mixture that can be polymerized by UV curing. It has been shown that, when applied in an electro-optical configuration, the lens action of an anisotropic lenticular can be successfully switched off without displaying any residual lens action.

We have also investigated the angular-dependent lens action of an advanced liquid-crystal GRIN lens structure for application in auto-stereoscopic 3D displays. Based on the ray-tracing results, we conclude that the lens action meets the requirements for small viewing angles, but needs improvement for large viewing angles ($> 30°$). To optimize the 3D performance for large oblique angles, the optical design of GRIN lenses for application in 3D displays is in need of further research. In general we conclude that the advanced ray-optics analysis procedures presented here form a useful tool in the search for improvements and enable a better understanding of the liquid-crystal technology discussed.

Recently, Philips announced that because of current market developments, the point in time where mass adoption of auto-stereoscopic 3D displays will occur has shifted significantly. As a consequence, Philips has decided to scale down its investments in this area. Evidently, this has resulted in a drop in activity in the field of auto-stereoscopic 3D displays within Philips Research. Besides Philips, other companies are also active in the field of stereoscopic imaging (with or without additional appliances), such as Samsung, SeeReal Technologies, DLP Texas Instruments, Sharp or Hyundai. Before auto-stereoscopic 3D displays become available for the consumer market on a large scale, it is likely that 3D technologies first reach a desired level of maturity in markets for digital signage (e.g. shopping malls, airports and hotels) and professional applications (medical and scientific imaging, design and prototyping).

Another liquid-crystal application investigated in this thesis is the light guide structure enabling a controlled local extraction of polarized light. The application of geometrical optics to the relatively small micro-sized liquid-crystal cells in the light guide is a subject of debate. However, for this optical system, the results of our ray-tracing simulations support the working principle of the light guide structure and show good qualitative agreement with experimental results. These conclusions fully agree with the conclusions on the applicability of geometrical optics mentioned above.

Finally, we have presented ray-tracing simulations of a liquid-crystal layer with a Freédericksz alignment applied between two parallel capacitive mirrors. The simulations show that such an optical configuration enables a back reflection phenomenon in which the direction of propagation of light rays can be reversed. When applied in an electro-optical configuration, the liquid-crystal profile can be switched and the system behaves like an optical switch. In an attempt to demonstrate this novel optical effect, we have succeeded in constructing a liquid-crystal sample with a Freédericksz alignment. However, we failed to reproduce the back reflection phenomenon due to imperfections in the optical design. In the end, we have concluded that the effect might be obtained experimentally by minimizing losses in the optical system and optimizing the gradients of the liquid crystal.

The theory discussed in this thesis applies to media with electrical anisotropy and linear birefringence, defined by a Hermitian permittivity tensor. This means that absorption, magnetic anisotropy, optical activity (circular birefringence) and other types of birefringence (both linear and non-linear) are subjects with which the theory can be extended. We remark that in these cases, we can apply the same systematic approach as presented in this thesis, but the mathematical equations and their physical interpretations will be different. We can expect that the theory will become more complex and whether the theory still provides a pragmatic approach to study complex optical systems by means of ray-optics analysis is subject to debate.

In general, we can conclude that we have worked out the electromagnetic theory of general inhomogeneous anisotropic media in the geometrical-optics approach for media with complex Hermitian dielectric permittivity tensors. The theory has been applied to investigate numerous novel liquid-crystal applications: these included display technologies for auto-stereoscopic imaging and micro structures with potential applications in the area of lighting and/or telecommunication systems. The theory also aided in providing a criterion for the applicability of geometrical optics to in-plane liquid-crystal configurations. In contrast with other methods addressing optical anisotropy, ray-optics analysis provides solid physical insight into the subject, is able to handle large computational domains and can be applied relatively easy to assess complex anisotropic electro-optical devices.

Appendix A

Hermitian permittivity tensor without optical axes

We will show that for a Hermitian dielectric permittivity tensor, there are in general no optical axes.

On the complex principal basis $\{\hat{\mathbf{u}}, \hat{\mathbf{v}}, \hat{\mathbf{w}}\}$, we can always find a direction along which the wave normal $\mathbf{p}$ satisfies (see Eq. 2.40)

$$|p_u| = \sqrt{\frac{\varepsilon_w(\varepsilon_v - \varepsilon_u)}{(\varepsilon_w - \varepsilon_u)}}, \tag{A.1}$$

$$|p_v| = 0, \tag{A.2}$$

$$|p_w| = \sqrt{\frac{\varepsilon_u(\varepsilon_w - \varepsilon_v)}{(\varepsilon_w - \varepsilon_u)}}, \tag{A.3}$$

$$|\mathbf{p}| = \sqrt{\varepsilon_v}. \tag{A.4}$$

In addition, the length of the wave normal is twofold because the optical indicatrix consists of two sheets: $|\mathbf{p}| = |\mathbf{p}_1| = |\mathbf{p}_2|$. For a real symmetric permittivity tensor, the basis $\{\hat{\mathbf{u}}, \hat{\mathbf{v}}, \hat{\mathbf{w}}\}$ is real and we would say that $\mathbf{p}$ is in the direction of the optical axis. However, since the basis $\{\hat{\mathbf{u}}, \hat{\mathbf{v}}, \hat{\mathbf{w}}\}$ is now complex, things are a bit more complicated: Eqs. A.1-A.4 determine the length of $\mathbf{p}$, but do not give any information about the phases of the complex vector components p_u, p_v and p_w. These phases are defined ϕ_u, ϕ_v and ϕ_w, respectively. Since $|p_v| = 0$, we have $\phi_v = 0$. As a result, the wave normal on the complex basis $\{\hat{\mathbf{u}}, \hat{\mathbf{v}}, \hat{\mathbf{w}}\}$ is given by

$$\mathbf{p} = |p_u|e^{i\phi_u}\hat{\mathbf{u}} + |p_w|e^{i\phi_w}\hat{\mathbf{w}}, \tag{A.5}$$

where $|p_u|$ and $|p_w|$ are given by Eqs. A.1 and A.3. Similarly, we write the wave normal on the real fixed basis $\{\hat{\mathbf{x}}, \hat{\mathbf{y}}, \hat{\mathbf{z}}\}$:

$$\mathbf{p} = |p_x|e^{i\phi_x}\hat{\mathbf{x}} + |p_y|e^{i\phi_y}\hat{\mathbf{y}} + |p_z|e^{i\phi_z}\hat{\mathbf{z}}. \tag{A.6}$$

Now consider the case for which the imaginary part of the wave normal is not zero: $\mathrm{Im}\{\mathbf{p}\} \neq 0$. Then there is a complex vector $\mathbf{p}$ on the real fixed basis $\{\hat{\mathbf{x}}, \hat{\mathbf{y}}, \hat{\mathbf{z}}\}$ for which

$|\mathbf{p}_1| = |\mathbf{p}_2| = |\mathbf{p}|$. This means that in real space there is no optical axis. In what follows, we will give an example of a Hermitian permittivity tensor for which there are no optical axes in real space $\mathbb{R}^3$.

Consider the Hermitian permittivity tensor given by

$$\underline{\underline{\varepsilon}} = \begin{pmatrix} 2 & 2i & 0 \\ -2i & 3 & 0 \\ 0 & 0 & 4 \end{pmatrix}. \tag{A.7}$$

This tensor can be diagonalized on the complex orthonormal basis $\{\hat{\mathbf{u}}, \hat{\mathbf{v}}, \hat{\mathbf{w}}\}$. On the real basis $\{\hat{\mathbf{x}}, \hat{\mathbf{y}}, \hat{\mathbf{z}}\}$, the normalized eigenvectors and corresponding eigenvalues are given by

$$\hat{\mathbf{u}} = i0.788\hat{\mathbf{x}} - 0.615\hat{\mathbf{y}}, \quad \varepsilon_u = 0.438, \tag{A.8}$$

$$\hat{\mathbf{v}} = \hat{\mathbf{z}}, \quad \varepsilon_v = 4, \tag{A.9}$$

$$\hat{\mathbf{w}} = i0.615\hat{\mathbf{x}} + 0.788\hat{\mathbf{y}}, \quad \varepsilon_w = 4.561. \tag{A.10}$$

Note that in accordance with our previous assumptions $\varepsilon_u < \varepsilon_v < \varepsilon_w$. If the wave normal direction is along an optical axis, we demand that $\mathrm{Im}\{\mathbf{p}\} = 0$. Then we obtain three equations for the vector components of $\mathbf{p}$:

$$\mathrm{Im}\left\{ \hat{u}_k |p_u| e^{i\phi_u} + \hat{w}_k |p_w| e^{i\phi_w} \right\} = 0, \quad k = x, y, z, \tag{A.11}$$

where $|p_u|$, $|p_w|$, $\hat{u}_k$ and $\hat{w}_k$ are given by Eqs. A.1, A.3 and A.8-A.10. For the Hermitian tensor given by Eq. A.7, Eq. A.11 results in two equations for the phases ϕ_u and ϕ_w:

$$-10.404 \cos\phi_u = \cos\phi_w, \tag{A.12}$$

$$6.342 \sin\phi_u = \sin\phi_w. \tag{A.13}$$

By eliminating ϕ_w we then obtain

$$F_1(\phi_u) = -10.404 \cos\phi_u, \tag{A.14}$$

$$F_2(\phi_u) = \cos\left[\arcsin(6.342 \sin\phi_u) \right], \tag{A.15}$$

$$F_1(\phi_u) = F_2(\phi_u). \tag{A.16}$$

When we analyze functions $F_1(\phi_u)$ and $F_2(\phi_u)$, we come to the conclusion that for arbitrary values of ϕ_u these functions are never equal. This means that $\mathrm{Im}\{\mathbf{p}\} \neq 0$. Hence there is a *complex* wave normal $\mathbf{p}$ on the real basis $\{\hat{\mathbf{x}}, \hat{\mathbf{y}}, \hat{\mathbf{z}}\}$ along which $|\mathbf{p}_1| = |\mathbf{p}_2| = |\mathbf{p}|$. Therefore there are no optical axes for the Hermitian tensor given by Eq. A.7. Therefore we say that in general an anisotropic medium with a Hermitian permittivity tensor does not have optical axes.

Appendix B

Optical anisotropy in photolithographic systems

Photolithography is a process to create high resolution images. In the semiconductor world, photolithography techniques are pushed to the physical limits to shrink the size of transistors. One of these techniques is immersion lithography. Immersion lithography is a photolithographic resolution enhancement technique that replaces the usual air gap between the final lens and the wafer surface with a liquid medium that has a refractive index greater than one. Current immersion lithography systems with deep-ultraviolet light (193 nm wavelength) use for example highly purified water. Totzeck et al. [98] mention that for these kind of systems it is desired to use a last lens element with a high refractive index. The problem is that high-index materials are not of a quality required for lithography and almost all of them suffer from a level of birefringence that is too high to be acceptable. In this section, we will show that the performance of a last lens element is indeed highly sensitive to the effect of optical anisotropy.

The size of the finest detail that can be resolved by a lens is

$$F = k_1 \frac{\lambda}{\mathrm{NA}}, \tag{B.1}$$

where λ is the wavelength of light and NA is the numerical aperture of the lens (cf. [3], p. 215). The factor k_1 is a process-related factor and is determined by the properties of the optical system. It has a physical limit of 0.25 [98]. This limit is called the diffraction limit. Current production processes are capable of minimizing k_1 to a value of approximately 0.28. The numerical aperture of a lens is given by

$$\mathrm{NA} = n \sin(\alpha_{max}), \tag{B.2}$$

where n is the index of refraction of the surrounding medium and α_{max} is the half-angle of the maximum cone of light that can enter or exit the lens (see Fig. B.1). Today the state-of-the-art is an immersion photolithography lens system with $\mathrm{NA} = 1.35$ operating at a wavelength of 193 nm, capable of printing structures with a 45 nm half pitch [98].

The definitions discussed above explain why replacing the surrounding air with water enhances the resolving power of a lens system, since $n_{air} < n_{water}$. In the case of deep-ultraviolet light with 193 nm wavelength, the index of refraction of water is $n_{water} = 1.44$.

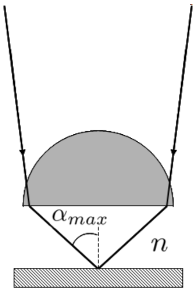

Figure B.1: *Schematic representation of the last lens element above a wafer surface applied in photolithographic systems. The refractive index of the medium between the last lens element and the wafer is defined* n*. The maximum half-angle of the light cone produced by the lens is* α_{max}*. Then the numerical aperture of the last lens element is defined* $NA = n \sin(\alpha_{max})$*.*

Then, the resolving power is improved by a factor of 1.44. However, at the same time, the angle α_{max} is reduced, since the difference in index of refraction between the lens and the surrounding medium is reduced. In fact, the numerical aperture is conserved. To overcome this effect, a lens with a higher index of refraction is required.

A possible high-index material for the last lens element is sapphire (Al_2O_3), which has a refractive index of approximately 1.83 and higher for wavelengths below 270 nm [99]. Because of its hexagonal crystalline structure, sapphire is uniaxially anisotropic. The birefringence $\triangle n = |n_e - n_o|$ of sapphire is approximately 0.008. An important question is whether this birefringence destroys the resolving power of the last lens element or if the effect of the optical anisotropy may be neglected.

In order to investigate the effect of optical anisotropy on the resolving power of a last lens element, we apply a theoretical test case. In this test case, we investigate a plano-convex last lens element (in air) with an a-spherical surface [100]. The a-sphericity of the lens surface is needed in order to minimize the lens aberrations and optimize the resolving power of the lens [101]. More details on the design of a-spherical lenses in the geometrical-optics approach can be found in for example Born & Wolf (cf. [6], p. 197). A cross section of the lens is depicted in Fig. B.2. The lens material is glass ($n_{lens} = 1.5$) and, in spherical coordinates, the a-spherical surface is given by

$$z(r) = \sum_{k=1}^{k_{max}} a_{2k} r^{2k}, \tag{B.3}$$

where a_{2k} are coefficients. Incident to this a-sphere is a spherical wavefront, denoted by the dashed curve in Fig. B.2. This wavefront has a virtual object point O at 40 mm above the origin. The coefficients are calculated in such a way, that the perfect image point O' is at 38.3333 mm above the origin, exactly on the wafer surface (for $\lambda = 193$nm). If $k_{max} \to \infty$, the spot size at the perfect image point O' approaches zero. In Fig. B.2, we have calculated the ray paths of several rays that correspond to the incident spherical wave front. These rays are refracted by an a-sphere having coefficients given by Table B.1 ($k_{max} = 8$). This a-sphere remains close to a sphere, but the a-sphericity is needed

Table B.1: *Coefficients a_{2k} for an a-spherical lens surface [100].*

k	a_{2k}
1	$0.12500029 \cdot 10^{-1}$
2	$0.10385061 \cdot 10^{-5}$
3	$-0.53303489 \cdot 10^{-9}$
4	$-0.64002390 \cdot 10^{-12}$
5	$-0.15463937 \cdot 10^{-14}$
6	$0.20233996 \cdot 10^{-17}$
7	$-0.43270707 \cdot 10^{-20}$
8	$0.29961636 \cdot 10^{-23}$

in order to correct for the last 3.3333 mm path in air. With these coefficients, the spot diameter at the perfect image point O' is approximately 2 nm, which is in the expected sub-wavelength region. The ray paths near the wafer surface are again depicted in Fig. B.2 for $x \in [-0.5, 0.5]$ and $z \in [38.0, 38.9]$.

Fig. B.3 shows the last lens element as defined in Eq. B.3, but now with uniaxial anisotropy. The optical axis $\hat{\mathbf{w}}$ lies in the vertical z-direction and the anisotropic lens material is defined with an ordinary index of refraction $n_o = 1.500$ and an extraordinary index of refraction $n_e = 1.505$. As a result, the light inside the last lens element contains both ordinary and extraordinary components. The ordinary rays are linearly polarized in the y-direction, orthogonal to the optical axis $\hat{\mathbf{w}}$. These rays result in exactly the same

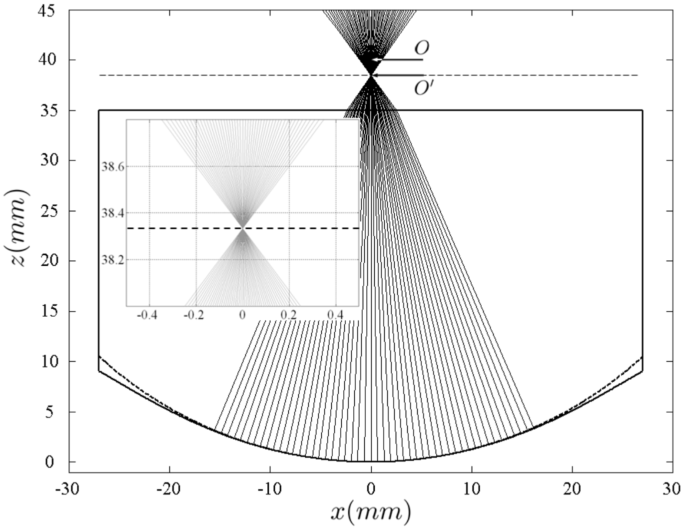

Figure B.2: *Cross section of a last lens element. A spherical wave front (dashed curve) with virtual object point O at 40 mm above the origin is refracted by the a-spherical lens surface. The light is focussed in the perfect image point O' on the wafer surface, 38.3333 mm above the origin. The spot diameter of the image is approximately 2 nm.*

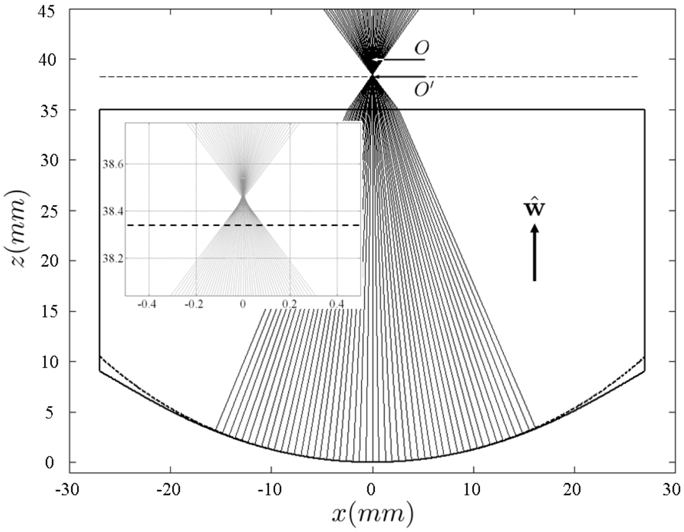

Figure B.3: *Cross section of the last lens element with a birefringence* $\triangle n = 0.005$*. The optical axis* $\hat{\mathbf{w}}$ *is in the* z*-direction. This time, the spot diameter in the perfect image point* O' *is approximately* 100 μ*m.*

optical behavior as depicted in Fig. B.2. On the other hand, the extraordinary light rays are linearly polarized in the xz-plane. This part of the light results in a different spot size on the wafer surface. The difference in spot size with Fig. B.2 is clearly demonstrated in the additional figure of Fig. B.3, for which $x \in [-0.5, 0.5]$. For the extraordinary polarization the spot diameter at the perfect image point O' is approximately 100 μm. This order of magnitude is unacceptable for photolithographic applications in the sub-wavelength region.

Apparently, the lens is prone to changes in the spot size in the perfect image point due to the effect of optical anisotropy. To determine the sensitivity of the spot size for optical anisotropy, we have calculated the radius r_s of the spot in the perfect image point O' as a function of the optical anisotropy $\triangle n$. Fig. B.4 shows the result for $0 \leq \triangle n \leq 1$. Clearly r_s does not scale linearly with $\triangle n$. In addition, the sensitivity increases with decreasing $\triangle n$. In Fig. B.5, we show r_s for $0 \leq \triangle n \leq 0.01$. For the range of $\triangle n$ depicted in this figure, the radius r_s satisfies

$$r_s = 97.96 \cdot 10^{-11} + 1.78 \cdot 10^{-2} \triangle n. \tag{B.4}$$

According to Eq. B.4, the spot diameter is approximately 50 nm when $\triangle n = 1.35 \cdot 10^{-6}$. This means that for a birefringence higher than approximately 10^{-6}, the performance of the last lens element is inferior to the state-of-the-art performance, without taking into account the diffraction limit. Hence the spot size at the perfect image point is highly sensitive to the presence of optical anisotropy in the last lens element.

Due to the birefringence of the lens, the perfect image point of the lens no longer corresponds to a focal point. The focal point now lies above the perfect image point. As a result, the spot size on the wafer surface can be reduced if the wafer surface is

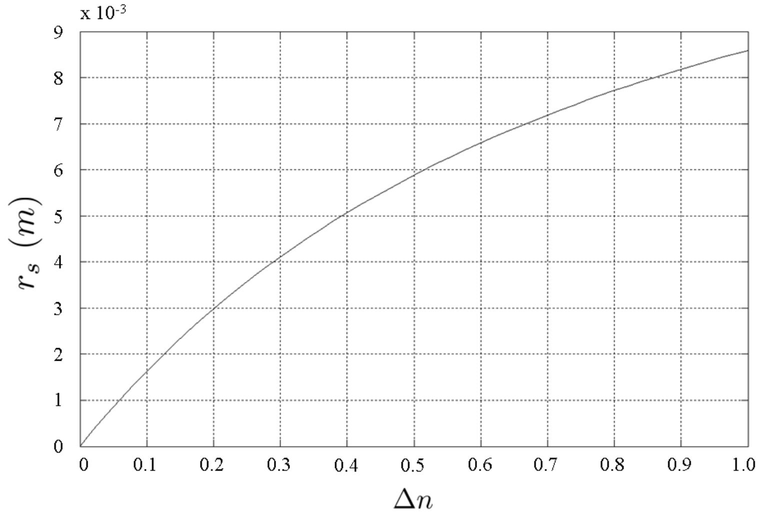

Figure B.4: *Radius r_s of the spot size in the perfect image point O' as a function of the optical anisotropy $\triangle n = |n_e - n_o|$.*

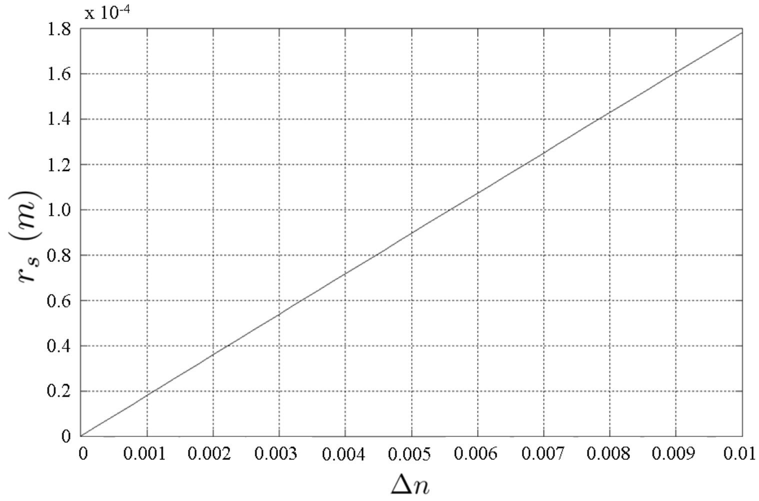

Figure B.5: *Radius r_s of the spot size in the perfect image point O' for $0 \leq \triangle n \leq 0.01$. For this range, the radius scales linearly with $\triangle n$: $r_s = 97.96 \cdot 10^{-11} + 1.78 \cdot 10^{-2} \triangle n$.*

translated in the positive z-direction, see Fig. B.3. The diameter of the spot size on the wafer surface can be minimized to approximately 12 μm at $z = 38.46$ mm. As a result, the spot size can be reduced one order of magnitude. However, this result is still not acceptable for photolithographic applications in the sub-wavelength region.

The results of the test case show that an optical anisotropy in the final lens element in the order of 10^{-6} corresponds to a spot diameter of approximately 50 nm on the wafer surface. Apparently, the resolving power of the last lens element is highly sensitive to the optical anisotropy. Based on these results, we can conclude that high-index material last lens elements with birefringent properties are not suitable for immersion lithography as a resolution enhancement technique, unless the birefringence is compensated for.

Appendix C

Runge-Kutta method and the Hamilton equations

In Chapter 4 and beyond we calculate ray paths in inhomogeneous media for which we have derived the Hamilton equations. These equations are a set of six coupled first-order differential equations for the position $\mathbf{r}(\tau)$ and wave normal $\mathbf{p}(\tau)$. In the appendix below, we discuss two methods that we can apply to calculate the position and wave normal numerically.

The generic problem in ordinary differential equations of a set of N coupled first-order differential equations for the functions y_i, with $i = 1, 2, ..., N$, reads

$$\frac{dy_i(x)}{dx} = f_i(x, y_1, ..., y_N), \tag{C.1}$$

where the functions f_i on the right-hand side are known. In our notation, the functions f_i correspond to the vector components of $\nabla_r \mathcal{H}$ and $\nabla_p \mathcal{H}$. In addition, x corresponds to the parameter τ and y_i corresponds to the vector components of the wave normal $\mathbf{p}$ and the position $\mathbf{r}$.

When we advance the function $y_i(\tau_n)$ from τ_n to $\tau_{n+1} = \tau_n + \triangle\tau$, we can write $y_i(\tau_n + \triangle\tau)$ as a Taylor series expansion:

$$\begin{aligned} y_i(\tau_n + \triangle\tau) &= y_i\Big(\tau_n, y_1(\tau_n), ..., y_N(\tau_n)\Big) \\ &\quad + \triangle\tau \frac{dy_i}{d\tau}\Big(\tau_n, y_1(\tau_n), ..., y_N(\tau_n)\Big) + O(\triangle\tau^2), \end{aligned} \tag{C.2}$$

where the term $O(\triangle\tau^2)$ incorporates the remaining higher-order terms. This formula is called the first-order Runge-Kutta method, also known as the Euler method. The error in Eq. C.2 is of order 2 in $\triangle\tau$. In general, the Runge-Kutta method is called nth order if its error term is $O(\triangle\tau^{n+1})$. If we apply the Hamilton equations to Eq. C.2, we obtain

$$\mathbf{r}_i(\tau_n + \triangle\tau) = \mathbf{r}_i(\tau_n) + \triangle\tau(\nabla_p\mathcal{H})_i(\tau_n) + O(\triangle\tau^2), \tag{C.3}$$

$$\mathbf{p}_i(\tau_n + \triangle\tau) = \mathbf{p}_i(\tau_n) - \triangle\tau(\nabla_r\mathcal{H})_i(\tau_n) + O(\triangle\tau^2), \quad i = x, y, z. \tag{C.4}$$

It is also possible to make a trial step to the midpoint of the interval $[\tau_n, \tau_n + \triangle\tau]$ and use the value of τ and y_i at that midpoint to calculate the step across the whole interval. Then, the equations for $y_i(\tau_n + \triangle\tau)$ become

$$c_1 = \triangle\tau \frac{dy_i}{d\tau}(\tau_n), \tag{C.5}$$

$$c_2 = \triangle\tau \frac{dy_i}{d\tau}\left(\tau_n + \frac{1}{2}\triangle\tau, y_1(\tau_n) + \frac{1}{2}c_1, ..., y_N(\tau_n) + \frac{1}{2}c_1\right), \tag{C.6}$$

$$y_i(\tau_n + \triangle\tau) = y_i(\tau_n) + c_2 + O(\triangle\tau^3), \quad i = 1, ..., N. \tag{C.7}$$

These equations define the second-order Runge-Kutta method. Since the error term of the Euler method is a factor $\triangle\tau^{-1}$ bigger than the error term of the second-order Runge-Kutta method, the latter is more accurate.

Appendix D

Hamilton equations applied to a surface of discontinuity

In Section 2.3, we have come to the conclusion that the optical properties of an (an)isotropic medium should change slowly over the distance of a wavelength. However, at (an)isotropic interfaces, the material properties are discontinuous and then condition 2.18 is not satisfied. In Chapter 3, we have discussed the classical optical theory of (an)isotropic media in the interface region. Although condition 2.18 is not satisfied in the interface region, the theory presented in Chapter 3 still applies within the framework of geometrical optics. In view of this discussion, an important question is whether the Hamilton equations derived for the bulk region can be applied to a surface of discontinuity, despite the fact that in that case condition 2.18 is not satisfied. In this section, we will find an answer to this question.

We consider a surface of discontinuity in the bulk region of an uniaxially anisotropic medium with $\underline{\underline{\varepsilon}}$ real and symmetric and a director profile as depicted in Fig. D.1. This surface of discontinuity is defined in the plane $z = 0$. If $z < 0$, the director is in the x-direction: $\hat{\mathbf{d}} = (1, 0, 0)$. If $z \geq 0$, the director is in the z-direction: $\hat{\mathbf{d}} = (0, 0, 1)$. Furthermore, the components of the director $\hat{\mathbf{d}}$ can be expressed in terms of a step function $u(z)$, defined as

$$u(z) = \begin{cases} 0 & \text{if } z < 0 \\ 1 & \text{if } z \geq 0 \end{cases} . \tag{D.1}$$

Then, the vector components of $\hat{\mathbf{d}}$ can be written as

$$\hat{d}_x = u(-z), \tag{D.2}$$

$$\hat{d}_y = 0, \tag{D.3}$$

$$\hat{d}_z = u(z), \tag{D.4}$$

where $u(-z)$ is given by

$$u(-z) = \begin{cases} 1 & \text{if } z < 0 \\ 0 & \text{if } z \geq 0 \end{cases} . \tag{D.5}$$

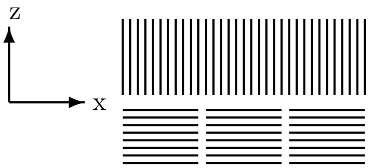

Figure D.1: *Director profile in the bulk region of an uniaxially anisotropic medium with a surface of discontinuity at $z = 0$. If $z < 0$, $\hat{\boldsymbol{d}} = (1,0,0)$, and if $z \geq 0$, $\hat{\boldsymbol{d}} = (0,0,1)$. The refractive indices n_o and n_e are independent of position.*

In addition, the refractive indices of the medium are independent of position. We consider an incident extraordinary light ray with a linear polarization in the xz-plane propagating from the bottom half space $z < 0$ into the upper half space $z \geq 0$. Hence, we can apply the Hamilton equations given by Eqs. 4.40 and 4.41. If we substitute Eqs. D.2-D.4 into Eq. 4.41 we obtain for all z

$$\frac{dp_{ex}}{d\tau} = 0, \tag{D.6}$$

$$\frac{dp_{ey}}{d\tau} = 0, \tag{D.7}$$

$$\begin{aligned} \frac{dp_{ez}}{d\tau} &= -2(n_e^2 - n_o^2) \\ &\times \Big(p_{ex}u(-z) + p_{ez}u(z)\Big)\Big(p_{ex}\delta(z) - p_{ez}\delta(z)\Big), \end{aligned} \tag{D.8}$$

where $\delta(z)$ is the derivative of the step function $u(z)$: the Dirac-delta function. Apparently, $p_{ex}(\tau)$ and $p_{ey}(\tau)$ are constant everywhere. For $z \neq 0$, this result is trivial, since the medium depicted in Fig. D.1 is homogeneous for $z \neq 0$. For $z = 0$, the result matches Snell's law, since Snell's law demands that the tangential vector components of $\mathbf{p}$ are continuous across the plane $z = 0$ (see Eq. 3.4). According to Eq. D.8, we can also conclude that $p_{ez}(\tau)$ is constant for $z \neq 0$. However, $p_{ez}(\tau)$ is discontinuous in the plane $z = 0$, as expected.

Now we consider Eq. 4.40. If we substitute Eqs. D.2-D.4 into Eq. 4.40, we find

$$\begin{aligned} \frac{dx}{d\tau} &= 2n_o^2 p_{ex} \\ &+ 2(n_e^2 - n_o^2)\Big(p_{ex}u(-z) + p_{ez}u(z)\Big)u(-z), \end{aligned} \tag{D.9}$$

$$\frac{dy}{d\tau} = 2n_o^2 p_{ey}, \tag{D.10}$$

$$\begin{aligned} \frac{dz}{d\tau} &= 2n_o^2 p_{ez} \\ &+ 2(n_e^2 - n_o^2)\Big(p_{ex}u(-z) + p_{ez}u(z)\Big)u(z), \end{aligned} \tag{D.11}$$

provided that $z \neq 0$, since $p_{ez}(\tau)$ is discontinuous in $z = 0$. For Eqs. D.9-D.11 it is convenient to apply the identities

$$1 - u(z) = u(-z), \tag{D.12}$$

and

$$u(z)u(-z) = 0. \tag{D.13}$$

Then, for $z \neq 0$, we can rewrite Eqs. D.9-D.11 yielding

$$\begin{aligned} \frac{dx}{d\tau} &= 2n_o^2 p_{ex} + 2(n_e^2 - n_o^2) p_{ex} u(-z), && \text{(D.14)} \\ \frac{dy}{d\tau} &= 2n_o^2 p_{ey}, && \text{(D.15)} \\ \frac{dz}{d\tau} &= 2n_o^2 p_{ez} + 2(n_e^2 - n_o^2) p_{ez} u(z). && \text{(D.16)} \end{aligned}$$

Since the vector components of the wave normal $\mathbf{p}_e$ are constant for $z \neq 0$, Eqs. D.14-D.16 suggest that the ray path is represented by a straight line. For $z < 0$, Eqs. D.14-D.16 can be further reduced to the form

$$\frac{d\mathbf{r}}{d\tau} = 2\left(n_e^2 p_{ex}, n_o^2 p_{ey}, n_o^2 p_{ez}\right) = \nabla_p \mathcal{H}_e\big|_{\hat{\mathbf{d}}=(1,0,0)}, \tag{D.17}$$

while for $z > 0$, Eqs. D.14-D.16 yield

$$\frac{d\mathbf{r}}{d\tau} = 2\left(n_o^2 p_{ex}, n_o^2 p_{ey}, n_e^2 p_{ez}\right) = \nabla_p \mathcal{H}_e\big|_{\hat{\mathbf{d}}=(0,0,1)}. \tag{D.18}$$

If we define $p_{ey} = 0$, we find that $y(\tau)$ is constant. This means that the ray path will lie in a plane parallel to the xz-plane. Note that this statement is only true for the director profile as defined in Fig. D.1, where the directors are also parallel to the xz-plane. If the directors would have a y-component, the ray path can also have a y-component.

By example, we define $\mathbf{p} = (0, 0, p_{ez})$. As a result, taking into account the discontinuity for p_{ez} at $z = 0$ (see Eq. D.8), Eqs. D.14-D.16 reduce to

$$\begin{aligned} \frac{dx}{d\tau} &= 0, && \text{(D.19)} \\ \frac{dy}{d\tau} &= 0, && \text{(D.20)} \\ \frac{dz}{d\tau} &= \begin{cases} 2n_o^2 p_{ez} & \text{if } z < 0 \\ 2n_e^2 p_{ez} & \text{if } z > 0 \end{cases}. && \text{(D.21)} \end{aligned}$$

From these equations for the ray path we can conclude that the extraordinary light ray is propagating in the z-direction for all values of the coordinate z. Only the speed of the light ray is altered when crossing the discontinuity surface at $z = 0$. We define the speed for $z < 0$ as v_1 and the speed for $z > 0$ as v_2. In addition, by reading Fig. D.1, p_{ez} must satisfy $p_{ez} = n_e$ for $z < 0$ and $p_{ez} = n_o$ for $z > 0$. Then from Eq. D.21 we conclude that the ratio of v_1 and v_2 yields

$$\frac{v_1}{v_2} = \frac{n_o}{n_e}. \tag{D.22}$$

This result is equivalent to the case when a light ray crosses the boundary between two isotropic media, having indices of refraction n_e and n_o.

Altogether, we have shown that the Hamilton equations applied to a surface of discontinuity are not in contradiction with Snell's law. Moreover, for the homogeneous director profile defined in Fig. D.1, the Hamilton equations give rise to a position-independent wave normal. Therefore the ray paths of light rays are represented by straight lines. We can conclude that the Hamilton equations are not in contradiction with the rules of geometrical optics when applied to a surface of discontinuity.

When the ray path in the bulk region of Fig. D.1 is calculated numerically, we first define an initial wave normal $\mathbf{p}(\tau_0)$ at an initial position $\mathbf{r}(\tau_0)$. Then we can apply the Runge-Kutta method to calculate the ray path $\mathbf{r}(\tau)$ and the corresponding wave normal $\mathbf{p}(\tau)$ for $\tau = \tau_0 + K\triangle\tau$, with $K \in \mathbb{N}$. According to Eqs. D.6-D.8, the wave normal is constant for $z \neq 0$ and undefined for $z = 0$. Therefore, for all values of $\tau = \tau_0 + K\triangle\tau$ (except for τ with $z(\tau) = 0$), the Hamilton equations give rise to a wave normal $\mathbf{p}(\tau) = \mathbf{p}(\tau_0)$. However, $\mathbf{p}(\tau_0)$ cannot satisfy $\mathcal{H} = 0$ for both $z < 0$ and $z > 0$ at the same time, unless the director $\hat{\mathbf{d}}$ is the same on both sides of the plane $z = 0$. Hence the corresponding ray path $\mathbf{r}(\tau)$ must be incorrect. In order to find the correct wave normals at the surface of discontinuity, we must apply the theory for anisotropic interfaces discussed in Chapter 3.

In general, we conclude that in theory, the Hamilton equations are not in contradiction with the rules of geometrical optics when applied to a surface of discontinuity in the bulk region of (in)homogeneous anisotropic media. However, in the ray-tracing procedure the Hamilton equations alone cannot provide the wave normal on both sides of a discontinuity surface. To find the wave normals on either side of a discontinuity surface, we need the theory discussed in Chapter 3. Then a surface of discontinuity can also be interpreted as an interface (rather than a bulk feature) between two homogeneous anisotropic media with different anisotropic properties. These conclusions support the condition (mentioned in Section 2.3) that in the bulk region we only consider anisotropic media for which there are no discontinuities and condition 2.18 is satisfied.

Appendix E

Mode independency and adiabatic propagation

Here we discuss two important consequences of geometrical optics: the mode independency and the adiabatic propagation of light rays in (an)isotropic media. These properties apply to light rays in both homogeneous and inhomogeneous non-absorbing media, provided that condition 2.18 is satisfied.

Mode independency

When a ray incident to an interface between two anisotropic media is refracted, there are in general two refracted wave normals. Each of these wave normals at the interface is considered an initial wave normal at 'time' $\tau = \tau_0$ for the ray-tracing procedure in the bulk region. The Hamilton equations then result in two independent light rays. Both light rays have a linear polarization state (in case of a real symmetric permittivity tensor), but in general have different polarization vectors. This mutual independency of rays in (an)isotropic media is called mode independency.

The mode independency of rays in the bulk region is particularly well demonstrated by the Hamilton equations for uniaxially anisotropic media. For uniaxial anisotropy, the Hamiltonian reads $\mathcal{H} = \mathcal{H}_o\mathcal{H}_e$. As a result, for extraordinary rays, the Hamilton equations only depend on the extraordinary Hamiltonian $\mathcal{H}_e$ (see Eqs. 4.26 and 4.27) whereas for ordinary rays the Hamilton equations solely depend on the ordinary Hamiltonian $\mathcal{H}_o$ (see Eqs. 4.30 and 4.31). This means that once a ray is, for example, ordinary, it will stay ordinary and, in geometrical optics, there is no reason whatsoever for an ordinary ray to become extraordinary, except at a surface of discontinuity. Hence the mode independency in geometrical optics does not apply at a surface of discontinuity.

Moreover, the mode independency is valid only to some approximation. Consider the limit where the birefringence $\triangle n \rightarrow 0$. Under these circumstances, two rays can interact after being refracted at an anisotropic interface. In this case, the anisotropy can be considered as a weak disturbance of the isotropic properties of the medium. The latter is called a quasi-isotropic approximation (cf. [105], p. 251). However, in this treatise, we will assume that mode independency applies in general provided that the birefringence

$\triangle n$ is sufficiently high.

Adiabatic propagation

Since the material properties in the bulk region are assumed to be continuous, the amplitude A and phase δ of a light ray are constant along the ray path. Then we say that the propagation of a ray in the bulk region is adiabatic. In other words, the total energy flow of a light ray is conserved and no energy is lost along the ray path.

To better understand this feature, we conduct a numerical experiment, of which the outcome is determined by a sequence of calculations. We consider a light ray traveling inside an uniaxially anisotropic medium with arbitrary position-independent n_o and n_e. In the medium, the director is rotated as a function of the coordinate z from the direction (0,0,1) at $z = 0$ towards the direction (1,1,0) at $z = h$ in the plane $x = y$ (see Fig. E.1). This rotation is described by a stepwise rotation. With each step, we define an artificial anisotropic interface with local normal vector $\hat{\mathbf{n}} = (0, 0, 1)$. We define the total number of steps, which is equivalent to the total number of artificial anisotropic interfaces, as the integer K with $K \in \mathbb{N}$. For step k, with $k = 1, ..., K$, the directors $\hat{\mathbf{d}}_{k-1}$ and $\hat{\mathbf{d}}_k$ are the directors on both sides of the anisotropic interface. If K has a small value, the dot product of $\hat{\mathbf{d}}_{k-1}$ and $\hat{\mathbf{d}}_k$ is expected to approach zero. On the other hand, if K has a large value, the dot product of $\hat{\mathbf{d}}_{k-1}$ and $\hat{\mathbf{d}}_k$ is expected to approach the value 1. In other words, in the limit where $K \to \infty$, $\hat{\mathbf{d}}_{k-1} = \hat{\mathbf{d}}_k$ so that the material properties change continuously per unit length in the bulk region of the medium.

Consider Fig. E.1. We will examine an incident ray with a normalized Poynting vector $\langle \hat{\mathbf{S}}_{inc} \rangle = \frac{1}{2}\sqrt{2}(0, 1, 1)$ and polarization vector $\hat{\mathbf{E}}_{inc} = (1, 0, 0)$ at $z = 0$. The refracted ray at $z = 0$ is then ordinary, since there $\hat{\mathbf{d}} = (0, 0, 1)$. We define $K = 10$, which means that the step size of the rotation of $\hat{\mathbf{d}}$ is 9°. For each step, we calculate the refracted Poynting vector $\langle \mathbf{S}_o \rangle$ for the ordinary ray at the artificial anisotropic interface with the help of the classical theory discussed in Chapter 3. In addition, we calculate the corresponding polarization vector $\hat{\mathbf{E}}_o$. Since $\hat{\mathbf{d}}$ is not in the plane of incidence for $z > 0$, the refraction of the ordinary ray at each artificial interface gives rise to both ordinary and extraordinary rays. Therefore, the intensity transmittance factor for the ordinary ray at an interface is smaller than 1. After K steps, when $\hat{\mathbf{d}} = (1, 1, 0)$, $\langle \hat{\mathbf{S}}_o \rangle = \frac{1}{2}\sqrt{2}(0, 1, 1)$ and $\hat{\mathbf{E}}_o = \frac{1}{\sqrt{3}}(-1, 1, -1)$, see Fig. E.1. Apparently, the direction of propagation has not changed, which is what we expect for an ordinary ray after K successive refractions at K parallel anisotropic interfaces with constant position-independent n_o.

In addition to the polarized ray tracing, we calculate the intensity transmittance factor T_o of the ordinary ray for each step. Then, for step k_z at position z, the total intensity transmittance factor is:

$$T_{\text{tot}} = \prod_{k=1}^{k_z} T_{ok}, \tag{E.1}$$

where $1 \leq k_z \leq K$. Fig. E.2 shows T_{tot} as a function of the step k_z for $K = 10$, $K = 100$, $K = 1000$ and $K = 10000$. From the results we can conclude that $T_{\text{tot}} \to 1$ if $K \to \infty$. As a result, if the material properties change continuously with position, the ordinary light ray propagates adiabatically in the bulk region of the medium. Then the

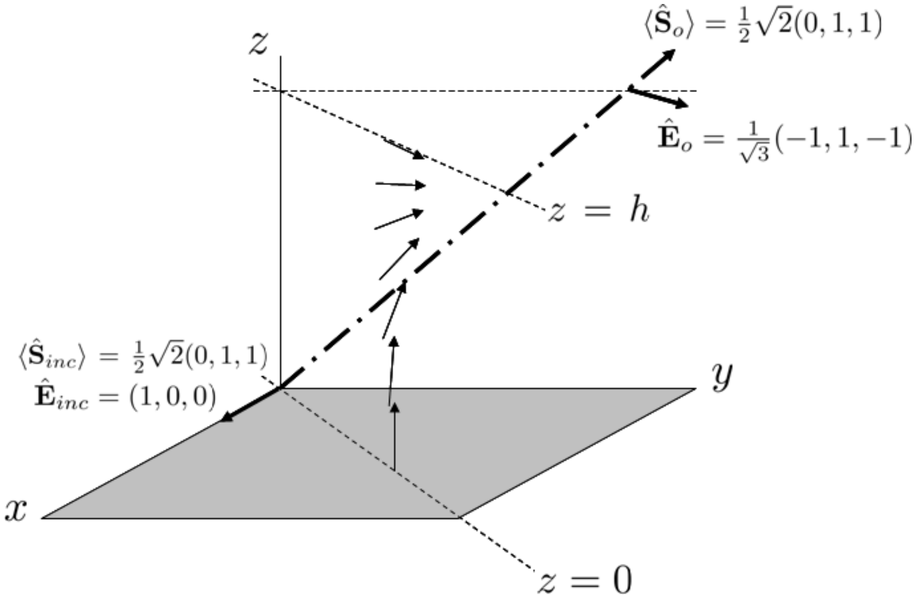

Figure E.1: *Anisotropic medium with thickness h in which the director is a function of the coordinate z. The rotation of the director is defined by K steps in the plane $x = y$, from $\hat{\boldsymbol{d}} = (0,0,1)$ at $z = 0$ to $\hat{\boldsymbol{d}} = (1,1,0)$ at $z = h$. In between two arbitrary successive steps we define an artificial anisotropic interface with local normal vector $\hat{\boldsymbol{n}} = (0,0,1)$. We consider an incident ray at $z = 0$ with a normalized Poynting vector $\langle \hat{\boldsymbol{S}}_{inc} \rangle = \frac{1}{2}\sqrt{2}(0,1,1)$ and polarization vector $\hat{\boldsymbol{E}}_{inc} = (1,0,0)$. Hence, the refracted ray at $z = 0$ is ordinary. When the ordinary ray arrives at $z = h$, the normalized Poynting vector is $\langle \hat{\boldsymbol{S}}_o \rangle = \frac{1}{2}\sqrt{2}(0,1,1)$ and the ordinary polarization vector is $\hat{\boldsymbol{E}}_o = \frac{1}{\sqrt{3}}(-1,1,-1)$.*

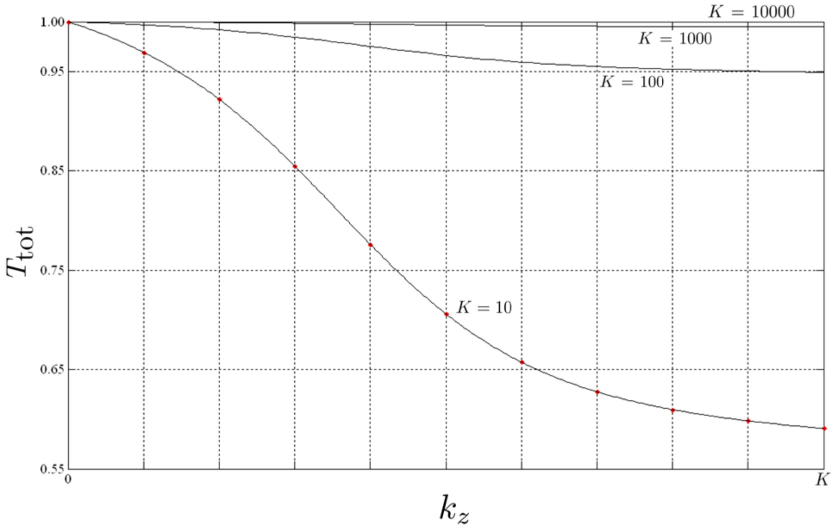

Figure E.2: *The total intensity transmittance factor T_{tot} as a function of the step k_z at height z. In the figure, we show the results for different values of the total number of steps K, namely $K = 10$, $K = 100$, $K = 1000$ and $K = 10000$. From the results we can conclude that $T_{tot} \to 1$ for any k_z if $K \to \infty$.*

total energy is confined to the ordinary light ray only and there is no extraordinary light present in the medium.

According to the numerical experiment conducted above, we can conclude that in the limit where the material properties change continuously with position in the bulk region a light ray propagates adiabatically.

Appendix F

Transport equations

In the following discussion, we will discuss the Maxwell equations for arbitrary values of k_0.

With the quasi-plane wave as a general solution of the electromagnetic wave field (see Eqs. 2.11 and 2.12), the Maxwell equations are of the form

$$\begin{aligned} \nabla\psi \times \tilde{\mathbf{H}} + c\varepsilon_0 \underline{\underline{\varepsilon}}\tilde{\mathbf{E}} &= -\frac{1}{ik_0}\nabla \times \tilde{\mathbf{H}}, && \text{(F.1)} \\ \nabla\psi \times \tilde{\mathbf{E}} - c\mu_0 \tilde{\mathbf{H}} &= -\frac{1}{ik_0}\nabla \times \tilde{\mathbf{E}}, && \text{(F.2)} \\ \nabla\psi \cdot \underline{\underline{\varepsilon}}\tilde{\mathbf{E}} &= -\frac{1}{ik_0}\nabla \cdot \underline{\underline{\varepsilon}}\tilde{\mathbf{E}}, && \text{(F.3)} \\ \nabla\psi \cdot \tilde{\mathbf{H}} &= -\frac{1}{ik_0}\nabla \cdot \tilde{\mathbf{H}}. && \text{(F.4)} \end{aligned}$$

In the geometrical optics, we are interested in solutions of the wave field for large values of k_0. However, for the moment, we do not make this approximation and explore the full Maxwell equations. When we combine Eqs. F.1 and F.2 and eliminate $\tilde{\mathbf{H}}$ we find (see also [6], p. 112):

$$\begin{aligned} &\nabla\psi \times (\nabla\psi \times \tilde{\mathbf{E}}) + \underline{\underline{\varepsilon}}\tilde{\mathbf{E}} + \frac{1}{ik_0}\left[\nabla\psi \times (\nabla \times \tilde{\mathbf{E}}) + \nabla \times (\nabla\psi \times \tilde{\mathbf{E}})\right] \\ &+\left(\frac{1}{ik_0}\right)^2 \left[\nabla \times (\nabla \times \tilde{\mathbf{E}})\right] = 0. \qquad \text{(F.5)} \end{aligned}$$

In the limit where $k_0 \rightarrow \infty$, we obtain Eq. 2.27, the 'eikonal equation' for media with electrical anisotropy in the geometrical-optics approach. Apparently, the full Maxwell equations result in an equation that is significantly more complex than Eq. 2.27.

A widely used approach consists of expanding the wave amplitude in powers of $\frac{1}{ik_0}$:

$$\tilde{\mathbf{E}}(\mathbf{r}) = \sum_{m=0}^{\infty} \left(\frac{1}{ik_0}\right)^m \tilde{\mathbf{E}}_m(\mathbf{r}). \qquad \text{(F.6)}$$

This type of series expansion is called a Debye expansion (cf. [105], p. 7). When we substitute Eq. F.6 into Eq. F.5 and collect the coefficients of terms of equal power in $\frac{1}{ik_0}$, we obtain a set of first-order partial differential equations. These equations are called the transport equations. The zeroth-order transport equation is given by

$$\nabla\psi \times (\nabla\psi \times \tilde{\mathbf{E}}_0) + \underline{\underline{\varepsilon}}\tilde{\mathbf{E}}_0 = 0, \tag{F.7}$$

while the first-order transport equation reads

$$\begin{aligned}&\nabla\psi \times (\nabla\psi \times \tilde{\mathbf{E}}_1) + \underline{\underline{\varepsilon}}\tilde{\mathbf{E}}_1\\ &+\nabla\psi \times (\nabla \times \tilde{\mathbf{E}}_0) + \nabla \times (\nabla\psi \times \tilde{\mathbf{E}}_0) = 0.\end{aligned} \tag{F.8}$$

The higher-order transport equations are given by

$$\begin{aligned}&\nabla\psi \times (\nabla\psi \times \tilde{\mathbf{E}}_m) + \underline{\underline{\varepsilon}}\tilde{\mathbf{E}}_m\\ &+\nabla\psi \times (\nabla \times \tilde{\mathbf{E}}_{m-1}) + \nabla \times (\nabla\psi \times \tilde{\mathbf{E}}_{m-1})\\ &+\nabla \times (\nabla \times \tilde{\mathbf{E}}_{m-2}) = 0,\end{aligned} \tag{F.9}$$

where the index $m \geq 2$. In the geometrical-optics approach, the optical wave field satisfies the zeroth-order transport equation. The higher-order transport equations define the higher-order corrections to the zeroth-order wave field.

References

[1] F.L. Pedrotti and L.S. Pedrotti, *Introduction to optics* (Prentice Hall, 1996).

[2] David R. Lide, *Handbook of Chemistry and Physics* (Taylor & Francis Group, 2006).

[3] E. Hecht, *Optics* (Addison Wesley, 2002).

[4] The calcite sample was provided by Remco Duits.

[5] P. Yeh and C. Gu, *Optics of Liquid Crystal Displays* (John Wiley & Sons, 1999).

[6] M. Born and E. Wolf, *Principles of Optics* (Pergamon Press, 1986).

[7] S. Chandrasekhar, *Liquid Crystals* (Cambridge University Press, 1992).

[8] L.M. Blinov, *Electro-optical and magneto-optical properties of liquid crystals* (John Wiley & Sons, 1983).

[9] P.J. Collings and M. Hird, *Introduction to liquid crystals, Chemistry and Physics* (Taylor & Francis, 1997).

[10] The Merck group, chemicals, www.merck.de.

[11] T.J. Sluckin, D.A. Dunmur and H. Stegemeyer, *Crystals that flow: Classic papers from the history of liquid crystals* (Taylor & Francis, 2004).

[12] ISI Web of Knowledge, databases inspec, compendex and pascal (20-02-2009).

[13] Giallorenzi et al., "Liquid crystal switch for optical waveguide," U.S. patent 3980395 (1976).

[14] Liu et al., "Liquid crystal fiber waveguide," U.S. patent 5361320 (1994).

[15] Boissier et al., "Liquid crystal-based electro-optical device forming, in particular, a switch," U.S. patent 6959124B2 (2005).

[16] Q. Wang, G. Farrell and Y. Semenova, "Design of integrated polarization beam splitter with liquid crystal," IEEE J. Selec. Top. Quant. Elect. **12**, 1349-1353 (2006).

[17] Gu et al., "Optical fiber coupling having liquid crystal adaptive coupler," U.S. patent 7260286 (2007).

[18] Okuwaki et al., "Liquid crystal microlens," U.S. patent 6768536B2 (2004).

[19] E. Hällstig, J. Stigwall, M. Lindgren and L. Sjöqvist, "Laser beam steering and tracking using a liquid crystal spatial light modulator," Proc. SPIE **5087**, 13-23 (2003).

[20] P.J.W. Hands, S.M. Morris, T.D. Wilkinson and H.J. Coles, "Liquid crystal laser arrays," 2nd Int. Workshop on Liquid Crystals for Photonics, book of abstracts, 44-45 (2008).

[21] Okada et al., "Liquid crystal spectacles," U.S. patent 4756605 (1988).

[22] Wang-lee et al., "Eyeshield for a welder's mask," U.S. patent 6021520 (2000).

[23] Tournilhac et al., "Cosmetic composition structured by a thermotropic liquid crystal polymer," U.S. patent 7153517B2 (2006).

[24] D.F. McAllister, *Stereoscopic computer graphics and other true 3D technologies* (Princeton University Press, 1993).

[25] S.T. de Zwart, W.L. IJzerman, T. Dekker and W.A.M. Wolter, "A 20" switchable auto-stereoscopic 2D/3D display," 11th Int. Display Workshop, 1459-1460 (2004).

[26] W.L. IJzerman, S.T. de Zwart and T. Dekker, "Design of 2D/3D switchable displays," J. SID **36/1**, 98-101 (2005).

[27] D.K.G. de Boer, M.G.H. Hiddink, M. Sluijter, O.H. Willemsen and S.T. de Zwart, "Switchable lenticular-based 2D/3D displays," Proc. of SPIE **6490**, 64900R (2007).

[28] J. Stroemer, G. Cennini, M. Sluijter and D.K.G. de Boer, "A novel light guide structure capable of local light outcoupling," to be published.

[29] H.J. Cornelissen, H.P.M. Huck, D.J. Broer, S.J. Picken, C.M.W. Bastiaansen, E. Erdhuizen and N. Maaskant, "Polarized light LCD backlight based on liquid crystalline polymer film: a new manufacturing proces," SID 04 Digest, 1178-1181 (2004).

[30] B.R. Acharya, A. Primak and S. Kumar, "Biaxial nematic phase in bent-core thermotropic mesogens," Phys. Rev. Lett. **92**, 145506 (2004).

[31] L.A. Madsen, T.J. Dingemans, M. Nakata and E.T. Samulski, "Thermotropic biaxial nematic liquid crystals," Phys. Rev. Lett. **92**, 145505 (2004).

[32] G.R. Luckhurst, "A missing phase found at last?" Nature **430**, 413-414 (2004).

[33] S. Kumar, "Biaxial liquid crystal electro-optic devices," U.S. patent WO/2007/025111 (2007).

[34] R.C. Jones, "New calculus for the treatment of optical systems. I. Description and discussion of the calculus," J. Opt. Soc. Am. **31**, 488-493 (1941).

[35] D.W. Berreman, "Optics in stratified and anisotropic media: 4×4-matrix formulation," J. Opt. Soc. Am. **62**, 502-510 (1972).

[36] P. Yeh, "Extended Jones matrix method," J. Opt. Soc. Am. **72**, 507-513 (1982).

[37] K. Yee, “Numerical solution of initial boundary value problems involving Maxwell’s equations in isotropic media,” IEEE Transactions on Antennas and Propagation **14**, 302-307 (1966).

[38] J. Schneider and S. Hudson, “The finite-difference time-domain method applied to anisotropic material,” IEEE Transactions on Antennas and Propagation **41**, 994-999 (1993).

[39] E.E. Kriezis and S.J. Elston, “Finite-difference time domain method for light wave propagation within liquid crystal devices,” Optics Communications **165**, 99-105 (1999).

[40] E.E. Kriezis and S.J. Elston, “A wide-angle beam propagation method for the analysis of tilted nematic liquid crystal structures,” J. Mod. Opt. **46**, 1201-1212 (1999).

[41] W. Qian, G. Farrell and Y. Semenova, “Modeling liquid-crystal devices with the three-dimensional full-vector beam propagation method,” J. Opt. Soc. Am. A **23**, 2014-2019 (2006).

[42] L. Li, “Reformulation of the Fourier modal method for surface-relief gratings made with anistropic materials,” J. Mod. Opt. **45**, 1313-1334 (1998).

[43] L. Li, “Fourier modal method for crossed anisotropic gratings with arbitrary permittivity and permeability tensors,” J. Opt. A: Pure Appl. Opt. **5**, 345-355 (2003).

[44] M. Xu, “Diffractive optics of anisotropic polarization gratings,” Ph.D. Thesis, Delft University of Technology, Lorentzweg 1, 2628 CJ Delft (2009).

[45] O.N. Stavroudis, “Ray-tracing formulas for uniaxial crystals,” J. Opt. Soc. Am. **52**, 187-191 (1962).

[46] W. Swindell, “Extraordinary-ray and -wave tracing in uniaxial crystals,” Appl. Opt **14**, 2298-2301 (1975).

[47] M.C. Simon, “Ray tracing formulas for monoaxial optical components,” Appl. Opt. **22**, 354-360 (1983).

[48] M.C. Simon and R.M. Echarri, “Ray tracing formulas for monoaxial optical components: vectorial formulation,” Appl. Opt. **25**, 1935-1939 (1986).

[49] M.C. Simon and R.M. Echarri, “Inhibited reflection in uniaxial crystals,” Opt. Lett. **14** 257-259 (1989).

[50] Q.T. Liang, “Simple ray tracing formulas for uniaxial optical crystals,” Appl. Opt. **29**, 1008-1010 (1990).

[51] J.D. Trolinger, R.A. Chipman and D.K. Wilson, “Polarization ray tracing in birefringent media,” Opt. Eng. **30**, 461-465 (1991).

[52] M.C. Simon and L.I. Perez, “Reflection and transmission coefficients in uniaxial crystals,” J. Mod. Opt. **38**, 503-518 (1991).

[53] Wei-Quan Zhang, "General ray-tracing formulas for crystal," Appl. Opt. **31**, 7328-7331 (1992).

[54] D.J. de Smet, "Brewster's angle and optical anisotropy," Am. J. Phys. **62**, 246-248 (1993).

[55] John Lekner, "Brewster angles in reflection by uniaxial crystals," Am. J. Phys. **10**, 2059-2064 (1993).

[56] S.C. McClain, L.W. Hillman and R.A. Chipman, "Polarization ray tracing in anisotropic optically active media. I Algorithms," J. Opt. Soc. Am. A **10**, 2371-2382 (1993).

[57] S.C. McClain, L.W. Hillman and R.A. Chipman, "Polarization ray tracing in anisotropic optically active media. II Theory and physics," J. Opt. Soc. Am. A **10**, 2383-2392 (1993).

[58] H.A. Buchdahl, *An introduction to Hamiltonian optics* (Courier Dover, 1993).

[59] Z. Shao and C. Yi, "Behavior of extraordinary rays in uniaxial crystals," Appl. Opt. **33**, 1209-1212 (1994).

[60] Z. Shao, "Refractive indices for extraordinary waves in uniaxial crystals," Phys. Rev. E **25**, 1043-1048 (1995).

[61] A.L. Rivera, S.M. Chumakov and K.B. Wolf, "Hamiltonian foundation of geometrical anisotropic optics," J. Opt. Soc. Am. A **12**, 1380-1389 (1995).

[62] Z. Zhang and H.J. Caulfield, "Reflection and refraction by interfaces of uniaxial crystals," Opt. & Laser Tech. **28**, 549-553 (1996).

[63] G.D. Landry and T.A. Maldonado, "Ray tracing through a two ball uniaxial sapphire lens system in a single mode fiber-to-fiber coupler," J. Lightwave Tech. **14**, 509-512 (1996).

[64] E. Cojocaru, "Direction cosines and vectorial relations for extraordinary-wave propagation in uniaxial media," Appl. Opt. **36**, 302-306 (1997).

[65] G. Beyerle and I.S. McDermid, "Ray-tracing formulas for refraction and internal reflection in uniaxial crystals," Appl. Opt. **37**, 7947-7953 (1998).

[66] John Lekner, "Reflection by uniaxial crystals: polarizing angle and Brewster angle," J. Opt. Soc. Am. A **16**, 2763-2766 (1999).

[67] Yi-Jun Jen and Cheng-Chung Lee, "Reflection and transmission phenomena of waves propagating between an isotropic medium and an arbitrarily oriented anisotropic medium," Opt. Lett. **26**, 190-192 (2001).

[68] K.V. Gottschalk and M.C. Simon, "Electric polarization and its relationship to Brewster's angle for interfaces with uniaxial crystals," J. Opt. Soc. Am. A **18**, 673-677 (2001).

[69] M. Avendaño-Alejo and O.N. Stavroudis, "Huygens's principle and rays in uniaxial anisotropic media. I. Crystal axis normal to refracting surface," J. Opt. Soc. Am. A **19**, 1668-1673 (2002).

[70] M. Avendaño-Alejo and O.N. Stavroudis, "Huygens's principle and rays in uniaxial anisotropic media. II. Crystal axis orientation arbitrary," J. Opt. Soc. Am. A **19**, 1674-1679 (2002).

[71] G. Panasyuk, J.R. Kelly. E.C. Gartland and D.W. Allender, "Geometrical-optics approach in liquid crystal films with three-dimensional director variations," Phys. Rev. E **67**, 041702 (2003).

[72] G. Panasyuk, J.R. Kelly, P. Bos, E.C. Gartland and D.W. Allender, "The geometrical-optics approach for multidimensional liquid crystal cells," Liquid Crystals **31**, 1503-1515 (2004).

[73] Lu Yonghua, Wang Pei, Yao Peijun, Xie Jianping and Ming Hai, "Negative refraction at the interface of uniaxial anisotropic media," Opt. Commun. **246**, 429-435 (2005).

[74] M. Avendaño-Alejo, "Analysis of the refraction of the extraordinary ray in a plane-parallel uniaxial plate with an arbitrary orientation of the optical axis," Opt. Exp. **13**, 2549-2555 (2005).

[75] M. Kline and I.W. Kay, *Electromagnetic theory and geometrical optics* (John Wiley & Sons, 1965).

[76] M.C. Simon, "Refraction in biaxial crystals: a formula for the indices," J. Opt. Soc. Am. A **4**, 2201-2204 (1987).

[77] T.A. Maldonado and T.K. Gaylord, "Light propagation characteristics for arbitrary wavevector directions in biaxial media by a coordinate-free approach," Appl. Opt. **30**, 2465-2480 (1991).

[78] D.B. Walker, E.N. Glytsis and T.K. Gaylord, "Surface mode at isotropic-uniaxial and isotropic-biaxial interfaces," J. Opt. Soc. Am. A **15**, 248-260 (1998).

[79] J.J. Stamnes, G.S. Sithambaranathan, "Reflection and refraction of an arbitrary electromagnetic wave at a plane interface separating an isotropic and a biaxial medium," J. Opt. Soc. Am. A **18**, 3119-3129 (2001).

[80] F. Yang, H. Gao and J.R. Sambles, "Relations between the critical angles and the optical tensor of a biaxial material," Appl. Opt. **41**, 7264-7274 (2002).

[81] C. Bellver-Cebreros and M. Rodriguez-Danta, "Amphoteric refraction at the isotropic-anisotropic biaxial media interface: an alternative treatment," J. Opt. A: Pure Apll. Opt. **8**, 1067-1073 (2006).

[82] Y. Wang, P. Shi, H. Xin and L. Wu, "Complex ray tracing in biaxial anisotropic absorbing media," J. Opt. A: Pure Appl. Opt. **10**, 1-7 (2008).

[83] L.D. Landau, E.M. Lifshitz and L.P. Pitaevskiĭ, *Electrodynamics of Continuous Media* (Butterworth-Heinemann, 1984).

[84] E.U. Condon, "Theories of optical rotatory power," Rev. Mod. Phys. **9**, 432-457 (1937).

[85] M.J. Gunning and R.E. Raab, "Systematic eigenvalue approach to crystal optics: an analytic alternative to the geometric ellipsoid model," J. Opt. Soc. Am. A **15**, 2199-2207 (1998).

[86] A. Sommerfeld and J. Runge, "Anwendung der Vektorrechnung auf die Grundlagen der Geometrischen Optiek," Ann. Phys. **35**, 277-298 (1911).

[87] L. Fletcher, *The optical indicatrix and the transmission of light in crystals* (Oxford University Press, 1892).

[88] W.R. Hamilton, "On a mode of deducing the equation of Fresnel's wave," Philosophical Magazine **19**, 381-383 (1841).

[89] J.J. Stamnes, G.S. Sithambaranathan, "Reflection and refraction of an arbitrary electromagnetic wave at a plane interface separating an isotropic and a biaxial medium," J. Opt. Soc. Am. A **18**, 3119-3129 (2001).

[90] W. Press et al., *Numerical recipes in FORTRAN, The art of Scientific Computing* (Cambridge University Press, 1992).

[91] L.W. Griffiths, *Introduction to the theory of equations* (John Wiley & Sons, 1946).

[92] J.D. Jackson, *Classical electrodynamics* (John Wiley & Sons, 1999).

[93] MatLab, The language of technical computing, *http://www.mathworks.com.*

[94] M.V. Berry, M.R. Jeffrey and J.G. Lunney, "Conical diffraction: observation and theory," Proc. R. Soc. A **462**, 1629-1642 (2006).

[95] M.V. Berry, "Conical diffraction asymptotics: fine structure of Pogendorff rings and axial spike," J. Opt. A: Pure Appl. Opt. **6**, 289-300 (2004).

[96] J.G. Lunney and D. Weaire, "The ins and outs of conical refraction," Europhysics News **37**, 26-29 (2006).

[97] M.V. Berry and M.R. Jeffrey, "Conical diffraction: Hamilton's diabolical point at the hart of crystal optics," Progress in Optics **50**, 13-50 (2007).

[98] M. Totzeck, W. Ulrich, A. Göhnermeier and W. Kaiser, "Pushing deep ultraviolet lithography to its limits," Nature Photonics **1**, 629-631 (2007).

[99] Melles Griot, *http://www.mellesgriot.com/products/optics/mp_3_5.htm.*

[100] Prof. dr. ir. J.J.M. Braat, *personal communication* (2007).

[101] J.J.M. Braat, A. Smid and M.M.B. Wijnakker, "Design and production technology of replicated aspheric objective lenses for optical disk systems," Appl. Opt. **24**, 1853-1855 (1985).

[102] M. Sluijter, D.K.G. de Boer and J.J.M. Braat, "General polarized ray-tracing method for inhomogeneous uniaxially anisotropic media," J. Opt. Soc. Am. A **25**, 1260-1273 (2008).

[103] M. Sluijter, D.K.G. de Boer and H.P. Urbach, "Ray-optics analysis of inhomogeneous biaxially anisotropic media," J. Opt. Soc. Am. A **26**, 317-329 (2009).

[104] M. Sluijter, D.K.G. de Boer and H.P. Urbach, "Ray-tracing simulations of liquid-crystal devices," Mol. Cryst. Liq. Cryst. **502**, 164-177 (2009).

[105] Y.A. Kravtsov and Y.I. Orlov, *Geometrical optics of inhomogeneous media* (Springer-Verlag, 1990).

[106] T.C. Kraan, T. van Bommel and R.A.M. Hikmet, "Modeling liquid-crystal gradient-index lenses," J. Opt. Soc. Am. A **24**, 3467-3477 (2007).

[107] M. Xu, L. Sio, R. Caputo, C.P. Umeton, A.J.H. Wachters, D.K.G. de Boer and H.P. Urbach, "Characterization of the diffraction efficiency of polymer-liquid-crystal-polymer-slices gratings at all incidence angles," Opt. Exp. **16**, 14532-14543 (2008).

[108] S. van Haver, *On the optical design of 3D displays*, Report Philips Research, TN-2005/00134 (2005).

[109] O.H. Willemsen, S.T. de Zwart and W.L. IJzerman, "Fractional viewing systems to reduce banding in lenticular-based 3D displays," 12^{th} Int. Display Workshop, 1789-1792 (2005).

[110] M. Sluijter, W.L. IJzerman, D.K.G. de Boer and S.T. de Zwart, "Residual lens effects in 2D mode of auto-stereoscopic lenticular-based switchable 2D/3D displays," Proc. of SPIE **6196**, 61960I (2006).

[111] W.L. IJzerman, S.T. de Zwart and M. Sluijter, "Oscopic display device using controllable liquid crystal lens array for 3D/2D mode switching," patent pub. no. WO/2007/099488 (2007).

[112] M.P.C.M. Krijn, S.T. de Zwart, D.K.G. de Boer, O.H. Willemsen and M. Sluijter, "2D/3D displays based on switchable lenticulars," J. SID **16**, 847-855 (2008).

[113] H. Hong, S. Jung, B. Lee and H. Shin, "Electric-field-driven LC lens for 3-D/2-D autostereoscopic display," J. SID **17/5**, 399-406 (2009).

[114] SHINTECH.Inc, http://www.shintech.jp.

[115] AUTRONIC MELCHERS GmbH, http://www.autronic-melchers.com.

[116] S. Sato, "LC-lens cell with variable focal length," Jpn. J. Appl. Phys. **18**, 1679-1684 (1979).

[117] D. W. Berreman, "Variable-focus LC-lens system," U.S. patent 4190330 (1980).

[118] S.T. Kowel, D.S. Clevery and P.G. Kornreich, "Focussing by electrical modulation of refraction in a liquid crystal cell," Appl. Opt. **23**, 278-289 (1984).

[119] P.F. Brinkley, S.T. Kowel and C. Chu, “Liquid crystal adaptive lens: beam translation and field meshing,” Appl. Opt. **27**, 4578-4586 (1988).

[120] J.S. Patel and K. Rastani, “Electrically controlled polarization-independent liquid-crystal Fresnel lens arrays,” Opt. Lett. **16**, 532-534 (1991).

[121] A.F. Naumov, M.Y. Loktev, I.R. Guralnik and G. Vdovin, “Liquid-crystal adaptive lenses with modal control,” Opt. Lett. **23**, 992-994 (1998).

[122] H. Ren and S.T. Wu, “Adaptive liquid crystal lens with focal length tunability,” Opt. Exp. **14**, 11292-11298 (2006).

[123] C. Jenkins, R. Bingham, K. Moore and G.D. Love, “Ray equation for a spatially variable uniaxial crystal and its use in the optical design of liquid-crystal lenses,” J. Opt. Soc. Am. A **24**, 2089-2096 (2007).

[124] G.E. Nevskaya and M.G. Tomilin, “Adaptive lenses based on liquid crystals,” J. Opt. Technol. **75**, 563-573 (2008).

[125] A. Herzog, D.K.G. de Boer and M.P.C.M. Krijn, *Angular-dependence of gradient-index (GRIN) lenses for 3D displays*, Report Philips Research, TN-2008/00698 (2008).

[126] R.A.M. Hikmet, T. van Bommel, T.C. Kraan, L.H.C. Kusters, S.T. de Zwart, O.H. Willemsen and M.P.C.M. Krijn, “Beam-shaping device,” patent pub. no. WO/2008/126049A1 (2008).

[127] L.H.C. Kusters, S.T. de Zwart and M.P.C.M. Krijn, *Liquid-crystal-based graded-index lenses for 3D displays*, Report Philips Research, TN-2006/00972 (2006).

[128] H.B.J. Plasschaert, D.K.G. de Boer and S.T. de Zwart, *Liquid-crystalline gradient-index lenses for 3D displays*, Report Philips Research, TN-2007/00290 (2007).

[129] M. Sluijter, D.K.G. de Boer and H.P. Urbach, “Simulations of a liquid-crystal-based electro-optical switch,” Opt. Lett. **34**, 94-96 (2009).

[130] M. Sluijter, D.K.G. de Boer, H.P. Urbach, J. Stroemer and G. Cennini, “Ray-tracing simulations and applications of liquid crystal beam control devices,” Proc. of SPIE **7232**, 72320S (2009).

[131] J. Beeckman, K. Neyts, X. Hutsebaut, C. Cambournac and M. Haelterman, “Simulation of 2D lateral light propagation in nematic liquid crystal cells with tilted molecules and nonlinear reorientational effect,” Opt. Quant. Electron. **37**, 95-106 (2005).

[132] ELDIM manufacturer of 2D photometers & colorimeters and inspection systems, www.eldim.fr.

Acknowledgements

In the last months of 2005, while finishing my graduation project, a PhD position at Philips Research was offered to me. The initiatives of Wilbert IJzerman, Dick de Boer, Joseph Braat, Mark Overwijk and Emile Aarts created the opportunity for me to do a PhD project in an industrial research environment. For this I would like to express my sincere gratitude. Especially, my Philips supervisor Dick de Boer and promotor Paul Urbach are gratefully acknowledged for the successful cooperation, professional expertise, humor, input and support. I have always considered Dick's physical line of approach and Paul's mathematical point of view as a synergetic combination.

Furthermore, I would like to thank all my colleagues of the Display Applications & Technologies group for their company and support in reviewing papers and reports, brainstorming, doing Friday-afternoon experiments and of course the socializing activities at the coffee corners, lunch tables and corridors. Special thanks to Jan Strömer, Giovanni Cennini, Dick de Boer, Thomas Kraan, Hugo Cornelissen and Romain Esteve with whom I worked together in the framework of the liquid-crystal light guide structure for backlights in LCDs. In particular, I always appreciated the enthusiasm in the frequent discussions I have had with Jan Strömer. The application of liquid crystal in auto-stereoscopic 3D displays forms the essence of two chapters in this thesis. This would not have been possible without the input and support of Dick de Boer, Wilbert IJzerman, Marcel Krijn, Siebe de Zwart, Martin Hiddink, Fetze Pijlman, Oscar Willemsen, Leon Kusters, Helena Plasshaert and Angie Herzog of the 3D project who are gratefully acknowledged. As I write these lines, I realize that I have witnessed the rise and fall of the 3D project. Last but not least, I thank my group manager Ans Saalberg for her enthusiasm, support, feedback and guidance.

During the past four years, I have been a group member of the Optics Research group at the Delft University of Technology. For the few moments I visited the group I always felt welcome which is much appreciated. In particular, I thank Man Xu for our successful cooperation in modeling optical anisotropy and Sven van Haver and Olaf Janssen for good company in the study.

The following people are acknowledged for different reasons: the team members of the football team 'de Oude WYVen', especially my fellow-captains Bernt Meerbeek and Tim Tijs; Willy Wolter, Johan 't Hart and Menno van Baardwijk for preparing liquid-crystal samples in the MiPlaza facilities; Peter Schumaker for discussing the meaning of life; my colleagues Marjolein van der Zwaag, Janneke Verhaegh, Nele van den Ende, Emile Kelkboom and Greg Dunn of the recently started Philips PhD & Postdoc Committee; Ruud Nagelkerke for his help in doing literature searches; Siebe van Mensfoort and Gerrit Kroesen for fruitful discussions; Henny Herps and Frans Schraven for realizing the cover of this thesis; Remco Duits for providing the calcite sample.

Last but not least, my dear parents, Rob and José, my siblings Jeroen and Babette and family are gratefully acknowledged for their mental support. I also appreciate my friends providing their own personal form of mental support. As I write these lines, Marjoke is my bride-to-be and I thank her as well as her family for their engagement. Marjoke, I admire the way in which you have supported me, provided a listening ear, the necessary patience and the jolly good times. You truly are a strong and exceptional woman.

Biography

Maarten Sluijter was born in 1980, in Weert, the Netherlands. In 1999 he obtained his VWO diploma from the Philips van Horne Scholengemeenschap in Weert and started his university education in Applied Physics at the Technical University of Eindhoven. In December 2004, he started his graduation project at Philips Research in Eindhoven. There he worked on the optical modeling of switchable liquid-crystal-based lenticulars for auto-stereoscopic 2D/3D displays. In December 2005 he obtained his MSc degree and as a continuation of his work on modeling optical anisotropy for display applications, he was offered a PhD position in the framework of the Philips Van der Pol program. As a PhD student he was a member of the Display Applications & Technologies group from Philips Research Eindhoven and the Optics Research group from the Delft University of Technology. His work resulted in several publications in renowned scientific journals, conference proceedings, oral presentations at international conferences and co-inventing three patent applications. In February 2009, his publication on the optical modeling of inhomogeneous biaxially anisotropic media appeared on the issue's journal page of the Optical Society of America. When most of the work on his PhD was finished in June 2009, he started a six-month assignment on mapping the technology landscape of energy-efficient buildings at Philips Lighting in Eindhoven.

List of Publications

Refereed journal papers

- M. Sluijter, D.K.G. de Boer and J.J.M. Braat, “General polarized ray-tracing method for inhomogeneous uniaxially anisotropic media,” J. Opt. Soc. Am. A **25**, 1260-1273 (2008).
- M. Sluijter, D.K.G. de Boer and H.P. Urbach, “Ray-optics analysis of inhomogeneous biaxially anisotropic media,” J. Opt. Soc. Am. A **26**, 317-329 (2009).
- M. Sluijter, D.K.G. de Boer and H.P. Urbach, “Simulations of a liquid-crystal-based electro-optical switch,” Opt. Lett. **34**, 94-96 (2009).
- M. Sluijter, D.K.G. de Boer and H.P. Urbach, “Ray-tracing simulations of liquid-crystal devices,” Mol. Cryst. Liq. Cryst. **502**, 164-177 (2009).
- M. Sluijter, A. Herzog, D.K.G. de Boer, M.P.C.M. Krijn and H.P. Urbach, “Ray-tracing simulations of liquid-crystal gradient-index lenses for three-dimensional displays,” J. Opt. Soc. Am. B **26**, 2035-2043 (2009).
- M. Sluijter, M. Xu, H.P. Urbach and D.K.G. de Boer, “On the applicability of geometrical optics to in-plane liquid-crystal configurations,” accepted for publication in Opt. Lett.

Conference proceedings

- M. Sluijter, W.L. IJzerman, D.K.G. de Boer and S.T. de Zwart, “Residual lens effects in 2D mode of auto-stereoscopic lenticular-based switchable 2D/3D displays,” Proc. of SPIE **6196**, 61960I (2006).
- D.K.G. de Boer, M.G.H. Hiddink, M. Sluijter, O.H. Willemsen and S.T. de Zwart, “Switchable lenticular-based 2D/3D displays,” Proc. of SPIE **6490**, 64900R (2007).
- M.P.C.M. Krijn, S.T. de Zwart, D.K.G. de Boer, O.H. Willemsen and M. Sluijter, “2D/3D displays based on switchable lenticulars,” J. SID **16/8**, 847-855 (2008).
- M. Sluijter, D.K.G. de Boer, H.P. Urbach, J. Stroemer and G. Cennini, “Ray-tracing simulations and applications of liquid crystal beam control devices,” Proc. of SPIE **7232**, 72320S (2009).

Conference contributions

- M. Sluijter, W.L. IJzerman, D.K.G. de Boer and S.T. de Zwart, "Residual lens effects in 2D mode of auto-stereoscopic lenticular-based switchable 2D/3D displays," oral presentation at SPIE conference, Photonics in Multimedia, Strasbourg, France (April 2006).
- M. Sluijter, D.K.G. de Boer and J.J.M. Braat, "General polarized ray-tracing of inhomogeneous uniaxially anisotropic media," poster presentation at Physics@FOM, Veldhoven, The Netherlands (January 2008).
- M. Sluijter, D.K.G. de Boer and J.J.M. Braat, "Ray-optics analysis of inhomogeneous uniaxially anisotropic media," oral presentation at European Optical Society (EOS) Topical Meeting on Photonic Devices, Utrecht, The Netherlands (April 2008).
- M. Sluijter, D.K.G. de Boer and H.P. Urbach, "Ray-tracing simulations of liquid crystal devices," poster presentation at 2^{nd} International Workshop on Liquid Crystals for Photonics, Cambridge, United Kingdom (July 2008).
- M. Sluijter, D.K.G. de Boer, H.P. Urbach, J.F. Stroemer and G. Cennini, "General polarized ray-tracing method for inhomogeneous anisotropic media," oral presentation at SPIE conference, Emerging Liquid Crystal Technologies IV, San Jose, USA (January 2009).

Reports

- M. Sluijter, *Ray-optics analysis of homogeneous uniaxially anisotropic media* (Philips Technical Note TN-2007/00025, 2007).
- R. Esteve, G. Cennini, J.F. Stroemer and M. Sluijter, *Light guiding in liquid crystal cells* (Philips Technical Note TN-2007/00653, 2007).
- M. Sluijter, *Ray-optics analysis of inhomogeneous uniaxially anisotropic media* (Philips Technical Note TN-2007/00892, 2008).

Filed patents

- W.L. IJzerman, S.T. de Zwart and M. Sluijter, *Oscopic display device using controllable liquid crystal lens array for 3D/2D mode switching*, international application number PCT/IB2007/050601 (2007).
- G. Cennini, R. Caputo, F. Pijlman, E.G. Onac, H.J. Cornelissen, J.F. Stroemer, M. Sluijter and T.C. Kraan, *Controllable light-guide and display device*, international application number PCT/IB2007/054503 (2007).
- J.F. Stroemer, E. Langendijk, G. Cennini and M. Sluijter, *A scanning backlight device with minimal temporal crosstalk*, international application number PCT/IB2009/051582 (2009).

Submitted ID's

- J.M.A. van den Eerenbeemd, F.A. Abeelen, G. Oversluizen and M. Sluijter, *Monitoring device for monitoring a movement of a fluid*, application number EP09169120.4 (2009).